CONTACT RESISTANCE EVOLUTION AND DEGRADATION OF HIGHLY

CYCLED MICRO-CONTACTS

THESIS

Christopher L. Stilson, Captain, USAF

AFIT-ENG-14-M-73

DEPARTMENT OF THE AIR FORCE
AIR UNIVERSITY

AIR FORCE INSTITUTE OF TECHNOLOGY

Wright-Patterson Air Force Base, Ohio

AFIT-ENG-14-M-73

CONTACT RESISTANCE EVOLUTION AND DEGRADATION OF HIGHLY

CYCLED MICRO-CONTACTS

THESIS

Presented to the Faculty

Department of Electrical and Computer Engineering

Graduate School of Engineering and Management

Air Force Institute of Technology

Air University

Air Education and Training Command

in Partial Fulfillment of the Requirements for the

Degree of Master of Science in Electrical Engineering

Christopher L. Stilson, B.S.E.E.

Captain, USAF

March 2014

AFIT-ENG-14-M-73

CONTACT RESISTANCE EVOLUTION AND DEGRADATION OF HIGHLY

CYCLED MICRO-CONTACTS

Christopher L. Stilson, B.S.E.E.
Captain, USAF

Approved:

//signed//	3 March 2014
Ronald A. Coutu, Jr., PhD (Chairman)	Date
//signed//	3 March 2014
Maj Derrick Langley, PhD (Member)	Date
//signed//	3 March 2014
Alex Li, PhD (Member)	Date

AFIT-ENG-14-M-73

Abstract

Reliable microelectromechanical systems (MEMS) switches are critical for developing high performance radio frequency circuits like phase shifters. Engineers have attempted to improve reliability and lifecycle performance using novel contact metals, unique mechanical designs and packaging. Various test fixtures including: MEMS devices, atomic force microscopes (AFM) and nanoindentors have been used to collect resistance and contact force data. AFM and nanoindentor test fixtures allow direct contact force measurements but are severely limited by low resonance sensors, and therefore low data collection rates.

This thesis reports the contact resistance evolution results and fabrication of thin film micro-contacts dynamically tested up to 3kHz. The contacts consisted of a lower contact of evaporated Au and a thin film upper contact, consisting of sputtered Au, Ru or RuO_2, with an Au electroplated structural layer. The fixed-fixed beam was designed with sufficient restoring force to overcome adhesion. The hemisphere-upper and planar-lower contacts are mated with a calibrated, external load resulting in approximately $200\mu N$ of contact force and are cycled in excess of 10^7 times or until failure. In addition, Au-Au contact pairs with a hemispherical upper an engineered lower contact were tested. These lower engineered contacts were constructed using gray-scale lithography. Contact resistance was measured, in-situ, using Holm's a cross-bar configuration and the entire apparatus was isolated from external vibration and housed in an enclosure to minimize contamination due to the ambient environment. Additionally, contact cycling and data collection are automated using a computer, integrated lab equipment and LabVIEW. Results include contact resistance measurements of Au, Ru and RuO_2 samples and lifetime testing up to 323.6 million cycles.

This is dedicated to my wife and loving family

Acknowledgments

Table of Contents

List of Figures

List of Tables

List of Symbols

Symbol	Definition
I	current (amps)
R	resistance (ohms)
V	voltage (volts)
M	moment
E	Young's modulus
I	inertia
δ"	rate of change for deflection

List of Acronyms

Acronym	Definition
MEMS	microelectromechanical systems
RF	Radio Frequency
AFM	atomic force microscope
CNT	carbon nanotubes
JKR	Johnson-Kendall-Roberts
DMT	Derjaguin-Muller-Toporov
FEM	Finite Element Methods
DUV	deep ultra violet light
SEM	scanning electron microscope
EDS	energy dispersive X-ray spectroscopy

CONTACT RESISTANCE EVOLUTION AND DEGRADATION OF HIGHLY CYCLED MICRO-CONTACTS

I. Introduction

Micro-contacts are used in a wide-range of applications from medical devices to overhead projectors. Micro-contacts are normally used in microelectromechanical systems (MEMS) relays or switches, where a micro-contact is opened and closed with relatively low force. Low power consumption, isolation, and reduced insertion loss are achieved by the mechanical actuation of the switch which physically opens or closes the circuit. The focus of this research will be on low power applications of micro-contacts with multiple contact materials and contact geometries. This chapter will describe micro-contact properties and operation, the problem statement, motivation, micro-contact test fixture solution, micro-contact support structure solution, and micro-contact failure modes.

1.1 Micro-contact properties and operation

MEMS switches can be utilized in the communication industry including in mobile phones [1]. Radio Frequency (RF) MEMS switches can be used as phase shifters, impedance tuners, and filters on control circuits found in many communication, radar and measurement systems [2]. MEMS switches offer higher isolation, lower insertion loss and less power consumption, compared to the conventional field-effect transistor; however, with lifetimes near 10^7 actuations, MEMS switch reliability is a major area for improvement for large-volume commercial applications [3]. These commercial opportunity present themselves as electronics continue to decrease in size but power

1

requirements increase or remain constant. The integrated circuit community is struggling to develop the future generations of ultra low-power digital integrated circuits [4]. With the better performance of MEMS micro-switches, the integrated circuit community is beginning to examine MEMS micro-switches to replace some integrated circuits [4] because of the better performance offered by MEMS Micro-switches.

1.2 Problem statement

To enhance reliability, circuit designers need simple and accurate behavioral models of embedded switches in CAD tools to enable system-level simulations [5]. One of the most common methods used to study the performance and reliability of micro-contacts is to cycle electrostatic actuated micro-contacts at high rates (in kHz range) until failure. Considering that the average number of cycles required for a micro-contact to reach failure can be beyond 10^7 cycles, the high cycle rate is a necessity for obtaining useful failure mode information from a micro-contact within a reasonable time frame [6]. But the use of electrostatic actuation is not without its issues. When using electrostatic actuation to open and close the micro-contact, the contact force must be then calculated. This calculation is based on the the applied voltage and the properties of the micro-contact. The issue with using a calculation for applied force is that applied micro-contact force is a key requirement for the determination of the effective contact area, as well as a potential influence on the development of a failure mode. This calculation of contact force can make the investigation into the influence of contact force on failure modes difficult.

To examine the effect of contact force on the performance and reliability of micro-contacts, researchers have used a modified atomic force microscope (AFM), with a micro-contact testing rate of ~ 0.5Hz, in order to apply a known contact force [7]. Considering the potential lifetime of a micro-contact being greater than 10^7 cycles, the modified AFM setup could require, if running continuously, more than 230 days for a micro-contact to reach failure [6]. There is a need for a micro-contact characterization

system which can apply a known contact force and permit further study into the performance and reliability of micro-contacts.

1.3   Motivation

Motivation for this research comes from the need to enhance a fundamental component of many RF systems which are used in defense technologies. This work focuses on the fabrication, improvement and development of a micro-contact test fixture and micro-contact support structures. The test fixture and micro-contact support structures enable lifecycle testing of micro-contacts for the study of micro-contact reliability as well as the underlying physics of micro-contact failure modes. By characterizing the physics of micro-contact failure modes, engineers will be able to advance technologies using micro-contacts and integrate them into new advanced systems.

1.4   Micro-contact test fixture solution

An important part of this research was improving a micro-contact test fixture capable of lifecycle testing as well as the fabrication and testing of micro-contact structures. First, the types of failure modes micro-contacts experienced in previous research have investigated in order to determine the modifications needed to the micro-contact test fixture [8]. Then the micro-contact test structure was modified, new test equipment integrated, and the automation software re-programmed.

1.5   Micro-contact support structure solution

As mentioned previously, this research focuses on the design, fabrication, and testing of micro-contact structures. First, research into the types of failures micro-contacts experience will be performed. This research will be used to develop a micro-contact structure suitable for diagnosing the micro-contact failures after lifecycle testing. The data gathered on the properties of the materials will be used and calculations will be performed to determine the appropriate thickness of the layers needed. Analytical methods are to be

used to characterize the behavior and physical phenomena of the micro-contact structures. The designed micro-contact structure will then be fabricated and tested using the micro-contact test fixture.

1.6   Micro-contact failure modes

It is important not only to cycle the micro-contacts to failure but to understand why they failed. First, research into the types of failures micro-contacts experience will be performed. Then the failures experienced was researched to identify the type of failure. Finally, the failures was investigated if the underlying causes can be identified. These underlying causes were used to direct changes to the micro-contact support structure or the test support structure.

1.7   Chapter Summary

Accurate predictors for the lifetime performance of micro-contacts are needed by engineers to enhance future technology. In order to develop accurate predictors, micro-contact physics and failure modes must be studied over the micro-contact's lifecycle. Proper characterization of the experienced failure mode by the micro-contact is vital to be able to determine if material properties or environmental factors limit the reliability of the micro-contact. An investigation will be performed to determine the requirements for a micro-contact structure suitable for the study of micro-contact physics and a micro-contact test fixture capable of lifecycle testing of micro-contact structures. The next section of this document provides a review of the relevant micro-contact knowledge areas, design, resistance modeling, contact materials, performance and reliability.

II.   Literature Review

2.1   Chapter overview

A review of relevant literature in micro-contacts is presented in this chapter. Advancements in micro-contact ares are discussed, to include, resistance modeling, contact materials, performance, and reliability.

2.2   Micro-contact resistance and modeling

Contact resistance modeling requires knowledge of the two contact material surfaces and their material properties. Holm initially studied clean contacts and did not consider contact contamination effects on contact resistance. Though it is not initially considered in the determination and description of micro-contact resistance, it can have a major effect [9]. Even though the bases of the cylinders appear to be similar, the contact areas are actually quite different, because no surface is perfectly smooth. The two surfaces are covered in asperity peaks or *a-spots*, which are what meet at the interface and become the contact area. These *a-spots* have been described as "small cold welds providing the only conducting paths for the transfer of electrical current" [10]. A graphical representation of the contacting a-spots and the effective radius of the contacting area can be shown in Figure 2.1 [11]. This effective area is used for making simplified contact resistance calculations.

Holm also investigated contact resistance changes due to plastic and elastic deformation of a-spots, which greatly affect the interface of the contact areas.

Majumder *et al.* model micro-contact switches with three steps. First was to determine the contact force available from the mechanical design of the electrostatically actuated micro switch. This contact force was a function of applied gate voltage. Second, was to determine the effective contact area as a function of contact force. Finally,
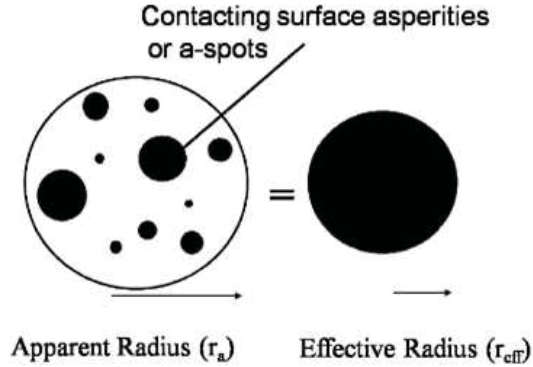
Figure 2.1: Picture of a-spots represented as effective radius. [11]

Majumder *et al.* determined the contact resistance as a function of the distribution and sizes of the contact areas [12]. Both Majumder and Holm note that the surface profile is sensitive to plastic and elastic deformation.

Elastic modeling is accurate for extremely low values of contact force of a few *mN* where surface asperities retain their physical forms after the contact force is removed. Plastic deformation permanent surface change occurs by the displacement of atoms in asperity peaks whereas neighboring atoms are retained under elastic deformation.

2.2.1 Elastic.

The a-spot contact area under elastic deformation is given by:

$$A = \pi r \alpha \tag{2.1}$$

where A is the contact area, r is the a-spot peak radius of curvature, and α is the a-spot vertical deformation [13].

For circular areas, 2.1 and 2.3 are related to the contact area effective radius (r_{eff}) through the Hertz's model [14]:

$$r_{eff} = \sqrt[3]{\frac{3F_{ce}R}{4E'}} \tag{2.2}$$

6

The normal contact force F_{ce} is given by:

$$F_{ce} = \frac{4}{3}E'\alpha\sqrt{r_{eff}\alpha} \qquad (2.3)$$

where E' is the effective Hertzian modulus derived from:

$$\frac{1}{E'} = \frac{1 - v_1^2}{E_1} + \frac{1 - v_2^2}{E_2} \qquad (2.4)$$

where E_1 and v_1 is the elastic modulus and Poisson's ratio for contact one respectively and E_2 and v_2 is the elastic modulus and Poisson's ratio for contact two respectively [14].

When deformation is no longer reversible and the applied load is approximately three times the yield point, ideal plastic material deformation begins.

2.2.2 Plastic.

Plastic material deformation is modeled using Abbott and Firestone's fully plastic contact model, which assumes sufficiently large contact pressure and no material creep [15].

Single a-spot contact area and force are defined using 2.5 and 2.6 [14]:

$$A = 2\pi R\alpha \qquad (2.5)$$

$$r_{eff} = \sqrt{\frac{F_{cp}}{H\pi}} \qquad (2.6)$$

where H is the Meyer hardness of the softer material, A is the contact area, R is the asperity peak radius of curvature, and α is the asperity vertical deformation. The effective contact area radius is then related to contact force by:

$$F_{cp} = HA \qquad (2.7)$$

An area discontinuity at the transition from ideal elastic to ideal plastic behavior is revealed when the elastic and plastic model are used together.

7

2.2.3 *"Classical" contact resistance modeling.*

The "Classical" contact resistance model for diffusive electron transport using Maxwell's spreading resistance theory:

$$R_{con} = \frac{\rho}{2r_{eff}} \tag{2.8}$$

where R_{con} is the constriction resistance and ρ is resistivity [9]. When the contaminate film resistance is neglected the Constriction resistance is equal to the contact resistance.

The "classical" macro switch contact resistance is shown in Equations 2.9 and 2.10 and shows that the elastic deformation $R_c \propto F_c^{-\frac{1}{3}}$ and plastic deformation $R_c \propto F_c^{-\frac{1}{2}}$ [9].

$$R_{cDE} = \frac{\rho}{2} \sqrt[3]{\frac{4E'}{3F_c R}} \tag{2.9}$$

where R_{cDE} is contact resistance for diffusive electron transport and elastic material deformation and

$$R_{cDP} = \frac{\rho}{2} \sqrt{\frac{H\pi}{F_c}} \tag{2.10}$$

where R_{cDP} is contact resistance for diffusive election transport and plastic material deformation.

Section 3.6 discusses the predicted contact resistance for the fixed-fixed micro-contact structure's micro-contact based on diffusive electron transport and elastic deformation with the assumption of a simplified contact area and no contaminant films. It was found that when modeling contacts of different metals, values like resistance and hardness were averaged [16].

2.2.4 *Spreading resistance.*

To model spreading resistance, Karmalkar *et al.* developed a closed-form model to predict accurate and complex calculations of circular and rectangular contact spreading resistances [17]. The method was to solve the three dimensional Laplace equation

$$\Delta^2 \Psi = 0 \tag{2.11}$$

subject to the appropriate boundary conditions in several iterations to consider changing geometries. This is different from Holm, who accounted for spreading resistance as a 5% increase in constriction resistance [9]. By incorporating the results of the different solutions, the resistance average was calculated [17]. Experimental tests revealed close (within 2%) agreement with standard numerical analysis software. Karmal *et al*. study found that the developed model accurately predicts all the trends of resistance, to include: a significant variation as a function of the smaller electrode location, dependence on the electrode separation-to-width ratio, and saturation with increase in the larger electrode area for both equipotential and uniform current density boundary conditions [17].

Timsit explored the effect of constriction resistance on thin film contacts [18]. He postulated that the spreading resistance of an asperity in a thin film will be drastically different than of an asperity in bulk material due to the different boundary conditions [18]. This convergence is visually represented in Figure 2.2.

Timist'e study revealed that the contact resistance for a contact with two identical films can be immediately calculated as twice the spreading resistance [18]. Also, the constriction resistance between two films of the same thickness, L, in contact over a constriction of radius, a, deviates greatly from the classical expression, $\rho/2\alpha$, for two contacting bulk solids wherever, a/L 0.02 [18]. A counter-intuitive discovery was shown revealing that spreading resistance in a radially-conducting film initially decreases with decreasing film thickness [18]. This result is counter-intuitive because the resistance of a solid conductor increases with decreasing thickness [18].

(a)

thin film

thin film

r_A

(b)
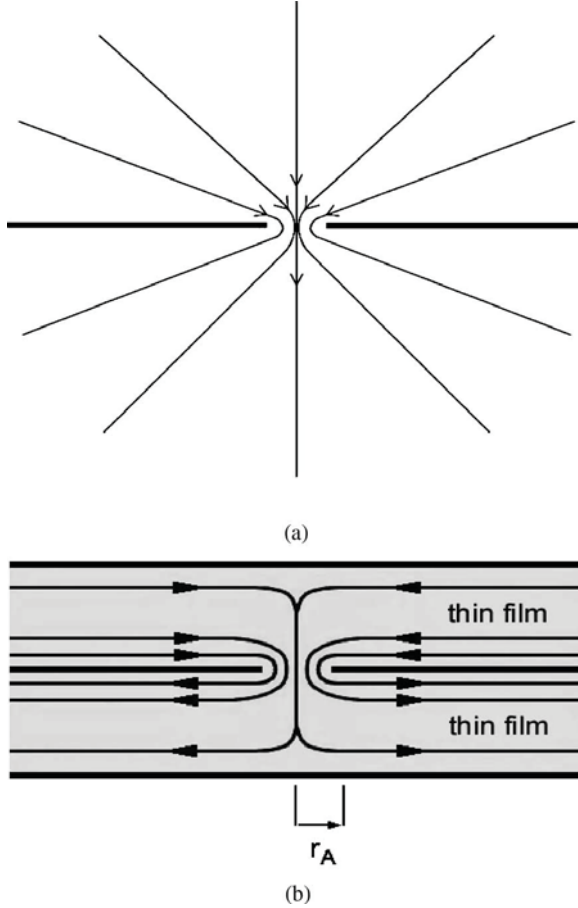
Figure 2.2: (a) Spreading of current streamlines in two "bulk" conductors in contact over a circular spot of radius a. (b) Spreading of current streamlines near a constriction between two thin films [18].

2.2.5 Thin film model.

A continuation of the spreading resistance is the Thin Film Model presented by Zhang *et al.* at the Holm 2013 conference [19]. In this paper, Zhang *et al.* focus only on the thin film geometry shown in Figure 2.3, which it was label either as a Cartesian (rectangular symmetry) film or as a cylindrical film [19]. The thin film is has a thickness h an electrical resistivity ρ. A voltage V_0 is applied uniformly along the edge of the thin film, at $y = b(r = b)$. A grounded electrode is attached to the top region, AB, where the B-coordinates are $y = +a(r = a)$ in the Cartesian (cylindrical) geometry. Following Holm,

Zhang *et al.* identify the terminal AB as the single a-spot [9, 20, 21]. Zhang *et al.* showed that our exact calculation of the spreading resistance for the contact geometry of Figure 2.3 yields insights for the proper interpretation of experimental measurements of constriction resistance [22–24]. For the cylindrical geometry, Zhang *et al.* found that the normalized spreading resistance can be represented by:

$$R_s = \frac{\rho}{4a}\bar{R}_s \tag{2.12}$$

where the normalized resistance can be shown in:

$$\bar{R}_s = 1 - 2.2968\left(\frac{a}{h}\right) + 4.9412\left(\frac{a}{h}\right)^2 - 6.1773\left(\frac{a}{h}\right)^3$$
$$+ 3.811\left(\frac{a}{h}\right)^4 - 0.8836\left(\frac{a}{h}\right)^5 \quad 0 \le a/h \le 1 \tag{2.13}$$

or:

$$\bar{R}_s = 0.28 + 0.0502\left(\frac{h}{a}\right) + 0.0523\left(\frac{h}{a}\right)^2 \qquad 1 \le a/h \le \infty \tag{2.14}$$
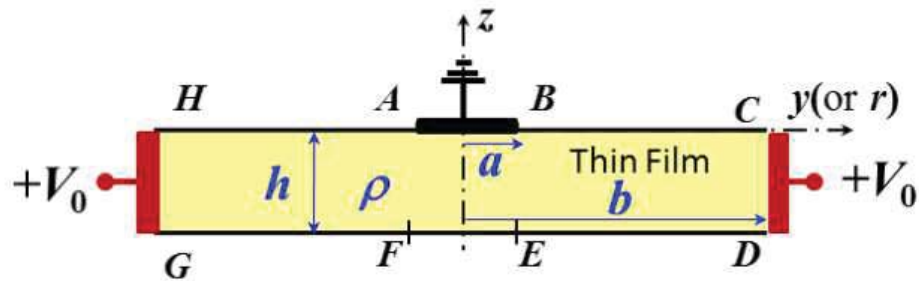
Figure 2.3: Cartesian (2D cross-sectional view) and cylindrical thin film. In the cylindrical geometry, the vertical axis at the center is the axis of rotation [19].

2.2.6 Resistance and contact modeling.

While dealing with quantum theory to describe current flow through nano-scale asperities is being explored, some researchers are developing methods to simulate electrical contact resistance of ohmic switches with Finite Element Modeling (FEM). Pennec *et al.* examined the impact of surface roughness on the electrical contact resistance under low actuation forces (from a $10\mu N$ to $10mN$) [25]. An important aspect of their work was to clearly define the surface roughness of the contact. Common practice is to take the average radius of curvature of the asperities, which is determined by a measurement of the surface profile [26]. The drawback to this method is that the determination of the average radius is subjective to the scale of the observation, and is also limited by the measurement resolution [27, 28]. In order to clearly define the surface roughness of the contact, three methods were examined: statistical, fractal, and deterministic [25]. A statistical approach is based on a stochastic analysis, which can be limited to the resolution of the measuring instrument [25]. A fractal method, on the other hand, random surface texture is characterized by scale-independent fractal parameters [25]. The deterministic approach was chosen due to its closest representation of the actual surface [25, 29]. Deterministic methods capture discrete data points for real heights on the surface which avoids assumptions of the micro geometry of the a-spots [25]. Kogut states that even though there are several methods to model contacting rough surfaces, the most convenient one is the probabilistic approach [29]. This approach replaces the two rough surfaces by a smooth surface in contact with an equivalent rough surface, replacing asperities with simple geometric shapes, and assuming a probability distribution for the asperity parameters [30]. The probabilistic model was developed by Greenwood and Williamson for elastic contacts [31].

As shown in Figure 2.4, using an AFM, the team was able to capture 3-D data points of contact bumps and apply a low resolution mesh in order to quickly determine the

effective contact area under $100\mu N$ of force [25]. By stepping up the resolution for the

effective contact area to the effective computation memory limits, Pennec *et al.* were able

to model a contact resistance in agreement with previous measurements[25]. While their

method did not take into account contaminant films, the results show that including the

fine-scale details of the surface roughness must be taken into account when calculating

contact resistance [25]. However, while AFM's can achieve 1nm resolution of surfaces,

the number of contact elements and definition of elastic-plastic materials in the model can

prevent the calculations from succeeding due to computer memory limitations [25].

Conclusive evidence is given that reducing the sampling interval from 1nm to 10nm is

sufficient for the calculation of electrical contact resistance [25].
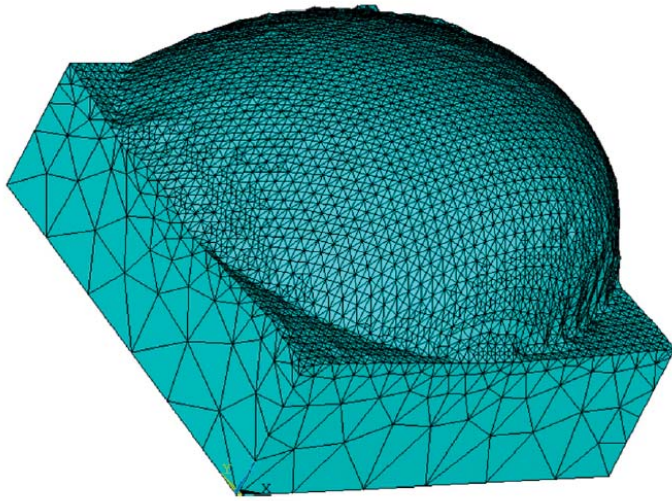
Figure 2.4: Geometry of finite element mesh in rough contact bump [25].

Similar to fractal, Jackson *et al.* considered multi-scale roughness to be sinusoids

stacked into layers to represent the rough surface [32]. While discrepancies exist between

the statistical methods and layered sinusoids, Jackson *et al.* was able to show similarities

for both elastic and elastic-plastic deformation [32]. The model is very much in agreement

with standard methods until higher force loads are reached [32]. However this model differs at higher loads, when the contact radius is relatively large compared to the asperity tip radius [32]. This method of stacking sinusoids however is not limited to contact resistance but is also employed to model adhesion [33]. The stacked sinusoids allow for a more practical representation of a multiscale surface, where the classical approximation for area is a simplified model that typically bundles asperities into a few contact areas as shown in Figure 2.1 [33].

2.2.7   *Resistance and Contact Modeling Conclusions.*

For contact resistance modeling, contact material deformation and the effective contact area radius are the two primary considerations [34]. An assumption that individual a-spots are sufficiently close and that a single effective area model is typically made to determine specific electron transport regions by comparing the effective radius and mean free path of an electron [34]. As presented in this section, the use of area models to characterize the surface topology, describing the appropriate effective area for modeling is difficult. From the modeling of the surface using statistical, deterministic, sinusoidal, or fractal means to the models of contact resistance based on all the deformation modes, the development of a thin film will widen the variance between simulated and actual results. Contact materials also have an integral role in determining the performance and reliability of micro-switches. Material properties influence the contact resistance and performance. Due to the low resistivity, Gold, palladium, and platinum are commonly used [35]. Due to the fact that these materials are very soft and wear easily, other materials, allows and combination materials have been examined for their effectiveness at lengthening the lifecycle and the performance of the contact. Some examples of materials used include Au, Pt, Ru, RuO_2 Rh, Ni, were compared in mixed configurations to try and increase reliability [36, 37].

2.3   Beam modeling
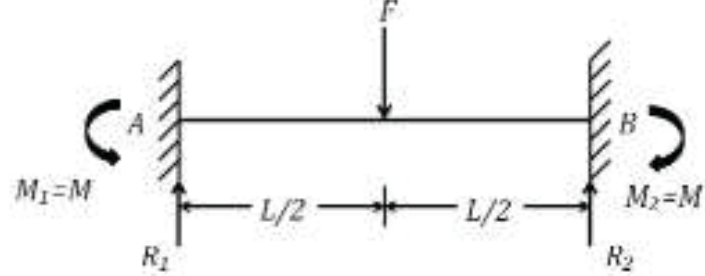
Figure 2.5: Fixed fixed beam model [38].

In order to determine the force required to make contact using the fixed-fixed beam micro-contact support structure, the micro-contact support structure is modeled as a simple fixed-end beam with a concentrated load, F, at the midpoint. Figure 2.5 shows the simplified beam's moment diagram. Because of beam symmetry and F in the vertical direction, the moments on either end of the beam are equivalent and lead to:

$$M = \frac{Fx}{2} - M_1 \qquad\qquad (0 \leq x \leq \frac{L}{2}). \qquad\qquad (2.15)$$

Mohr's theorems provide the relationship between the moment M, Young's modulus E, inertia I, and rate of change for deflection $\ddot{\delta}$:

$$EI\ddot{\delta} = M = \frac{Fx}{2} - M_1 \qquad\qquad (0 \leq x \leq \frac{L}{2}). \qquad\qquad (2.16)$$

Integrating 2.16 twice to obtain deflection δ gives:

15

$$EI\delta = \frac{Fx^3}{12} - \frac{M_1 x^2}{2} + C_1 x + C_2 \qquad (0 \le x \le \frac{L}{2}). \qquad (2.17)$$

Boundary conditions and symmetry reveal:

$$C_1 = C_2 = 0 \qquad (2.18)$$

$$M_1 = \frac{FL}{8} = M_2 \qquad (2.19)$$

Substitution of 2.18 and 2.19 into 2.17 provides the deflection equation:

$$\delta = \frac{FX^2}{48EI}(3L - 4x) \qquad (0 \le x \le \frac{L}{2}) \qquad (2.20)$$

Maximum deflection is found at $x = \frac{L}{2}$, which reveals:

$$\delta = \frac{FL^3}{192EI} \qquad (2.21)$$

where δ is deflection, F the applied center load, L the length of the beam, E the Young's modulus of the beam material, and I is the moment of inertia [38]. The moment of inertia is given by:

$$I = \frac{wt^3}{12} \qquad (2.22)$$

where w is the width of the beam and t is the thickness of the beam [38]. Further investigation into the beam thickness and force required to close can be found in the Analysis chapter.

2.4   Device fabrication techniques

MEMs is defined by Lee as "systems that consist of small scale electrical and mechanical components built for a specific purpose" [39]. MEMs fabrication can be separated into three categories, bulk micromachining, surface micromachining, and micromolding. The following sections will discuss each of these three fabrication techniques.

2.4.1   Surface micromachining.

Lee describe surface micromachining as "formation of a structural layer on a sacrificial structure and removal of the sacrificial layer to form a structure" [39]. These structures can be formed using a combination of photolithography, film deposition, and etching. Photolithography was used to imprint desired patterns to form the shapes of structures either through etching or deposition. This surface micromachining was used in many portions of this research.

2.4.2   Bulk micromachining.

Lee defined bulk micromachining as "direct machining of bulk material". This bulk micromachining is done with an etching process. The art of selectively removing precise amounts of silicon from a substrate has been thoroughly studied, and is used to fabricate membranes, trenches, holes, and undercut surface structures [39]. Liquid or "wet" etching or "dry" etching techniques are used to form either isotropic or anisotropic etch profiles. Wet etching typically involves aqueous chemistry, typically acids in bases in which the bulk silicon is submerged [39]. Dry etching does not submerge the wafer in a liquid and consists of vapor and/or plasma [39]. Bulk micromachining was used in the processing involving gray-scale lithography and etching which will be discussed in more detail in the next section.

17

2.4.3   Micromolding.

A third process, known as micromolding, builds a polymer mold with subsequent material deposition into the mold volume to form a structure [39]. These devices are then released from the molds. These molds can either be a one time used or made for multiple uses. Micromolding was not used in the research.

2.5   Device fabrication used for research

The following section discusses the fabrication used during this research. Including the fabrication of polyMUMPs devices, fixed-fixed beam and gray-scale lithography.

2.5.1   PolyMUMPs fabrication.

The PolyMUMPs process is a three-layer polysilicon surface micromachining process that is available for MEMS engineers to have their designs fabricated; one layer of polysilicon is used as a ground layer and the other two are mechanical layers [40]. The process includes a total of seven layers, with the remaining four layers being metal layers and sacrificial oxide layers, as shown in Figure 2.6 [40].

Nitride is used as an electrical isolation layer between the polysilicon (poly) layers and the substrate. The oxide layers are used as sacrificial layers while the poly 0 layer is a ground layer and poly 1 and poly 2 are structural layers. The metal layer is a gold layer which is commonly used for electrical contact pads and electrical wiring.

2.5.2   Fixed-fixed beam micro-contact support structure.

The fixed-fixed beam micro-contact support structure is fabricated using surface micromachining processes. Surface micromachining involves depositing, patterning, and etching sacrificial and structural layers. A structure made by surface micromachining is released when sacrificial layers are removed and the structural layers remain. Figure 2.7 shows the surface micromachining process used to fabricate the fixed-fixed beam micro-contact structure [8].

18

	Poly0		Poly1		Poly2		Metal
	Nitride		1st Oxide		2nd Oxide		
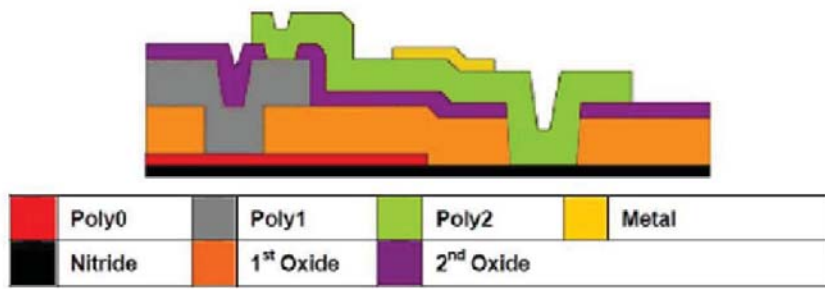
Figure 2.6: Cross-section of PolyMUMPS seven process layers [40].
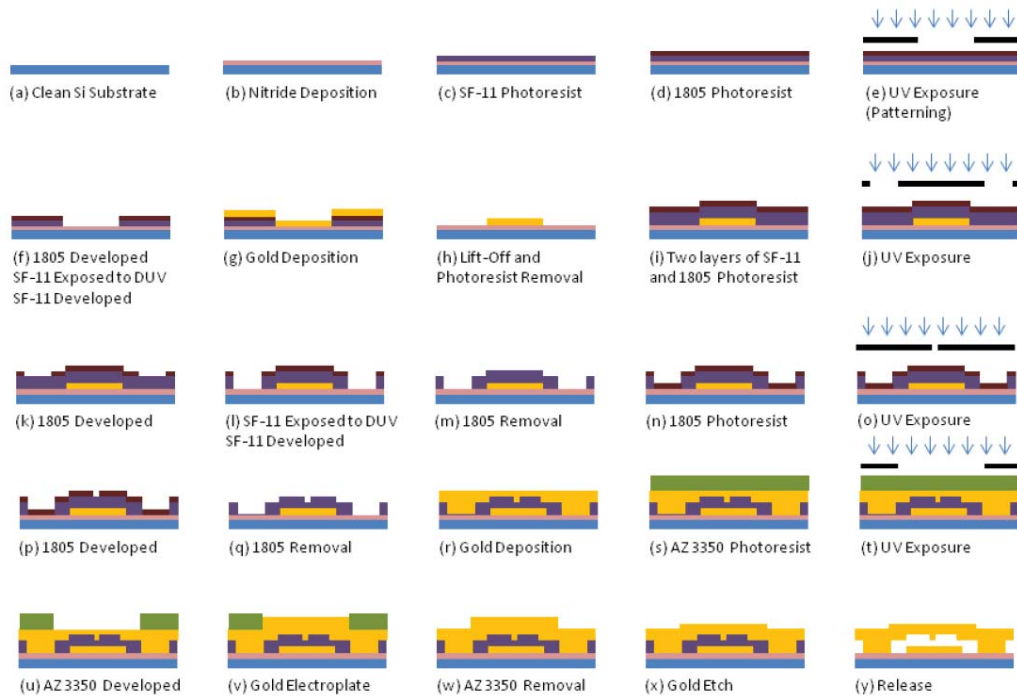
Figure 2.7: Surface micromachining process for fixed-fixed beam micro-contact support structure [8].

19

Beginning with (a), a silicon substrate is cleaned before a layer of nitride is deposited (b). The nitride layer acts as an electrical isolation layer. In (c) and (d), a layer of SF-11 photoresist and 1805 photoresist is established on the surface of the nitride coated wafer. The 1805 serves as a mask for patterning the layer of SF-11. In (e), the 1805 is patterned by a mask and exposed to ultraviolet light. The ultraviolet light breaks the chemical bonds of the photoresist in the exposed areas and allows the exposed 1805 to be developed away (f). After the 1805 is developed, the exposed SF-11 is subjected to deep ultra violet light (DUV) which, similar to the 1805, breaks the chemical bonds of the exposed SF-11 and allows the exposed area to be removed. A gold layer is then deposited in (g). Following deposition, the remaining gold is lifted off and all photoresist is removed (h). What remains in (h) is the bottom metal layer of the fixed-fixed beam micro-contact support structure.

For the mechanical layer of the fixed-fixed beam micro-contact support structure, two layers of SF-11 and a layer of 1805 photoresist are coated on the wafer. The 1805 is patterned and developed in (j) and (k) and then the SF-11 is exposed to DUV and developed away (l). The 1805 is then removed in (m) and 1805 is placed on the wafer in (n). This process allows for the patterning of the micro-contact bump. The 1805 is patterned and developed and the exposed SF-11 is exposed again to a partial DUV to establish the micro-contact bump (o) and (p). In (q), the 1805 is removed and Au is sputtered in (r) as a seed layer for electroplating. AZ 3350 photoresist is applied in (s) and patterned (t) and developed (u) for electroplating (v). Once the desired amount of Au has been electroplated, the AZ 3350 is removed (w). To remove the seed layer, an Au etch is performed (x). To release the device, the sacrificial SF-11 is removed (y). Pictures and descriptions of the masks used in this process that was modified from previous research can be found in Appendix D [8].

2.5.3   *Gray-scale lithography.*

The ability to develop 3D micro-structures is of great importance for increasing optical and electro-mechanical device performance. Previous technologies used multiple direct writing and photolithography steps, or customized equipment [41–43]. However, these technologies are restricted to a limited range of shapes and do not utilize batch processing. Gray-scale technology has emerged and has enabled the development of arbitrary 3D micro-structures in various materials [43–45]. Use of gray-scale technology allows 3D shaping of silicon to be performed in a single photolithography step with subsequent dry etching [46].

Gray-scale lithography utilizes an optical mask patterned with varying intensities of gray pixels and spacing. This optical mask combined with laser lithography allows a uniform intensity on the photoresist surface across the pattered region. Changing the size of the pattern and color of the gray, changes the intensity of the laser power; with each distinct power level corresponding to a gray level. The height profile in the photoresist after development (composed of photoresist gray levels) will depend upon the incident intensity, time of exposure, and photoresist contrast.

Gray-scale optical masks were designed and developed for a Heidelberg lithography system to produce various structures in positive photoresist for characterization of the profile. The gray levels were patterned on the optical mask by varying the size of structures. Due to machine limitations, only 100 of the 255 gray color variations are used to produce 100 unique height levels exist within the chosen method of patterning [47]. This can lead to a stepped profile in the photoresist [47]. Also included on the optical masks were features to measure non-uniformity in the photoresist: fully exposed level heights and a opaque region (no exposure). These features will provide information regarding the uniformity of the photoresist. The gray level features include non-uniformity coming from all steps: photoresist spinning, exposure, and development [41].

2.6 Contact materials for performance and reliability

As discussed in Section 2.2 on resistance modeling, material properties can have an impact on contact resistance. The inherent properties of the material chosen for the contact are important to the life-cycle of the contact. Some material properties that are taken into account when selecting materials included resistivity, oxidation properties, hardness, and melting points. In general, contacts are desired to have excellent electrical conductivity for low loss, high melting point to handle the heat dissipated from power loss, appropriate hardness to avoid material transfer, and chemical inertness to avoid oxidation [48]. In this section the discussion of materials will be discussed in two sections, metals and use of carbon nanotubes (CNT) in micro-contacts

2.6.1 Metals.

Due to its low electrical resistivity and low sensitivity to oxidation, gold is widely used as a contact material in MEMS [49]. To also take advantage of other material properties, alloys are often used. These alloys can be created to take advantage of material properties to minimize the effect of material transfer [3]. As seen in Figure 2.8 and Figure 2.9, Au-Ni alloy contact resists material transfer better than an Au-Au contact [3].

McGruer *et al*. showed that ruthenium (Ru), platinum (Pt), and rhodium (Rh) were susceptible to contamination and the contact resistance increased after a characteristic number of cycles, while gold alloys with a high gold percentage showed no contact resistance degradation under the same test conditions [3, 50]. Similarly, Coutu *et al*. showed that alloying gold with palladium (Pd) or Pt extended the lifetimes of micro-switches with only a small increase in contact resistance [14].

Broue *et al*. characterized upper and lower contact materials of Au/Au, Au/Ru, and Ru/Ru by examining the temperature of the contact with power applied to determine its performance limitations [37]. The contact with the best performance was the Au/Ru
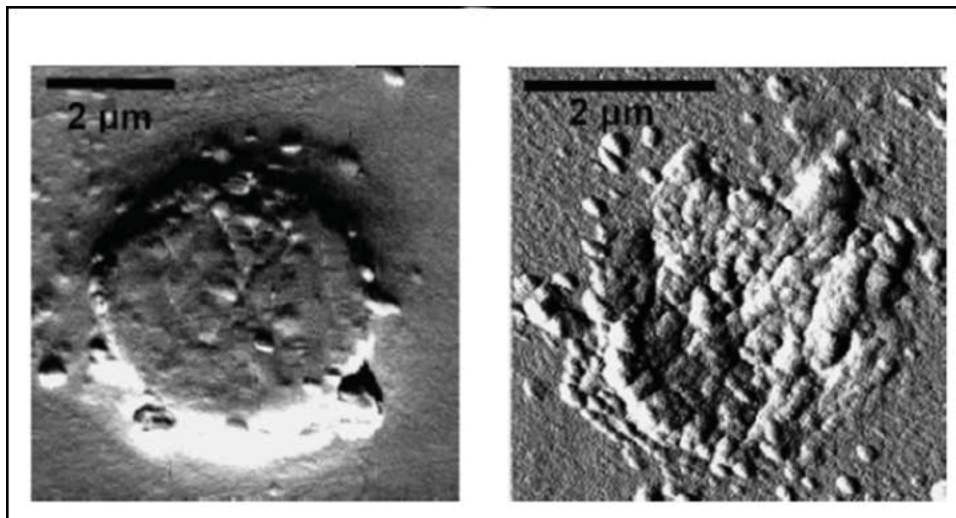
Figure 2.8: Au on Au contact scanning electron microscope images of contact surfaces. Left:the top electrode. Right:the bottom electrode [3].
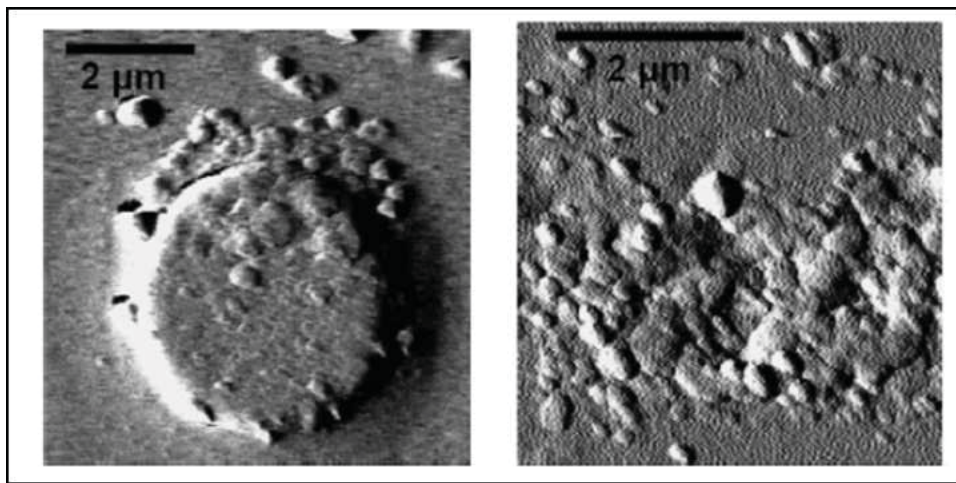
Figure 2.9: Au-Ni alloy contacts scanning electron microscope images of contact surfaces. Left:the top electrode: Right is the bottom electrode [3].

combination contact, where the contact temperature increased with the current level

without reaching a maximum [37]. An explanation to the difference in performance was

offered that the contact temperature of the Au/Ru contact is more stable because the softening temperature is theoretically not reached for the same contact current [37].

In the interest of exploring the limitations of Ru, Fortini *et al.* compared how asperity contacts form and separate in gold and ruthenium [51]. Their technique established an appropriate interatomic potential in order to apply the Molecular dynamics simulation. Molecular dynamics simulation is a powerful tool for studying defect formation, deformation, and adhesion on the nano-scale level [51]. The Molecular dynamics technique enabled the team to understand the formation and separation of nanoscale asperity contacts by simulating the motion of the atoms [51]. The simulations showed that Ru was ductile at T=600K and more brittle at T=300K, where it separated by a combination of fracture and plasticity [51]. Gold exhibited ductile behavior at both T=150K and T=300K [51].

Another metal is the use of conductive oxides, such as RuO_2. In thin film form, RuO_2 is a stable conducting oxides in rutile structure [52]. A relatively low resistivity value of $40 m\Omega \cdot cm$ for a sputtered RuO_2 film has been reported [52]. Futher Lee *et al.* reported that Ru and RuO_2 electrode prepared by dc sputtering in an Ar/O2 mixture ambient exhibited low contact resistance [53].

2.6.2   *Use of CNTs in micro-contacts.*

Despite carbon being a key component of frictional polymers, Yaglioglu *et al.* examined the electrical contact properties of CNT coated surfaces [54] . The high Young's Modulus and potential for low resistance of CNTs make them suitable candidates for micro-switch contacts. For instance, Au contacts with a substrate coated with tangled single-walled CNTs were shown to have a resistivity between 1×10^{-4} and $1.8 \times 10^{-4} \Omega m$ [54]. Yunus *et al.* explored two contact pairs with carbon nanotubes: Au to multiwall carbon nanotubes (MWCNTs), where one electrode is Au and the other is MWCNTs, and Au to Au/MWCNT composite in a vertical configuration, where the contact interface is

Au on Au [55]. Figure 2.10 shows an SEM image of the Au/MWCNT composite. This vertical configuration differs from the CNT clumps discussed earlier, as the CNT clumps have no set direction.
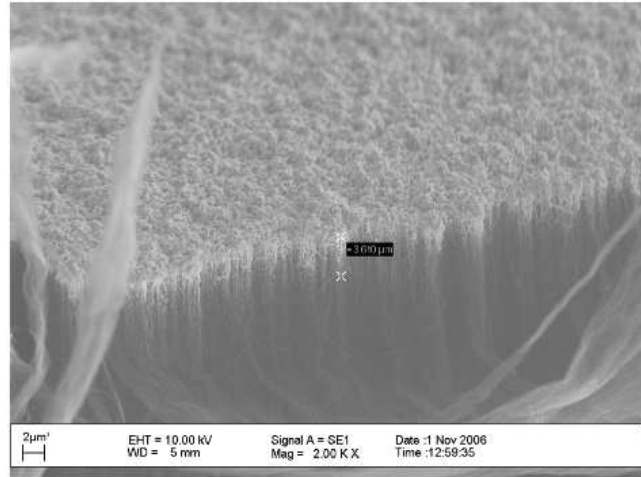
Figure 2.10: Scanning electon microscope image of 2-4μm of Au coating on multi-walled carbon nanotubes [55].

A study was conducted by Choi *et al.* to explore the current density capability of a CNT array with an average CNT diameter of 1.2nm, site density of 2$CNT/\mu m$, and the number of CNTs for devices with 1μm channel width ranged from one to three [56]. It was reported that a high current density of 330A/cm^2 at 10V bias was successfully transmitted through the contact without any noticeable degradation or failure [56]. A reliability test, as seen in Figure 2.11, with an input current of 1mA showed repeatable and consistent contact characteristics over a million cycles of operation [56].

Additional information regarding the use of CNTs in micro-contacts can be found in research done previously at AFIT [57]
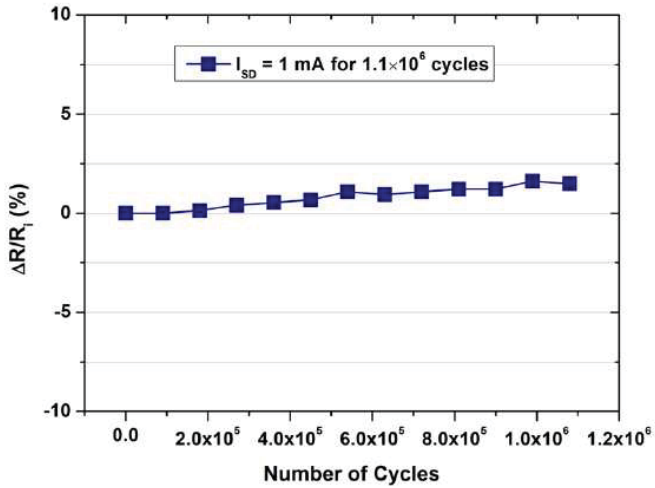
Figure 2.11: Reliability test results shown the resistance change over $1.1x10^6$ cycles at 1mA in non-hermetic environment [56].

2.7 Failure modes and reliability

Failures can be separated into three categories, cold switch failure, hot switch failures and contaminate failures. *Cold* switching is a term that represent switching where power is applied only when the contact is in the closed position. Conversely, *hot* switching is where power is applied to the switch when the contact is opening and/or closing. An in-depth review of failure modes can be found in Toler *et al.* [57]. In this section it will focus on stiction, fretting, material transfer, electromigration and contaminant films.

2.7.1 Stiction.

Stiction, or adhesion, is a failure mode which is caused by capillary, electrostatic, chemical and van der Waals forces [58]. Adhesion can be described by Hertz, Johnson-Kendall-Roberts (JKR), or Derjaguin-Muller-Toporov (DMT) models [59]. The Hertz model is traditionally used for modeling elastic adhesion between non-deformable surfaces [59]. For deformable surfaces, the JKR or DMT model is utilized. The JKR model accounts for surface energy of the contacting surfaces and is valid for soft elastic materials with higher surface energies [59]. The DMT model emphasizes the cohesive

26

forces at the contact periphery and is valid for hard, stiff solids with low surface energies [59]. These two models, JKR and DMT, represent the two extreme cases in adhesion interactions and most materials lie between these two models [59]. Another model was developed by Wu *et al*. to predict stiction due to van der Waal forces [60]. The key advantage for this model is that it accounts for a wide variety of parameters such as surface topography, or surface cleanliness, while still enabling complete modeling of the larger MEMS structures using Finite Element Methods (FEM) [60]. The disadvantage of this approach is the absence of the effect due to capillary forces [60].

2.7.2 *Fretting.*

Another type of cold switch failure is fretting. Fretting is a form of structural fatigue which is defined as accelerated surface damage occurring at the interface of contacting materials which is subjected to small oscillatory movements [61]. Braunovic *et al*. state that the lack of published information of failures caused by fretting is due to the fact that fretting is a "time-related process causing an appreciable effect only after a long period of time as a result of accumulation of wear debris and oxides in the contact zone". The fretting condition also is significantly influenced by contact force. As contact force is increased, the contact resistance declines. This decline continues until the insulating layer forms from wear debris and the formation of an oxide . This insulating layer prohibits the continued increase of force to lower resistance [61].

2.7.3 *Material transfer and electromigration.*

Many of these failures stem from the large temperature rise which occurs in a contact region when the contact area is small, and only a few a-spots are in contact [1]. This increased contact temperature at these localized spots may cause softening of the metal and lead to bridge transfer. Bridge transferring can cause internal stresses in the contact and cause the metal to crack [61]. Cracking leads to limited conduction paths and areas to

promote non-conducting oxides and contaminates to form, ultimately leading to failure of the contact [61].

Electromigration is another form of material transfer which can cause micro-switch failure. Electromigration is defined as "the forced motion of metal ions under the influence of an electric field" [62]. As electromigration occurs, voids form and ultimately these voids cause device failure [62]. Braunovic states that an increase in current density in the a-spots can be substantial and create the right conditions for electromigration to occur [62].

2.7.4 Contaminant film.

Another type of failure mode is the development of contaminant film development such as frictional polymers. Metals most susceptible to the development of frictional polymers are the platinum group metals and any other "catalytically active metal" [61]. Holm points out that thin films, like oxides, develop over time on the contact surface and act as insulators, greatly increasing contact resistance [63]. The same is true for micro-switches. The effects of the films which develop on a micro-contact are orders of magnitude greater than those on macro scale contacts. Films on micro-contacts can render the contact useless and disabled. A particularly damaging film is the development of a frictional polymer [61]. Frictional polymers are organic films, sometimes referred to as deposits, that develop on commonly used contact materials when there are low levels of organic vapors or compounds evident in the operating environment of the contact [61].

2.8 Chapter summary

This review provides insight into the properties and concepts necessary for designing micro-electrical contacts for DC and RF MEMS switches. The basic theories behind the aspects of contact resistance modeling, contact materials, and failure modes are discussed and explored. A survey of the challenges for these areas in ohmic contacts is provided. Complete models of contact resistance for various deformation models are shown. The

decision for contact materials is investigated by examining the impact of material properties on the characterization of the contact. The next chapter will provide insight into the methods used to test these micro-contacts.

III. Methodology

3.1   Chapter overview

When collecting data for investigating the evolution of the micro-contact, it is important to have a methodical and succinct process to produce reliable and repeatable data. This chapter describes the research methodology used to explore and characterize the evolution of micro-contacts over their lifetime of performance. The methodology will include describing the test stand, the types of test to be performed, the micro-contact support structure, contact modeling and the types of post test examinations that will be performed.

3.2   Test stand

The test stand was designed to characterize the performance over the lifetime of a micro-contact. The test stand consists of a nitrogen environment that still allows for manipulation of the micro-contact and connections to be able to monitor the contact throughout testing.

The test stand allows for rapid actuation of a micro-contact with a known force and frequency. A Femto Tools FT-S270 force sensor was used to determine the amount of force applied to the micro-contact test structure. A Thorlabs BPC301 piezo motor and controller was used to apply force to the micro-contact and to actuate the sensor towards the micro-contact support structure. Micro-manipulators were used to align the force sensor with the micro-contact support structure.

Testing in a nitrogen environment reduces the opportunity for oxides and other organic films to develop prematurely and simulates a hermetic environment that a micro-contact would normally operate in.

The micro-test structure fixture is a fabricated device on a wafer that is attached to a carrier using crystal bonder. The micro-contact test structure was then wire bonded to the breakouts of the carrier to make it easier to measure the current and voltage across the contact. This configuration also reduces the probability of physically interacting with and changing the surface of the micro-contact test structure and removes the necessity for probes. The wafer was wire bonded to the carrier and placed into the carrier socket which has pins for every wire bond. These pins were wire wrapped separately and the wires were guided outside of the enclosed test fixture. Micro-manipulators are available in the x, y and z axes to allow for the alignment of the force sensor with micro-contact. This configuration is shown in Figure 3.1.
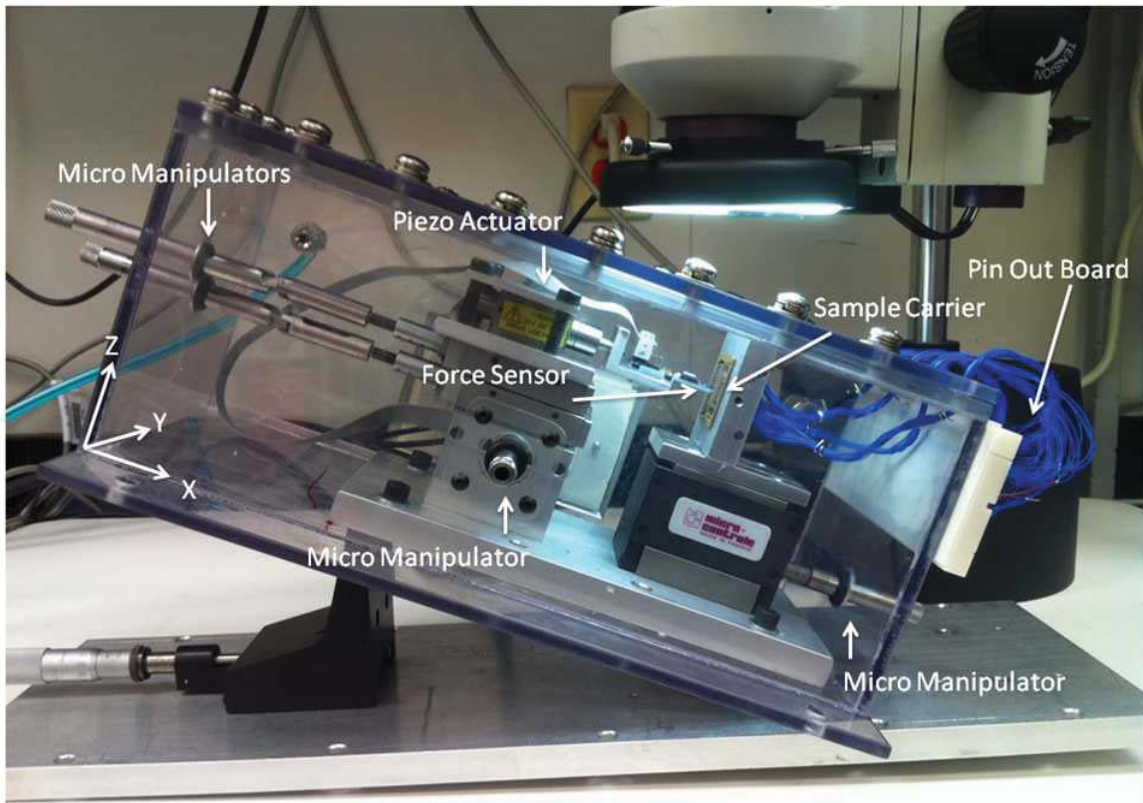
Figure 3.1: Test stand, showing major components encased in a nitrogen environment.

Using this test stand, three types of tests were performed, the initial contact test, cold switch test and hot switch test.

3.3   Equipment upgrade

This research started with the task of upgrading of the test equipment. It was found in previous research with the test equipment that many of the test runs had a minimum contact value around 0.2Ω [64, 65]. One of the possible explanation for this was that the measurement of the current through and voltage across the micro-contact was near the measurement floor of the Agilent equipment. It was determined that an equipment upgrade was needed. The upgrade was to National Instruments (NI) devices, this was due to the integration between NI and LabVIEW software, as well as the modular aspects of the NI equipment. The NI equipment comes as cards that can be added to boxes so that each box can be customized to the needs of the user. The boxes include power, computer communications, and interconnects buses between cards for triggering and clock synchronization. The following equipment was purchased:

- NI-4070 digital multimeter to measure the voltage across the contact with a measuring range used in this testing of $1V$ it has a resolution of $1\mu V$.
- NI-4072 digital LCR multimeter to measure current through the contact with a range used in this testing of $20mA$ and a resolution of $10nA$.
- NI-5402 arbitrary Function Generator was used to drive the piezoelectric actuator during cycle testing when the piezoelectric actuator is moved in response to an input waveform. The waveform used in this test was a sine wave.
- NI-5402 arbitrary function generator was used to drive signal across the micro-contact during cycling. The waveform used in testing for this was a square wave.

- NI-4110 programmable DC power supply was used during measurement cycles for applying the potential across the micro-contact. During testing the system was set up with a constant current of $0.02mA$ with a max applied volage of $1V$.

With this equipment, the devices displayed a much lower contact resistance than previously observed.

3.4 Types of tests

The following is an overview of the tests that the fixture can preform. A more in-depth review of the Labview program and the types of test preformed can be found in Appendix F

3.4.1 Initial contact testing.

The initial contact test applies a load to the micro-contact and determines the amount of force needed to initiate surface contact. For this research, the initial contact test was applied for every cycle that required a measurement. The step size, time interval, and maximum applied force was set and the system incremented the force sensor in the set step size until the force sensor limit was reached. At each increment, voltage, current, and force measurements were recorded. Following the virgin contact test, either a cold or hot switch test could be performed to examine failure modes.

3.4.2 Cold switch testing.

Cold switching promotes the mechanical failure of the micro-contact by applying current only when contact is already made and removing current before contact break; thereby reducing the probability of electrical failure modes. For the cold switch program, the micro-contact is first closed before current is applied. With the contact closed, the desired current level is applied to the micro-contact and the current and voltage is measured. After the measurement of current and voltage, the applied current is then

turned off and the micro-contact is opened. These steps are repeated for the desired number of cycles. Figure 3.2b shows an example of the cold switch test waveform.

3.4.3   Hot switch testing.

The hot switch test applies a given current while actuating the micro-contact open and closed for a given number of iterations. The user is required to input the position of desired contact force, the maximum applied contact force, the number of cycles, the applied current, as well as the number of cycles between measurements. Using this information, the program applies the set level of current and actuates the micro-contact open and closed for the set number of cycles. Figure 3.2a shows an example of the hot switch test waveform.
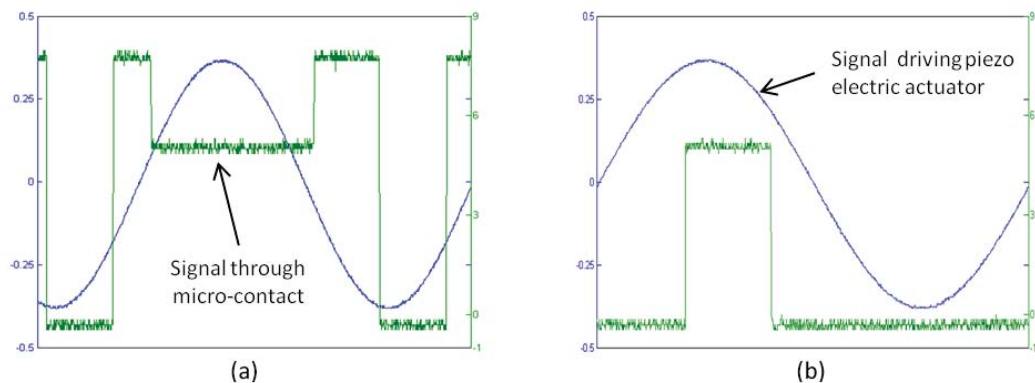
Figure 3.2: This shows an example of the (a) hot switching and (b) cold switching waveforms. The blue line is the signal line driving the piezo electric actuator and green line is the signal line across the micro-contact.

3.4.4   Reliability testing.

Reliability testing used the previous types of test, cold or hot switch test, and repeats that test until the micro-contact displays a failure. Type of failures experience included failure to close when contact between the upper and lower contact was never made due to

the presence of an isolating layer. Another failure observed was the switch failing to open, this is due to stiction and/or plastic deformation of the beam.

3.5   Fixed-fixed beam micro-contact support structure

The micro-contact support structure used for this experiment was the fixed-fixed beam micro-contact structure that emulates Holm's crossed bar experiment on the micro-scale. This design allows a four-wire measurement in which current only flows through the micro-contact at contact. Voltage is then measured across the micro-contact through the Au traces connected to the anchor of the beam and micro-contact area.

Fixed-fixed beams have a width of $250\mu m$ and lengths of $350\mu m$, $400\mu m$, $450\mu m$ and $500\mu m$. The beams are designed with a gap of $2\mu m$ between the contact bump and contact pad. The contact bump allows for the contact to be made between a plane for the bottom contact and a hemispherical contact on the beam. Figure 3.3 shows a 3D model of the fixed-fixed beam micro-contact structure. The micro-contact support structure is constructed for a Au-Au micro-contact and utilizes a structural layer to enhance the micro-contact structure's stiffness and to reduce the risk of stiction, but can be easily modified to investigate other contact materials.
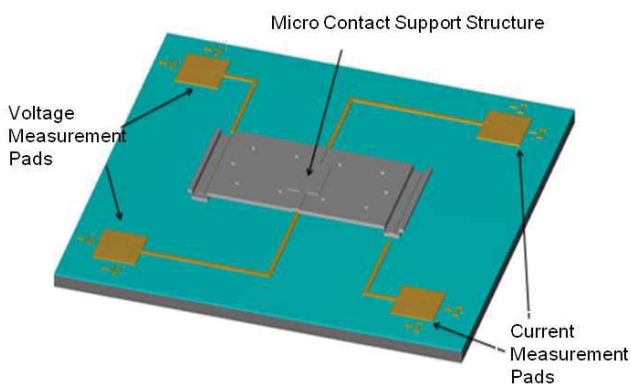
Figure 3.3: 3D model of fixed-fixed beam micro-contact support structure.

3.5.1 *Metal contacts construction.*

The first testing done was completed using an evaporated Au lower planar contact and a sputtered Au upper hemispherical contact. These Au-Au contacts were used as a baseline measurement to verify system performance and was used for comparison of all other testing. Two other sputtered contact metal that was tested was Ru, and RuO_2. Ru and RuO_2 thin films have been receiving much attention because of their good conductivity, low temperature coefficient of resistance (TCR), and high thermal stability [66]. Ruthenium oxide (RuO_2) belongs to the family of transition metal oxides [67]. It has metallic conductivity in a wide temperature range, which is a positive in micro-contact where spot heating can occur [67]. In addition, it has high thermal stability, namely up to $700°C$ [67]. Due to these properties, RuO_2 thin Films have been an attractive material for interconnects, contacts, gate electrodes, and interdiffusion barriers in Si devices [67]. Due to these properties, devices were created by replacing gold in the upper contact with Ru and RuO_2.

The Ru and RuO_2 were added to the contact by DC sputtering Ruthenium in an Ar or Ar:O_2 environment. The percentage of oxygen is the identifier for the samples, therefor a 25% RuO_2 does not necessarily means that the concentration of the RuO_2 is 25%, but there was a 25% O_2 content in the chamber while sputtering. Once sputtered to create the upper hemispherical contact for the device, an Au sputtered seed layer of gold was sputtered which was then electroplated with gold for the structural layer. Figure 3.4 shows an example device cross-section diagram of a micro-contact support device with Ru in the upper hemispherical contact. These Au-Ru and Au-RuO_2 devices were tested and results were compared to the Au-Au baseline.

Figure 3.4: Example cross-section of a Au-Ru contact device.

3.5.2   CNT encapsulated beams.

CNTs were added to the upper hemispherical contact of the device by encapsulating them by sputtering a layer of gold for the contact, applying the CNTs, and electroplating gold over them. The resultant device is not an Au-CNT or alloy type structure; it is an Au structure with encapsulated CNTs. Figure 3.5 shows an example diagram of a micro-contact support device with CNTs encapsulated in the upper hemispherical contact device cross-section, and the planar/hemispherical contact. The CNTs can, in effect, change the paths of conduction through the beam since the beam is no longer uniform. Research has shown that creating a structure with two different materials does not always produce an alloy or composite that has better, or even comparable performance, to individual metals. By itself, CNTs are better conductors than gold, both thermally and electrically.
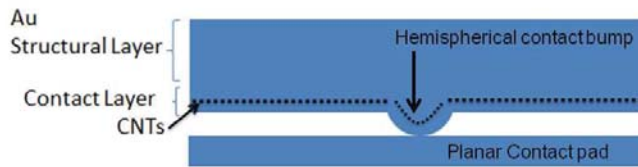
Figure 3.5: Example cross-section of a Au-CNT contact device.

The CNTs were applied by spinning on a mixture of CNTs diluted in isopropyl alcohol and put into suspension using ultrasonic vibrations. After deposition of the CNTs, a thermal image was taken to demonstrate the thermal conductivity of the CNTs. The analysis of the CNT coverage is discussed more in Section 5.4

3.6 Contact modeling

Taking the formulas from Section 2.2.3 the following plots were created using measured values for resistivity, hardness and Young's Modulus. For contacts with different contact metals, the average resistivity and average hardness are used. The following plots show the modeled values used in the results in Section 5. Figure 3.6 is the elastic model for a $4\mu m$ contact radius. Figure 3.7 is the elastic model for a $6\mu m$ contact radius. Figure 3.8 is the elastic model for a $8\mu m$ contact radius. Figure 3.9 is the plastic model for all contact radius.
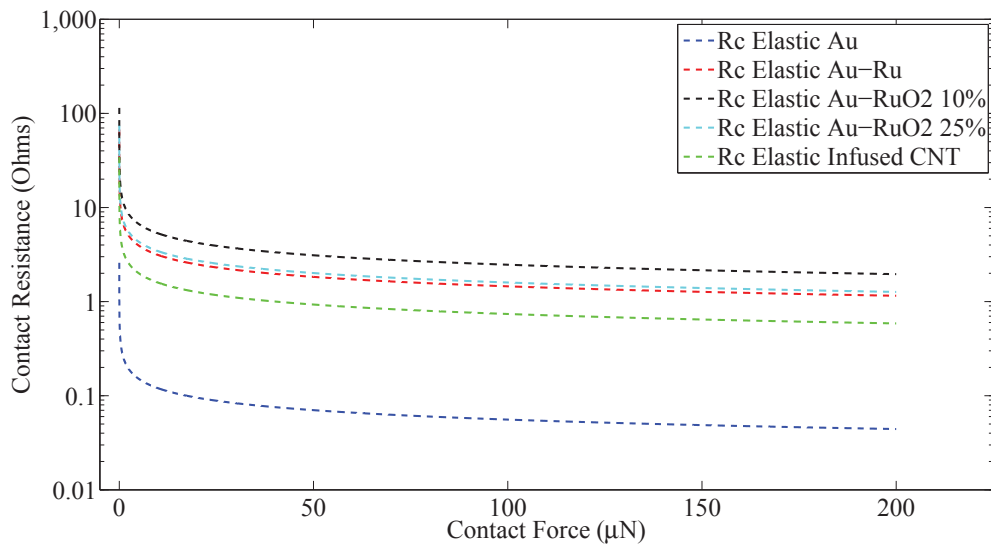
Figure 3.6: Elastic deformation model assuming diffusive electron transport for a $4\mu m$ contact radius plotting the 5 different contact types tested.
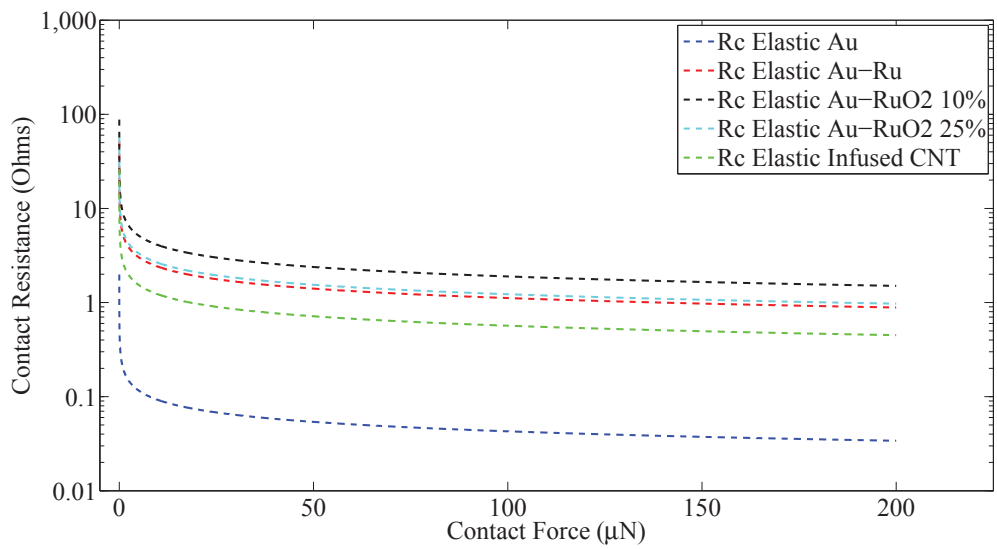
Figure 3.7: Elastic deformation model assuming diffusive electron transport for a $6\mu m$ contact radius plotting the 5 different contact types tested.
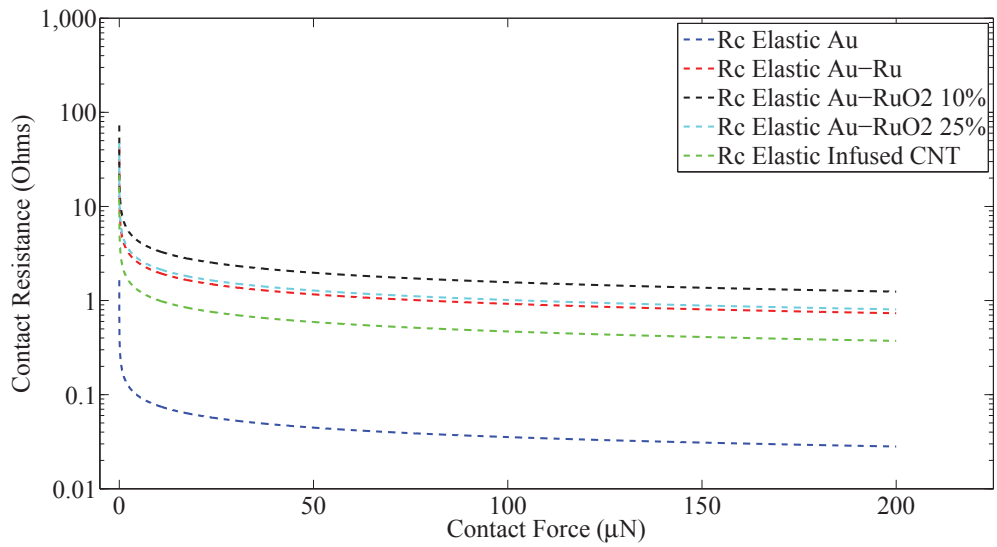
Figure 3.8: Elastic deformation model assuming diffusive electron transport for a $8\mu m$ contact radius plotting the 5 different contact types tested.
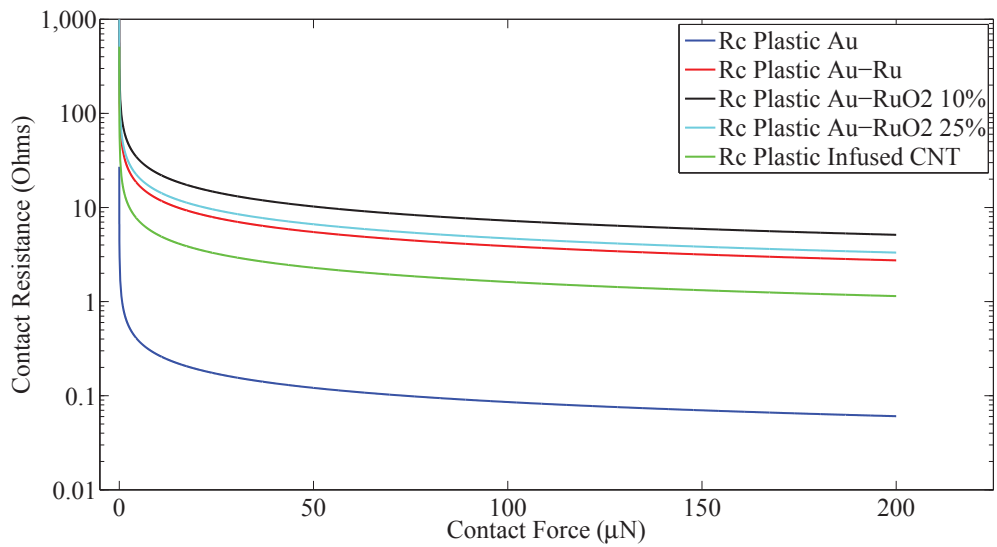
Figure 3.9: Plastic deformation model assuming diffusive electron transport for all contact radii, plotting the 5 different contact types tested.

3.7   Gray-scale lithography

The first attempt at gray-scale lithography utilized Matlab to create a gray-scale image. This first image can be seen in Figure 3.10. However, Matlab saved the image as a color .bmp format that resulted in blue-gray hues at different levels. These blue-gray hues caused an issue in the first optical mask that led to errors when writing into the photoresist, as shown in Figure 3.10. It was discovered that exporting the image into a different program and saving in the correct format, a 24-bit bitmap pure gray image, fixed the error. Figure 3.10 also exhibits partially exposed border which should be fully exposed. Further discussion on how these structures were design and created can be found in Appendix B.
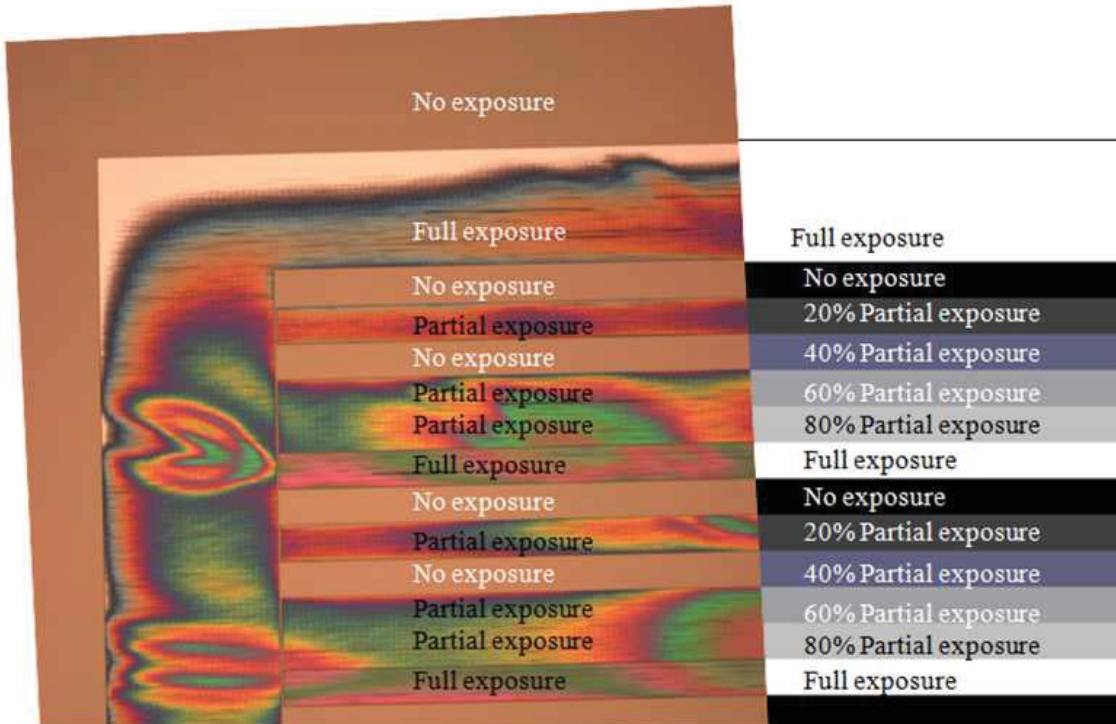
Figure 3.10: Image showing the comparison of the blue-gray hue with the resulting image in 1818 photoresist, this should be a step down from full height of photoresist down to no photoresist.

41

3.8   Post test examination

To examine the effects of testing on the micro-contact, the micro-test support structure will be dissected to examine the micro-contact surfaces. The inspection will be performed to determine the development of any films on the contact as well as physical changes to the micro-contact. This will be done using two devices a Zygo white light interferometer and a scanning electron microscope (SEM) to examine the contact.

3.8.1   Zygo measurement.

Using a Zygo white light interferometer, the tested micro-contact support structure was inspected for a visible change in structural architecture. The Zygo creates a 3D image of the structure by measuring the reflection of the light emitted by the system.

3.8.2   SEM measurement.

The SEM was used for examining the contact surfaces to document changes to the contact area. In order to examine the contact area, the support structure needs to be exposed. Since this process destroys the contact, the examination could not look at a micro-contact before and after testing. But the before examination was conducted on micro-contacts that were not tested and those that were tested were examined to look for any noticeable differences.

The other post test examination to be performed using the SEM is using energy dispersive X-ray spectroscopy (EDS) detector. The EDS can examine a surface and return the chemical make-up of that surface. This process will be similar to the SEM images, where an untested group will be examined for the baseline. Once the composition of the untested contacts is determine, tested contact will be examined to document the change in the chemical make-up between the samples. This comparison will point to the growth of any films due to use, and the chemical composition of these films.

3.9   Chapter summary

This chapter detailed the methodology for the design, fabrication and testing for this research. This chapter included a discussion of the test fixture that will be used, how it is controlled and how it works. There was a discussion of the types of contact test that will be performed and the differences between the three. The micro-contact support structure for micro-contact lifecycle testing was characterized and the construction was discussed. Modeling was performed to set the expectations for contact resistance and contact physics modeling. Finally there was an explanation of the types of post test data collection will be performed to characterize the types of failures observed.

IV. Results

4.1 Chapter overview

The types of contacts tested for this research included; Au-Au, Au-Ru, Au-RuO$_2$ 10% and 25% O$_2$ concentration, and Au-CNT. In addition to a hemisphere/planar contact area, Au-Au devices equipped with hemisphere/engineered lower contact surfaces. Each micro-contact support structure was subjected to initial contact testing and cold switch testing. With typical forces for micro-contacts in the range of a few hundreds of μN, a maximum contact force limit of $200\mu N$ was used [68]. During initial contact testing and measurement cycles, the current was kept constant at $0.02mA$ and the voltage was measured to calculate the contact resistance. During cold switch testing the current was constant at $46mA$. Devices were tested for a predetermined amount of cycles to examine the evolution of contact resistance. Between measurements, the micro-contact was cycled at a predetermined actuation rate and force. This system has proven to be an effective test fixture for cycling micro-contacts at relatively fast cycle rates to examine the evolution of micro-contact resistance.

4.2 Testig of Au-Au micro-contact samples

4.2.1 Initial Contact Test 6μm radius contact bump.

Figure 4.1 shows the measured micro-contact resistance for an Au-Au, fixed-fixed micro-contact support structure with a contact radius of $6\mu m$ and the modeled values of micro-contact resistance based on the equations in Section 2.2.3. The data presented is the average of 15 ICT measurements with the standard deviation of that data indicated by error bars.
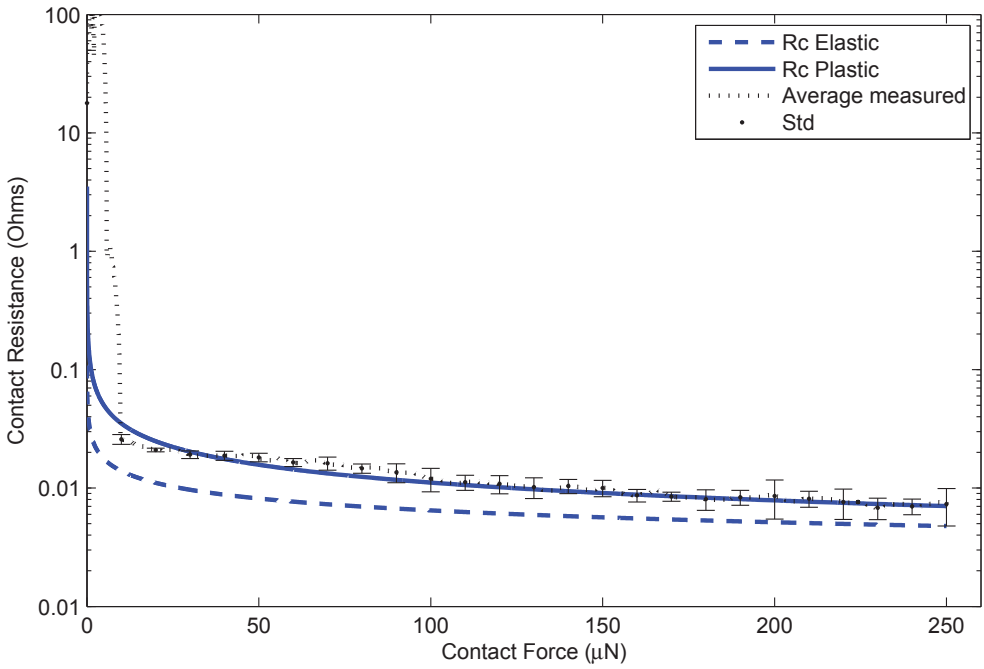
Figure 4.1: Contact resistance of Au-Au $6\mu m$ radius contacts; 'Rc Elastic' and 'Rc Plastic' are modeled values, 'Average Measured' data is the average of 15 initial contact test measurements and 'Std' is the standard deviation of those measured values.

Figure 4.1 shows that at low contact force, less than $10\mu N$, the measured contact resistance is much higher than the model. After this area the average measured values matches the plastic model.

4.2.2 *Initial Contact Test* 8μm *radius contact bump.*

Figure 4.2 is similar to what was just presented, but with a $8\mu m$ contact bump radius. This data is the average of 15 ICT measurements with the standard deviation of that data indicated by error bars.
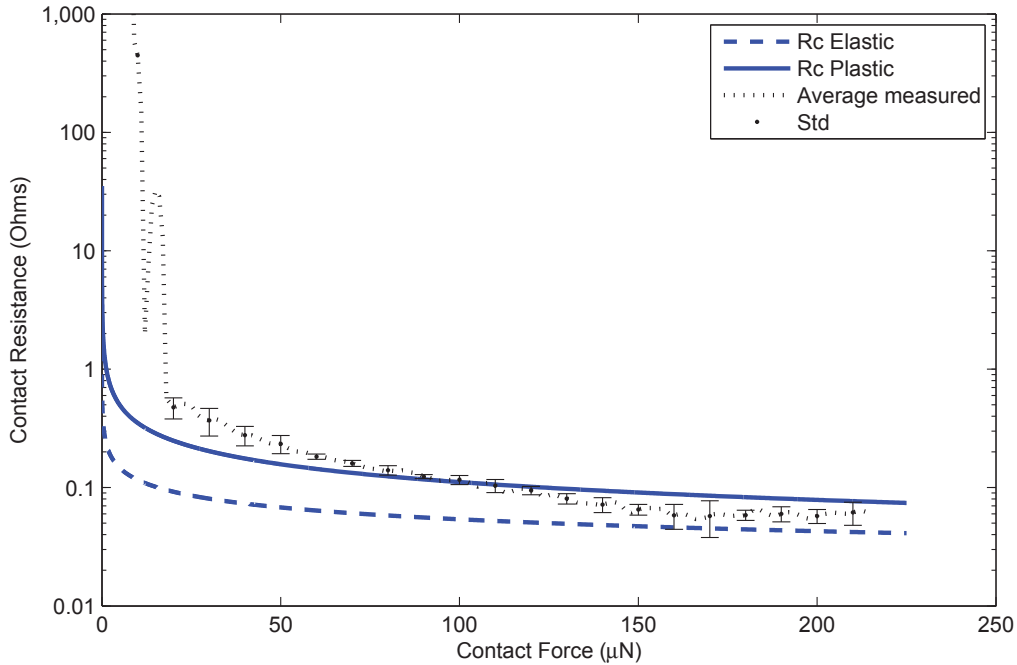
Figure 4.2: Contact resistance of Au-Au $8\mu m$ radius contacts; 'Rc Elastic' and 'Rc Plastic' are modeled values, 'Average Measured' data is the average of 15 initial contact test measurements and 'Std' is the standard deviation of those measured values.

Figure 4.2 shows that at low contact force, less than $10\mu N$, the measured contact resistance is much higher than the model. With this data the measured data mimics the measured but never follows it exactly. One solution to this deviation is proposed in Section 5.10.

4.2.3   Cold Switch Test.

The evolution of the Au-Au contact area was observed by actuating the micro-contact to 1, 10^2, 10^3, 5×10^3, 10^4, 5×10^4, 10^5, 5×10^5, 10^6, 5×10^6 and 10^7 cycles. The micro-contacts were actuated using an external, calibrated point load. To examine the micro-contact performance, the contact resistance and force required to close the contact were recorded simultaneously throughout testing. At each of the above stated end point, the micro-contact was folded back to evaluate the wear of the upper hemisphere and planar lower contact. All the Au-Au data can be found in Appendix A. The following are examples of representative data focusing on cycles that produced interesting results. These examples will include micro-contacts tested to 10^4, 5×10^5 and 10^7 cycles.

4.2.3.1   *Micro-contact with* 10^4 *cycles, Sample (1,2).*

The 10^4 cycle test of a micro-contact was performed on Sample (1,2), Beam 8 displayed some interesting results. The contact resistance plot is shown in Figure 4.3. SEM images for the contact bump is shown in Figure 4.4a and for the contact pad in Figure 4.4b.

This contact shows signs of wear after 10^4 cycles. On the contact bump there are indications where material transfer has occurred. The loss of material created a hole that is shown on the pad. It is also important to point out the sharp rise in resistance around 8×10^3 cycles. It is believed that this spike in resistant is due to the material transfer that occurred. This sharp change of resistance differs from other contacts tested. This contact, unlike the previous example, exhibits no wear after 10^4 cycles.
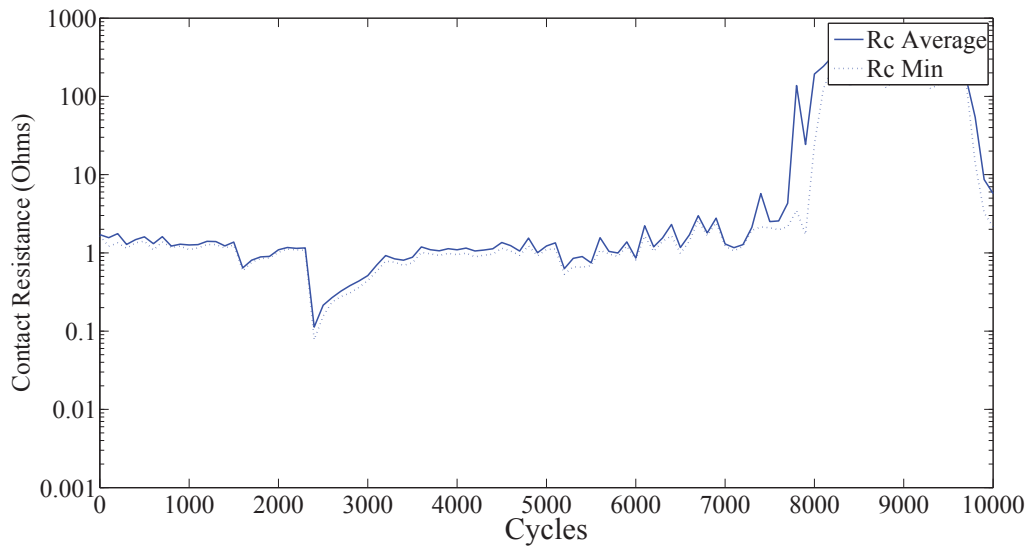
Figure 4.3: Contact resistance of Au-Au $6\mu m$ radius contact for 10^4 cycles. 'Rc Average' is the average for the last 5 resistance measurements at $\sim 200\mu N$ of contact force during the measurement cycle. 'Rc Min' is the minimum contact resistance measured during the measurement cycle. This contact displays an unusual increase in contact resistance at 8×10^3 cycles.

(a) Upper contact (Anode) (b) Lower contact (Cathode)
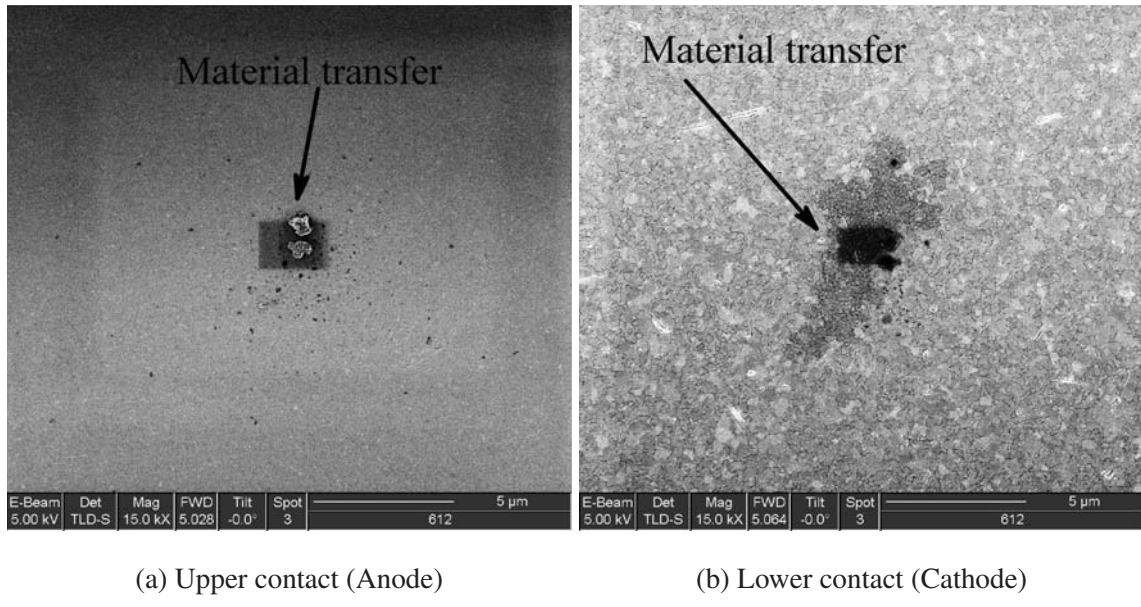
Figure 4.4: Scanning electron microscope image of contact pad after 10^4 cycles. A large dark area is shown in the middle of each contact where the bottom pad lost material to the beam.

4.2.3.2 Micro-contact with 10^4 cycles, Sample (1,4).

The 10^4 cycles test of a micro-contact was performed on Sample (1,4), Beam 9. The contact resistance plot is shown in Figure 4.5. SEM images for the contact bump is shown in Figure 4.6a and for the contact pad in Figure 4.6b.
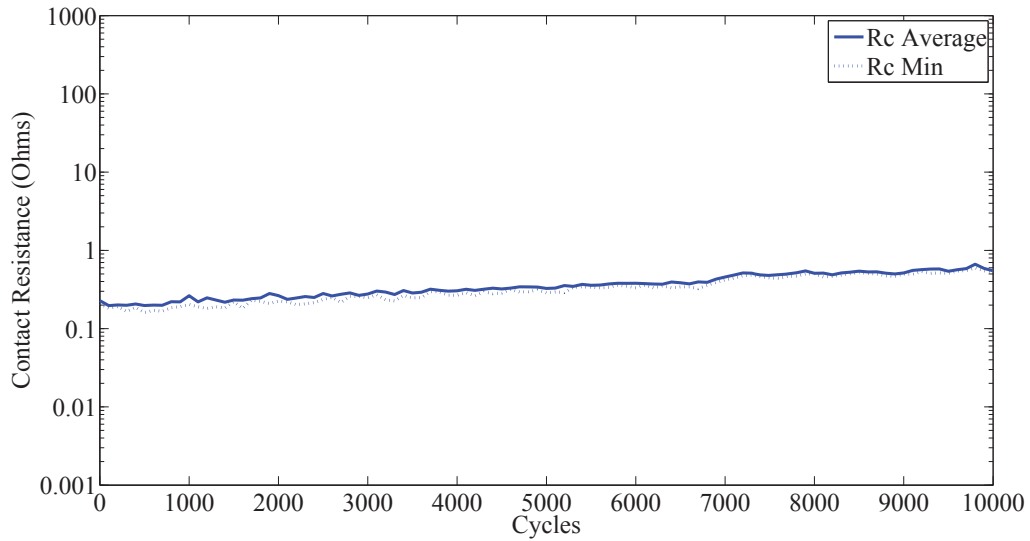
Figure 4.5: Contact resistance of Au-Au $6\mu m$ radius contact bump for 10^4 cycles. 'Rc Average' is the average for the last 5 resistance measurements at $\sim 200\mu N$ of contact force during the measurement cycle. 'Rc Min' is the minimum contact resistance measured during the measurement cycle.

| (a) Upper contact (Anode) | (b) Lower contact (Cathode) |
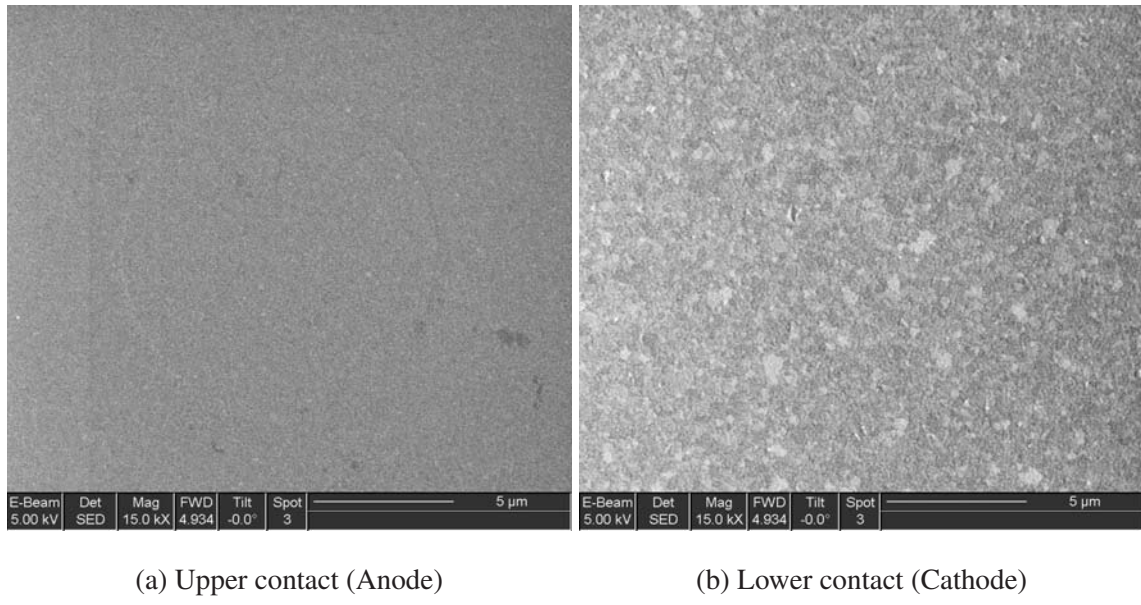
Figure 4.6: Scanning electron microscope image of contact pad after 10^4 cycles. No contact wear is shown on either contact.

4.2.3.3 *Micro-contact with* 5×10^5 *cycles, Sample (1,2).*

The 5×10^5 cycles test of a micro-contact was performed on Sample (1,2), Beam 1. The contact resistance plot is shown in Figure **??**. SEM images for the contact bump is shown in Figure 4.7a and for the contact pad in Figure 4.7b.

This contact exhibits large indications of wear after 5×10^5 cycles. On the beam there is an area in the middle were material transfer has occurred. The pad displays a corresponding hole where this material transferred from. This contact, with the large material transfer area also exhibited a high contact resistance for most of the life of the micro-contact.
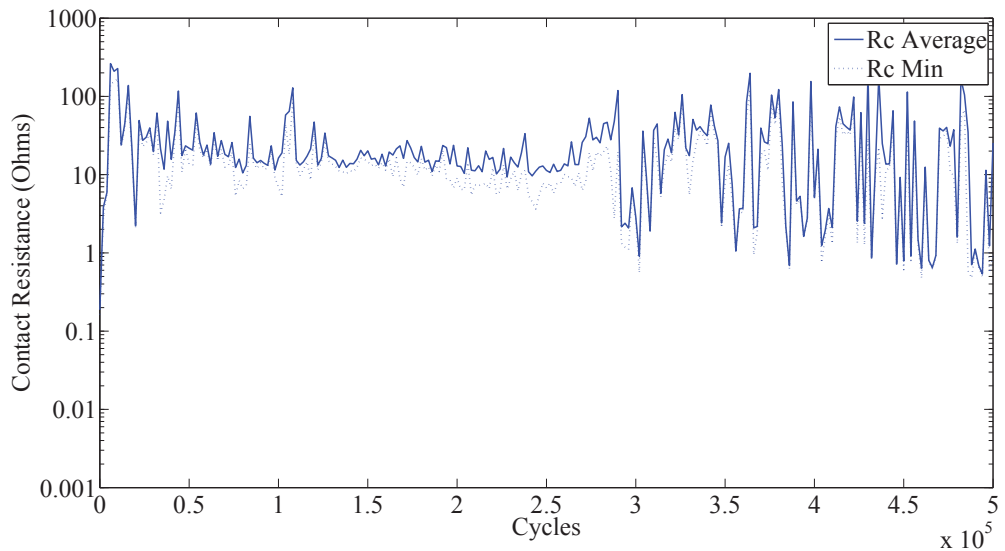
Contact resistance of Au-Au 6μm radius contact for 5×10^5 cycles. 'Rc Average' is the average for the last 5 resistance measurements at $\sim 200\mu N$ of contact force during the measurement cycle. 'Rc Min' is the minimum contact resistance measured during the measurement cycle.

(a) Upper contact (Anode)　　　　(b) Lower contact (Cathode)
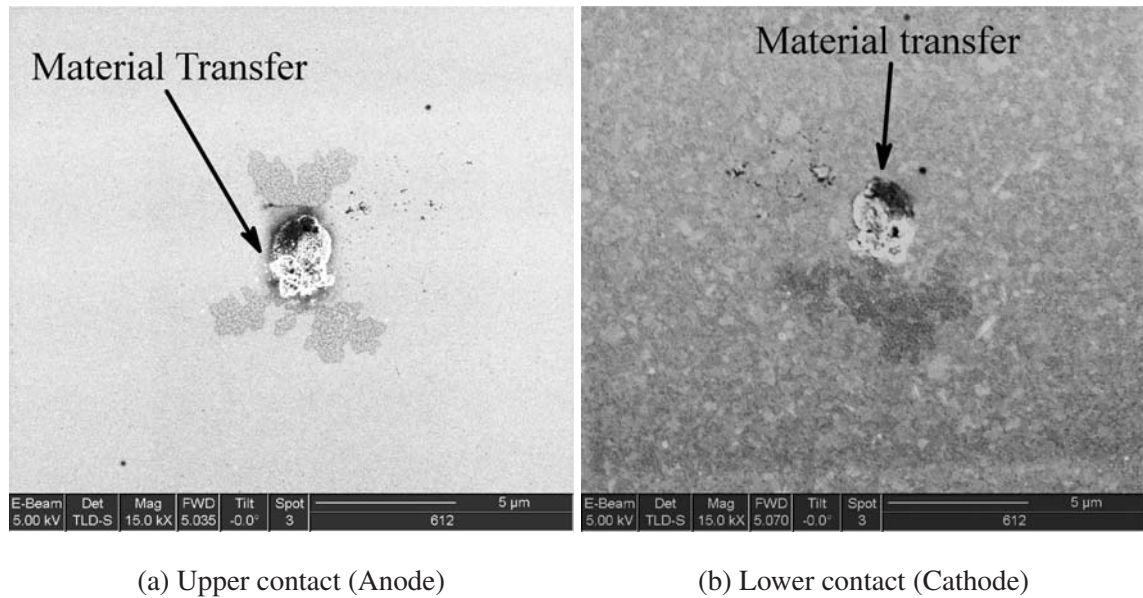
Figure 4.7: Scanning electron microscope image of contact pad after 5×10^5 cycles. A large material transfer area is shown in the middle of the contact.

4.2.3.4 Micro-contact with 5×10^5 cycles, Sample (1,4).

The 5×10^5 cycles test of a micro-contact was performed on Sample (1,4), Beam 12. This contact has the same amount of cycles as the previous example, but does not display the same contact wear. The contact resistance plot is shown in Figure **??**. SEM images for the contact bump is shown in Figure 4.8a and for the contact pad in Figure 4.8b.
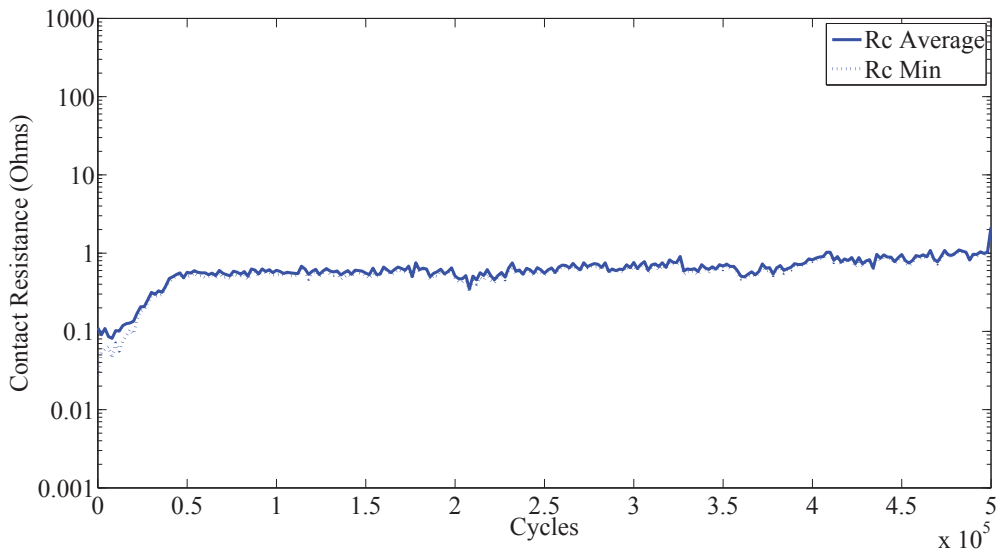
Contact resistance of Au-Au $6\mu m$ radius contact for 5×10^5 cycles. 'Rc Average' is the average for the last 5 resistance measurements at $\sim 200\mu N$ of contact force during the measurement cycle. 'Rc Min' is the minimum contact resistance measured during the measurement cycle.

This contact exhibits no wear after 5×10^5 cycles. Which is in contrast to the sample previously shown and will be discussed more in Section 5.5.

(a) Upper contact (Anode)   (b) Lower contact (Cathode)
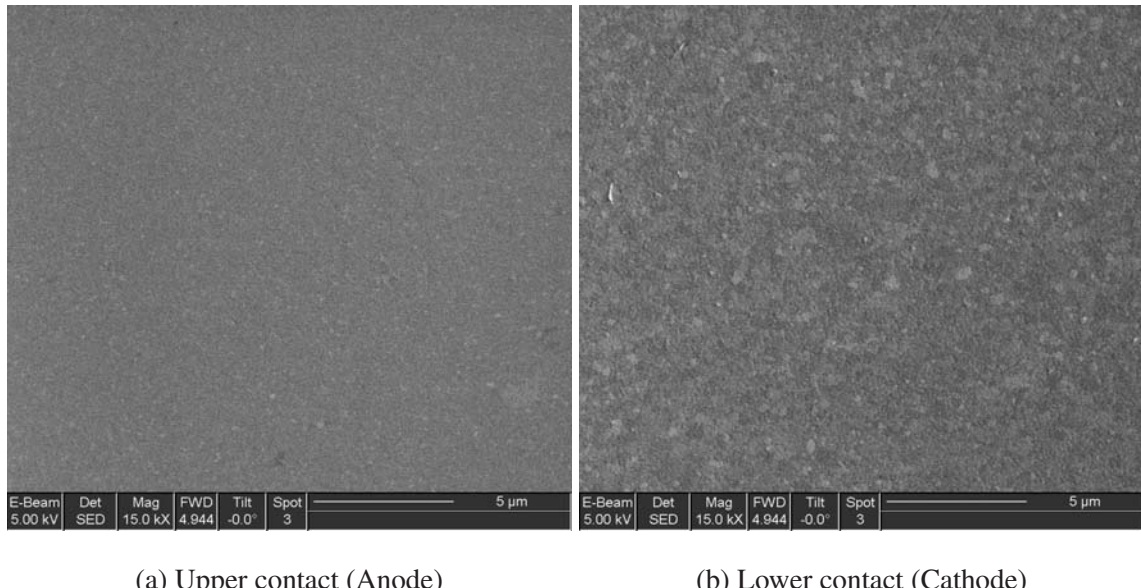
Figure 4.8: Scanning electron microscope image of contact pad after 5×10^5 actuations. No material transfer is shown.

4.2.3.5 Micro-contact with 10^7 cycles Sample (1,4).

The 10^7 cycle test of a micro-contact was performed on Sample (1,4) Beam 2. The contact resistance plot is shown in Figure 4.9. SEM images for the contact bump is shown in Figure 4.10a and for the contact pad in Figure 4.10b.

This contact shows some wear after 10^7 cycles. On the beam there is an area in the middle on the contact bump where material transfer has occurred. This build up of material corresponds to a hole that is shown on the pad.
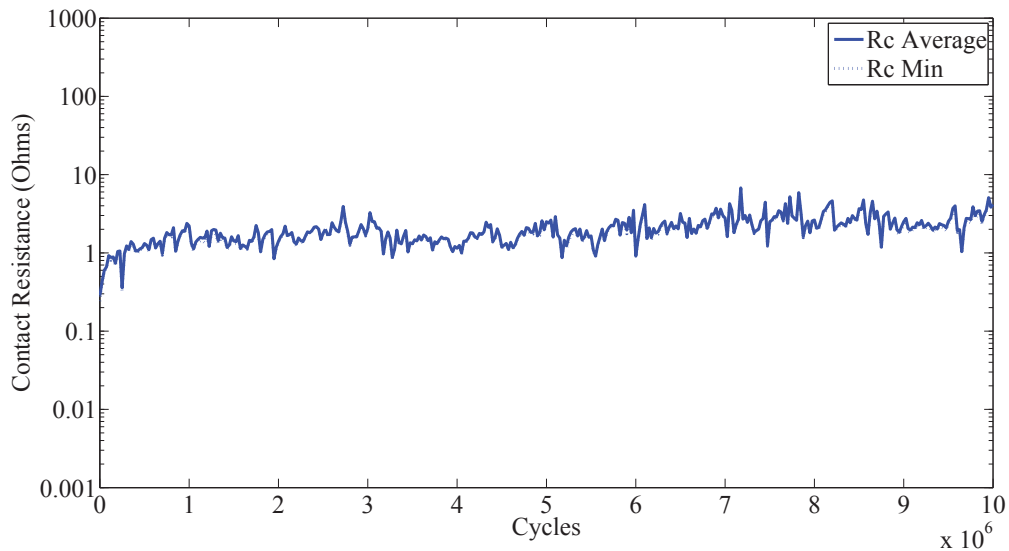
Figure 4.9: Contact resistance of Au-Au $6\mu m$ radius contact for 10^7 cycles. 'Rc Average' is the average for the last 5 resistance measurements at $\sim 200\mu N$ of contact force during the measurement cycle. 'Rc Min' is the minimum contact resistance measured during the measurement cycle.

(a) Upper contact (Anode)

(b) Lower contact (Cathode)
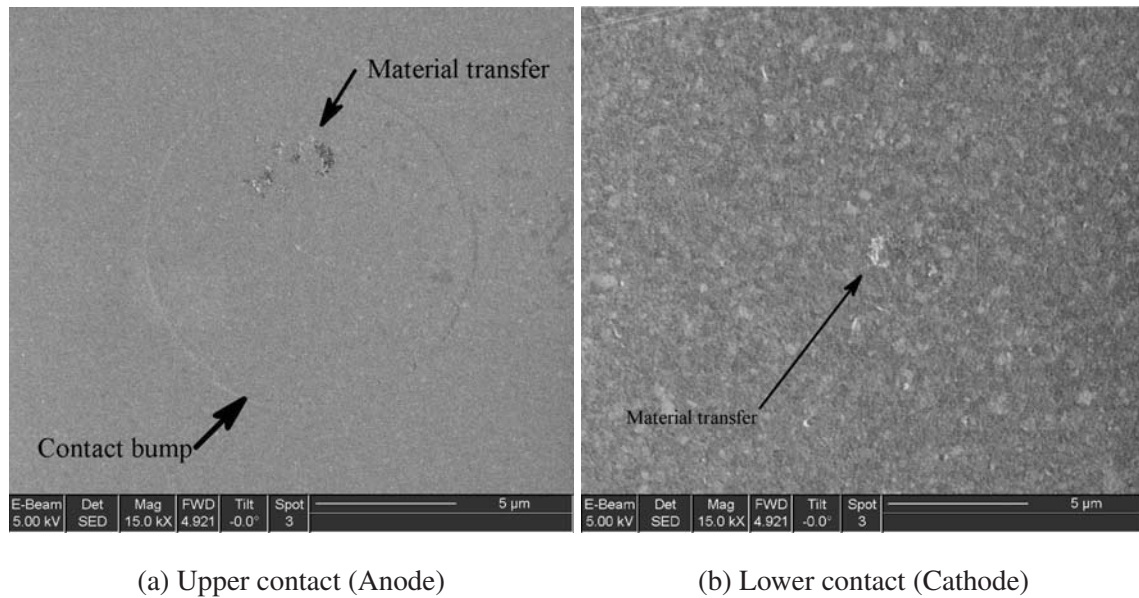
Figure 4.10: Scanning electron microscope image of contact pad after 10^7 cycles. Material transfer is shown in the contact area.

4.2.3.6   *Micro-contact with* 10^7 *cycles, Sample (2,3).*

The 10^7 cycles test of a micro-contact was performed on Sample (2,3), beam 2. The
contact resistance plot is shown in Figure 4.11. SEM images for the contact bump is
shown in Figure 4.12a and for the contact pad in Figure 4.12b.
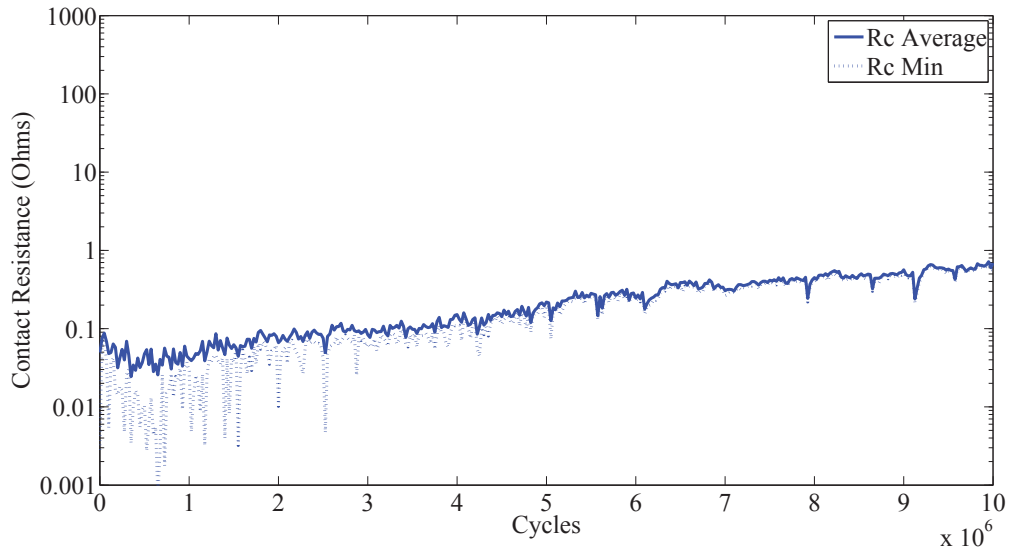
Figure 4.11: Contact resistance of Au-Au $6\mu m$ radius contact for 10^7 cycles. 'Rc Average'
is the average for the last 5 resistance measurements at $\sim 200\mu N$ of contact force during
the measurement cycle. 'Rc Min' is the minimum contact resistance measured during the
measurement cycle.

This contact displays only a small amount of wear after 10^7 cycles. This low amount
of wear matches the very low contact resistance seen throughout the lifetime of the
micro-contact.

(a) Upper contact (Anode)   (b) Lower contact (Cathode)
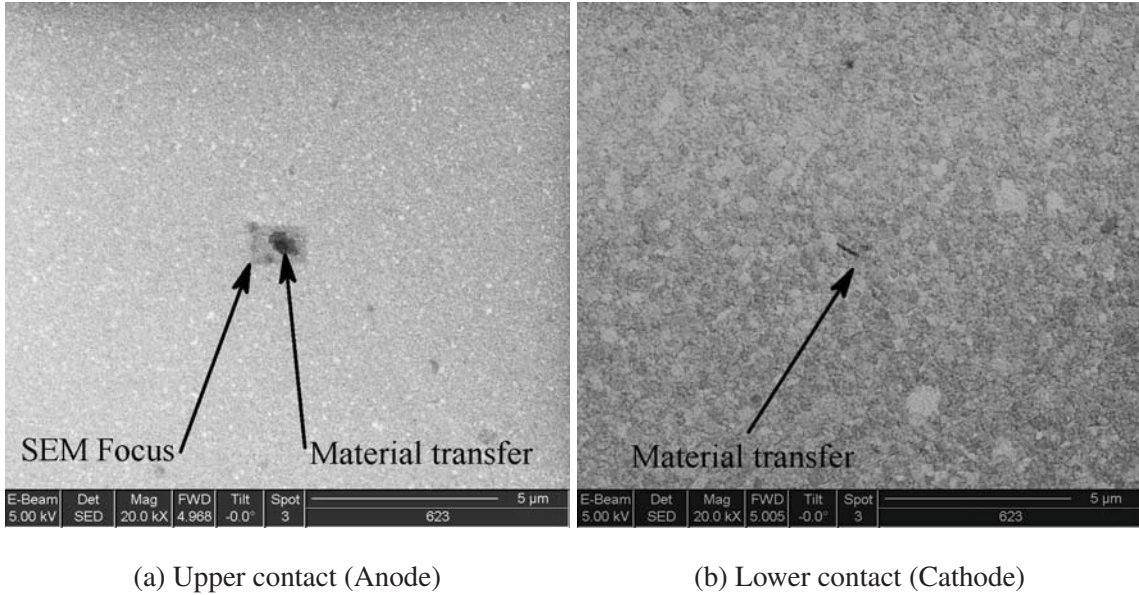
Figure 4.12: Scanning electron microscope image of upper contact bump and lower contact pad after 10^7 cycles. A small area of material transfer is shown in the contact area.

4.2.4   Lifetime Contact Resistance Evolution.

Using the cold-switch test (CST), the $6\mu m$ contact radius Au-Au device was tested until failure. The device was actuated to 3.5×10^8 cycles with measurements at every 10^5 cycles for the first 5×10^7 cycles. Measurements were taken every 2.5×10^5 from 50×10^7 to 1.45×10^8. Finally the device was measured every 5×10^5 cycles for the remaining life of the micro-contact. The contact resistance plot is shown in Figure 4.13.

There are several noteworthy trends in Figure 4.13. The first was the steady increase of contact resistance from $10^5 - 2.8 \times 10^7$ cycles. At 2.8×10^7 cycles there was the first of two software glitches. During these times, at 2.8×10^7 cycles and 3.2×10^7 cycles, the micro-contact structure was cycled, but the measurement cycles were not collected as planned. After this period of cycling, the next contact resistance measurement was much lower than the previous data showed. This could be caused by the long continuous cycling ability to clean the contact area and cause a drop in contact resistance. After continuing

57
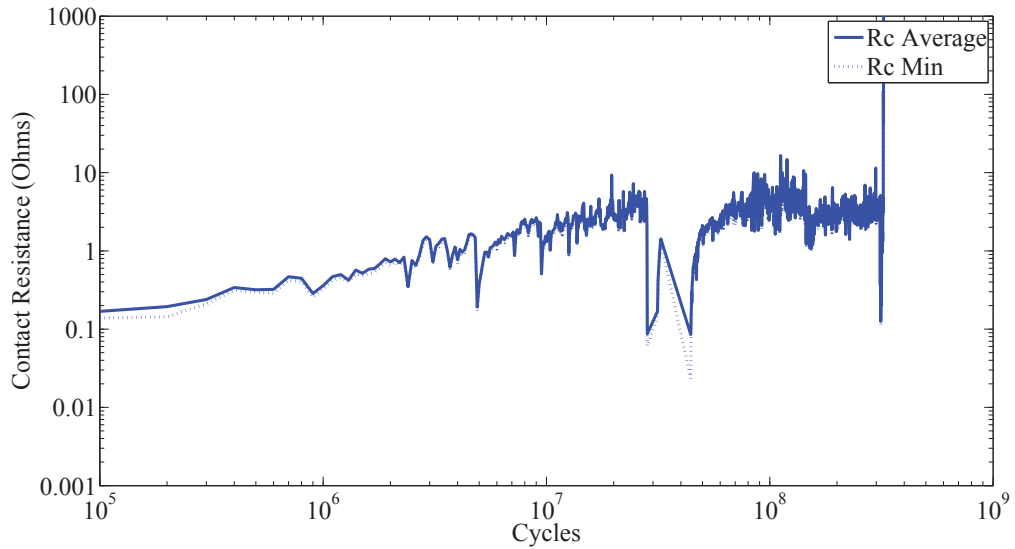
Figure 4.13: Contact resistance of Au-Au $6\mu m$ radius contact until failure. 'Rc Average' is the average for the last 5 resistance measurements at $\sim 200\mu N$ of contact force during the measurement cycle. 'Rc Min' is the minimum contact resistance measured during the measurement cycle. Two software glitches 2.8×10^7 cycles and 3.2×10^7 cycles caused prolong cycling and the sudden drops in contact resistance.

from these two long cycles, the contact resistance remained steady until 322.6 million cycles, where the contact resistance spiked to 109Ω. After another million cycles, the contact failed to close. SEM images for the contact bump is shown in Figure 4.14a and for the contact pad in Figure 4.14b.

This contact shows three distinct wear spots on the upper and lower contact area. This material in the contact area is what caused the resistance to spike for the last set of measurements.

(a) Upper contact bump (Anode)   (b) Lower contact pad (Cathode)
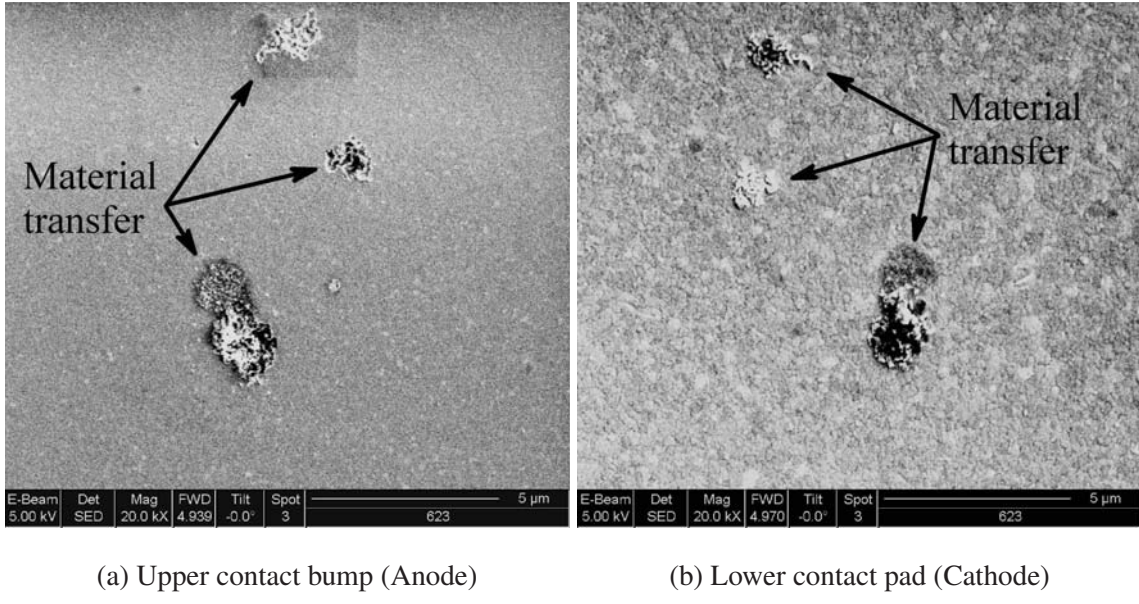
Figure 4.14: Scanning electron microscope image of upper contact bump and lower contact pad after reliability testing. Multiple areas of material transfer are visible in the contact area.

4.3 Au-Ru contact with $6\mu m$ radius contact bump

4.3.1 Initial Contact Test.

Figure 4.15 shows a comparison of the measured micro-contact resistance for an Au-Ru fixed-fixed micro-contact support structure with a contact bump radius of $6\mu m$ and the modeled values of micro-contact resistance. This data is the average of 20 ICT measurements; also shown is the standard deviation of that data.

Figure 4.15 shows that at extremely low contact force, less than $20\mu N$, the measured contact resistance is much higher than the model. But after this small area of light loading, the average measured values drops below all the modeled values. Discussion of why the model does not match the collected data is discussed in more detail in Section 5.3.
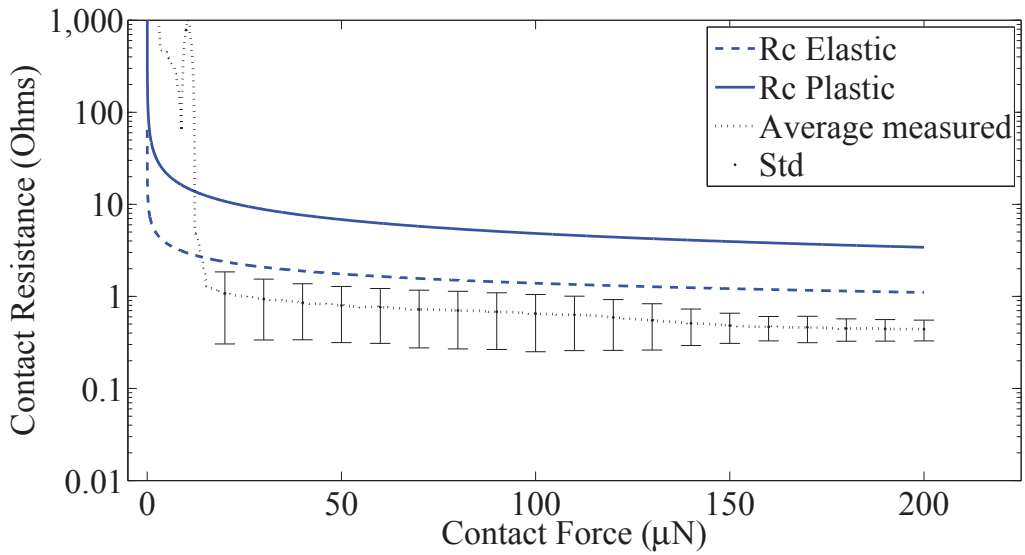
Figure 4.15: Contact resistance of Au-Ru with 6μm radius contacts: 'Rc Elastic' and 'Rc Plastic' are modeled values, 'Average Measured' data is the average of 20 initial contact test measurements and 'Std' is the standard deviation of those measured values represented as error bars.

4.3.2 Cold Switch Test.

The 10^7 cycles test of a micro-contact was performed on two Au-Ru contacts. The contact resistance plot for the first contact is shown in Figure 4.16. SEM images for the contact bump is shown in Figure 4.17a and for the contact pad in Figure 4.17b.
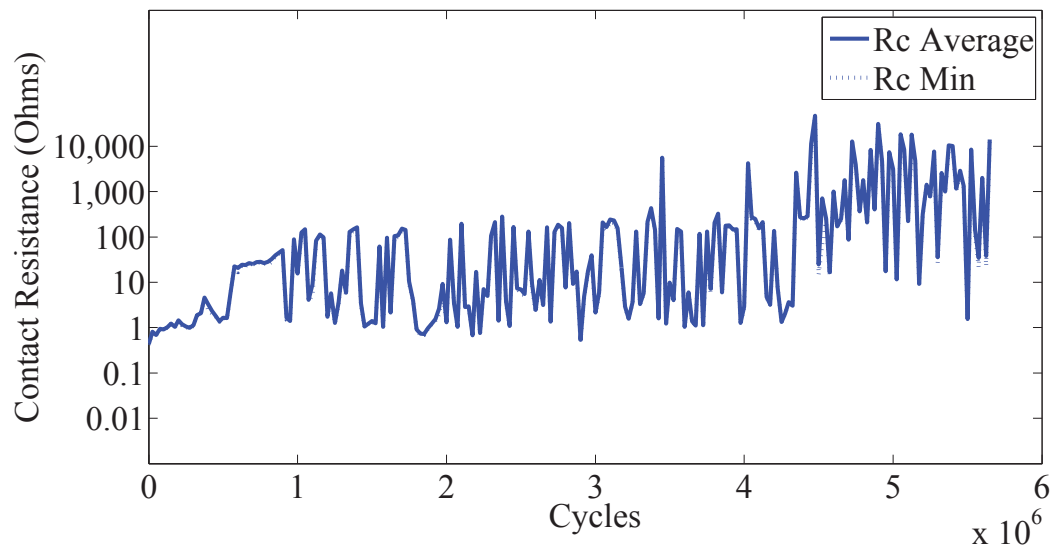
Figure 4.16: Contact resistance of Au-Ru with $6\mu m$ radius contact for 10^7 cycles, failing after 5.65×10^6 cycles. 'Rc Average' is the average for the last 5 resistance measurements at $\sim 200\mu N$ of contact force during the measurement cycle. 'Rc Min' is the minimum contact resistance measured during the measurement cycle.

(a) Upper contact (Anode)   (b) Lower contact (Cathode)
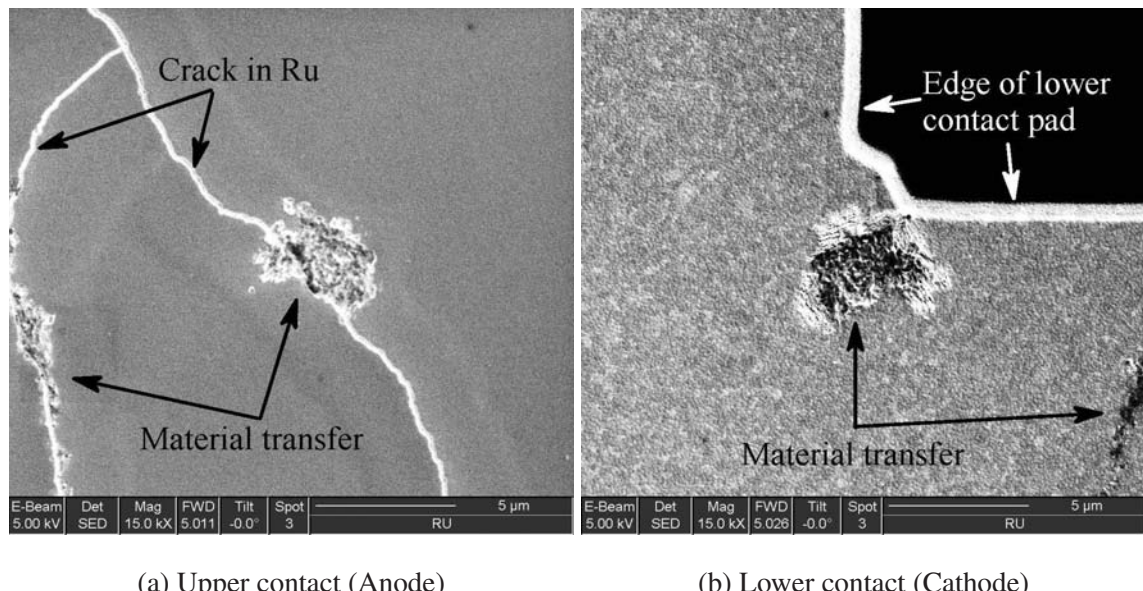
Figure 4.17: Scanning electron microscope image of upper contact area and lower contact area after 5.65×10^6 cycles. This contact area did not happen on the desired contact bump but rather near the edge of the beam and pad.

This contact exhibits a large amount of wear after only 5.65×10^6 cycles. This amount of transfer caused the contact to fail to close after less than the desired amount of cycles. For an unknown reason this contact made contact in the upper corner of the pad rather than the center bump. Since it was not discovered until after the beam was folded back, it is assumed that the beam was deformed. This deformation was such that this portion of the beam was lower than the contact bump, causing the upper portion of the pad to be the contact point. Another contact was also actuated to 10^7 cycles, but on this contact the connection for the anode and cathode was swapped This contact is shown in Figure 4.18. SEM images for the contact bump is shown in Figure 4.19a and for the contact pad in Figure 4.19b.
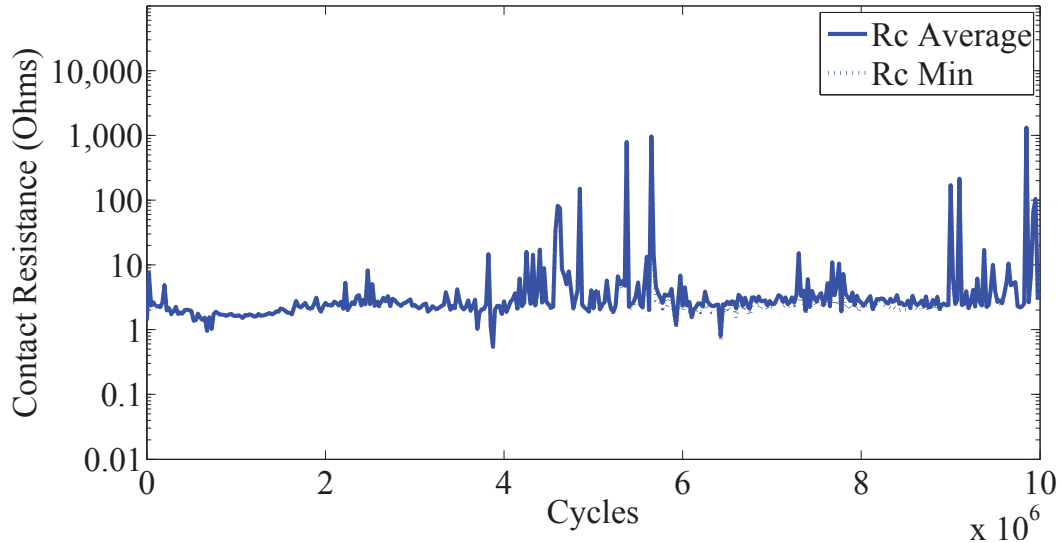
Figure 4.18: Contact resistance of Au-Ru with *6μm* radius contact for 10^7 cycles. 'Rc Average' is the average for the last 5 resistance measurements at $\sim 200\mu N$ of contact force during the measurement cycle. 'Rc Min' is the minimum contact resistance measured during the measurement cycle.

(a) Upper contact (Cathode) (b) Lower contact (Anode)

Figure 4.19: Scanning electron microscope image of contact pad after 10^7 cycles. Areas of wear is shown on both contacts

This contact also indicates that material transfer had occurred. But unlike the previous example contact was made at the contact bump. Further analysis of these contacts is contained in Section 5.6.

4.4 Au-RuO$_2$ 10% contact with 8μm radius contact bump

4.4.1 Initial Contact Test.

Figure 4.20 shows a comparison of the measured micro-contact resistance for an Au-RuO$_2$ 10% fixed-fixed micro-contact support with a contact radius of 8μm and the modeled values of micro-contact resistance. This data is the average of 5 ICT measurements; also shown is the standard deviation of that data.
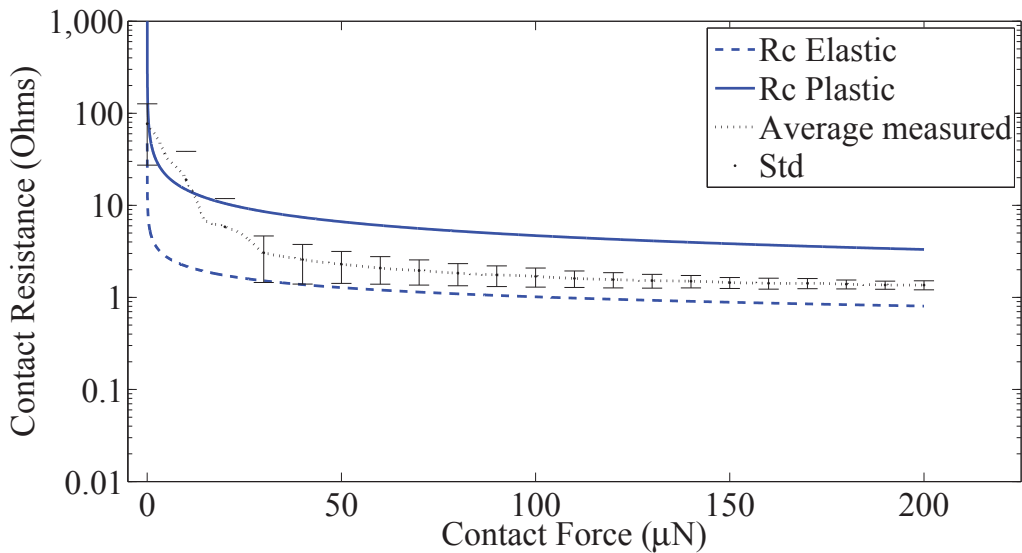
Figure 4.20: Contact resistance of Au-RuO$_2$ 10% with 8μm radius contacts; 'Rc Elastic' and 'Rc Plastic' are modeled values, 'Average Measured' data is the average of 5 initial contact test measurements and 'Std' is the standard deviation of those measured values represented by error bars.

Figure 4.20 displays that at low contact force, less than 30μN, the measured contact resistance is slightly higher than the model. But after this area, the average measured values are between the elastic and plastic models.

4.4.2   Cold Switch Test.

The 10^7 cycles test of a micro-contact was performed on two RuO_2 beams. The contact resistance plot for the first beam is shown in Figure 4.21. SEM images for the contact bump is shown in Figure 4.22a and for the contact pad in Figure 4.22b.
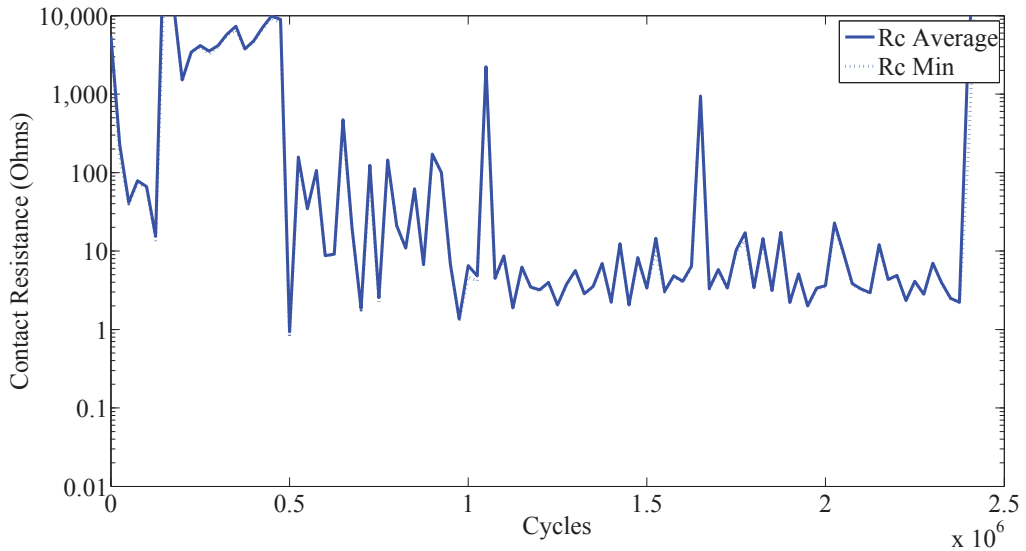
Figure 4.21: Contact resistance of Au-RuO_2 10% with $8\mu m$ radius contact for a 10^7 cycles, this contact failed after only 2.5×10^6 cycles. 'Rc Average' is the average for the last 5 resistance measurements at $\sim 200\mu N$ of contact force during the measurement cycle. 'Rc Min' is the minimum contact resistance measured during the measurement cycle.
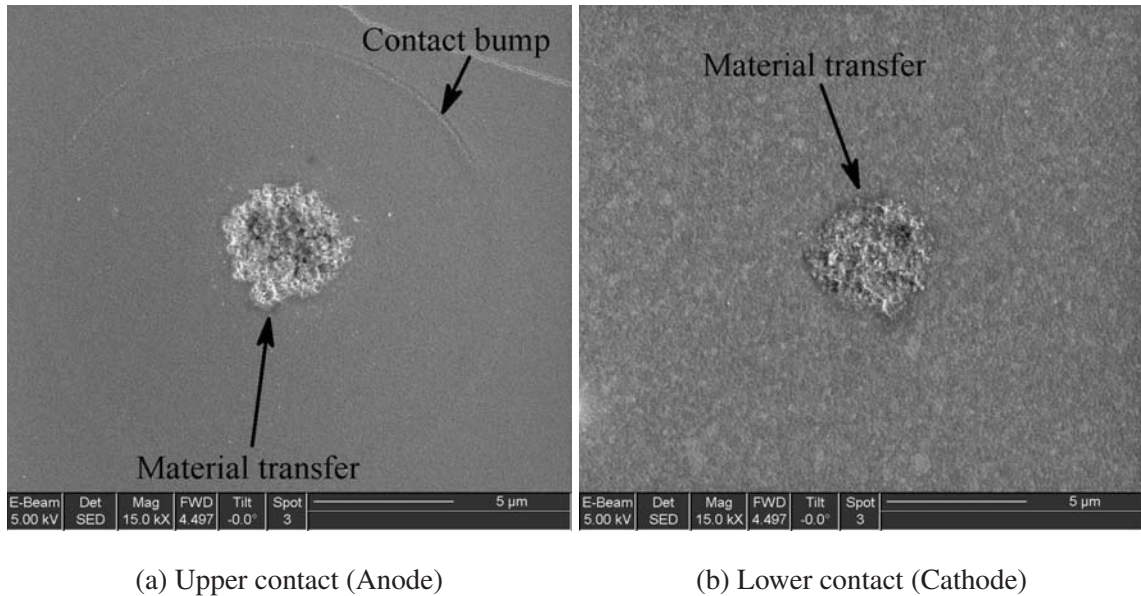
Figure 4.22: Scanning electron microscope image of Upper contact bump and lower contact pad after 2.5×10^6 cycles. After cycling the contact shows large area of material transfer.

This contact shows a large amount of wear after only 2.5×10^6 cycles. This amount of transfer caused the contact to fail to close well short of the 10^7 cycles planned. Another contact was also actuated to 10^7 cycles, but on this contact the connection for the anode and cathode was changed. This contact lasted twice as long, to 5×10^6 cycles and is shown in Figure 4.23. SEM images for the contact bump is shown in Figure 4.24a and for the contact pad in Figure 4.24b. Further analysis of these contacts is contained in Section 5.7.
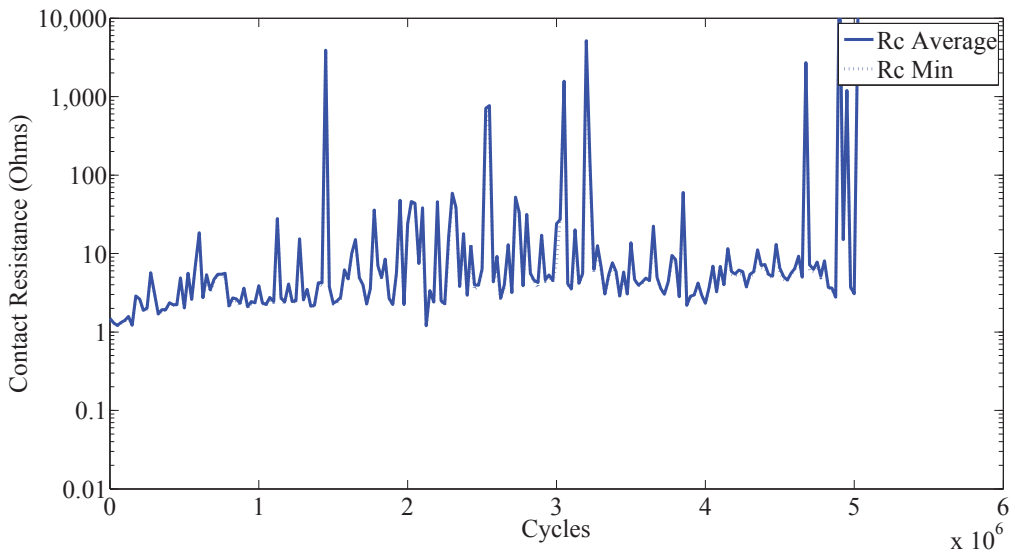
Figure 4.23: Contact resistance of Au-RuO$_2$ 10% with $8\mu m$ radius contact for 5×10^6 cycles. 'Rc Average' is the average for the last 5 resistance measurements at $\sim 200\mu N$ of contact force during the measurement cycle. 'Rc Min' is the minimum contact resistance measured during the measurement cycle.

(a) Upper contact (Cathode)

(b) Lower contact (Anode)
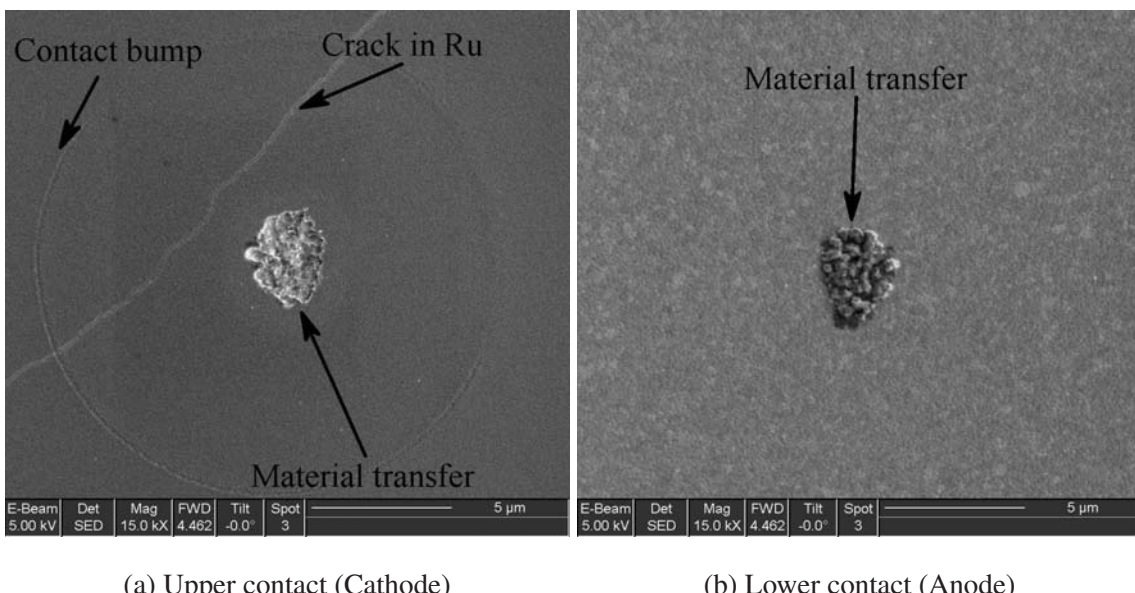
Figure 4.24: Scanning electron microscope image of upper contact bump and lower contact pad after 5×10^6 cycles. Material transfer can be seen from the lower contact to the upper contact.

4.5 Au-RuO$_2$ 25% contact with $8\mu m$ radius contact bump

4.5.1 Initial Contact Test.

Figure 4.25 displays the measured micro-contact resistance for an Au-RuO$_2$ 25% contact fixed-fixed micro-contact support structure with a contact bump radius of $8\mu m$ and the modeled values of micro-contact resistance. This data is the average of 5 ICT measurements; also shown is the standard deviation of that data.
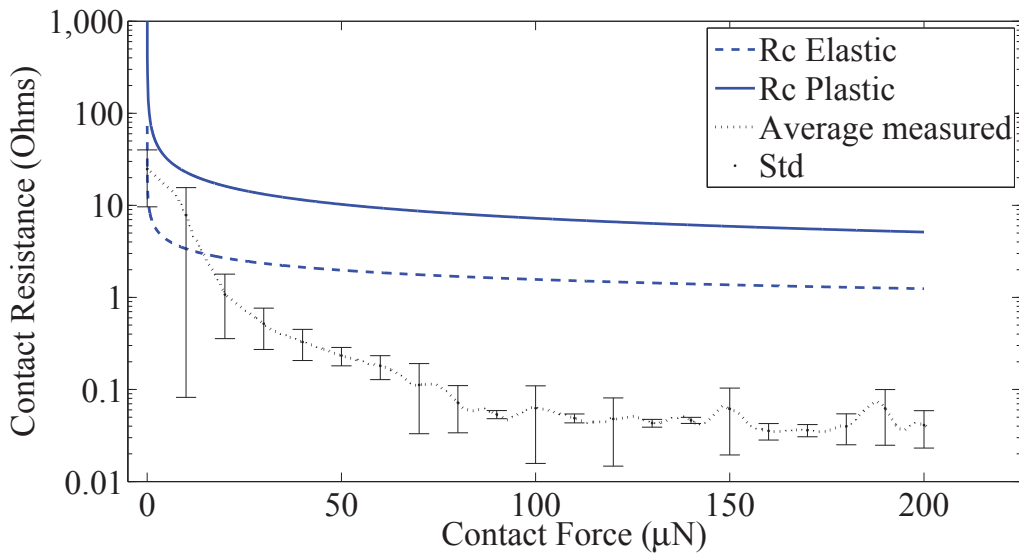
Figure 4.25: Contact resistance of Au-RuO$_2$ 25% contact with $8\mu m$ radius contact; 'Rc Elastic' and 'Rc Plastic' are modeled values, 'Average Measured' data is the average of 5 initial contact test measurements and 'Std' is the standard deviation of those measured values.

Figure 4.25 shows that the modeled values are much higher than the measured values. This is due to the assumptions made to model the contacts with different metal types. Further analysis of these models is shown in Section 5.3.

4.5.2 Cold Switch Test.

The 10^7 cycles test of a micro-contact was performed on two devices. The contact resistance plot for the first device is shown in Figure 4.26. SEM images for the contact area is shown in Figure 4.27a and for the contact pad in Figure 4.27b.
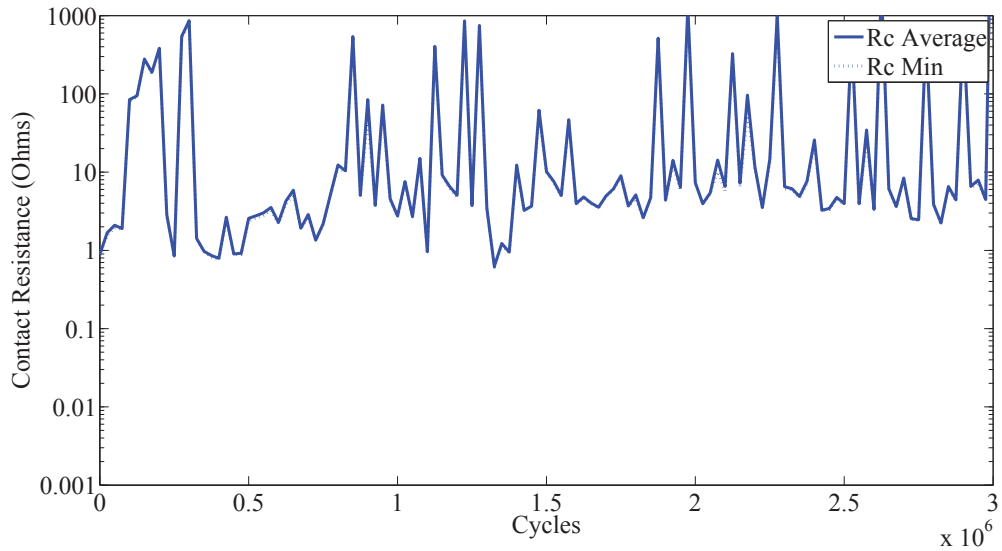
Figure 4.26: Contact resistance of Au-RuO$_2$ 25% contact with $8\mu m$ radius contact for a 10^7 cycles. This contact failed after 3×10^6 cycles. 'Rc Average' is the average for the last 5 resistance measurements at $\sim 200\mu N$ of contact force during the measurement cycle. 'Rc Min' is the minimum contact resistance measured during the measurement cycle.

(a) Upper contact (Anode)   (b) Lower contact (Cathode)
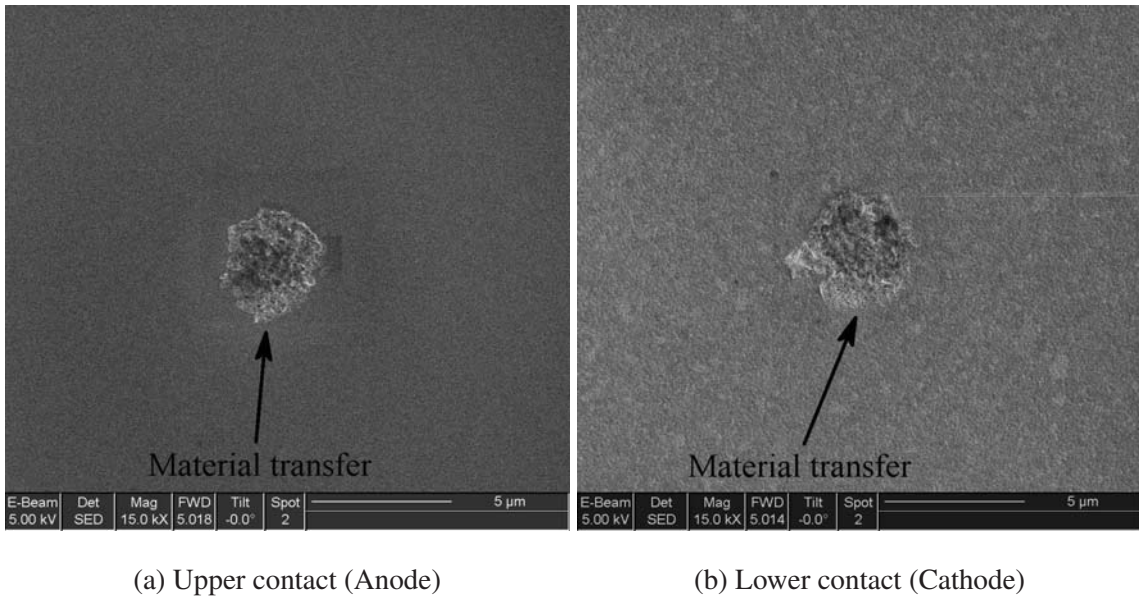
Figure 4.27: Scanning electron microscope of Upper contact bump and lower contact pad after 3×10^6 cycles. After 3×10^6 cycles the contact shows large area of material transfer.

This contact shows indications of wear. Large amounts of material transfer cause the contact to fail to close after only 3×10^6 cycles. Another contact was also actuated to 10^7 cycles, but on this contact the connection for the anode and cathode was switched. This device is shown in Figure 4.28. SEM images for the contact area is shown in Figure 4.29a and for the contact pad in Figure 4.29b.

This contact showed no wear after 10^7 cycles. This contact also showed a lower contact resistance throughout testing similar to the Au-Au contact. Analysis of why this might be is contained in Section 5.8
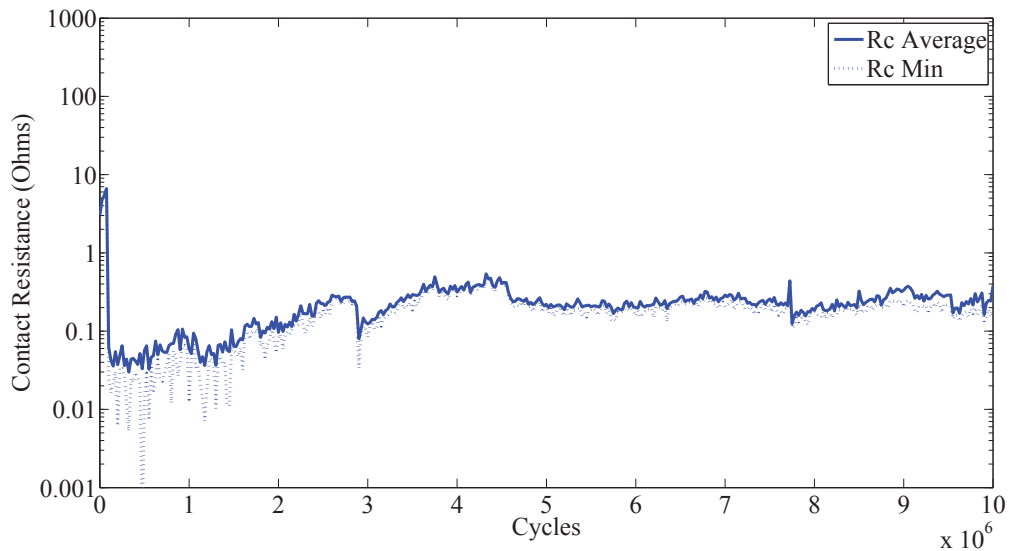
Figure 4.28: Contact resistance of Au-RuO$_2$ 25% contact with 8μm radius contact for a 10^7 cycles. 'Rc Average' is the average for the last 5 resistance measurements at $\sim 200\mu N$ of contact force during the measurement cycle. 'Rc Min' is the minimum contact resistance measured during the measurement cycle.

(a) Upper contact (Cathode)

(b) Lower contact (Anode)
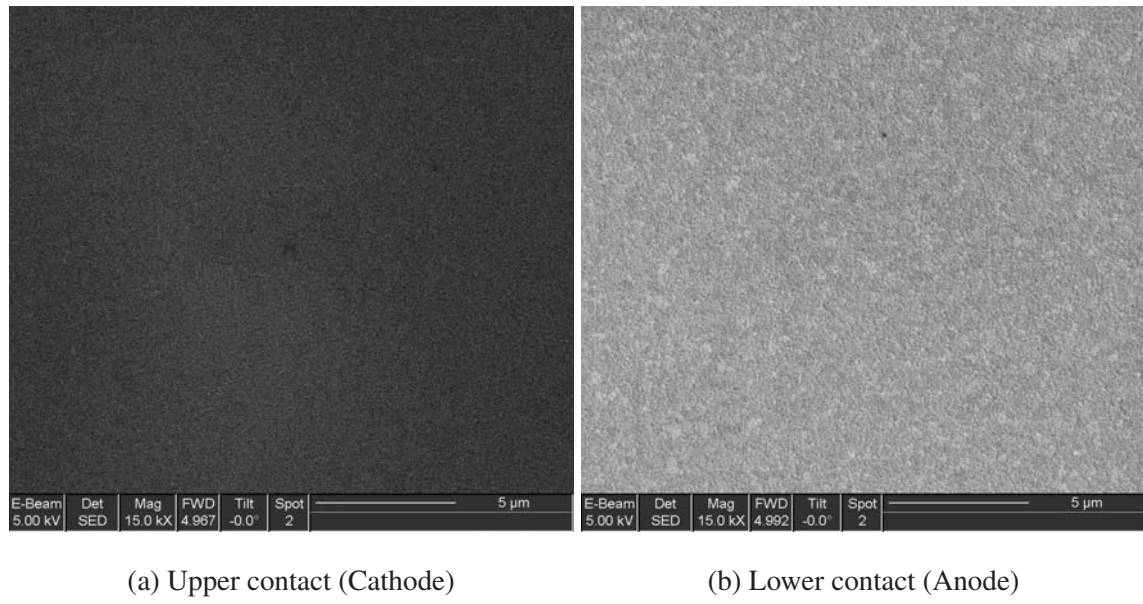
Figure 4.29: Scanning electron microscope image of contact pad after 10^7 cycles. The contact area was clear of defects. With the upper contact as the cathode, no material transfer is observed and no other defects can be seen.

4.6 Gray-scale results

The goal of this research was to create a lower contact surface for use in micro-contact testing. The first attempt at designing a lower contact structure was to load the engineer lower contact design and superimpose the new contact pads into the existing design. This would ensure that the size and spacing would be correct. Due to a limitation of the design software, the images cannot be superimposed onto the mask design, so an alternate way to write these lower contacts was required. Two methods were attempted to create these lower pads with the 2D pyramid pattern. The first was an image representing the entire die, which consisted of 16 beams, and therefore 16 lower contacts in a $5000\mu m \times 5000\mu m$ area. This image was scaled to the correct overall size. Figure 4.30 shows a picture of one of these lower contact pads that was approximately $70\mu m \times 150\mu m$ in area. The second method used the manual alignment of the Heidelberg system to direct write each lower contact design. This method was more labor intensive, but with the addition of some alignment marks on the wafer, it allowed for precise alignment of the lower contact. SEM images of the final structures etched into the Si wafer is shown in Figure 4.31a (2D Pyramid) and 4.31b (3D pyramid). SEM images of the final structures after application of the isolation layer and lower contact metal is shown in Figure 4.32a (2D Pyramid) and 4.32b (3D pyramid).
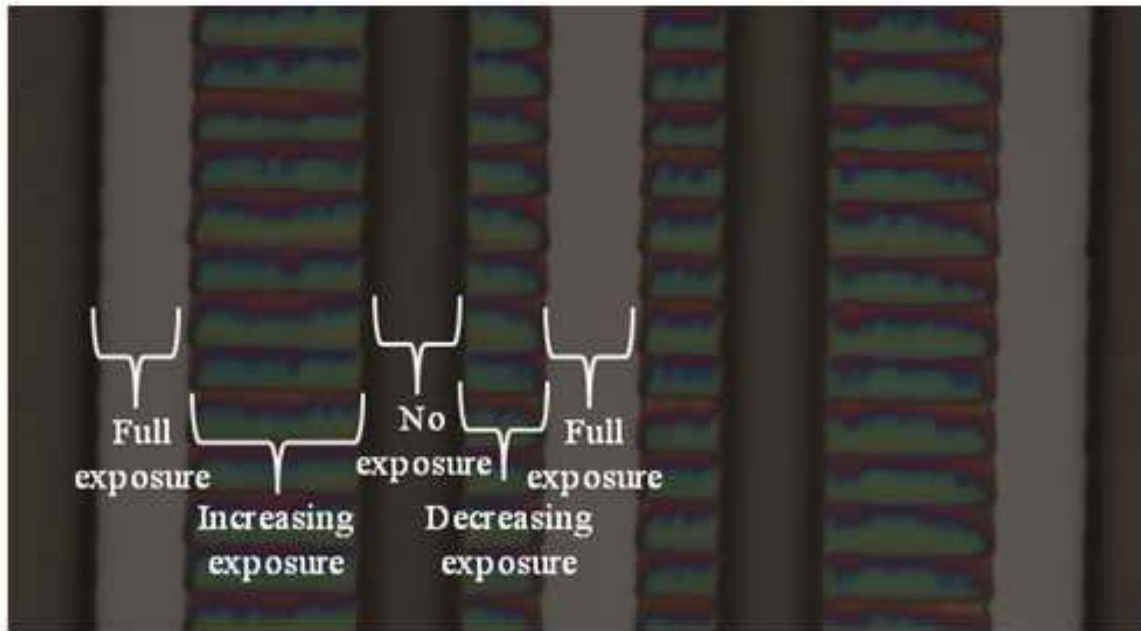
Figure 4.30: 2D pyramid design imposed onto the overall die image. Due to the laser direction moving from left to right, lines were created against the grain of the 2D pyramid.

(a) 2D pyramid design
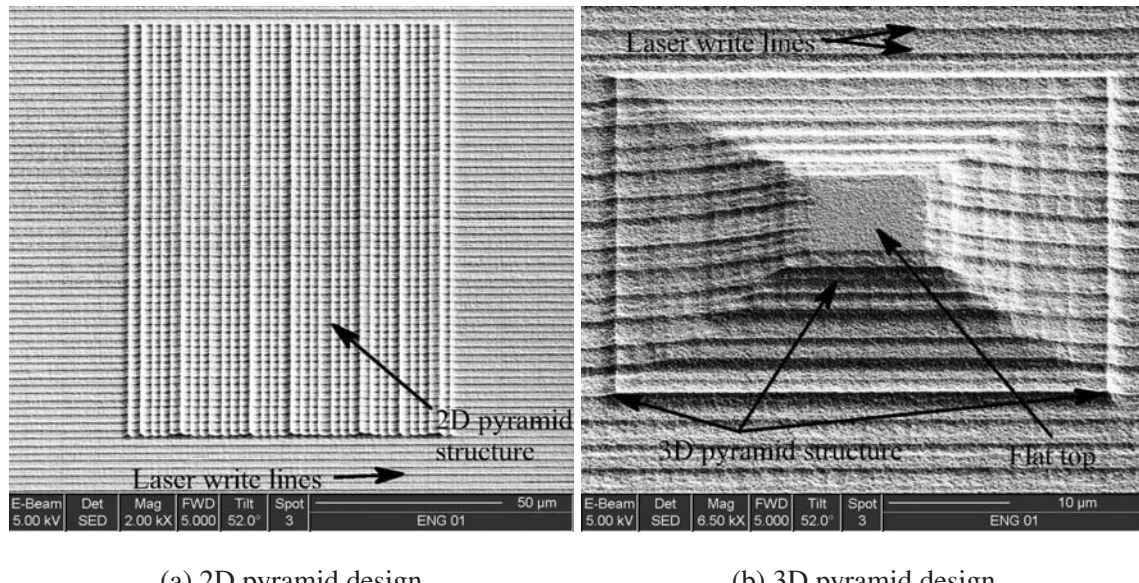
(b) 3D pyramid design

Figure 4.31: Scanning electron microscope image of the 2D and 3D pyramid design after etching.

73
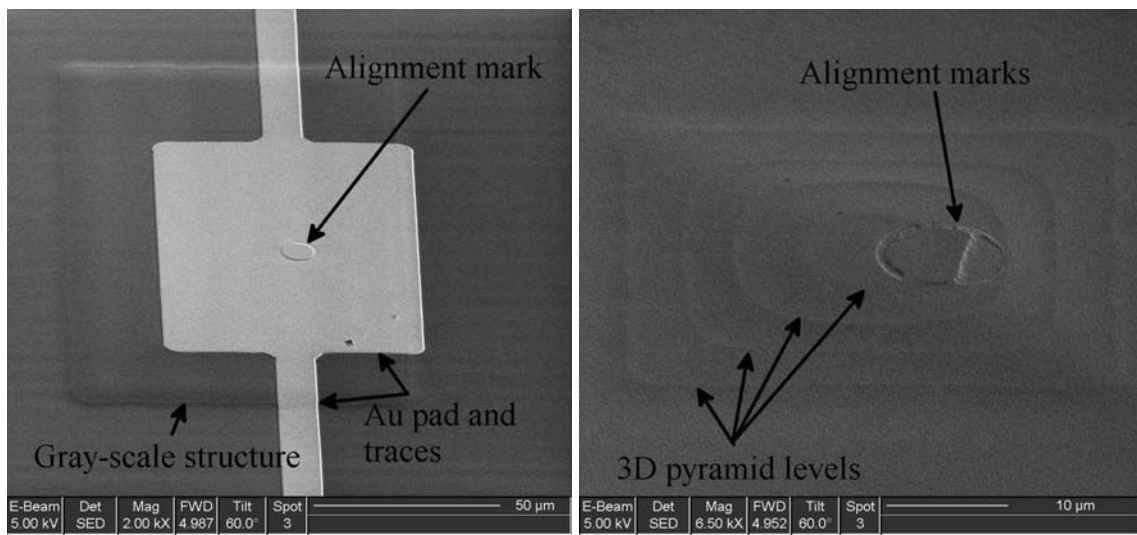
(a) 2D pyramid design   (b) 3D pyramid design

Figure 4.32: Scanning electron microscope image of the 2D and 3D pyramid design with isolation layer the lower contact metal applied.

4.7 Au-Au contact with $4\mu m$ radius contact bump on 2D pyramids

4.7.1 Initial Contact Test.

Figure 4.33 shows the measured micro-contact resistance for an Au-Au only fixed-fixed micro-contact support with a contact radius of $4\mu m$ on an engineered lower contact and the modeled values of micro-contact resistance. This data is the average of 15 ICT measurements; also shown is the standard deviation of that data. The data shows that the measured data is higher than the modeled data but at a higher resistance. Possible reasons for this will be discussed in Section 5.9
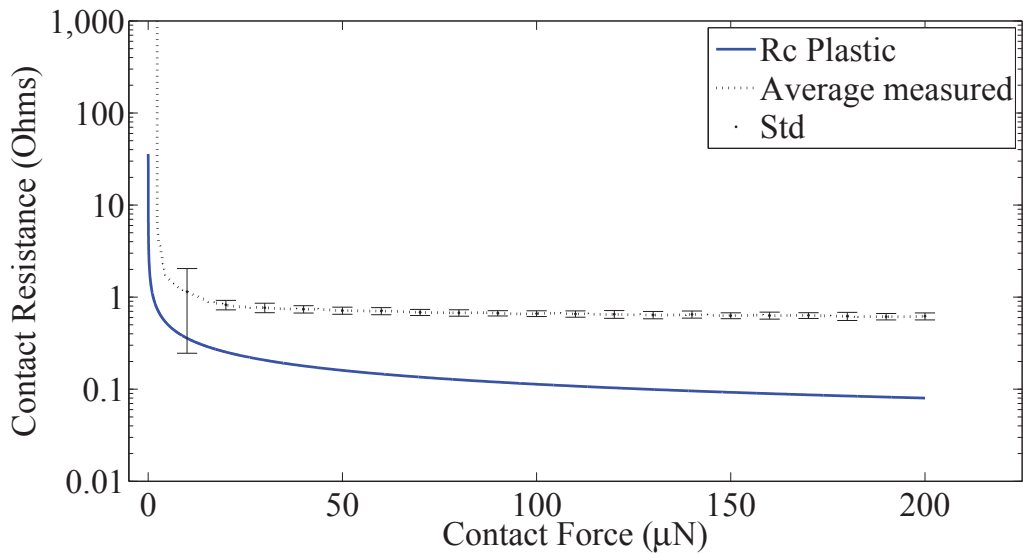
Figure 4.33: Contact resistance of Au-Au $4\mu m$ radius contacts on an engineered lower contact consisting of 2D pyramids; 'Rc Plastic' is modeled, 'Average Measured' data is the average of 15 ICT measurements and 'Std' is the standard deviation of those measured values

4.7.2 Cold Switch Test.

The 10^7 cycles test of a micro-contact was performed on the engineered lower contact as well. The contact resistance plot is shown in Figure 4.34. SEM images for the contact bump is shown in Figure 4.35a and for the contact pad in Figure 4.35b.
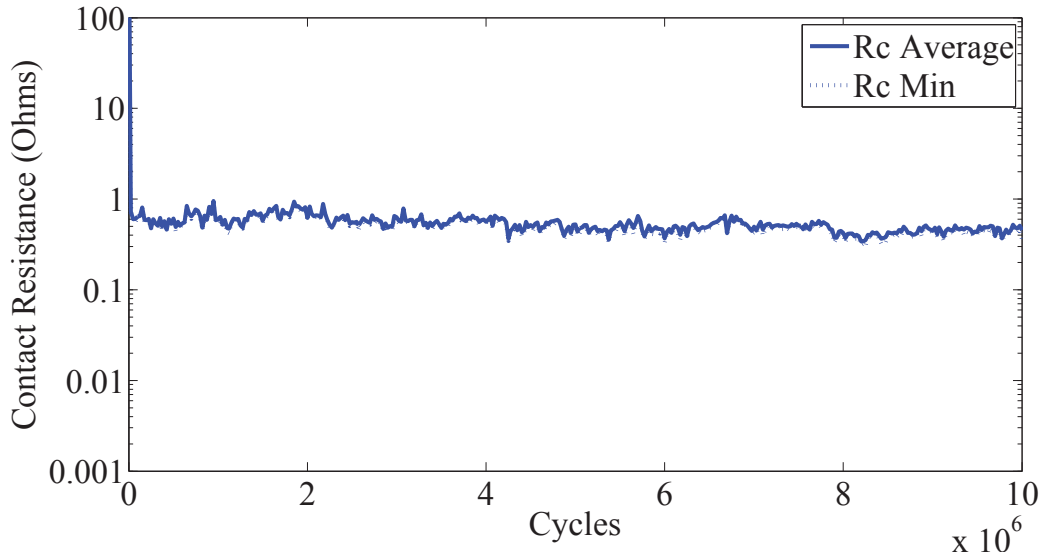
Figure 4.34: Contact resistance of Au-Au $4\mu m$ radius contact bump on 2D pyramids for 10^7 cycles. 'Rc Average' is the average for the last 5 resistance measurements at $\sim 200\mu N$ of contact force during the measurement cycle. 'Rc Min' is the minimum contact resistance measured during the measurement cycle.

This contact shows no wear after 10^7 cycles. This clean contact area matches well with the low contact resistance seen throughout the testing of the micro-contact.

(a) Upper contact (Anode)   (b) Lower engineered contact (Cathode)
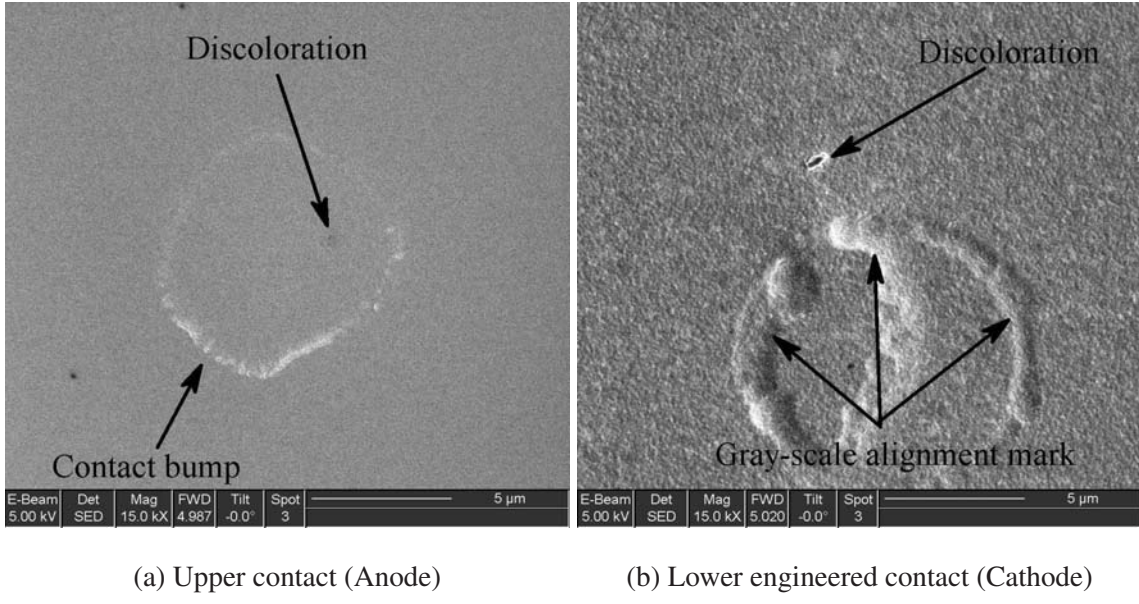
Figure 4.35: Scanning electron microscope image of upper contact bump and lower engineered contact pad after 10^7 cycles.

4.8 Au-Au contact with $4\mu m$ radius contact bump on 3D pyramid

4.8.1 Initial Contact Test.

Figure 4.36 shows the measured micro-contact resistance for an Au-Au only fixed-fixed micro-contact support with a contact radius of $4\mu m$ on an engineered lower contact and the modeled values of micro-contact resistance. This data is the average of 15 ICT measurements; also shown is the standard deviation of the data.

Figure 4.36 shows that the average measured values follow the plastic model very closely. These results matches the ICT test of the hemisphere/planar contact.
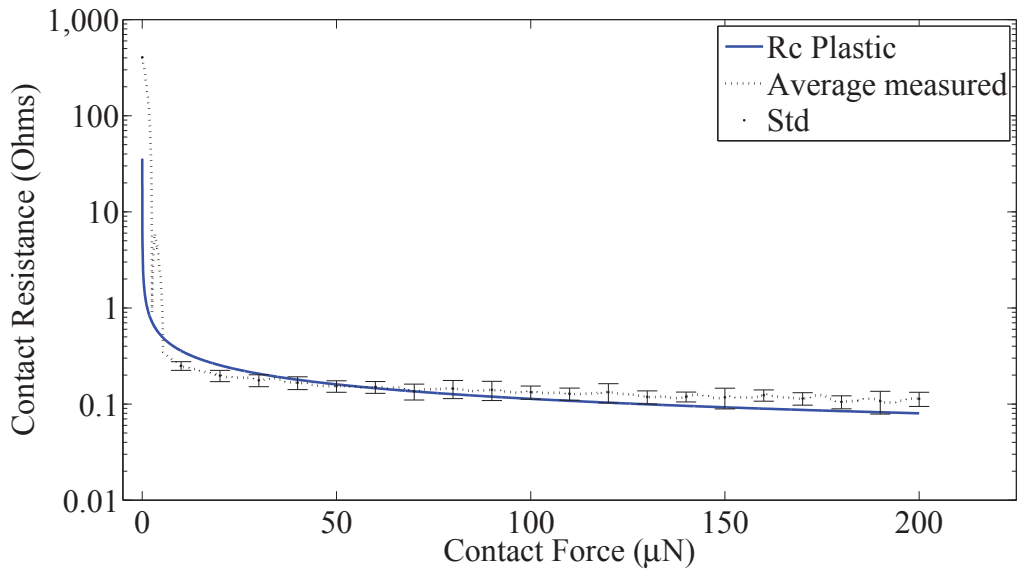
Figure 4.36: Contact resistance of Au-Au $4\mu m$ radius contacts on an engineered lower contact consisting of 3D pyramids; Rc Plastic is modeled, Average Measured data is the average of 15 initial contact test measurements and Std is the standard deviation of those measured values

4.8.2 Cold Switch Test.

The 10^7 cycle test of a micro-contact was performed on the engineered lower contact as well. The contact resistance plot is shown in Figure 4.37. SEM images for the contact bump is shown in Figure 4.38a and for the contact pad in Figure 4.38b.

This contact shows only a amount of material transfer after 10^7 actuation. This matches the very low contact resistance seen throughout the lifetime of the micro-contact.
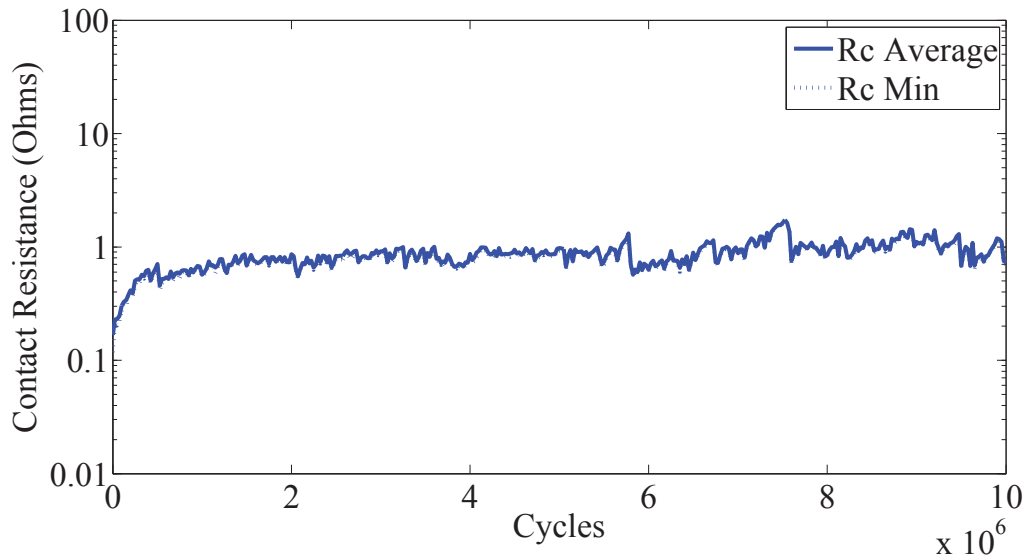
Figure 4.37: Contact resistance of Au-Au $4\mu m$ radius contacts on an engineered lower contact consisting of 3D pyramids for a 10^7 cycles. Rc Average is the average for the last 5 data poinst at $\sim 200\mu N$ of contact force. Rc Min is the minimum contact resistance measured during the measurement cycle

(a) Upper contact (Anode) (b) Lower contact (Cathode)
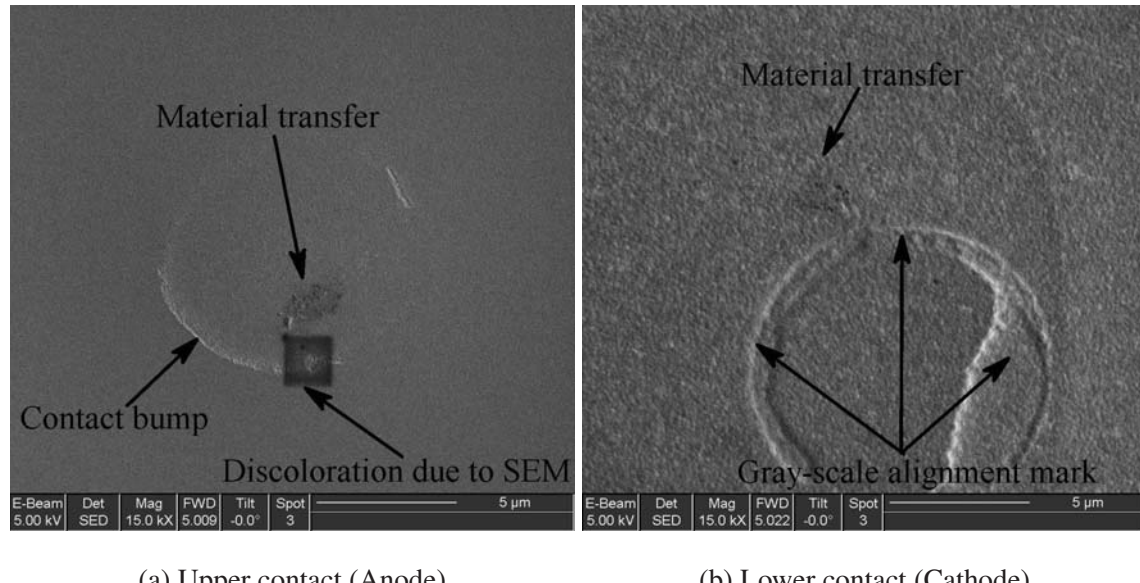
Figure 4.38: Scanning electron microscope image of upper contact bump and lower contact pad after 10^7 cycles. A small amount of material transfer is shown in the contact area.

4.9 CNT encapsulated beams

CNTs were added to the upper hemisphere contact by encapsulating them with a sputtered a layer of gold for the contact, applying the CNTs, and electroplating gold over them. The resultant device is not an Au-CNT or alloy type structure; it is an Au structure with encapsulated CNTs. The CNTs were applied by spinning on a mixture of CNTs ultrasonically diluted in isopropyl alcohol. After application the witness samples were analyzed to determine the amount of coverage. This analysis can be found in Section 5.4.

It is important to point out that this data was taken before the measurement equipment was upgraded to increase the sensitivity, Therefore the minimum contact resistance during the ICT is the measurement floor of the equipment used.

4.9.1   CNT film in upper hemisphere contact.

4.9.1.1   Initial contact test.
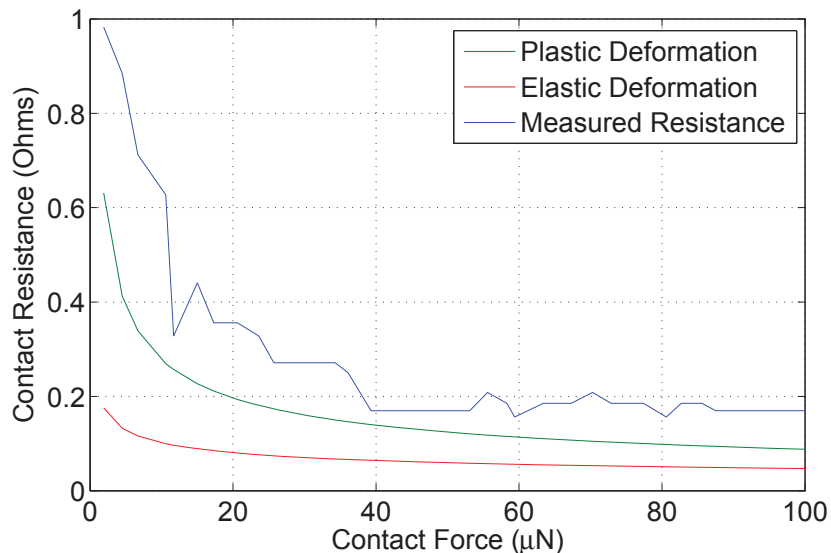
Figure 4.39: Contact Resistance of Au-Au Beam with CNT encapsulated into the beam. The results mimic the model until around $40\mu N$.

Figure 4.39 shows a comparison of the measured micro-contact resistance for an Au contact with CNTs encapsulated film in the upper hemisphere planar contact of a fixed-fixed micro-contact support structure. With less than $40\mu N$ of force applied, initial contact resistance mimics the plastic deformation resistance model.

4.9.1.2 Cold switch test.

For the cold-switch test (CST), the devices under test were first cycled up to 100 times at $10Hz$ with measurements taken at every 10 cycles. Following the initial 100 cycles, the devices were actuated up to $1,000$ cycles at $100Hz$ with measurements performed every 100 cycles. Then $10,000$ cycles at $1kHz$ with measurements every $1,000$ cycles. In addition, the micro-contact structures were actuated to $100,000$ cycles at $3kHz$ with measurements every $10,000$ cycles. Lastly, the devices were cycled to 10^7 cycles with measurements at every $100,000$ cycles.

4.9.1.3 Micro-contact resistance evolution.
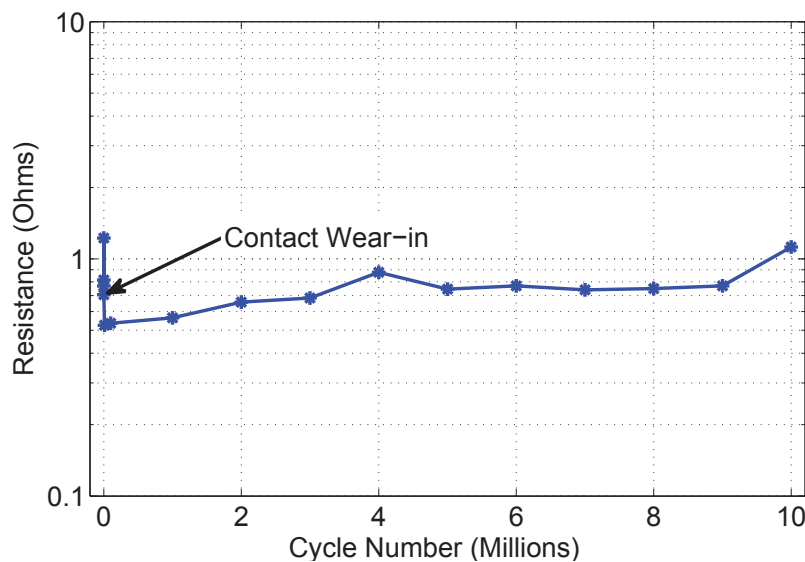
Figure 4.40: Resistance values for fixed-fixed Au-CNT in the beam in the micro-contact support structure.

81

Results of these tests are shown in Figure 4.40. This contact showed an initial high resistance at 1.22Ω. Followed by a wearing in period until resistance dropped below 1Ω, where it remained until testing was stopped at 10^7 cycles.

4.9.2 *CNT composite film in lower planar contact.*

4.9.2.1 *Initial contact test.*
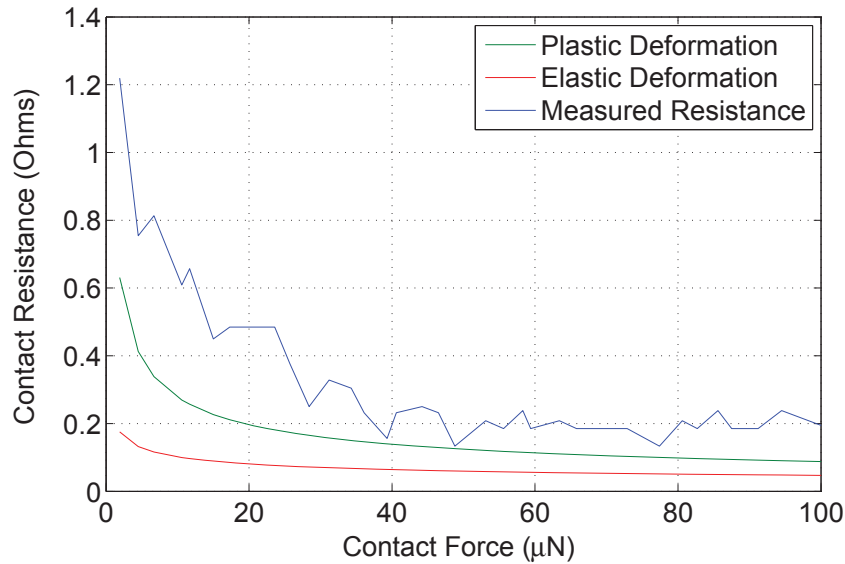
Figure 4.41: Contact resistance of Au-Au Beam with CNT encapsulated into the lower contact pad. The results followed the model until around $50\mu N$.

Figure 4.41 is a plot of the measured micro-contact resistance for a Au contact with CNTs encapsulated into the lower contact pad fixed-fixed micro-contact support structure. Similarly to what was seen in Figure 4.39, the initial contact resistance with less than $50\mu N$ applied is close to the plastic deformation resistance model. After the first $50\mu N$, contact resistance begins to deviate from the model. As stated with the first micro-contact, this deviation is attributed to the measurement equipment.

4.9.2.2 Cold switch test.

For the CST, the devices under test were first cycled same as the other CNT infused contact, only this time, the device was actuated to failure. Which for this contact was to 4×10^7 cycles with measurements at every 10^5 cycles. This increase in cycling was to actuate the switch to failure to see what failure mode(s) would surface.
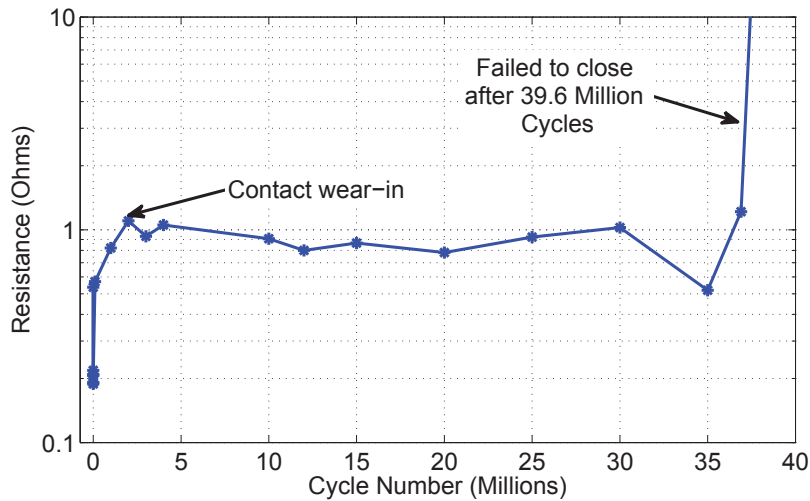
Figure 4.42: Resistance values for fixed-fixed Au-CNT in the lower contact in the micro-contact support structure.

Results of these tests are shown in Figure 4.42. This contact showed an initial increase in contact resistance from starting at 0.19Ω, to maxing out at 1.1Ω, followed by a wear in. Finally, the fixed-fixed micro-contact with CNTs encapsulated into the lower contact was cycled 36.9 million times, at which point the closed contact resistance was 1.21Ω. At the 37 million cycle mark, which was the next data collection point, the contact failed to close.

4.10 Flip switch

One of the drawbacks to the fixed-fixed beam design was the inability to check the contact area without destroying the beam. To address this issue a flip switch design was created in PolyMUMPS. The flip switch is a hinged switch that rest on the anchors, this allows the beam to be flip closed for testing and flipped open for examination. Following examination, the switch can be flipped closed once again for additional testing. An image of the open flip switch is shown in Figure 4.43. A image after the flip switch is closed is shown in Figure 4.44.
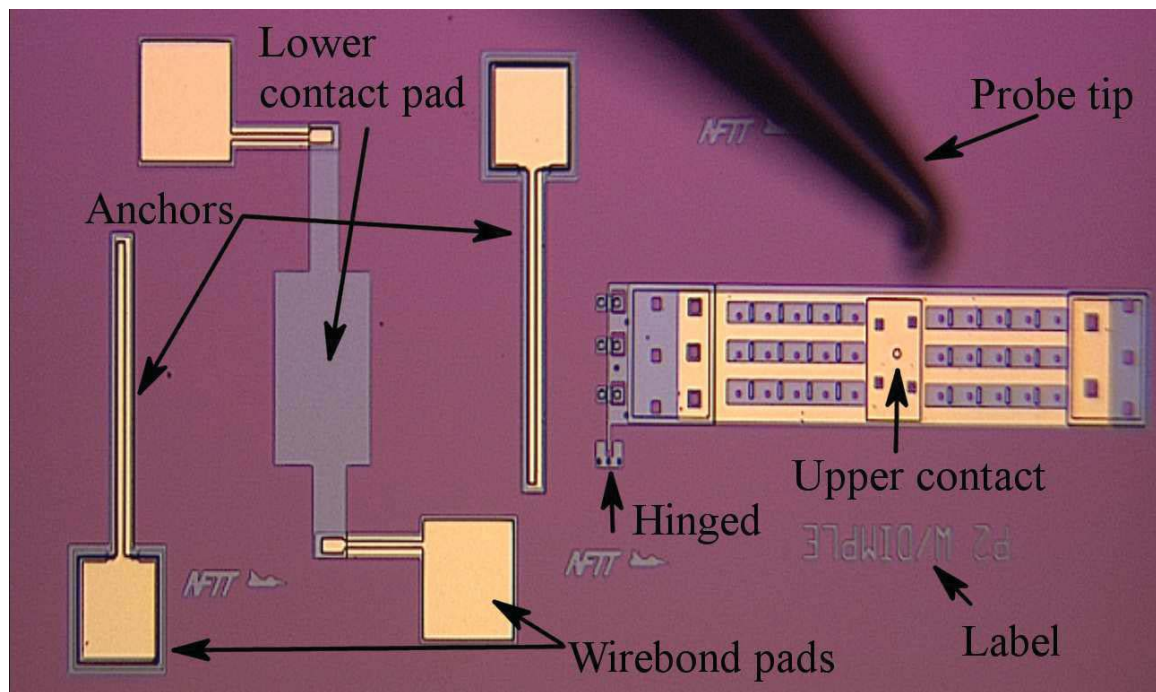
Figure 4.43: Image of the flip switch in the open position, major parts are labeled.

Layouts of the beams included different beam thickness and upper contact layouts. The complete PolyMUMPS layout can be found in Appendix C. The assumption was the contact area on the anchors is much greater than the contact area for the upper contact
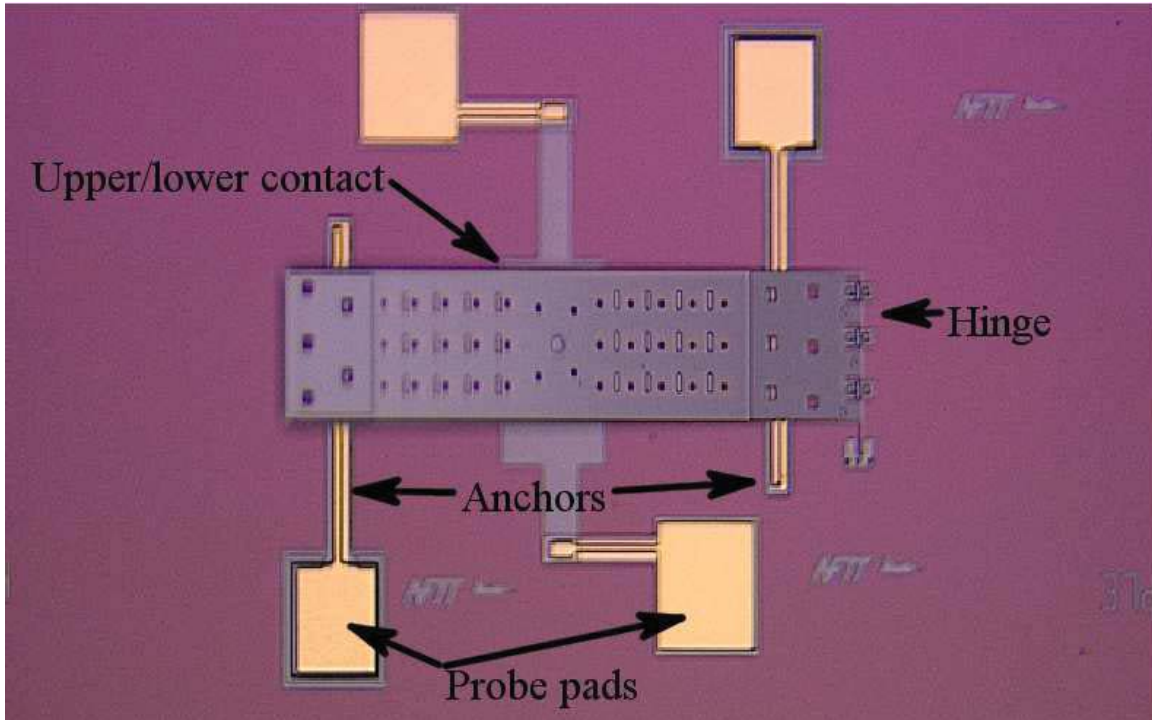
Figure 4.44: Image of the flip switch in the closed position, major parts are labeled.

bump. Thus the resistance measurement would be dominated by the upper contact bump/lower planar contact resistance.

Testing of this design was not done in the test fixture, but preliminary testing were done at the probe station. This testing showed that pressing on the upper contact area would cause electrical contact between the anchor points before the upper and lower contact area came into contact. This order of contact is needed for successful use of the Holm cross-bar measurement used in previous testing.

4.11 Chapter summary

This chapter detailed the representative tests of the fixed-fixed micro-contact support structures as well as described the success of using the micro-contact test fixture. The reasons for why the fixed-fixed Au micro-contact support structure. Testing of Au-Au,

Au-Ru, Au-RuO$_2$, Au-CNTs and Au-Au with engineered micro-contact were all tested to track performance of the micro-contact materials and proving the viability of the fixed-fixed micro-contact support structure as a test structure. The next chapter presents detailed the analysis of the data presented in this chapter.

V. Analysis

5.1 Chapter overview

This chapter will present analysis of the results presented in the previous chapter. This chapter will discuss analysis of the following topics: Beam Modeling, Ru and RuO_2 models, the combination of the Hertz and Thin Film Model, Material transfer in Au-Au contacts, electromigration in RuO_2 contacts, engineered lower contact, plastic deformation, and lastly an analysis of the CNT micro-contacts.

5.2 Beam modeling

To ensure that the force sensor would be able apply the appropriate amount of force, calculations were done using the formulas from Section 2.3 to approximate the force needed to apply to close the micro-contact. These values are then compared to the measured values for thickness and force applied. For this research, the applied force to the micro-contact when closed is $200\mu N$. But to apply this, first an appropriate amount of force needs to be applied to move the upper contact bump to be in contact with the lower planar contact. Figure 5.1 is an example showing the difference in the amount of force needed to close the micro-contact as measured from the force sensor, and the amount of force applied to the micro-contact.

Assuming a $3\mu m$ gap, width of $250\mu m$, electroplated thickness of $2.4\mu m$ and a Young's modulus for electroplated gold of 79.42 Gpa [69] the data for Table 5.1 was calculated using the formulas from Section 2.3.
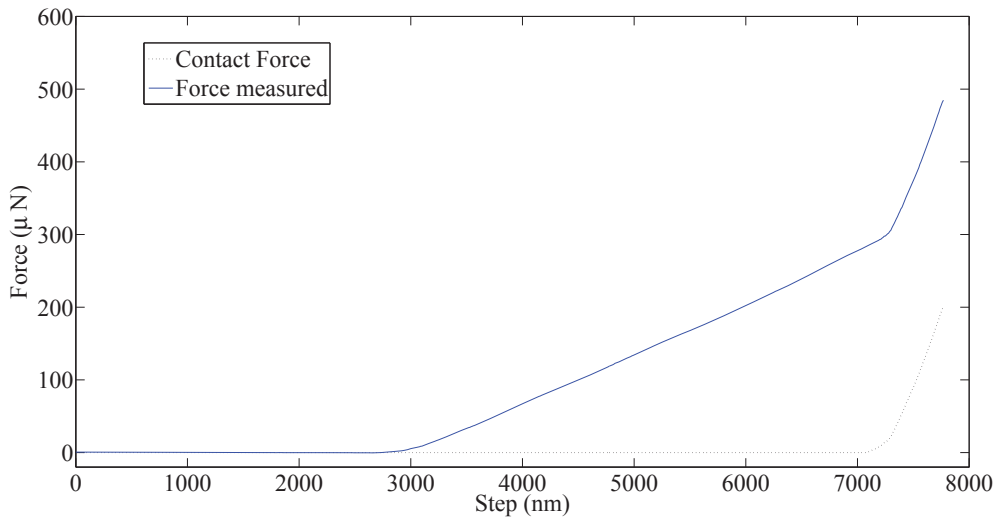
Figure 5.1: An examples comparing the force measured by the Force Sensor, and the Contact force applied to the micro-contact

Table 5.1: Calculation of required force to bend the beam the required $2\mu m$ to mate the upper and lower contacts

Beam length (μm)	I (10^{-22})	Force to close (μN)
350	2.88	486
400	2.88	325
450	2.88	228
500	2.88	166

To compare the model to the measured contact force, measured data was used for beam thickness and gap. These results are shown in Figure 5.2. It shows that the model closely predicted the force needed to mate the upper and lower contacts. Deviations can be explained by the hardness of the RuO_2 is not taken into account for the stiffness of the

88

beam. The large modeled values are due to the much greater beam thickness that occurred during processing of the RuO$_2$ samples, these samples had beam thickness more than double the expected. Thus had a much high prediction and measure closing force. But since the focus of the research was the contact force, this addition force needed to close the contact did not effect the test data.
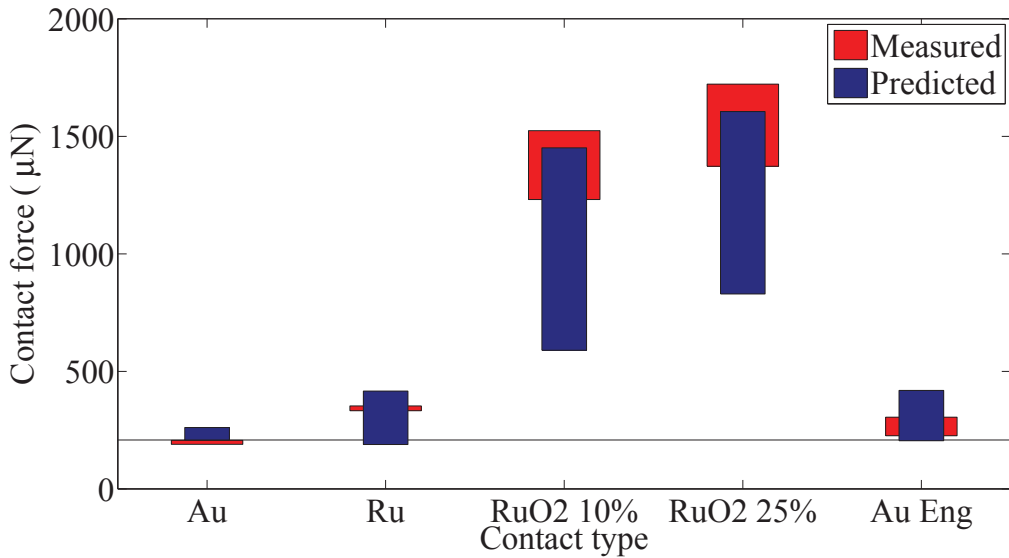
Figure 5.2: Compare measured contact mating force to predicted. Predicted values are based off of measured beam thickness and gap taken dring construction. Deviations can be due to the model is only using the hardness of the structure electroplated Au layer and the contact metal is ignored.

5.3 Ru and RuO$_2$ modeling

When modeling the Au-Ru and Au-RuO$_2$ contacts, there was a large variation between the predicted values and measured values for the ICT. This was seen in Figures 4.15, 4.20 and 4.25 there is a large difference between the modeled values and the measured values. The reason for this difference is the approach taken to model these

contact. In these models, values like resistivity and hardness were averaged to create the model between the Au-Ru, and Au-RuO$_2$ micro-contacts. This averaging of the two values is the cause of the overestimation. The majority of area of both the upper and lower contact is Au, only a small 200μm strip of the upper contact is a higher resistivity. A comparison of the two RuO$_2$ measured ICT values were compared to different contact modeling techniques including averaging of hardness and resistivity, and different combinations of hardness and resistivity. Figure 5.3 compares the models with the RuO$_2$ 10% and Figure 5.4 compares these models with the RuO$_2$ 25%.
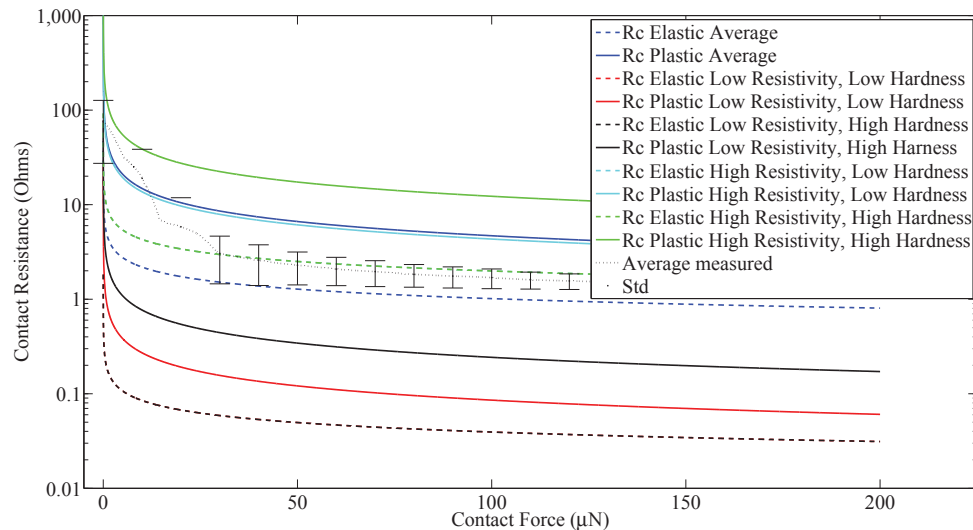
Figure 5.3: Contact Resistance model comparison. This shows that for the RuO$_2$ 10% the average of the hardness and resistivity gave the closes model to the actual data.

This comparison shows that not one of these techniques will work for both contacts, more work will need to be done to find a model that will work for the mixed metal contacts.

90
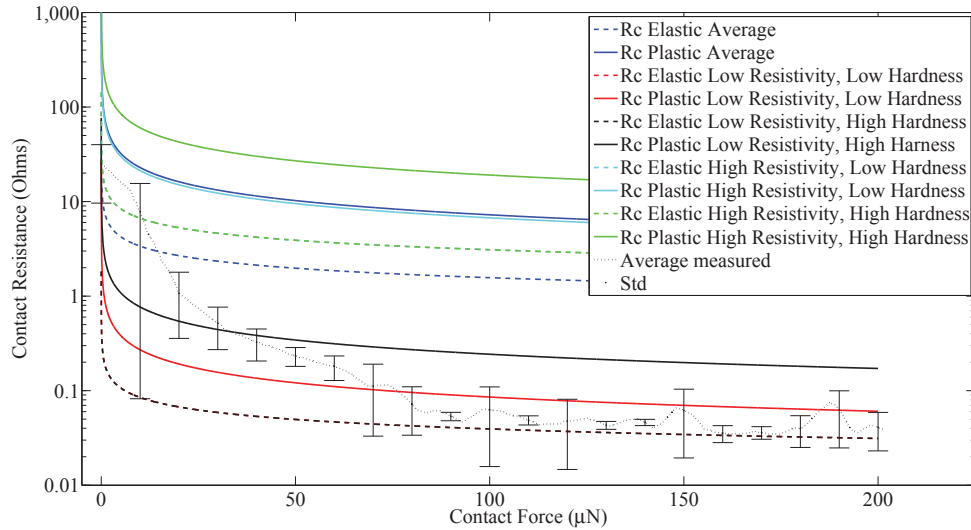
Figure 5.4: Contact Resistance model comparison. This shows that for the RuO$_2$ 25% the lower values of the hardness and resistivity gave the closes model to the actual data.

5.4 CNT coverage analysis

After deposition of the CNTs, a thermal image was taken to demonstrate the thermal conductivity of the CNTs. The thermal image is shown in Figure 5.5. The more readily identifiable CNT groupings or "clumps" appear as the bright green and red spots, indicating better thermal conduction than the dark blue nitride coated silicon substrate and Au bottom metal layer. The reason for the CNT clumps appearing in different colors is due to the fact that these clumping of CNTs are not all the same size and thus conduct heat differently. The thermal image was processed in Matlab to calculate the percent coverage by separating the areas with only Au and the area with a Au-CNT film. The final product of this processing is shown in Figure 5.6. The image analysis revealed a 55% coverage of Au-CNT film.
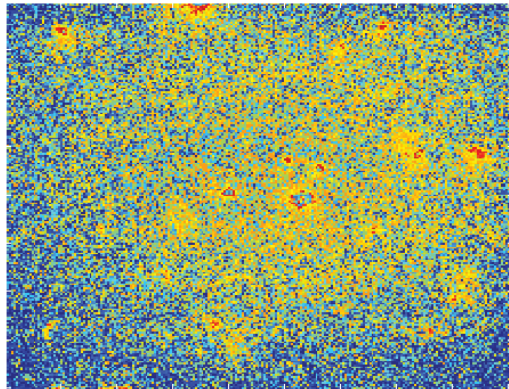
Figure 5.5: Thermal image if the CNT witness sample. Dark blue represents am Au-only area and grean/yellow/reds highlighting the areas of an Au-CNT film
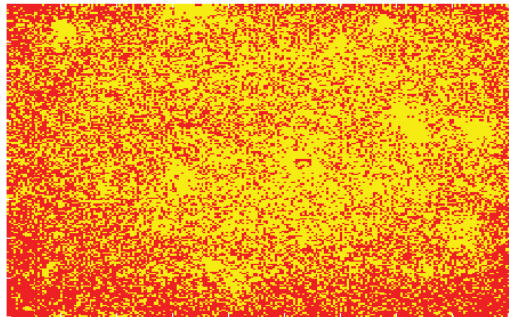
Figure 5.6: Post processed digital image, red showing areas of only Au and yellow highlighting the areas of an Au-CNT film.

To intensify the visibility of the larger clumps, another thermal image was taken at a higher temperature, as can be seen in Figure 5.7. The large CNT groupings or "clumps" appear as the bright green and red spots. The addition of CNTs may not only enhance the thermal conductivity of the micro-contact support structure, which would help maintain lower contact temperatures, but increase resistivity due to the CNTs changing the

92

conducting paths of the electrons. Depending on the application, the higher contact resistance may be a potential drawback to the design.
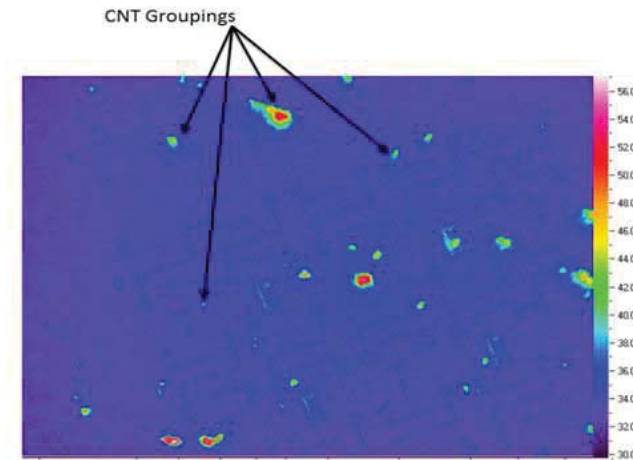
Figure 5.7: Thermal Image of CNT 'clumps' with sample heated to $60 \deg C$.

5.5   Au-Au analysis

The baseline for testing of the test fixture and the comparison data for the contacts was the Au-Au data. What was found is that the micro-contact performed as expected, with lower contact resistance and low contact resistance into the 10's of millions of cycles. This is confirmed by the data shown in Section 4.2.

In the Au-Au cold switch test results, there were a number of examples of contacts that exhibited very different contact resistance. What can be drawn from these examples is that these specific contacts, for an unknown reason, exhibited material transfer. This change of the contact area was in conjunction with a change of the contact resistance. What cannot be determined is the root cause for the start of this material transfer. Since all the Au-Au contacts went through the same processing, and different contacts on the same sample showed different results it is difficult to draw one conclusion as to why material transfer occurred. More research would need to be done to determine what cause this

sudden material transfer and increase resistance. This is where the flip switch design would be useful to observe the contact areas as the resistance increases and continue to track the contact area as the number of cycles are increased. Figure A.10 is the perfect example to show where a flip switch would have been useful. When the sharp rise of resistance occurred at 8×10^3, the contact could have been examine as soon as the resistance changed. After examination the contact could have returned to the test structure to resume cycling.

Since the anode and cathode connections were kept consistent on all the Au-Au samples, a comparison based off of current flow cannot be made. But looking at two examples of switches both cycles to 10^7 in Figure 5.8. Both contacts were cycled to 10^7 cycles, but first contact (a & b) demonstrates material transfer between the lower contact (b) to the upper contact(a). This is different than the other contact pair (c & d) contact where the material transfer was from the upper contact (c) to the lower contact (d). This leads to the conclusion that on the Au-Au contacts, the material transfer was independent of the current flow and therefore not completely due to electromigration.

(a) Upper contact (Anode)

(b) Lower contact (Cathode)

(c) Upper contact (Anode)

(d) Lower contact (Cathode)
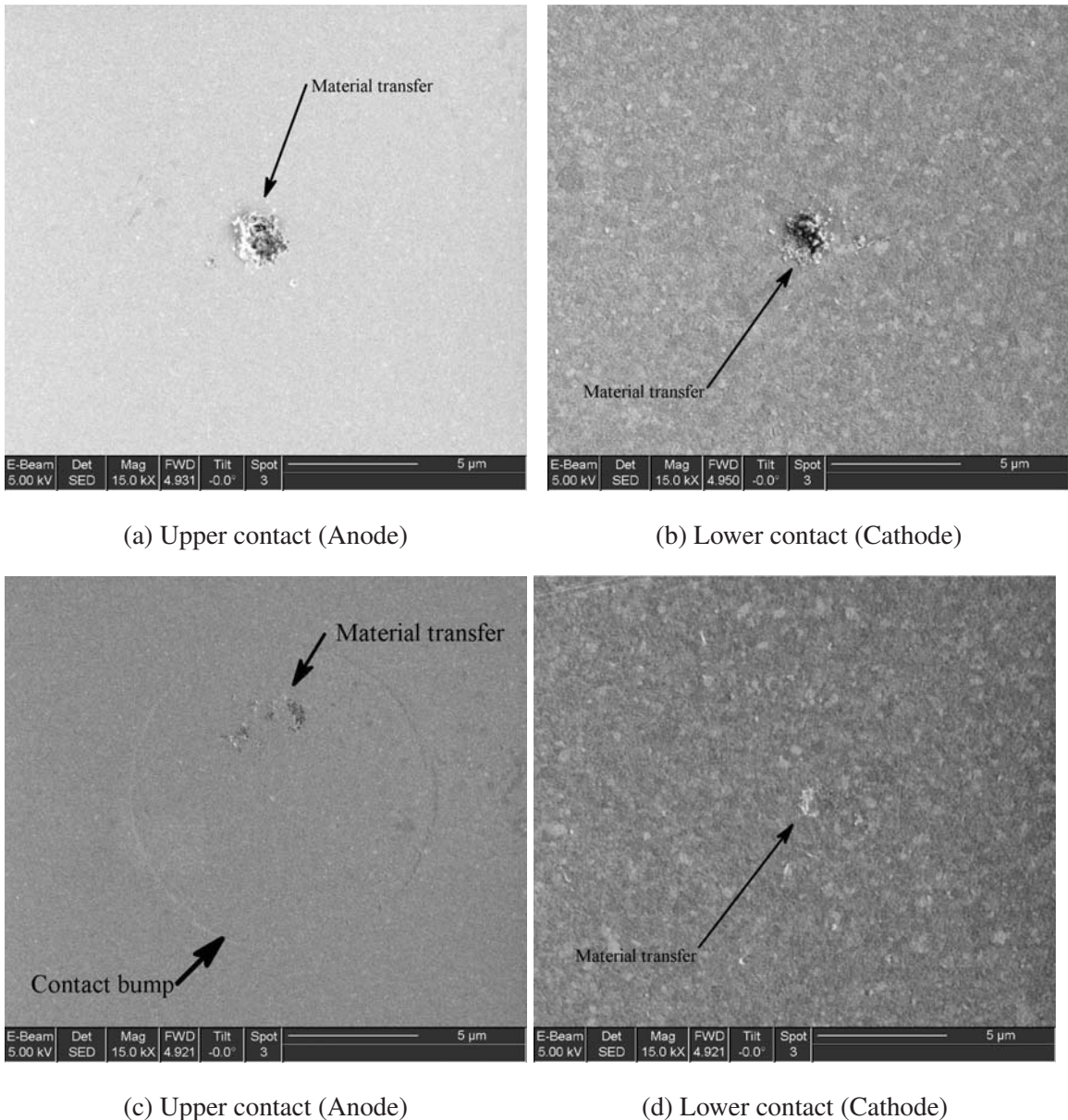
Figure 5.8: Scanning electron microscope Image of two contacts (a & b, c & d) and for comparison, both contacts were cycled to 10^7 cycles, but first contact (a & b) demonstrates material transfer between the lower contact (b) to the upper contact(a). This is different than the other contact pair (c & d) contact where the material transfer was from the upper contact (c) to the lower contact (d).

5.6   Au-Ru analysis

The Au-Ru contacts displayed a much shorter lifetime than similar Au-Au contacts. With the same power connection with the upper Ru contact as the anode and the lower Au contact as the cathode. In this configuration the best contacts displayed similar results we only to 5×10^5 cycles. These similar results were less than 10Ω resistance and limited material transfer. This is much less than the 10^7 seen on the Au-Au contacts. To determine if electromigration was present, there were test done with the contacts switched. This switch changed the harder material, the Ru, to the cathode which in theory would inhibit the material from transferring. It was shown in Figure 4.18 with SEM images for the contact bump is shown in Figure 4.19a and for the contact pad in Figure 4.19b. With the harder material as the cathode this contact showed lower contact resistance into 4×10^6 cycles and less material transfer material than the other Ru contact cycled to 10^7 cycles. It can be concluded from these results that electromigration is effecting the material transfer on the Au-Ru contacts. Therefor for future reliability testing the cathode should be connected to the harder material to improve contact performance and limit material transfer.

5.7   Au-RuO$_2$ 10% analysis

When comparing the results from the Au-RuO$_2$ 10% to the Au-Au micro-contacts it once again performs poorly. On contacts with the contact pad as the cathode, contacts displayed material transfer and contact resistance much higher than 10Ω. These contacts only showed similar contact resistance and material transfer when limited to 5×10^4 cycles. These contact displaying similar behavior to the Au-Ru samples were also subjected to the RuO$_2$ as the cathode. On these test the results were shown in Figure 4.23 with SEM images for the contact bump is shown in Figure 4.24a and for the contact pad in Figure 4.24b. This contact, even though it still has a higher contact resistance, the mico-contact lasted twice as long as the the contacts with the softer Au as the cathode. On

the RuO$_2$ 10% the same conclusion can be drawn where the micro-contact displayed electromigration. Similarly for reliability testing the cathode connection should be made to the RuO$_2$ to promote contact lifetime.

5.8 Au-RuO$_2$ 25% analysis

Once again, when comparing the results from the Au-RuO$_2$ 25% to the Au-Au micro-contacts it performs poorly. On contacts with the contact pad as the cathode, contacts displayed material transfer and contact resistance much higher than 10Ω. The Au-RuO$_2$ 25% micro-contact displayed the best example where as the contact was connected to promote material transfer. When the cathode was connected to the Au pad, material transferred from the soft, evaporated gold lower contact to the hard RuO$_2$ upper contact. In this case, there was a large amount of material transfer and the contact failed after only 3×10^6 cycles. However, when the anode and cathode connections were switched the contact had a lower contact resistance, lasted to 10^7 cycles, and showed little sign of wear. These contacts display the most definitive proof of electromigration. The contact with the RuO$_2$ 25% as the cathode displayed the contact that most resembled the Au-Au results. It can be concluded that the RuO$_2$ 25% displayed electromigraton and that for contact reliability, the harder material should be the cathode.

5.9 Engineered Lower Contact Analysis

From the results of the engineered lower contact we can draw a few conclusions from the structures that were tested. The results of the ICT (Figure 4.36) and CST (Figure 4.37) show that the 3D pyramid pattern cause similar results in contact resistance when compared to the hemispherical/planar contact. From these similar result and the SEM pictures (Figure 4.38b) it can be concluded that the peak of the 3D pyramid is much bigger than the 4μm radius contact bump. Therefore there is no difference in the contact

97

area between the hemisphere/3D pyramid and the hemisphere/planar contact. Even though this is the case for the 3D pyramid, this is not the case for the 2D pyramid design.

The 2D pyramid design, the lower contact area changed enough to cause a smaller contact area. This can be seen in the higher contact resistance during the ICT (Figure 4.33). This change of contact area was even through processing done on the wafer, to ensure electrical isolation, a 200nm layer of silicon nitride is deposited. This silicon nitride layer smoothed out some of the features when comparing Figure 4.31a to Figure 4.32a This smaller contact area caused a higher contact resistance compared to the modeled values and those seen in the hemisphere/planar contact data.

Further research is required to examine the ideal isolation layer thickness and gray-scale design to maximize the structure features to better alter contact area.

5.10   Combination of a Hertz and thin film model

One of the models previously discussed was the thin film model in Section 2.2.5. One of the assumptions was the contact radius a was assumed to be a single a-spot. Since there were already classic models that would take a contact bump and reduce it to an effective radius a combination of the Hertz and Thin Film models was investigated. It was found that this combined model closely match the measured data found in Section 4.2.2. For this combined model the equations for the thin film model (Equations 2.12, 2.13 and 2.14) were used for the bases of the spreading resistance. But instead of the assumed single a-spot, the classical equations for r_{eff} (Equations 2.2 and 2.6) were used as a replacement for a. The results of this model with the data from Section 4.2.2 and previously collected Au data can be seen in Figure 5.9.
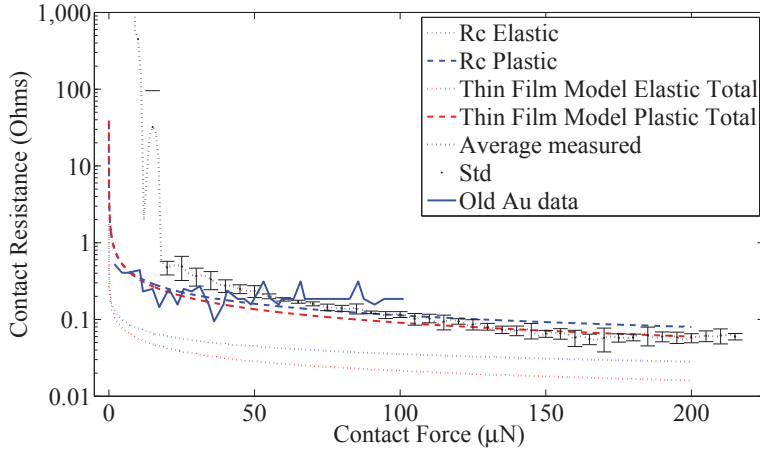
Figure 5.9: Contact Resistance model comparison. This shows that for the $8\mu m$ contact bump radius, the measured data closely matches the combined thin film model for contact greater than $100\mu N$.

5.11 Plastic Deformation

Figure 5.10 shows the CST data collected for the fixed-fixed Au micro-contact support structure with the CNT film in the hemisphere upper contact. Looking at the figure, the force required to make contact decreases from $100\mu N$ to $80\mu N$ after 100 actuations. The cause of reduced required force for contact make is most likely due to a change in the micro-contact support structure's shape.

Using a Zygo white light interferometer (IFM), the tested micro-contact support structure was inspected for a visible change in structural architecture. As seen in Figure 5.11 and Figure 5.12, the force sensor left an impression in the Au-CNT composite film in upper contact of the micro-contact support structure.

The beam was approximately $2.7\mu m$ thick. For plastic deformation, the applied force must meet and surpass the yield stress of the material, which is the lowest value for stress to cause permanent deformation. According to Volinksky *et al*., the yield stress for Au

99

CNT Upper Hemispherical Contact
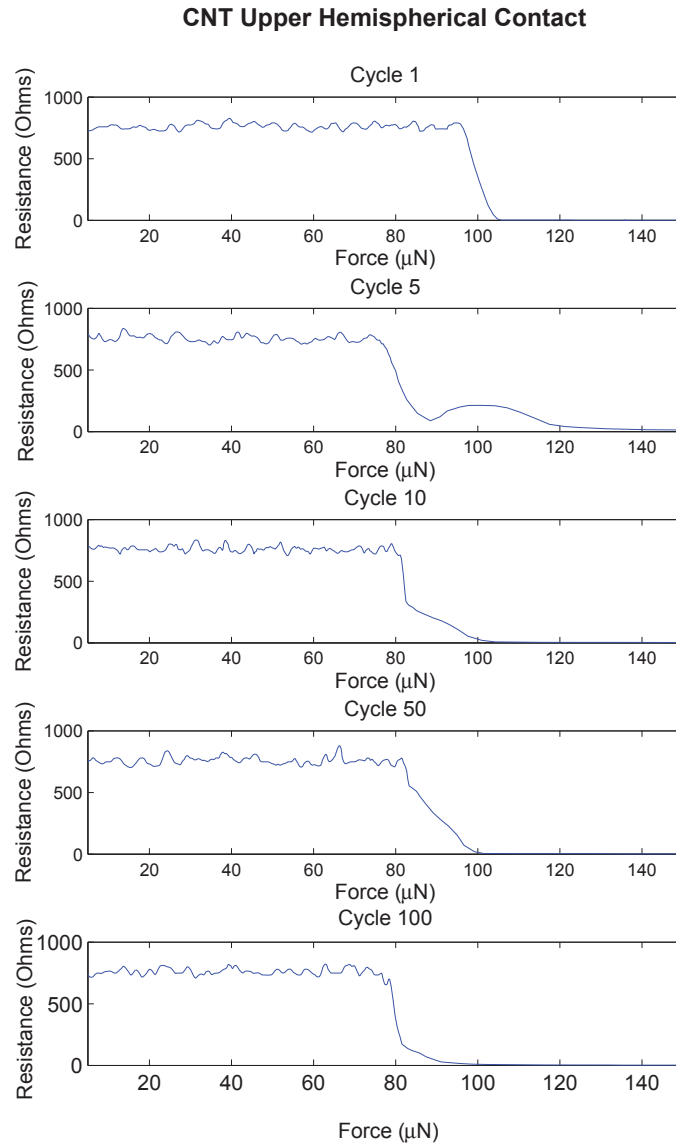
Figure 5.10: Fixed-Fixed Micro Contact support structure with CNTs encapsulated in in upper hemisphere planar contact.

films decreases with a rise in material temperature, which can increase due to the flow of current through the micro-contact and the beam supporting structure. They also reported that for a 2.7μm thick Au film, the yield stress of the support structure was shown to be
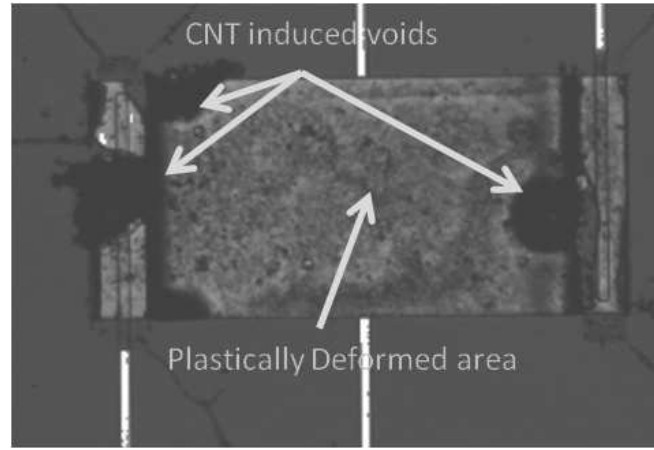
Figure 5.11: Zygo intensity map showing contour of micro-contact support structure. Voids caused by the CNT encapsulation can be seen on the beam and the area that was deformed by cycling is labeled.
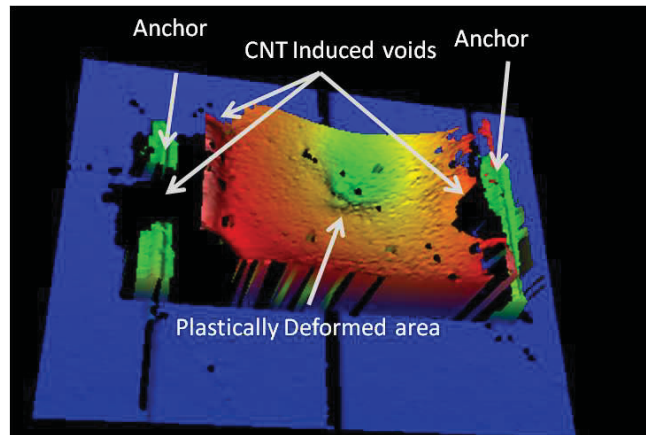
Figure 5.12: Zygo 3D image of fixed-fixed Au micro-contact support structure. The voids do not return an image, but the plastical deformed portion of the beam can be seen.

about $400MPa$ (or $400N/mm^2$) at room temperature and become $250MPa$ (or $160N/mm^2$) at $120\,^{\circ}C$ [70]. Considering that the maximum applied force to the beam was $200\mu N$ in order to achieve near $100\mu N$ of contact force in this case, it is likely that the yield stress

threshold of the support structure was surpassed, causing the beam to be plastically deformed.

5.12 CNT micro-contact resistance analysis
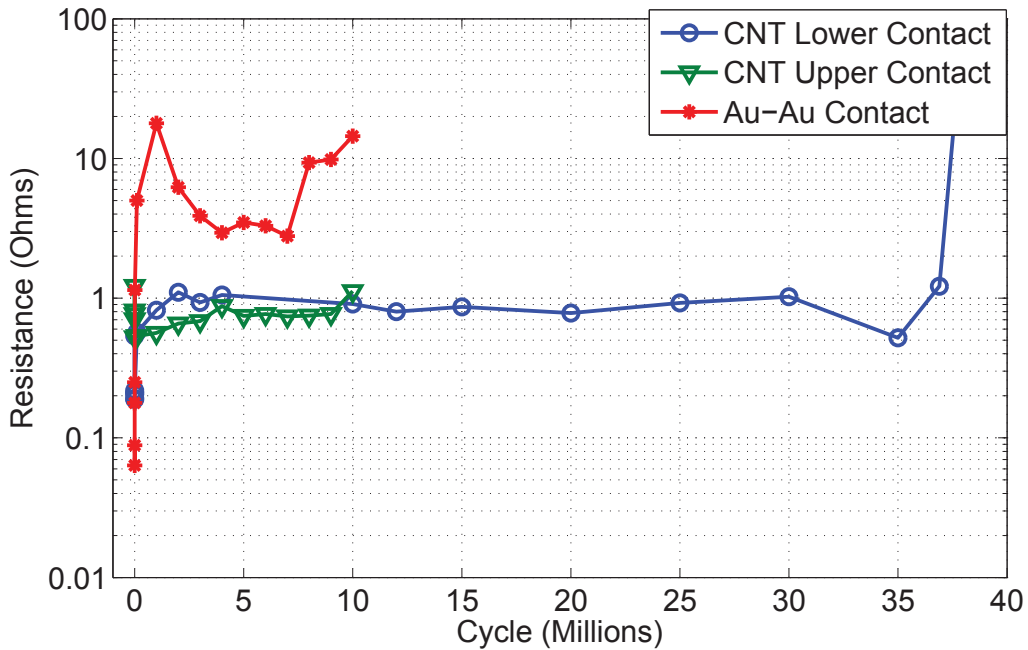
Figure 5.13: Resistance values for functional fixed-fixed Au and AU-CNT encapsulated micro-contact support structure

Figure 5.13 shows the life cycle data for three different style beams, one Au-Au, the other CNTs composite film in the upper and lower contact. The fixed-fixed Au micro-contact support structure experienced steadily increasing contact resistance as the number of actuations increased. This particular micro-contact was cycled nearly 10.2 million times, at which point the closed contact resistance was 14.43Ω. However, the CNT composite film in neither the lower or upper contact displayed this rise in resistance. The micro contact support structure with CNTs in the upper contact was also cycled to

nearly 10.2 million times, at which point the closed contact resistance was 1.1Ω. Finally, the fixed-fixed micro-contact with CNTs composite film in the lower contact was cycled to approximately 36.9 million times, at which point the closed contact resistance was 1.21Ω. At the next test point, 37 million cycles, the contact failed to make electrical contact. This failure is most likely due the the build-up of an insulating film.

The most promising results were with the CNT composite film in the lower contact. This beam had a much lower and consistence resistance until failure compared to a similarly constructed Au-Au beam. This could be because the CNT are providing a highly conductive thermal layer to diffuse the heat to allow for a longer life and help prevent catastrophic plastic deformation to occur. The CNT film might also allow some current to flow through the CNT, reducing overall resistance. The CNT in the lower contact also had fewer surface defects due to the CNTs encapsulation in the lower contact rather than in upper contact, thus not causing the voids seen in Figure 5.11.

After testing, the this contact was pulled back for examination as to what caused the contact to fail. The SEM image of the contact area (Figure 5.14) was taken to reveal a large area of film developed on the lower contact pad.

Other contacts in this samples a basis of comparison. To further evaluate this contaminate film, an energy dispersive spectroscopy (EDS) measurement was taken, the results are shown in Figure 5.15. An uncharacteristically high carbon content was discovered, unique to this contact.

The amount of carbon present in the film on the lower contact was 20% of the return on the spot EDS measurement ($\sim 1\mu m$ in diameter). This possibly uncovered an issue with the encapsulated CNTs, where after wearing through the thin encapsulation Au layer, the exposed CNTs accelerated the growth of an insulating carbon film. This rapid rise of resistance is similar to what was seen in literature in the presence of frictional polymers [61]. Frictional polymers are organic films, that develop on commonly used contact
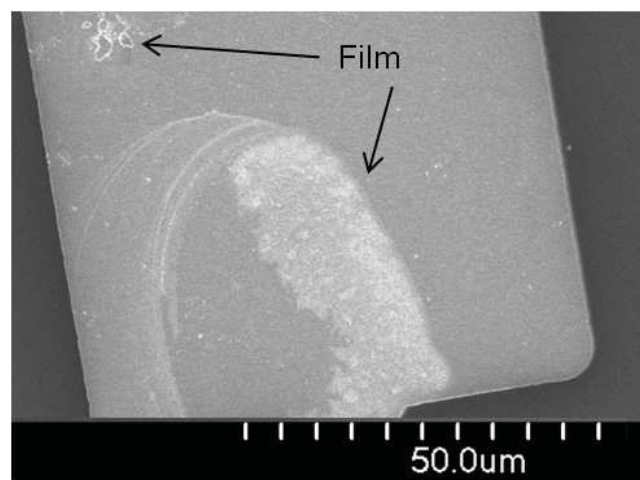
Figure 5.14: Scanning electron microscope image of lower contact pad revealing contaminate film.
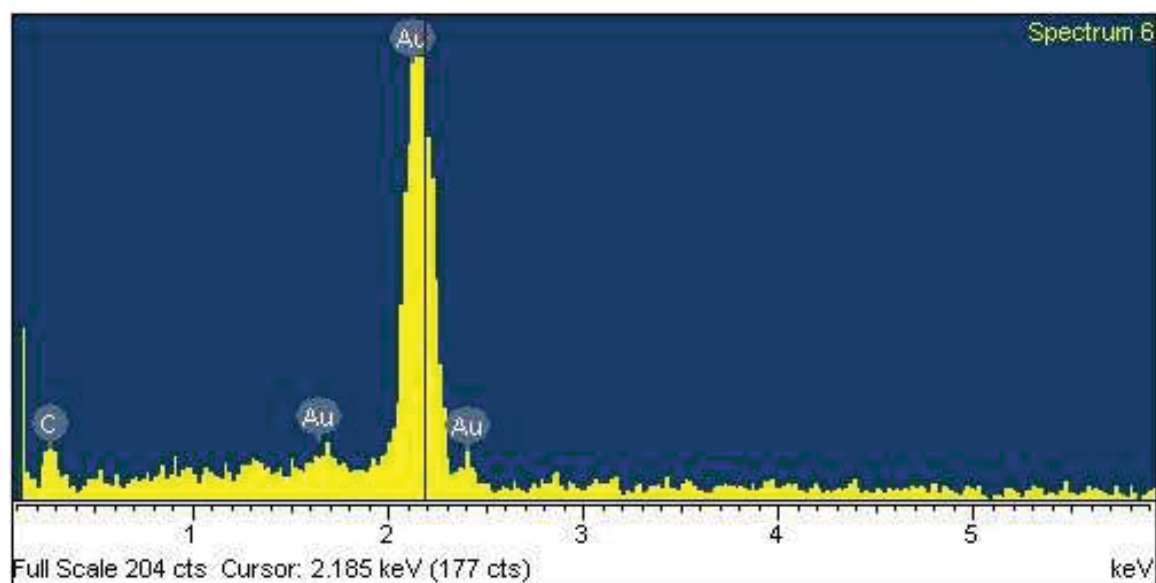
Figure 5.15: EDS results of the contaminate film, revealing a return of carbon which was unique to this sample

materials when there are low levels of organic vapors or compounds are evident in the operating environment of the contact [61]. It appears that the breakdown of the encapsulating layer, which exposed some carbon contamination, led to a growth of a frictional polymer.

5.13   Chapter summary

This concludes the analysis of the data from Chapter 5. Sections covered in this chapter included: Ru and RuO_2 models, the combination of the Hertz and Thin Film Model, Material transfer in Au-Au contacts, electromigration in RuO_2 contacts, engineered lower contact, plastic deformation, and lastly an analysis of the CNT micro-contacts. The next chapter will cover the contributions of this research and recommendations for future work.

VI. Conclusions

6.1 Chapter overview

The improvement of micro-contacts will provide benefits in many areas of technology. These benefits may include greater bandwidths, lower power consumption, and enhanced performance. To make these improvements, MEMS engineers need the capability to study the performance evolution of micro-contacts by examining the physical and chemical phenomena at the interface under controlled conditions. Previously at AFIT, a novel test fixture concept was realized, but never fully utilized. This research focused on full utilization of a test fixture that would allow future MEMS engineers to study the performance evolution of micro-contacts. The groundwork for exploring micro-contact physics was also put into place. This chapter summarizes the research effort with the lessons learned from the detailed results from chapter four as well as other work outside of this research. First, the main contributions of this research are discussed. Following this discussion, the recommendations for future research are provided.

6.2 Contributions

The contributions of this research included the following:

- Novel micro-contact support structures which replicated Holm's well known crossed-rod experiment were fabricated and tested. This mask set allowed for testing of all devices on a reticle.
- Micro-contact performance characterization of Au-Au, Au-Ru, and $AuRO_2$ micro-contacts.
- Upgraded the test fixture with new measurement devices. These upgraded measurement units allowed for more accurate measurements of contact resistance.
- Used gray-scale lithography to create an engineered structures.

106

- Used gray-scale lithography to make engineered structures for the lower contact.
  Tested these devices and compared the results to Au-Au hemisphere/planar contacts.

- Micro-contact performance characterization of CNT-Au composite micro-contacts.
  Including the comparison of Au-Au and Au-CNT micro-contacts with CNT infused
  in the upper and lower contact.

- Micro-contact reliability test of Au-Au contacts to 326 million cycles.

- Provided data to be able to create a Figure of Merit for micro-switches.

- Provided the initial research into a new subset of the thin film model to include
  a-spot size and spreading resistance.

A foundation for future work on this effort is provided. This foundation gives clear
insight into the design, fabrication, and characterization methodologies so a clear direction
of how this research may continue is apparent.

6.3   Recommendations for future research

6.3.1   Testing micro-contact material types.

One recommendation is continued research into the use of different contact materials
including ruthenium and other contact metal types. As the most common type of contact
in literature, Au-Au will be used for comparison to literature and as a baseline for
comparison to the other micro-contact candidates. In order to test these contact material
types, Holm's crossed rod contact experiment is adapted as a suitable method to measure
micro-contact resistance.

Materials can focus on the desired results including hard materials to further research
into use of hard thin films to combat electromigration or reactive metal films to promote
film growth.

6.3.2   Testing using flip switches.

The design of the flip switch allows researches to look at the contact area without
destroying the beam for the first time. This will allow the tester to track and investigate the

contact area. One investigation is complete, the contact can be further tested due to the flip switch design. This ability to track the changes of contact area will offer great insight into the contact area change.

6.3.3   Software changes to investigate other failure modes.

The micro-contact test fixture allows for the upgrade of software, which will increase the capability to investigate failure modes. This includes the ability to monitor not only closure forces, but also the forces need to separate the contact. This can help identify van der Waals forces and stiction which are currently not monitored. Another software upgrade can be to monitor the changes in contact resistance and compare current measure resistance to previous. This would allow for additional stopping criteria, including if contact resistance is higher than a set value, or if contact resistance changes greater than a certain percentage.

6.3.4   Failure mode analysis.

Now that it has been shown that the test fixture functions effectively, more analysis is needed on the failure modes. This includes the ability to identify the make-up of contaminate films found on the micro-contact and the cause of these contaminate films. Also further investigating into showing how the direction of current, specifically harder metals as the cathode, can offer a solution to micro-contact reliability.

6.3.5   Accelerated test methods.

This research focused on only two, initial and cold switch testing, of the three test types. No significant amount of hot switch testing was done other than to verify the software worked. Hot switch testing in another avenue to investigate failure mode. Hot switch test types currently supported include testing of a leading edge, trailing edge and a combination of both. Leading edge is when there is signal across the contact before it is closed, but is removed when the contact is open. Trailing edge is where the contact first closed before the signal is a applied, but remains until after the contact is opened. A

combination is when the signal is allied when the contact is both opening and closing, this is what is shown in Figure 3.2(a).

6.4   Chapter summary

This research focused on full utilization of a test fixture that would allow future MEMS engineers to study the performance evolution of micro-contact. This chapter summarized the research effort with the lessons learned from the detailed results from chapter four as well as other work outside of this research. First, the main contributions of this research were discussed. Following this discussion, the recommendations for future research were provided. This research provided insight in the performance, reliability and failure modes discovered of Au-Au, Au-Ru, Au-RuO$_2$, Au-CNTs and Au-Au with engineered micro-contacts.

Appendix A: Collected Data

A.1 Appendix overview

For testing of micro-contact resistance the types of contacts tested included; Au-Au, Au-Ru, Au-RuO$_2$ 10% and 25% concentration, and Au-CNT. Each micro-contact support structure tested was subjected to the initial contact testing and cold switch testing. Testing also consisted of Au-Au with engineered lower contacts.

A.2 Testing of Au-Au micro-contact sample (1,2)

A.2.1 Initial Contact Test.

Figure A.1 shows a comparison of the measured micro-contact resistance for an Au-Au only fixed-fixed micro-contact support with a contact radius of 6μm and the modeled values of micro-contact resistance based on the equations in Section 2.2.3. This data is the average of 15 ICT measurements; also shown is the standard deviation of that data.

Figure A.1 shows that at extremely low contact less than 10μN, the measured contact resistance in much higher than the model. But after this small area of light loading, the average measured values follow the plastic model very closely.
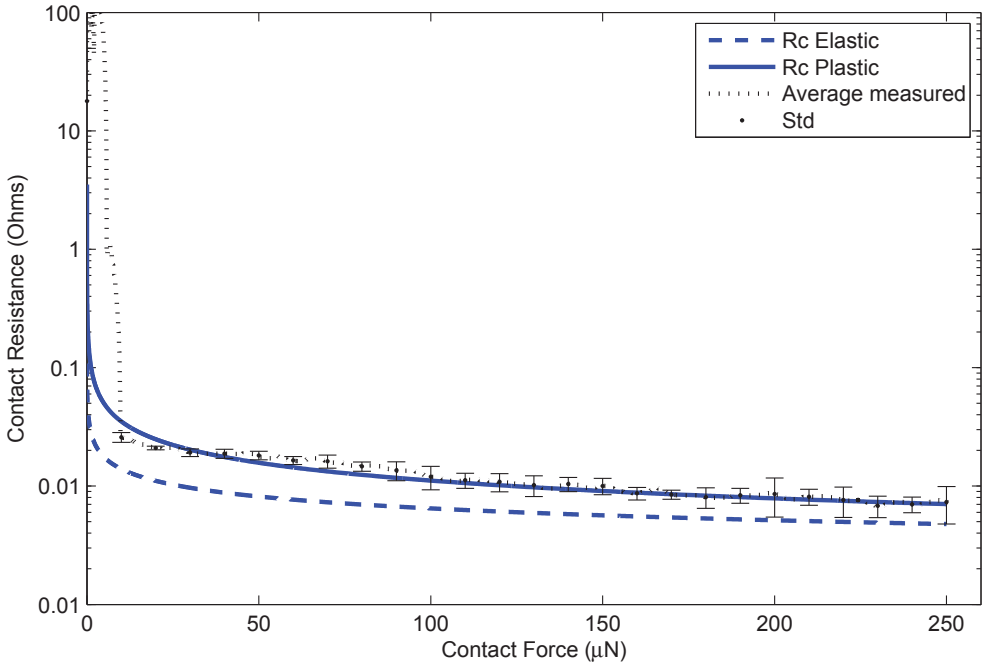
Figure A.1: Contact resistance of Au-Au 6μm radius contacts, Rc Elastic and Rc Plastic are modeled values, Average Measured data is the average of 15 initial contact test measurements and Std is the standard deviation of those measured values.

A.2.2   Cold Switch Test.

The evolution of the Au-Au contact area was observed by actuating the micro-contact to 1, 10^2, 10^3, 5×10^3, 10^4, 5×10^4, 10^5, 5×10^5, 10^6, 5×10^6 and 10^7 cycles. The micro-contacts were actuated using an external, calibrated point load. To examine the micro-contact performance, the contact resistance and force required to close the contact, were monitored simultaneously throughout testing. At the above stated end point, the micro-contact was folded back to evaluate the wear of the upper hemispherical and planar lower contact.

A.2.2.1 Micro-contact with a single actuation.

The single actuation of the micro-contact was performed on Beam 14. The contact resistance plot is shown in Figure A.2. SEM images for the contact bump is shown in Figure A.3a and for the contact pad in Figure A.3b.
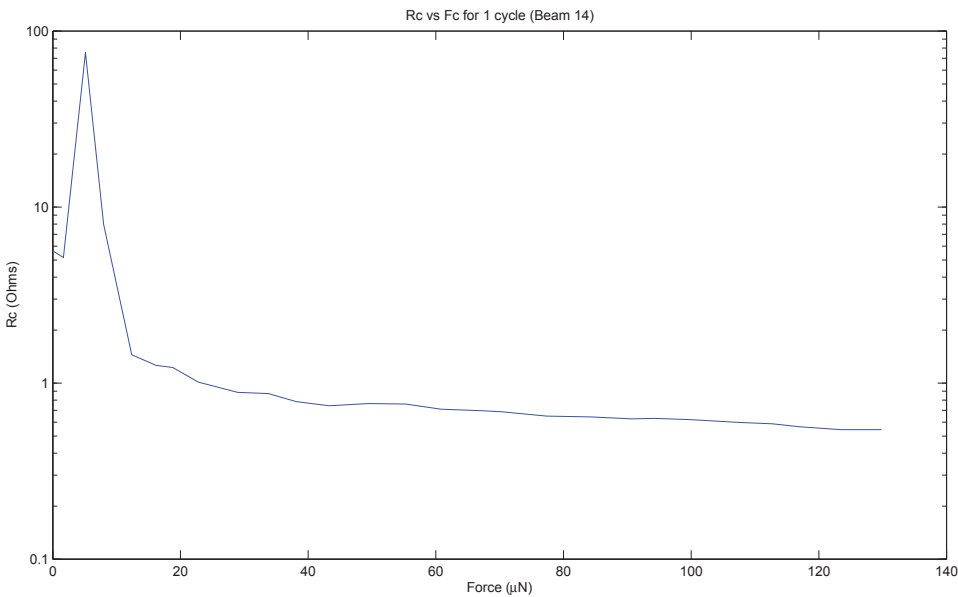
Figure A.2: Contact resistance of Au-Au $6\mu m$ radius contact for a single actuation

Since this contact only had a single actuation, the contact areas do not show any wear.

(a) Upper contact (Anode)　　　　(b) Lower contact (Cathode)
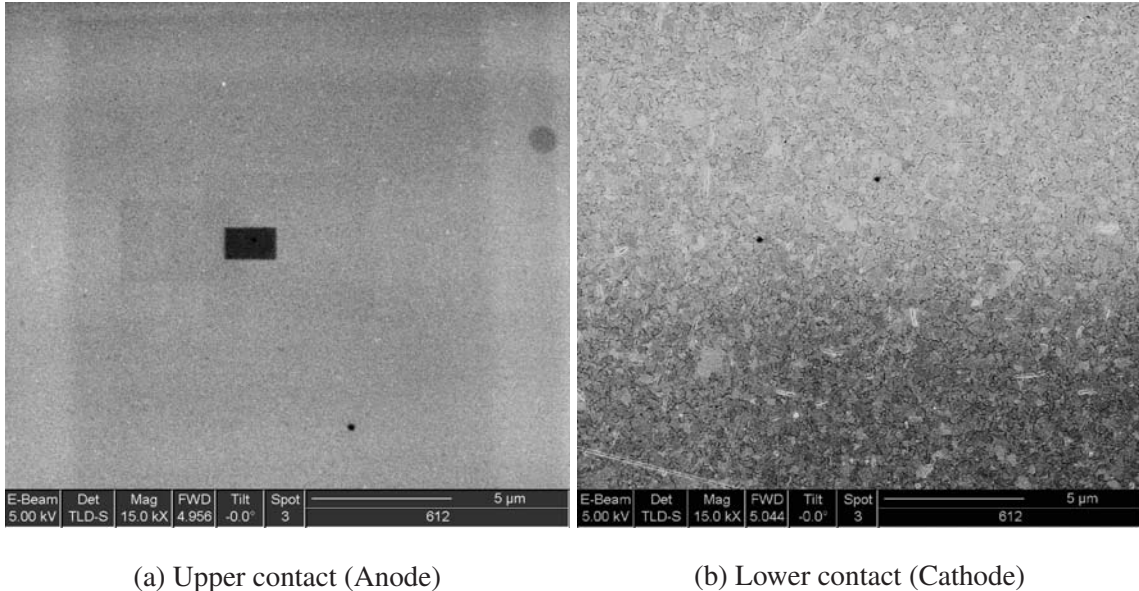
Figure A.3: SEM image of upper contact bump and lower contact pad after single actuation, no visible wear is seen in the contact area

A.2.2.2   *Micro-contact with 100 cycles.*

The 100 cycles test of a micro-contact was performed on Beam 15. The contact resistance plot is shown in Figure A.4. SEM images for the contact bump is shown in Figure A.5a and for the contact pad in Figure A.5b.

Since this contact only had 100 cycles, the contact areas do not show any signs of wear.
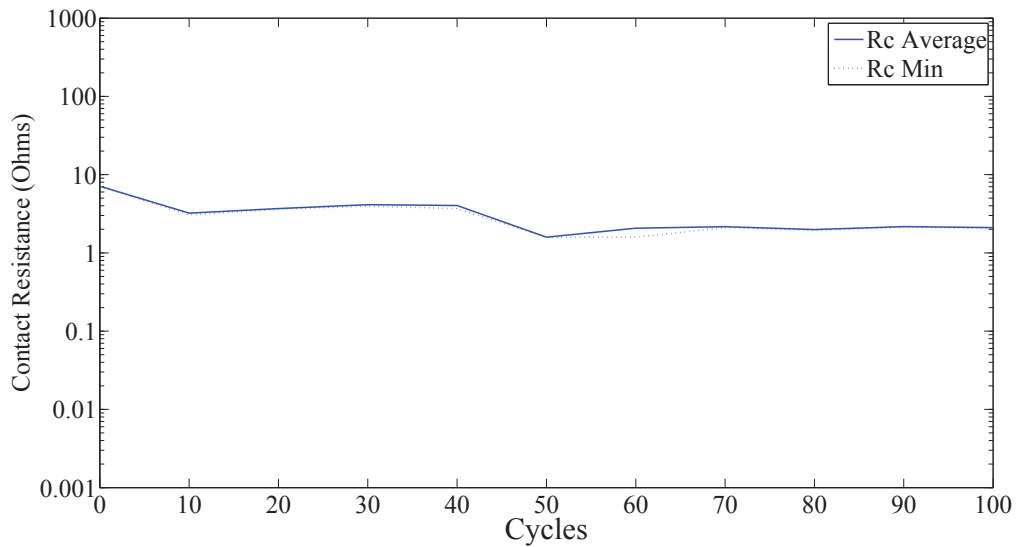
Figure A.4: Contact resistance of Au-Au 6μm radius contact for 100 cycles. 'Rc Average' is the average for the last 5 resistance measurements at $\sim 200\mu N$ of contact force. 'Rc Min' is the minimum contact resistance measured during the measurement cycle.

(a) Upper contact (Anode)　　　　　　(b) Lower contact (Cathode)
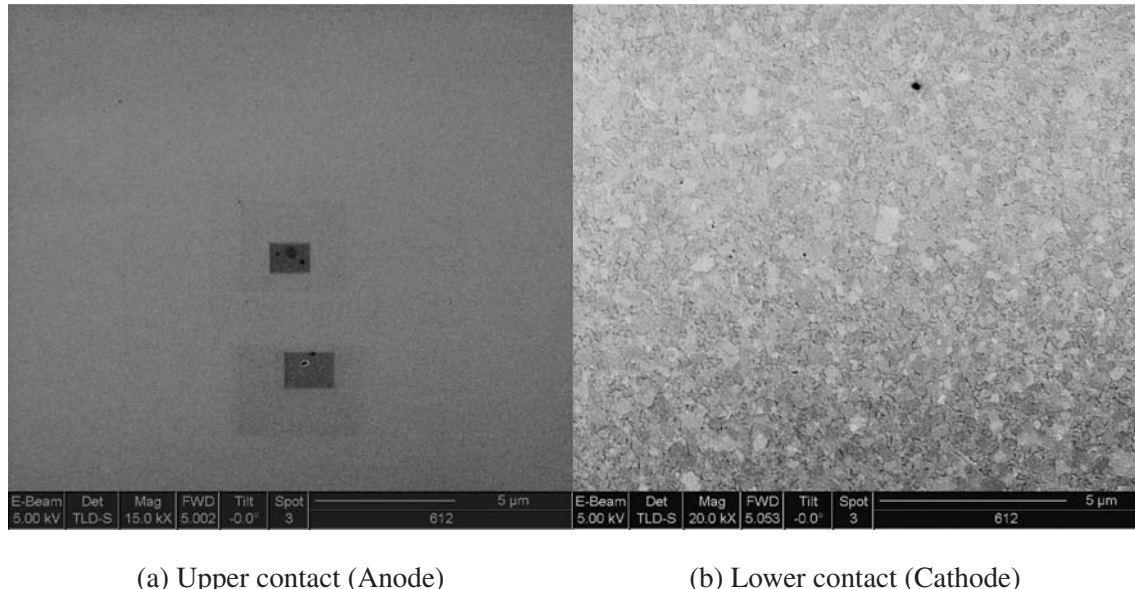
Figure A.5: SEM image of upper contact bump and lower planar contact pad after 100 cycles, no visible wear is seen in the contact area

A.2.2.3 Micro-contact with 1,000 cycles.

The 10^3 cycles test of a micro-contact was performed on Beam 16. The contact resistance plot is shown in Figure A.6. SEM images for the contact bump is not available due to damage it received when the reticle was removed from the sample from the carrier and for the contact pad in Figure A.7b.
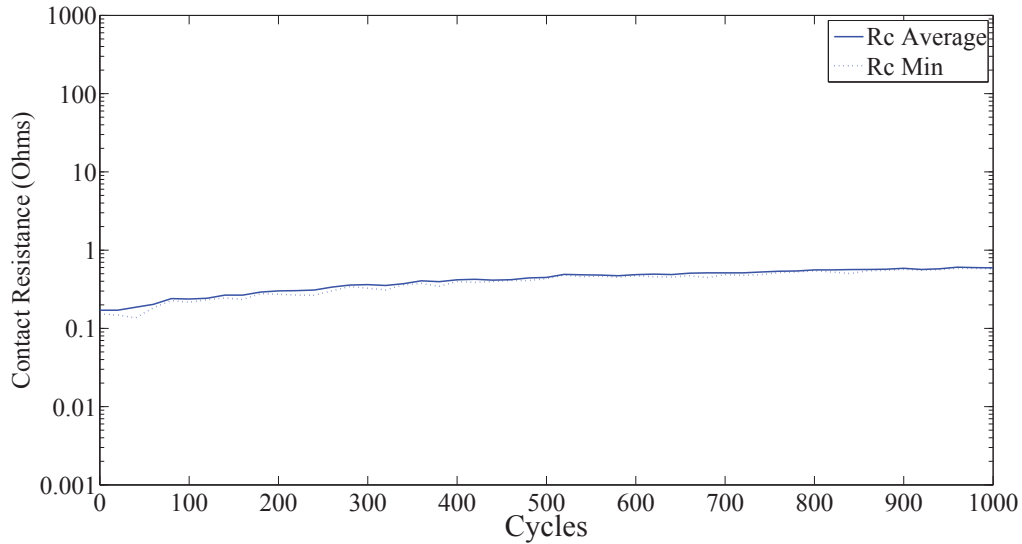
Figure A.6: Contact resistance of Au-Au $6\mu m$ radius contact for 10^3 cycles. 'Rc Average' is the average for the last 5 resistance measurements at $\sim 200\mu N$ of contact force. 'Rc Min' is the minimum contact resistance measured during the measurement cycle.

This contact does exhibit some wear. With three spots seen on the pad where wearing of the the contact is shown.

(a) No image available
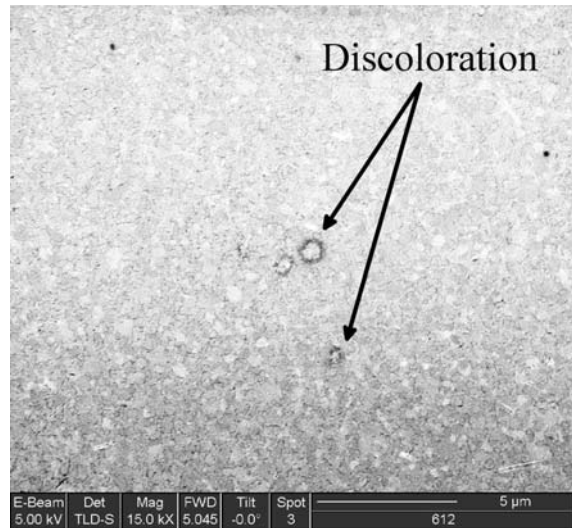
(b) Lower contact (Cathode)

Figure A.7: SEM image of upper contact bump and lower planar contact pad after $1,000$ cycles

A.2.2.4 *Micro-contact with 5×10^3 cycles.*

The 5^3 cycles test of a micro-contact was performed on Beam 12. The contact resistance plot is shown in Figure A.8. SEM images for the contact bump is shown in Figure A.9a and for the contact pad in Figure A.9b.

This contact show some wear after 5^3 cycles. There is an area in the center left that shows some discoloration and a mating set on the pad.
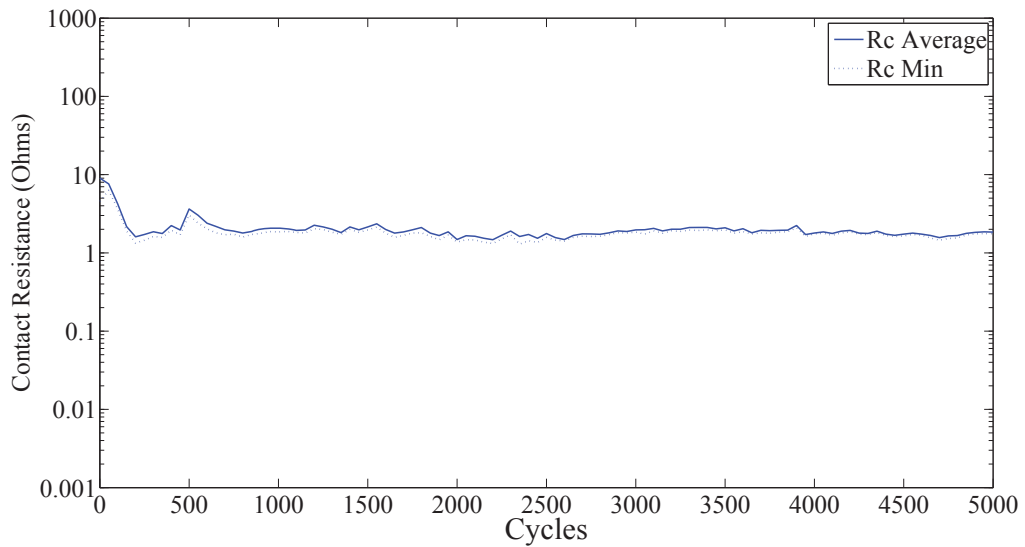
Figure A.8: Contact resistance of Au-Au $6\mu m$ radius contact for a 5^3 cycles. 'Rc Average' is the average for the last 5 resistance measurements at $\sim 200\mu N$ of contact force. 'Rc Min' is the minimum contact resistance measured during the measurement cycle.

(a) Upper contact (Anode)

(b) Lower contact (Cathode)
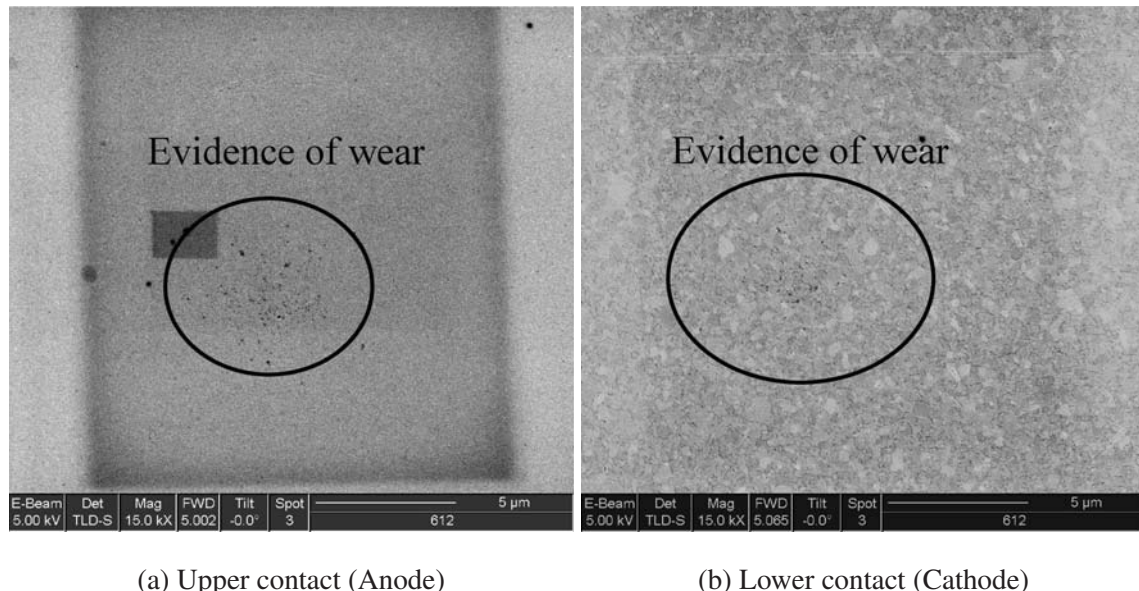
Figure A.9: SEM image of contact pad after 5^3 cycles. Evidence of wear is shown in the grouping of dark spots seen on the lower contact pad.

A.2.2.5 Micro-contact with 10^4 cycles.

The 10^4 cycles test of a micro-contact was performed on Beam 8. The contact resistance plot is shown in Figure A.10. SEM images for the contact bump is shown in Figure A.11a and for the contact pad in Figure A.11b.
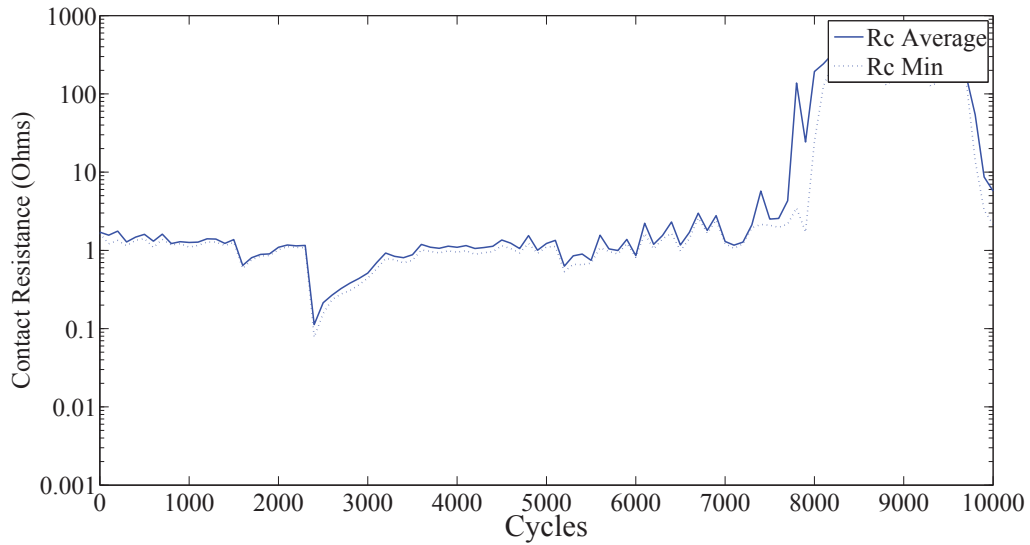
Figure A.10: Contact resistance of Au-Au $6\mu m$ radius contact for a 10^4 cycles. 'Rc Average' is the average for the last 5 resistance measurements at $\sim 200\mu N$ of contact force. 'Rc Min' is the minimum contact resistance measured.

This contact show some wear after 10^4 cycles. On the beam there is an area in the middle on the contact bump that has material transfer has occurred. This material created a hole that is shown on the pad. The resulting effective change of the contact area is the likely cause of the sharp rise in resistance around 8k cycles.

(a) Upper contact (Anode) (b) Lower contact (Cathode)
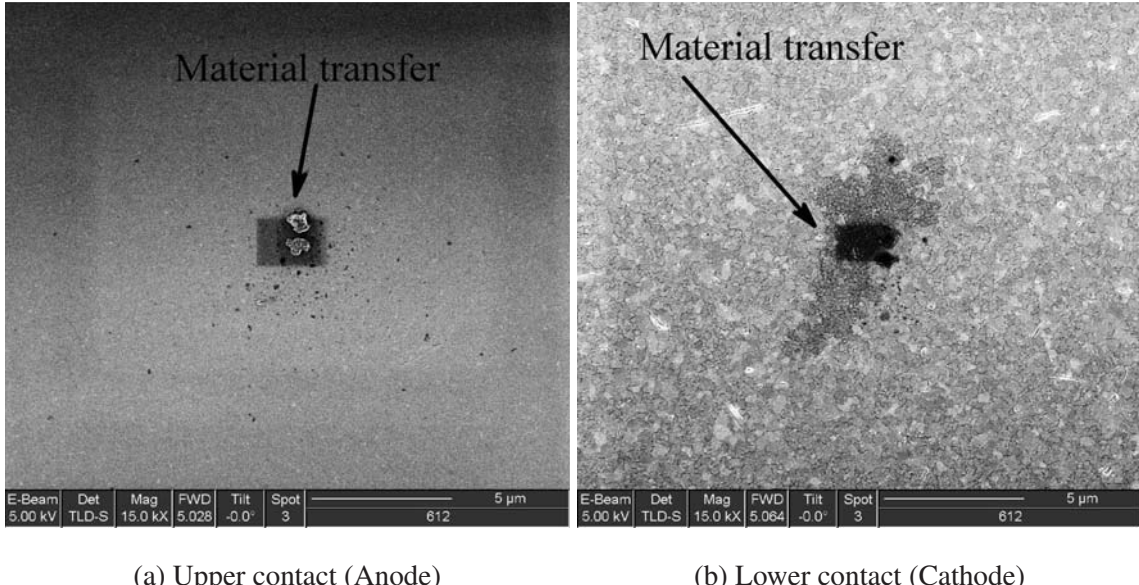
Figure A.11: SEM image of contact pad after 10^4 cycles. A large dark area is shown in the middle where the bottom pad lost material to the beam.

A.2.2.6   *Micro-contact with 5×10^4 cycles.*

The 5×10^4 cycles test of the micro-contact was performed on Beam 7. The contact resistance plot is shown in Figure A.12. SEM images for the contact bump is shown in Figure A.13a and for the contact pad in Figure A.13b.

This contact show some wear after 5×10^4 cycles. On the beam there is an area in the middle on the contact bump that has material transfer has occurred. This material created a hole that is shown on the pad. This change of the contact area is the likely cause of the sharp rise in resistance after the first few hundred cycles.
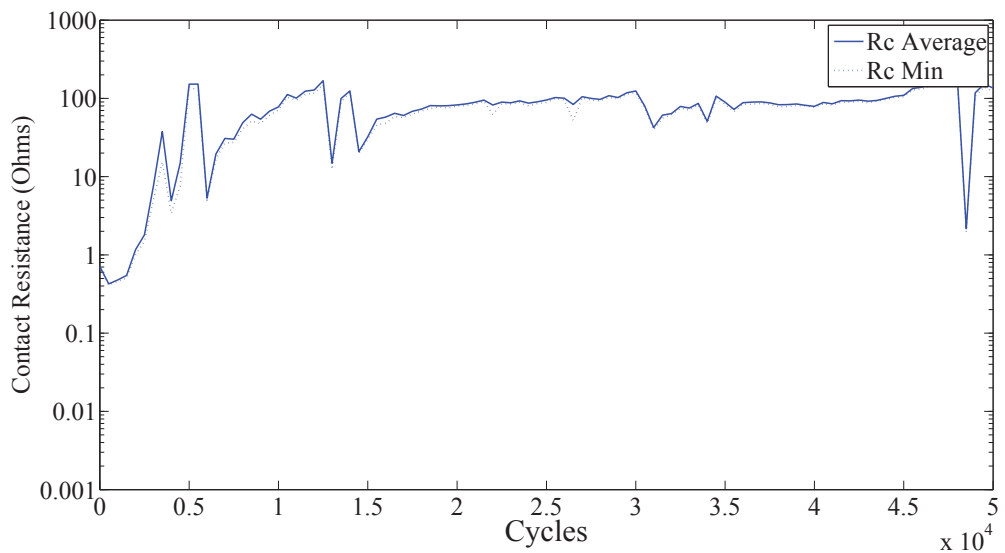
Figure A.12: Contact resistance of Au-Au $6\mu m$ radius contact for a 5×10^4 cycles. 'Rc Average' is the average for the last 5 resistance measurements at $\sim 200\mu N$ of contact force. 'Rc Min' is the minimum contact resistance measured.

(a) Upper contact (Anode)

(b) Lower contact (Cathode)
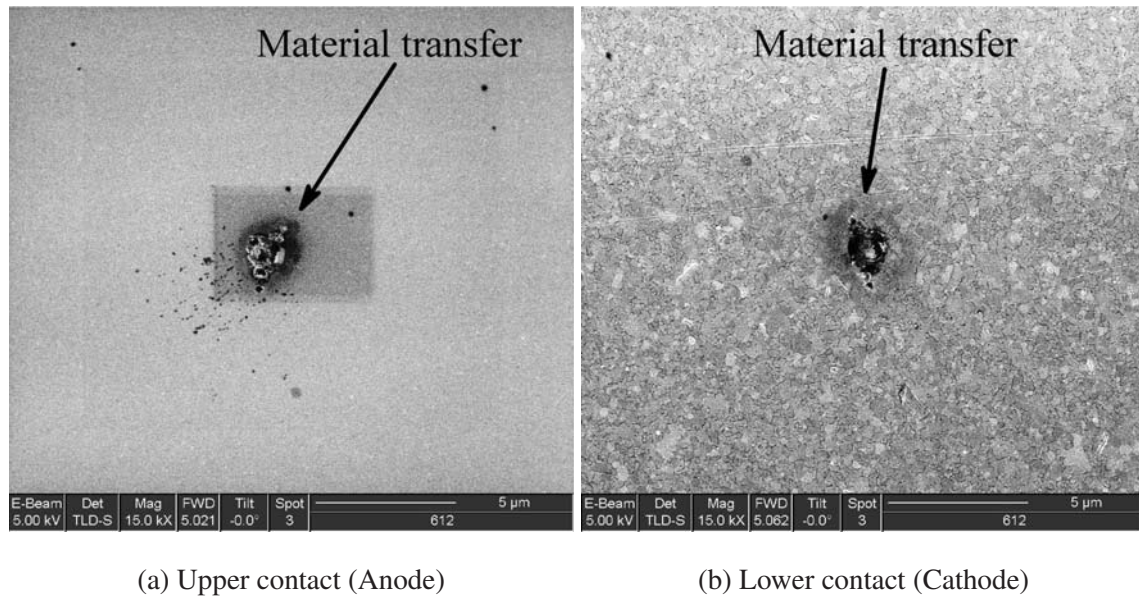
Figure A.13: SEM image of contact pad after 5×10^4 cycles. A large material transfer area is shown in the middle of the contact.

A.2.2.7 Micro-contact with 10^5 *cycles.*

The 10^5 cycles test of a micro-contact was performed on Beam 5. The contact resistance plot is shown in Figure A.14. SEM images for the contact bump is shown in Figure A.15a and for the contact pad in Figure A.15b.
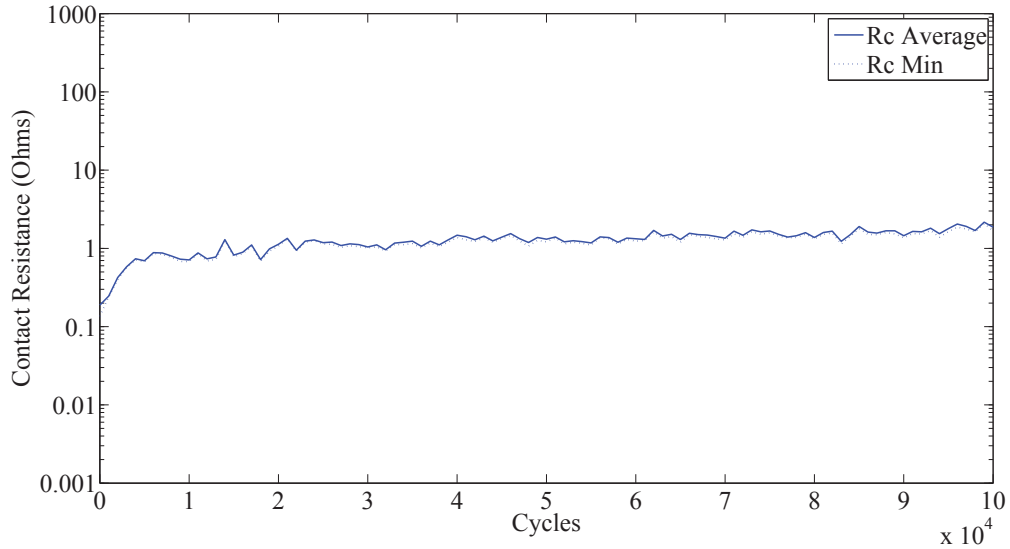
Figure A.14: Contact resistance of Au-Au $6\mu m$ radius contact for a 10^5 cycles. 'Rc Average' is the average for the last 5 resistance measurements at $\sim 200\mu N$ of contact force. 'Rc Min' is the minimum contact resistance measured.

This contact show some wear after 10^5 cycles. On the beam there is an area in the middle on the contact bump that is discoloration. There is a matching area on the pad. Comparing the material transfer to Figure A.13b and A.13a, the amount of transfer is much less. This difference in material transfer could be the cause of the resistance being much less over the life of the contact rather than the high contact resistance seen in Figure A.12.

121

(a) Upper contact (Anode)   (b) Lower contact (Cathode)
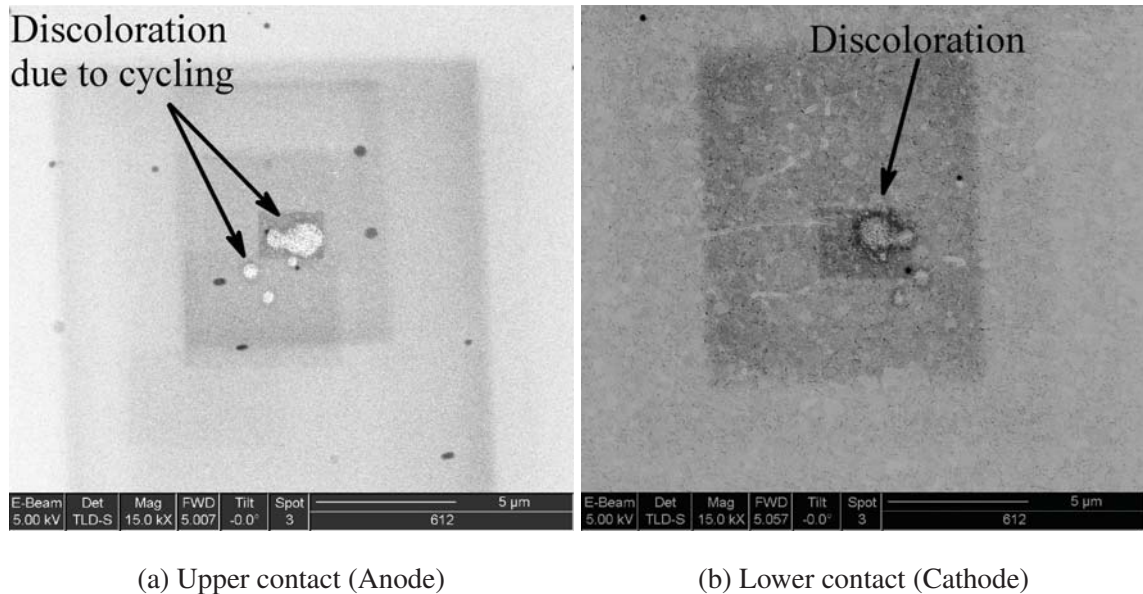
Figure A.15: SEM image of contact pad after 10^5 cycles. A large area of discoloration is shown in the middle of the contact

A.2.2.8 Micro-contact with 5×10^5 cycles.

The 5×10^5 cycles test of a micro-contact was performed on Beam 1. The contact resistance plot is shown in Figure A.16. SEM images for the contact bump is shown in Figure A.17a and for the contact pad in Figure A.17b.

This contact show a lot of wear after 5×10^5 cycles. On the beam there is an area in the middle on the contact bump that material transfer has occurred. This material created a hole that is shown on the pad. This material is the cause of high contact resistance throughout the life of the contact.
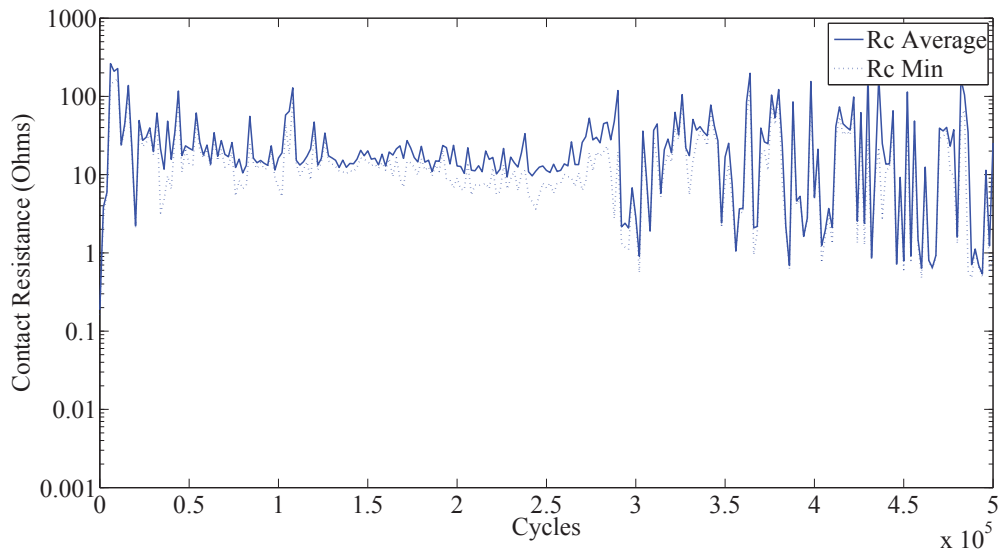
Figure A.16: Contact resistance of Au-Au $6\mu m$ radius contact for a 5×10^5 cycles. 'Rc Average' is the average for the last 5 resistance measurements at $\sim 200\mu N$ of contact force. 'Rc Min' is the minimum contact resistance measured.

(a) Upper contact (Anode) (b) Lower contact (Cathode)
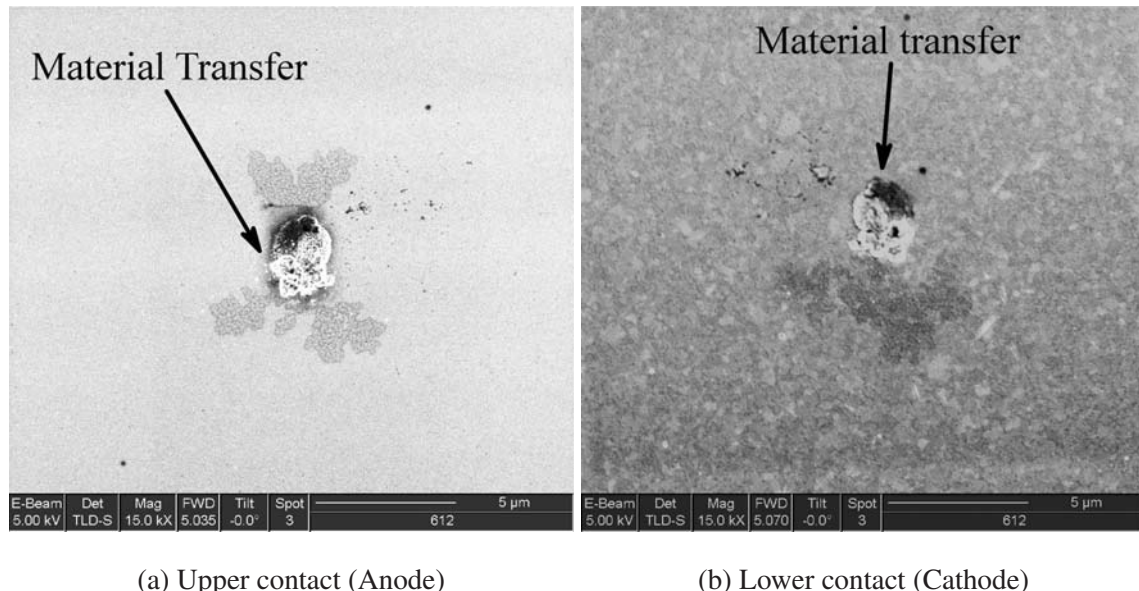
Figure A.17: SEM image of contact pad after 5×10^5 cycles. A large material transfer area is shown in the middle of the contact.

A.2.2.9   *Micro-contact with* 10^6 *cycles.*

The 10^6 cycles test of a micro-contact was performed on Beam 6. The contact resistance plot is shown in Figure A.18. SEM images for the contact bump is shown in Figure A.19a and for the contact pad in Figure A.19b.
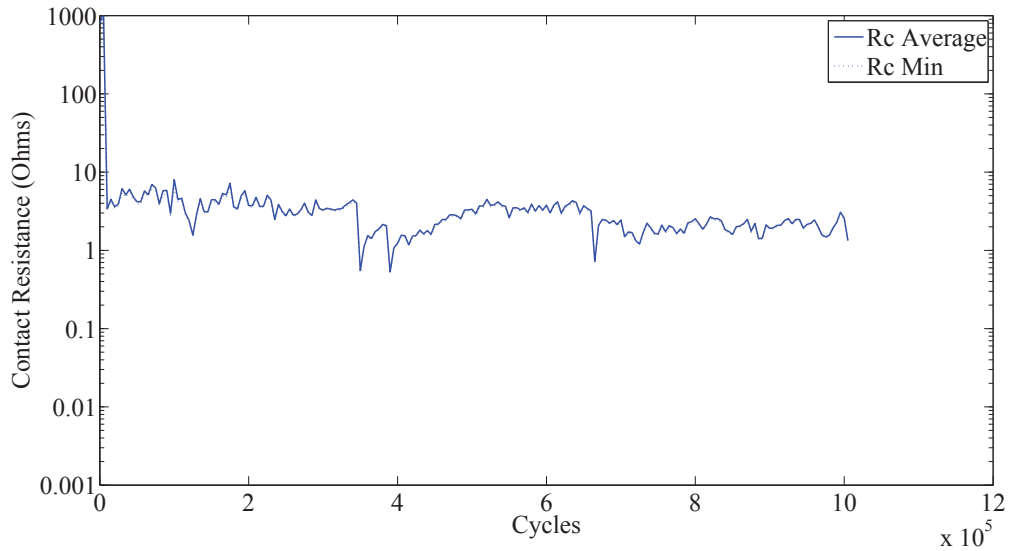

Figure A.18: Contact resistance of Au-Au $6\mu m$ contact for a 10^6 cycles. 'Rc Average' is the average for the last 5 resistance measurements at $\sim 200\mu N$ of contact force. 'Rc Min' is the minimum contact resistance measured.

This contact show some wear after 10^6 cycles. On the beam there is an area in the middle on the contact bump that has material transfer has occurred. This material created a hole that is shown on the pad. This smaller amount of material transfers also corresponds to the contact resistance being lower. The initial high contact resistance can be attributed to contamination in the contact area that was broken though during the first set of cycles.

(a) Upper contact (Anode)   (b) Lower contact (Cathode)
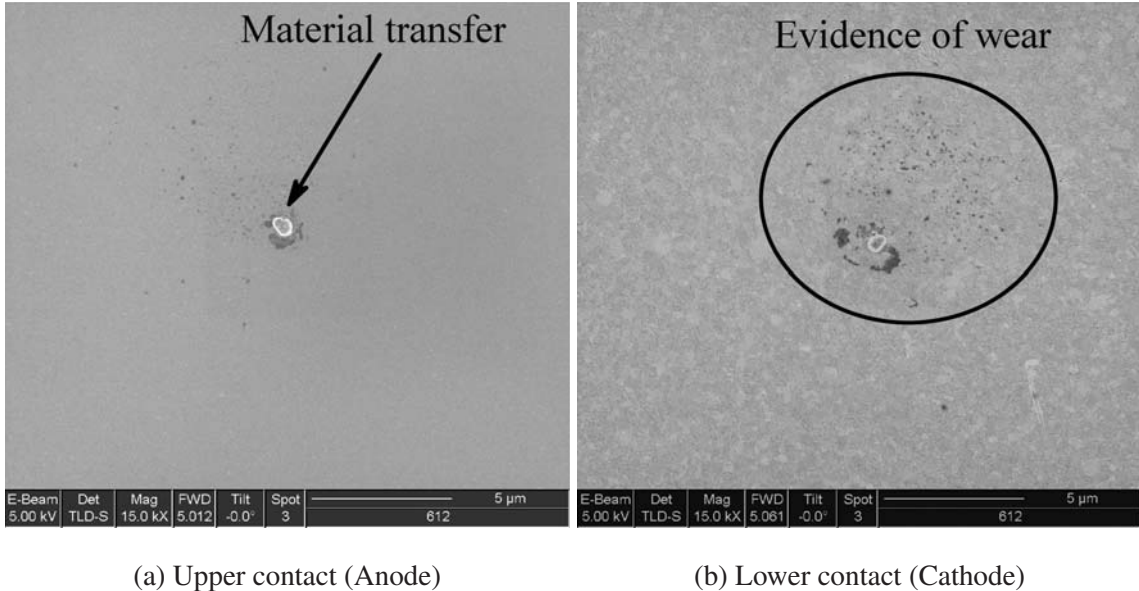
Figure A.19: SEM image of the upper contact bump and lower contact pad after 10^6 cycles. A small material transfer area is shown in the middle of the contact.

A.2.2.10   *Micro-contact with 5×10^6 cycles.*

The 5×10^6 cycles test of a micro-contact was performed on Beam 10. The contact resistance plot is shown in Figure A.20. SEM images for the contact bump is shown in Figure A.21a and for the contact pad in Figure A.21b.

This contact show some wear after 5×10^6 cycles. On the beam there is an area in the middle on the contact bump that has material transfer has occurred. This material created a hole that is shown on the pad. Once again, the material transfer area is relatively small and corresponds to the contact resistance, focusing on Rc min, is low throughout the life of the contact.
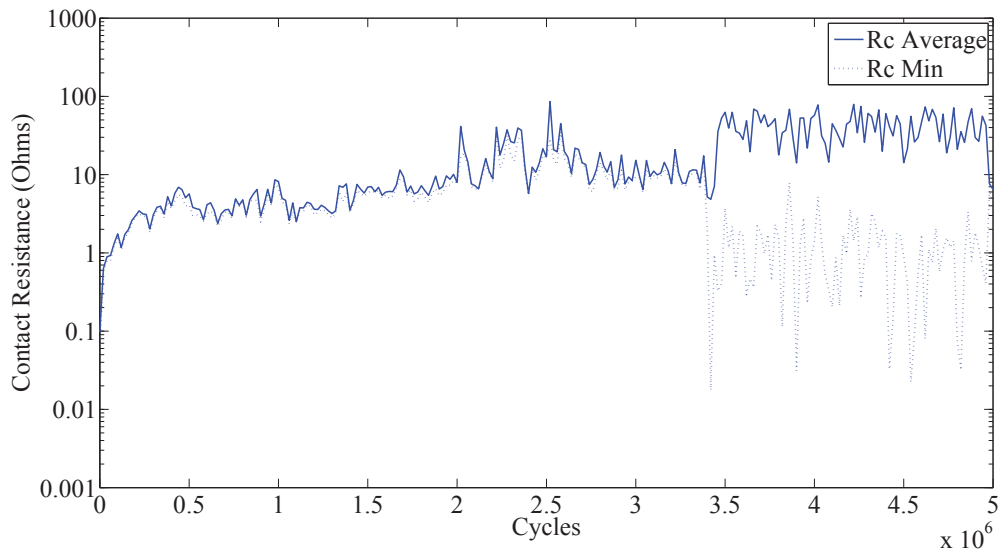
Figure A.20: Contact resistance of Au-Au $6\mu m$ radius contact for a 5×10^6 cycles. Rc Average (solid blue) is the average for the last 4 data point at $\sim 200\mu N$ of contact force. Rc Min (dashed blue) is the minimum contact resistance measured during the measurement cycle.

(a) Upper contact (Anode)

(b) Lower contact (Cathode)
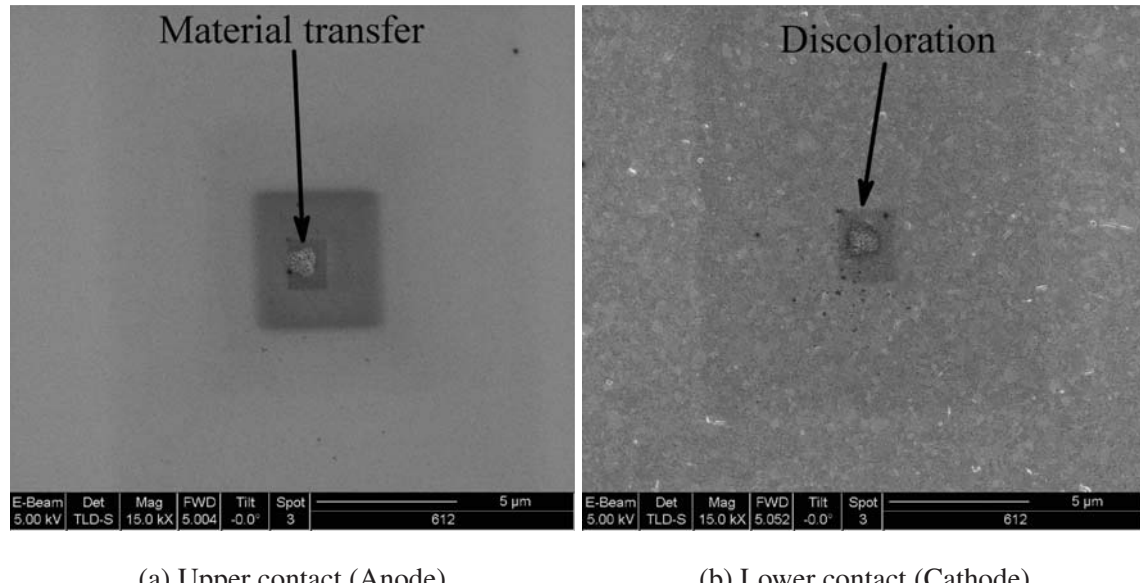
Figure A.21: SEM image of upper contact bump and lower contact pad after 5×10^6 cycles. A small material transfer area is shown in the middle of the contact.

A.2.2.11 *Micro-contact with* 10^7 *cycles.*

The 10^7 cycles test of a micro-contact was performed on Beam 11. The contact resistance plot is shown in Figure A.22. SEM images for the contact bump is shown in Figure A.23a and for the contact pad in Figure A.23b.
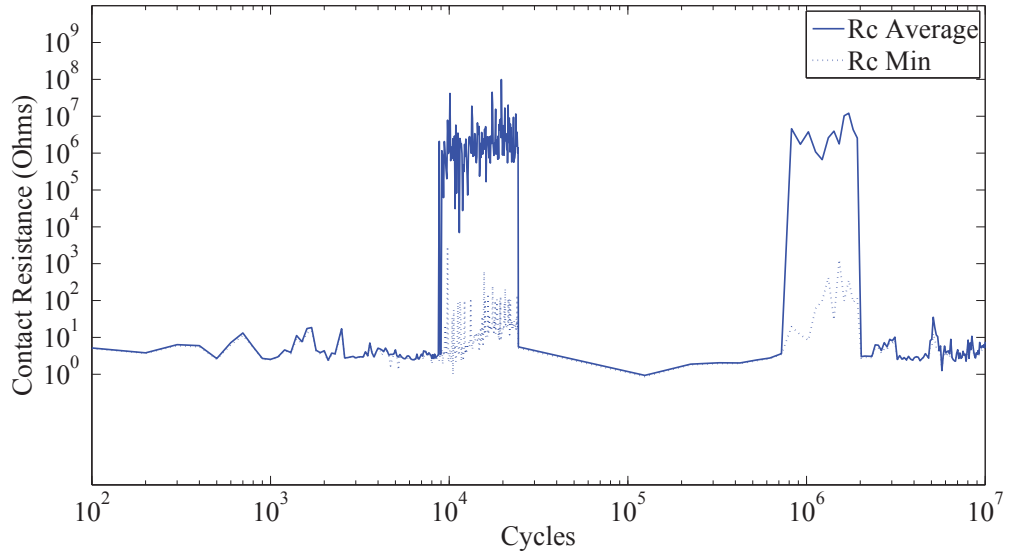

Figure A.22: Contact resistance of Au-Au $6\mu m$ contact for a 10^7 cycles. Rc Average (blue) is the average for the last 4 data point at $\sim 200\mu N$ of contact force. Rc Min (green) is the minimum contact resistance measured during the measurement cycle

This contact show some wear after 10^7 cycles. On the beam there is an area in the middle on the contact bump that has material transfer has occurred. This material created a hole that is shown on the pad.

127

(a) Upper contact (Anode)   (b) Lower contact (Cathode)
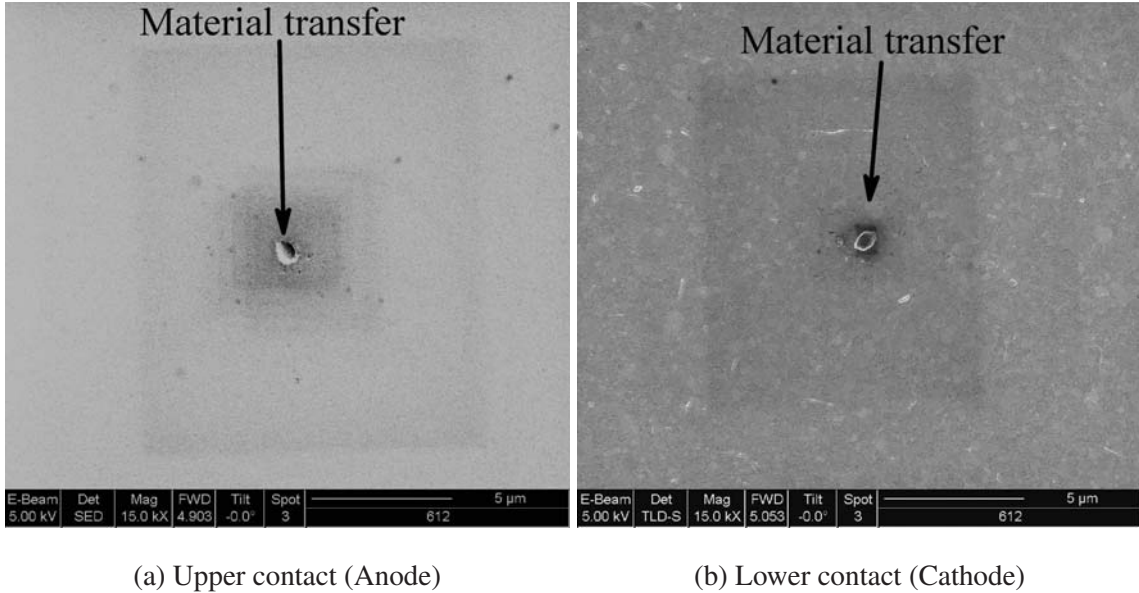
Figure A.23: SEM image of upper contact bump and lower contact pad after 10^7 cycles. A small material transfer area is shown in the middle of the contact.

A.3 Testing of Au-Au micro-contact sample (1,3)

A.3.1 Cold Switch Test.

The evolution of the contact area was observed by actuating the micro-contact same as previously stated. The micro-contacts were actuated using an external, calibrated point load. To examine the micro-contact performance, the contact resistance and force required to close the contact, were monitored simultaneously throughout testing. This sample was damage in removal from the carrier and no SEM images were taken

A.3.1.1 Micro-contact with a single actuation.

The single actuation micro-contact was performed on Beam 13. The contact resistance plot is shown in Figure A.24.
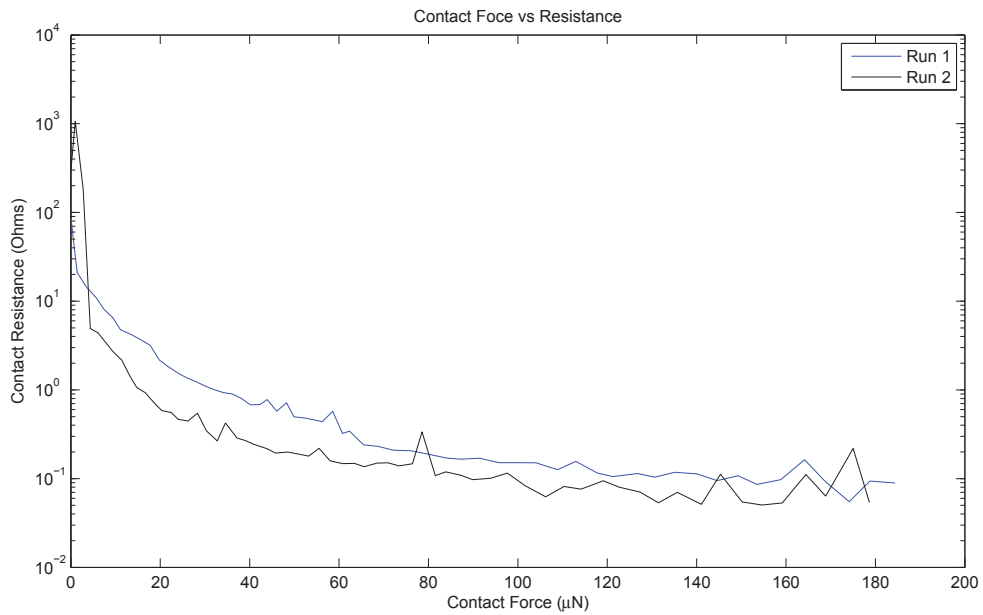
Figure A.24: Contact resistance of Au-Au 6*μm* contact for a single actuation. The difference of the measurement runs can be due to plastic deformation of the contact area

A.3.1.2   Micro-contact with 100 cycles.

The 100 cycles test of a micro-contact was performed on Beam 14. The contact resistance plot is shown in Figure A.25.
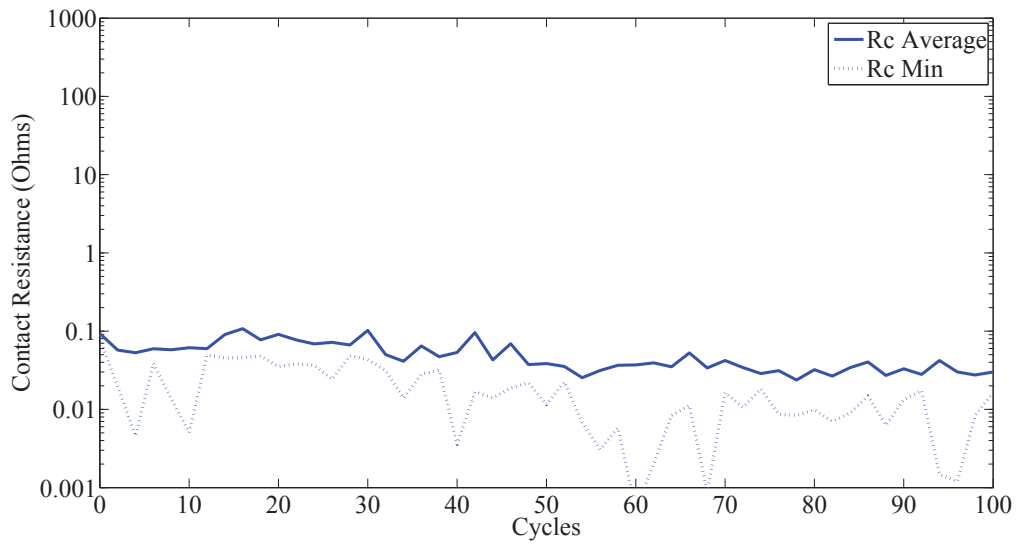
Figure A.25: Contact resistance of Au-Au *6μm* radius contact for 100 cycles. Rc Average is the average for the last 4 data point at ∼ 200*μN* of contact force. Rc Min is the minimum contact resistance measured during the measurement cycle

A.3.1.3   *Micro-contact with 1,000 cycles.*

The 10^3 cycles test of a micro-contact was performed on Beam 11. The contact resistance plot is shown in Figure A.26.
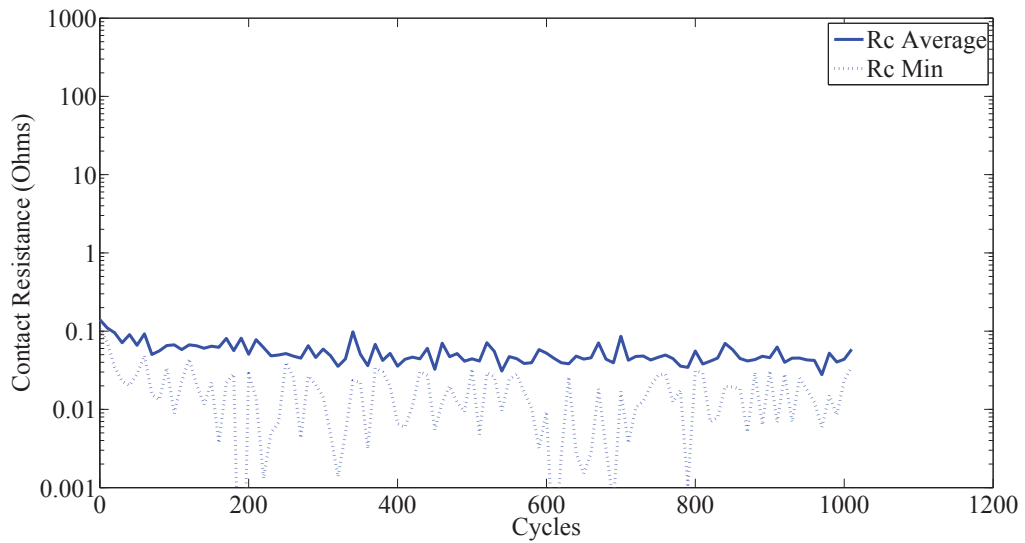
Figure A.26: Contact resistance of Au-Au 6μm radius contact for 10^3 cycles. Rc Average is the average for the last 4 data point at ~ 200μN of contact force. Rc Min is the minimum contact resistance measured during the measurement cycle

A.3.1.4   *Micro-contact with 5,000 cycles.*

The 5×10^3 cycles of a micro-contact was performed on Beam 10. The contact resistance plot is shown in Figure A.27.
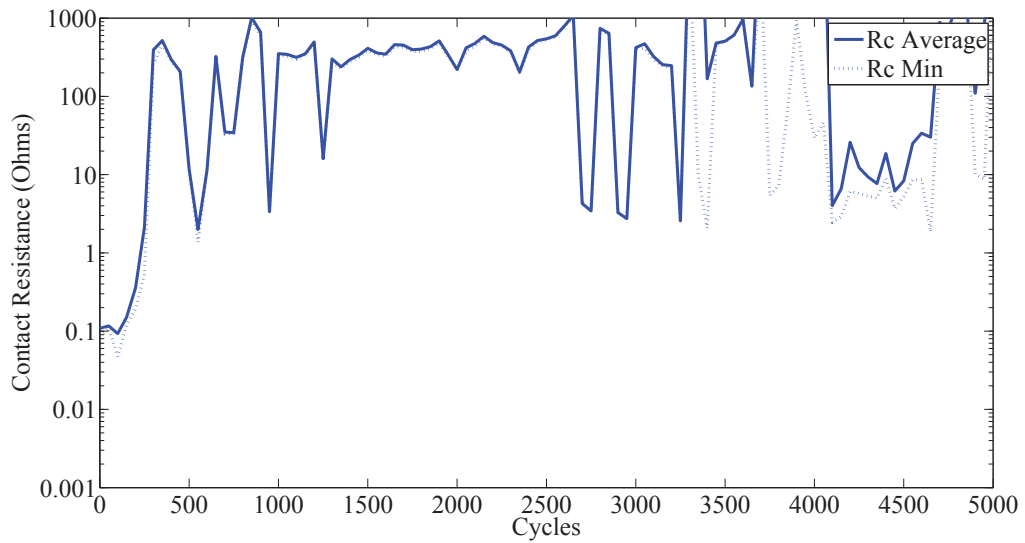
Figure A.27: Contact resistance of Au-Au $6\mu m$ contact for 5×10^3 cycles. Rc Average is the average for the last 4 data point at $\sim 200\mu N$ of contact force. Rc Min is the minimum contact resistance measured during the measurement cycle

A.3.1.5 *Micro-contact with* 10^4 *cycles.*

The 10^4 cycles test of a micro-contact was performed on Beam 9. The contact resistance plot is shown in Figure A.28.
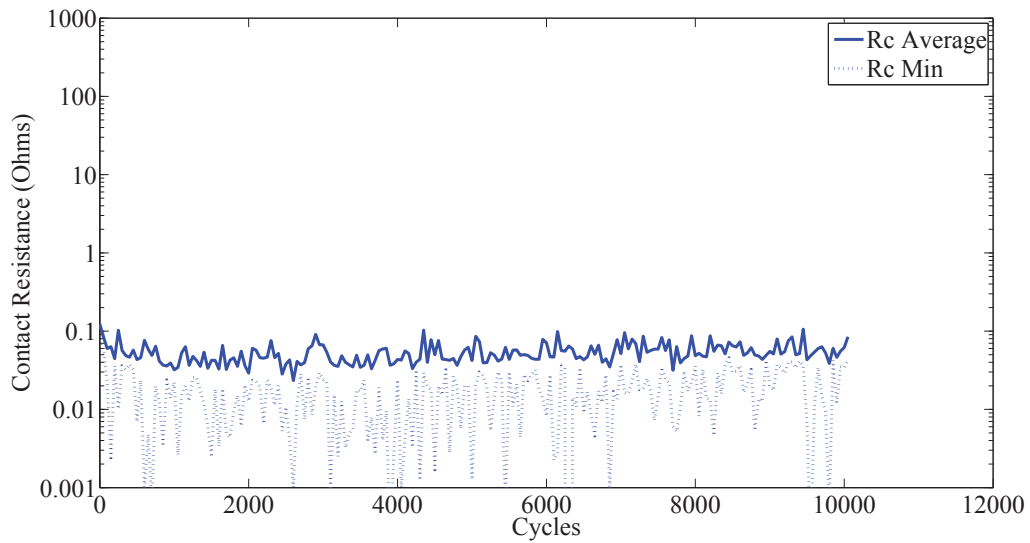
Figure A.28: Contact resistance of Au-Au $6\mu m$ radius contact for a 10^4 cycles. Rc Average is the average for the last 4 data point at $\sim 200\mu N$ of contact force. Rc Min is the minimum contact resistance measured during the measurement cycle

A.3.1.6 *Micro-contact with* 5×10^4 *cycles.*

The 5×10^4 cycles test of a micro-contact was performed on Beam 5. The contact resistance plot is shown in Figure A.29.
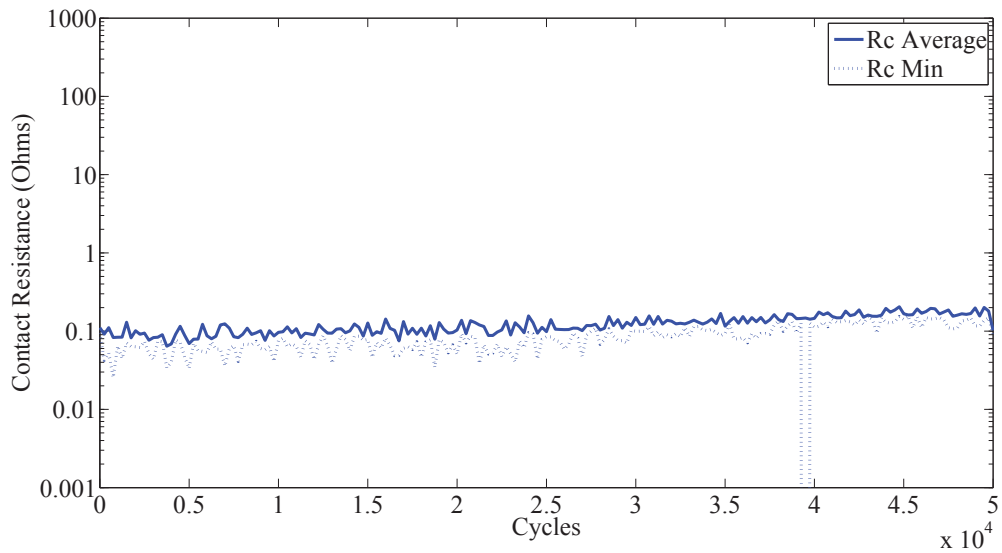
Figure A.29: Contact resistance of Au-Au $6\mu m$ radius contact for a 5×10^4 cycles. Rc Average is the average for the last 4 data point at $\sim 200\mu N$ of contact force. Rc Min is the minimum contact resistance measured during the measurement cycle

A.3.1.7 *Micro-contact with* 10^5 *cycles.*

The 10^5 cycles test of a micro-contact was performed on Beam 6. The contact resistance plot is shown in Figure A.30.
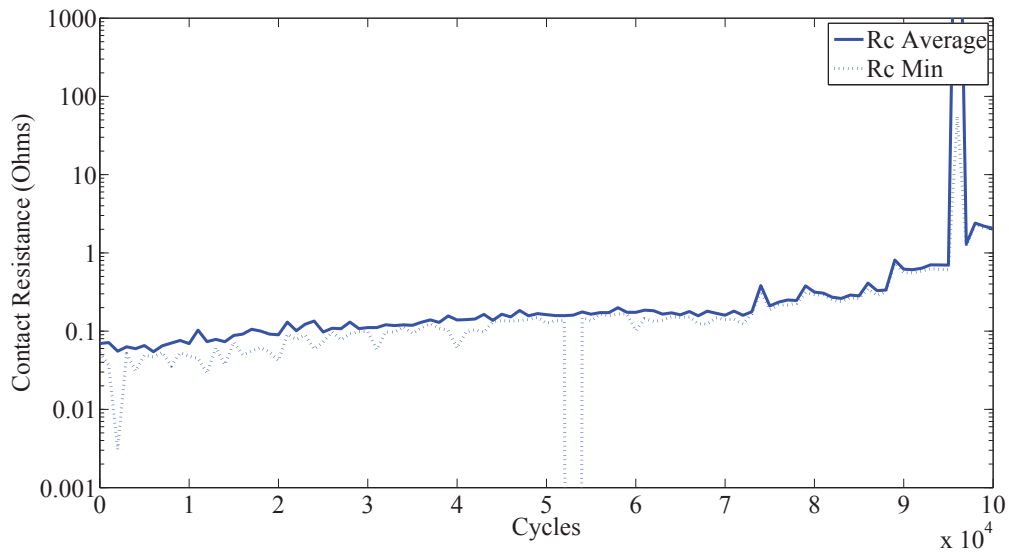
Figure A.30: Contact resistance of Au-Au $6\mu m$ radius contact for a 10^5 cycles. Rc Average is the average for the last 4 data point at $\sim 200\mu N$ of contact force. Rc Min is the minimum contact resistance measured during the measurement cycle

A.3.1.8 *Micro-contact with* 5×10^5 *cycles.*

The 5×10^5 cycles test of a micro-contact was performed on Beam 7. The contact

resistance plot is shown in Figure A.16. This contact failed after 100,000 cycles.
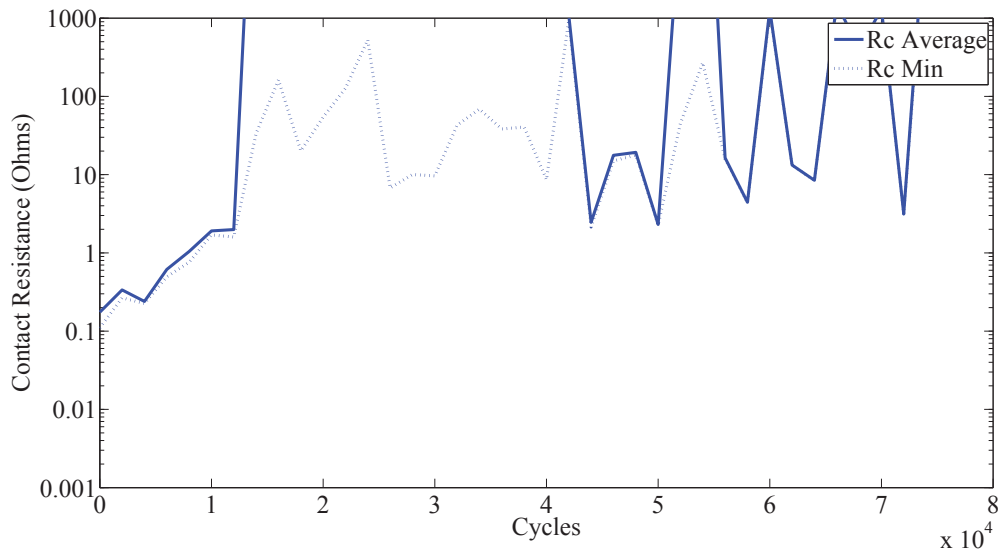
Figure A.31: Contact resistance of Au-Au $6\mu m$ radius contact for a 5×10^5 cycles. Rc Average is the average for the last 4 data point at $\sim 200\mu N$ of contact force. Rc Min is the minimum contact resistance measured during the measurement cycle. This contact failed after 100,000 cycles.

A.3.1.9 *Micro-contact with* 10^6 *cycles.*

The 10^6 cycles test of a micro-contact was performed on Beam 4 The contact

resistance plot is shown in Figure A.32.
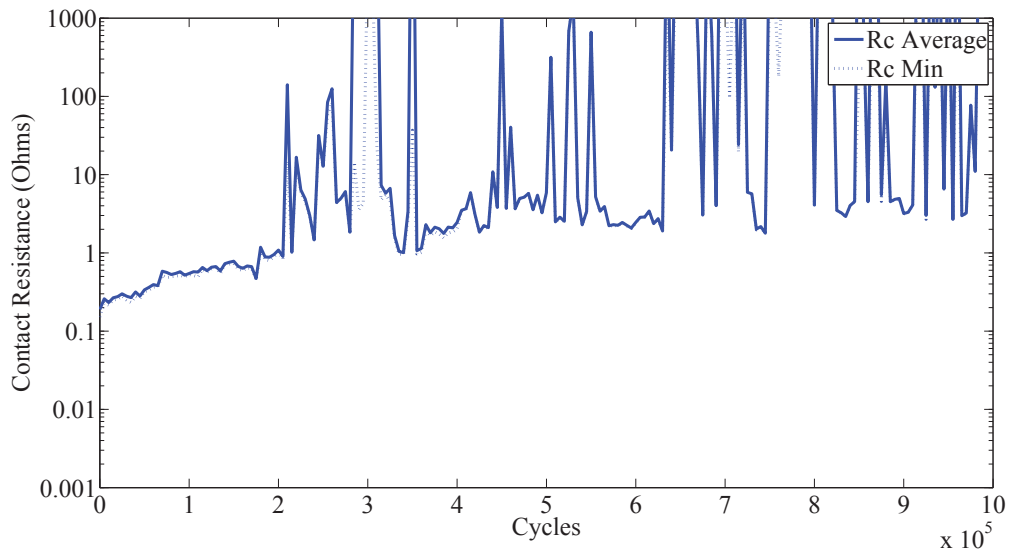
Figure A.32: Contact resistance of Au-Au $6\mu m$ radius contact for a 10^6 cycles. Rc Average is the average for the last 4 data point at $\sim 200\mu N$ of contact force. Rc Min is the minimum contact resistance measured during the measurement cycle

A.3.1.10   *Micro-contact with* 5×10^6 *cycles.*

The 5×10^6 cycles test of a micro-contact was performed on Beam 3. The contact resistance plot is shown in Figure A.33. This contact failed after 3.5 million cycles.
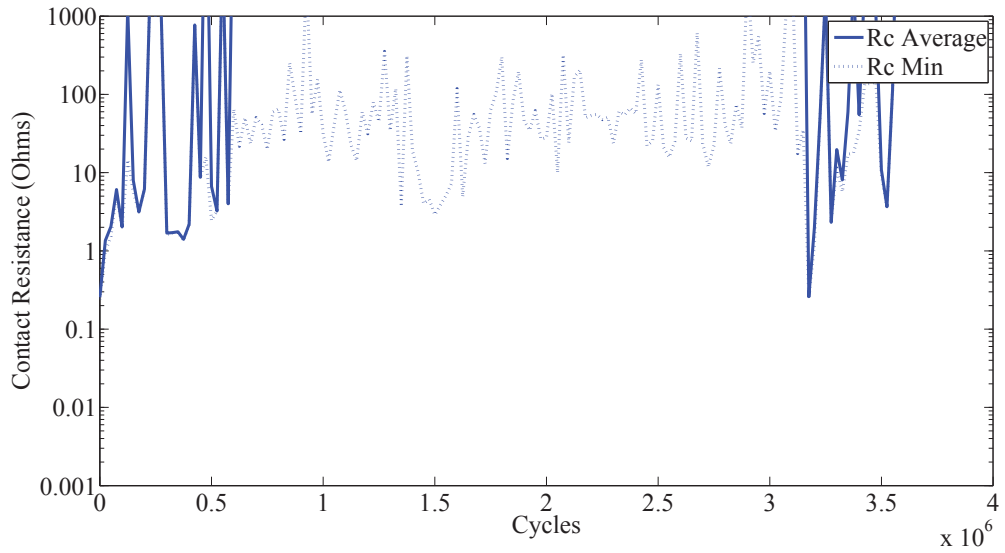
Figure A.33: Contact resistance of Au-Au $6\mu m$ radius contact for a 5×10^6 cycles. Rc Average is the average for the last 4 data point at $\sim 200\mu N$ of contact force. Rc Min is the minimum contact resistance measured during the measurement cycle. This contact failed after 3.5 million cycles.

A.3.1.11 *Micro-contact with* 10^7 *cycles.*

The 10^7 cycles test of a micro-contact was performed on Beam 2. The contact resistance plot is shown in Figure A.34.
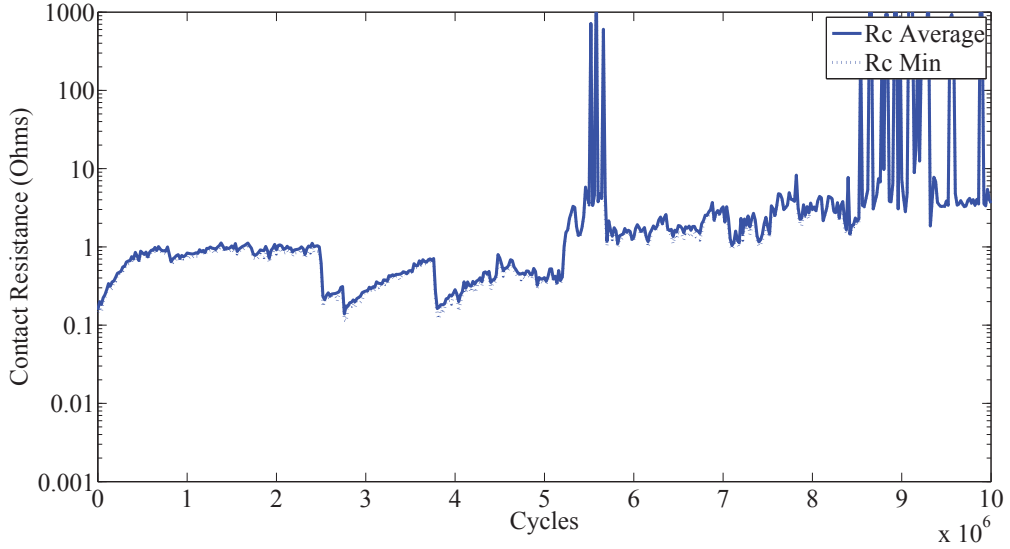
Figure A.34: Contact resistance of Au-Au $6\mu m$ radius contact for a 10^7 cycles. Rc Average is the average for the last 4 data point at $\sim 200\mu N$ of contact force. Rc Min is the minimum contact resistance measured during the measurement cycle

A.4 Testing of Au-Au micro-contact sample (1,4)

A.4.1 Cold Switch Test.

The evolution of the contact area was observed by actuating the micro-contact same as previously stated. The micro-contacts were actuated using an external, calibrated point load. To examine the micro-contact performance, the contact resistance and force required to close the contact, were monitored simultaneously throughout testing. At the above stated end point, the micro-contact was folded back to evaluate the wear of the upper hemispherical and planar lower contact.

A.4.1.1 Micro-contact with 100 cycles.

The 100 cycles test of a micro-contact was performed on Beam 16. The contact resistance plot is shown in Figure A.35. SEM images for the contact bump is shown in Figure A.36a and for the contact pad in Figure A.36b.
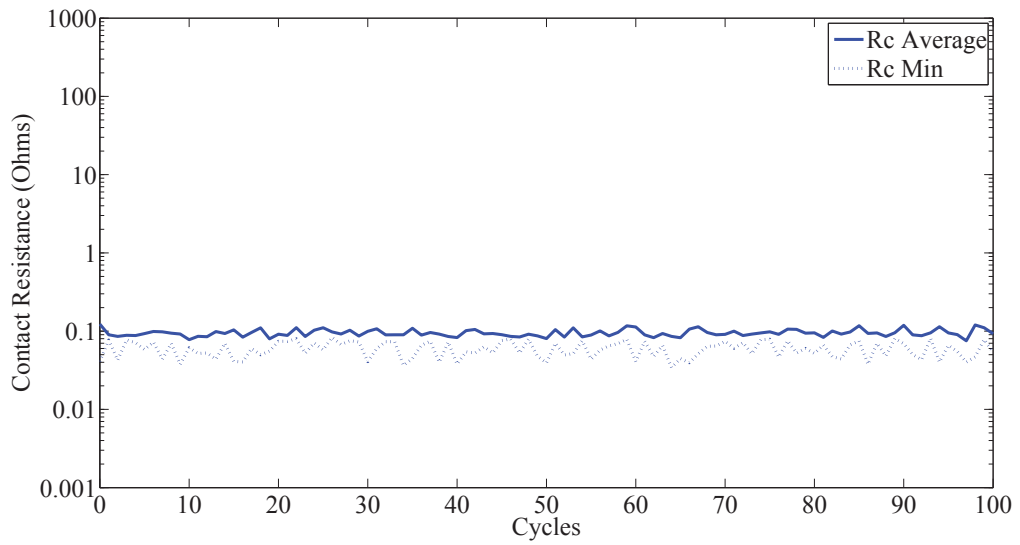
Figure A.35: Contact resistance of Au-Au $6\mu m$ radius contact for 100 cycles. 'Rc Average' is the average for the last 5 resistance measurements at $\sim 200\mu N$ of contact force. 'Rc Min' is the minimum contact resistance measured.

(a) Upper contact (Anode)

(b) Lower contact (Cathode)
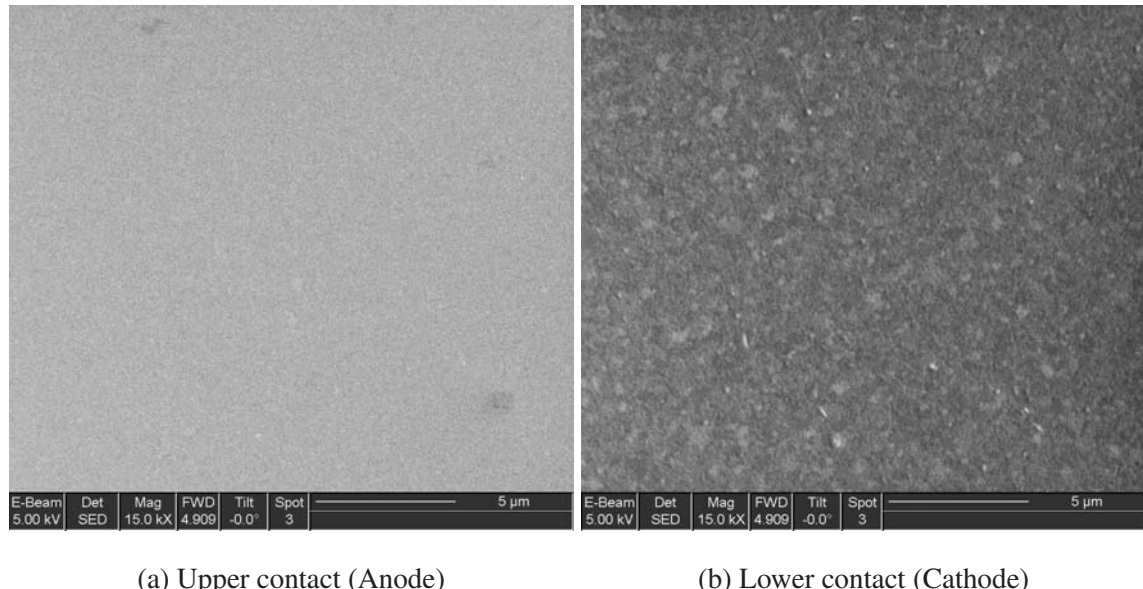
Figure A.36: SEM image of the upper contact bump and lower contact pad.

A.4.1.2   Micro-contact with 10^3 cycles.

The 10^3 cycles test of a micro-contact was performed on Beam 15. The contact resistance plot is shown in Figure A.37. SEM images for the contact bump is shown in Figure A.38a and for the contact pad in Figure A.38b..
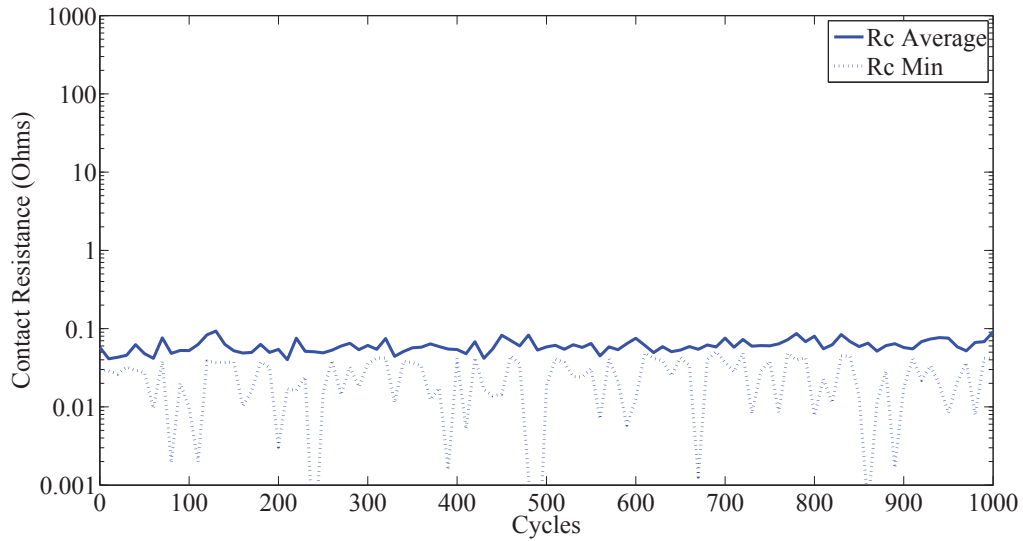
Figure A.37: Contact resistance of Au-Au $6\mu m$ radius contact for 10^3 cycles. 'Rc Average' is the average for the last 5 resistance measurements at $\sim 200\mu N$ of contact force. 'Rc Min' is the minimum contact resistance measured.

Contact bump

(a) Upper contact (Anode)   (b) Lower contact (Cathode)
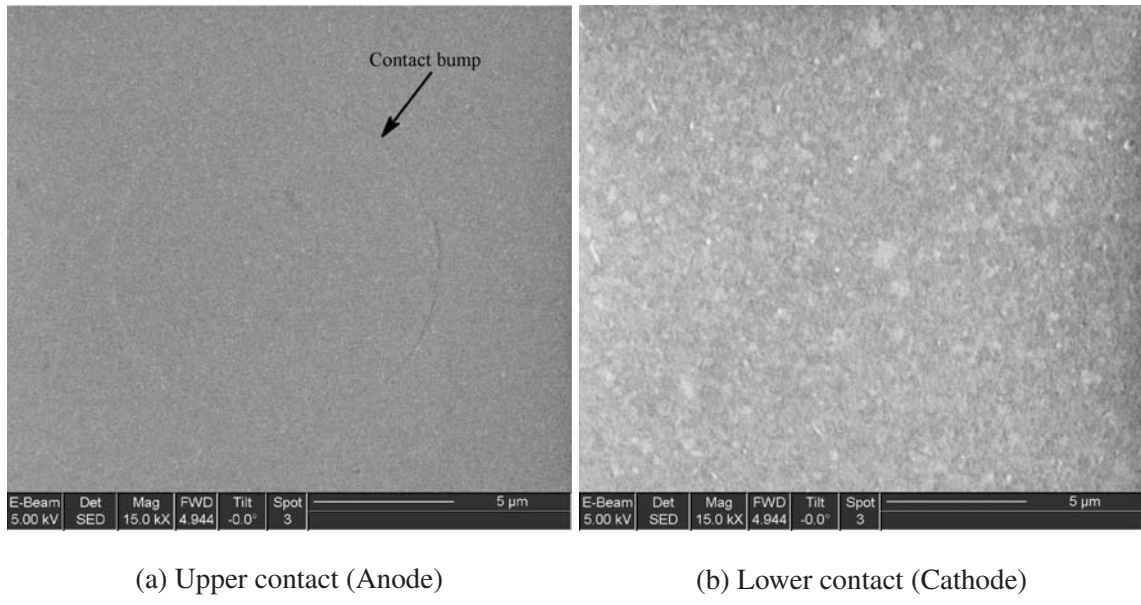
Figure A.38: SEM image of the upper contact bump and lower contact pad.

A.4.1.3 *Micro-contact with* 5×10^3 *cycles.*

The 5×10^3 cycles of a micro-contact was performed on Beam 13. The contact resistance plot is shown in Figure A.39. SEM images for the contact bump is shown in Figure A.40a and for the contact pad in Figure A.40b.
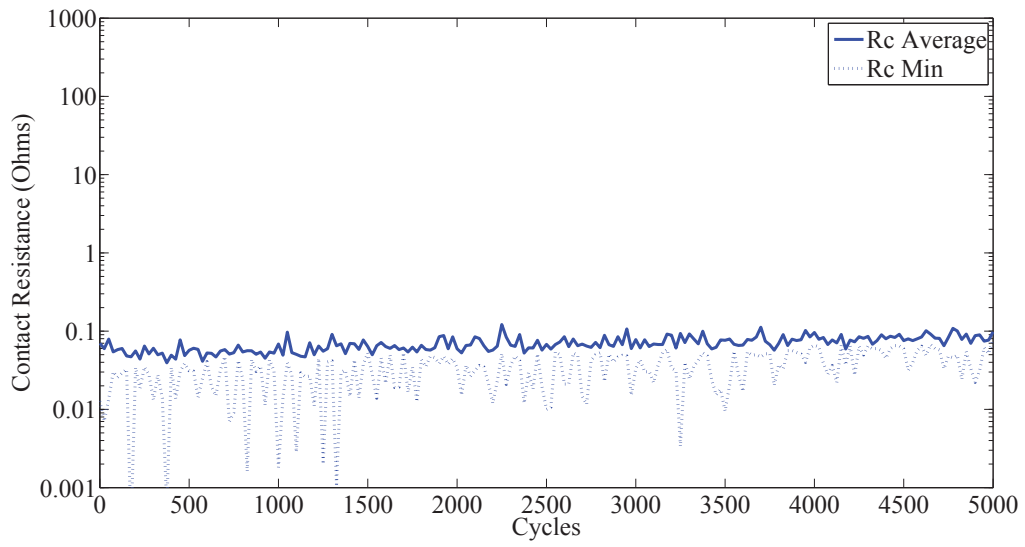
Figure A.39: Contact resistance of Au-Au $6\mu m$ contact for 5×10^3 cycles. 'Rc Average' is the average for the last 5 resistance measurements at $\sim 200\mu N$ of contact force. 'Rc Min' is the minimum contact resistance measured.

(a) Upper contact (Anode)　　　　　　　(b) Lower contact (Cathode)
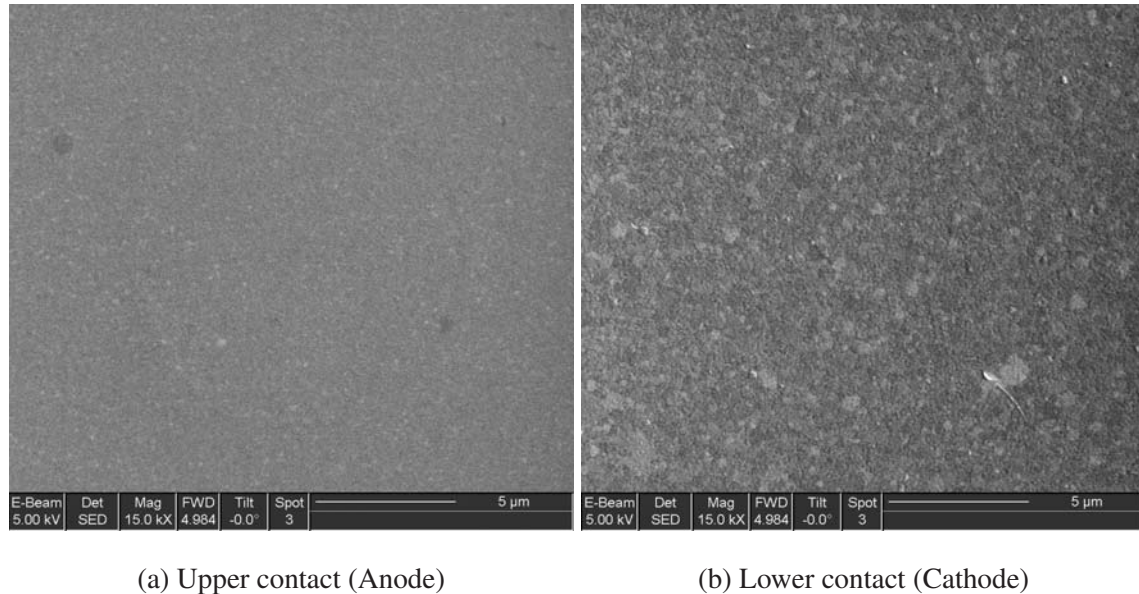
Figure A.40: SEM image of the upper contact bump and lower contact pad.

A.4.1.4 Micro-contact with 10^4 *cycles.*

The 10^4 cycles test of a micro-contact was performed on Beam 9. The contact resistance plot is shown in Figure A.41. SEM images for the contact bump is shown in Figure A.42a and for the contact pad in Figure A.42b.
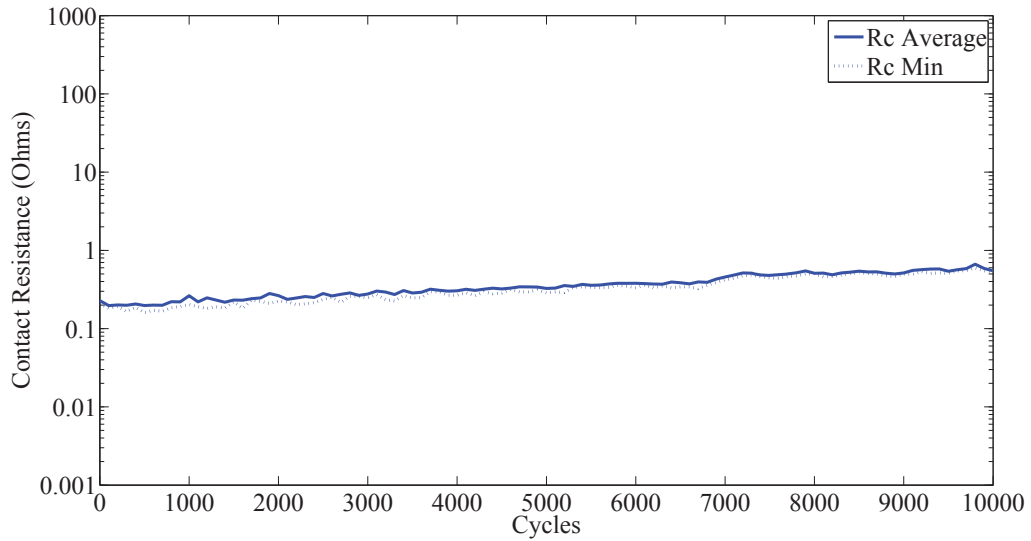
Figure A.41: Contact resistance of Au-Au $6\mu m$ radius contact for a 10^4 cycles. 'Rc Average' is the average for the last 5 resistance measurements at $\sim 200\mu N$ of contact force. 'Rc Min' is the minimum contact resistance measured.

(a) Upper contact (Anode)   (b) Lower contact (Cathode)
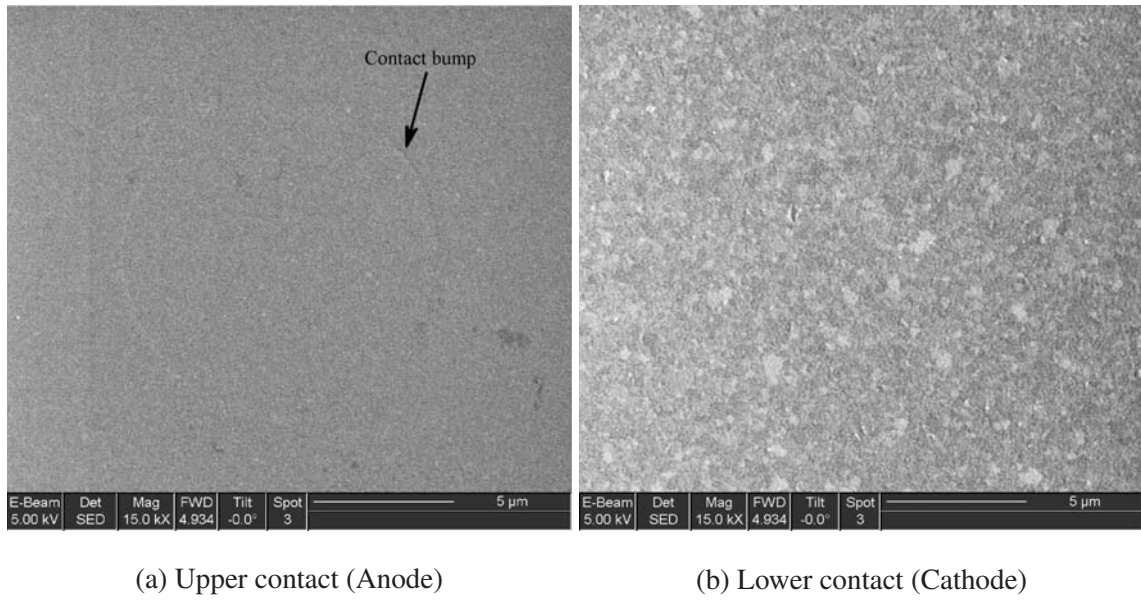
Figure A.42: SEM image of the upper contact bump and lower contact pad.

A.4.1.5   *Micro-contact with* 5×10^4 *cycles.*

The 5×10^4 cycles test of a micro-contact was performed on Beam 10. The contact resistance plot is shown in Figure A.43. SEM images for the contact bump is shown in Figure A.44a and for the contact pad in Figure A.44b.

This contact show some wear after 5×10^4 actuation. On the beam there is an area in the middle on the contact bump that has material transfer has occurred. This material created a hole that is shown on the pad.
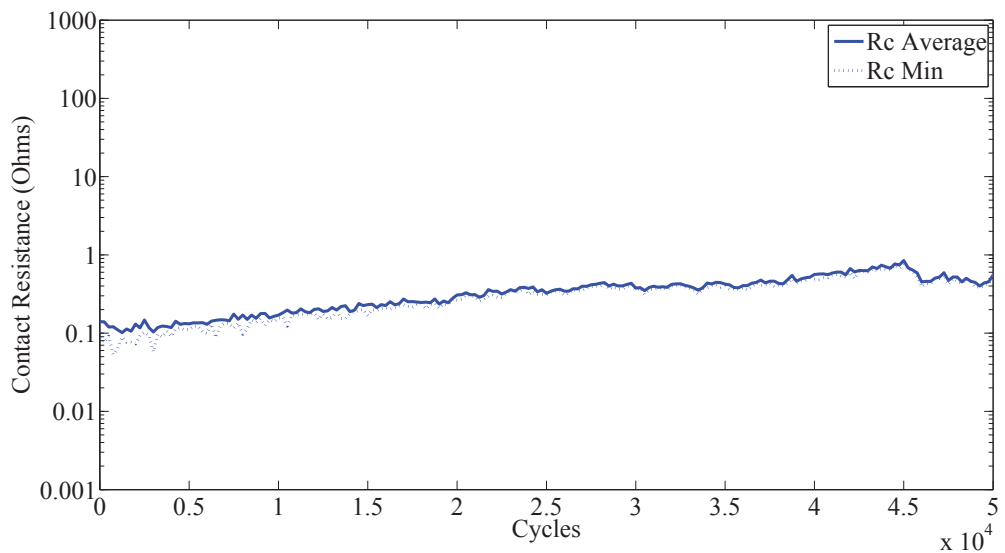
Figure A.43: Contact resistance of Au-Au $6\mu m$ radius contact for a 5×10^4 cycles. 'Rc Average' is the average for the last 5 resistance measurements at $\sim 200\mu N$ of contact force. 'Rc Min' is the minimum contact resistance measured.

(a) Upper contact (Anode)

(b) Lower contact (Cathode)
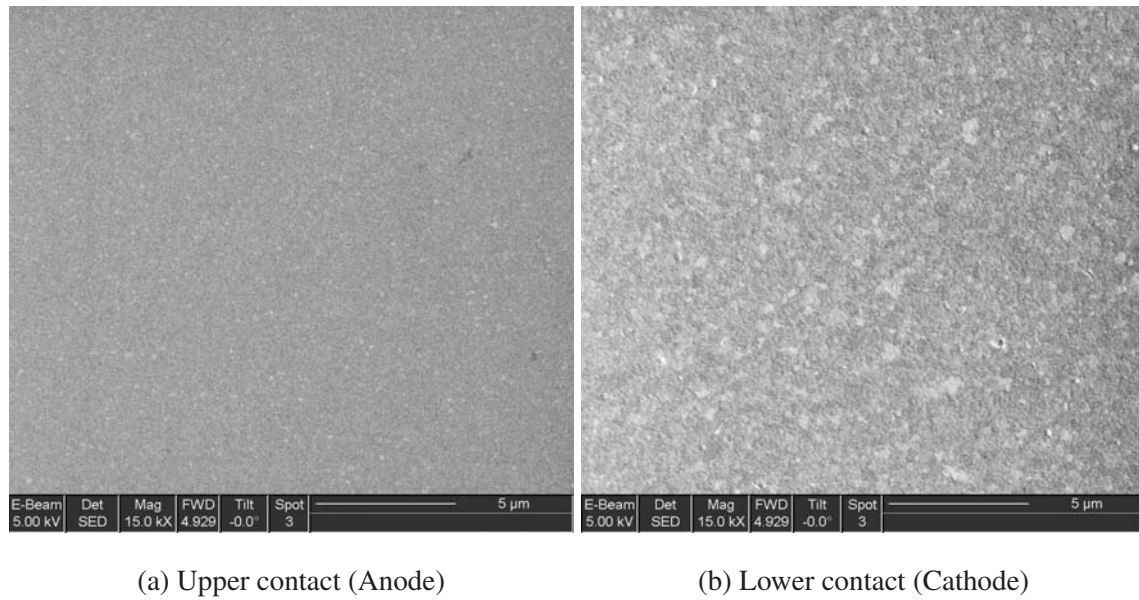
Figure A.44: SEM image of the upper contact bump and lower contact pad.

A.4.1.6   Micro-contact with 10^5 cycles.

The 10^5 cycles test of a micro-contact was performed on Beam 11. The contact resistance plot is shown in Figure A.45. SEM images for the contact bump is shown in Figure A.46a and for the contact pad in Figure A.46b.
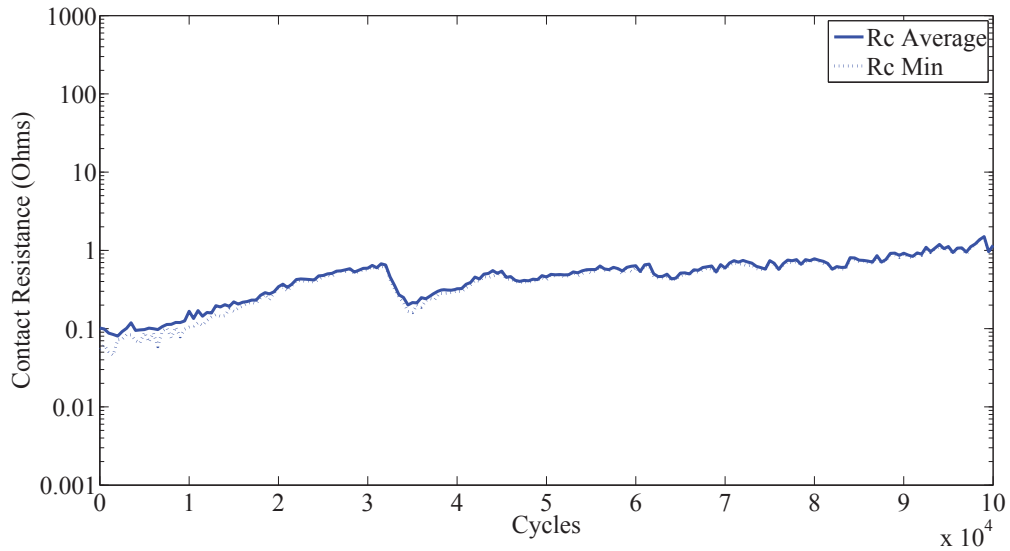
Figure A.45: Contact resistance of Au-Au $6\mu m$ radius contact for a 10^5 cycles. 'Rc Average' is the average for the last 5 resistance measurements at $\sim 200\mu N$ of contact force. 'Rc Min' is the minimum contact resistance measured.
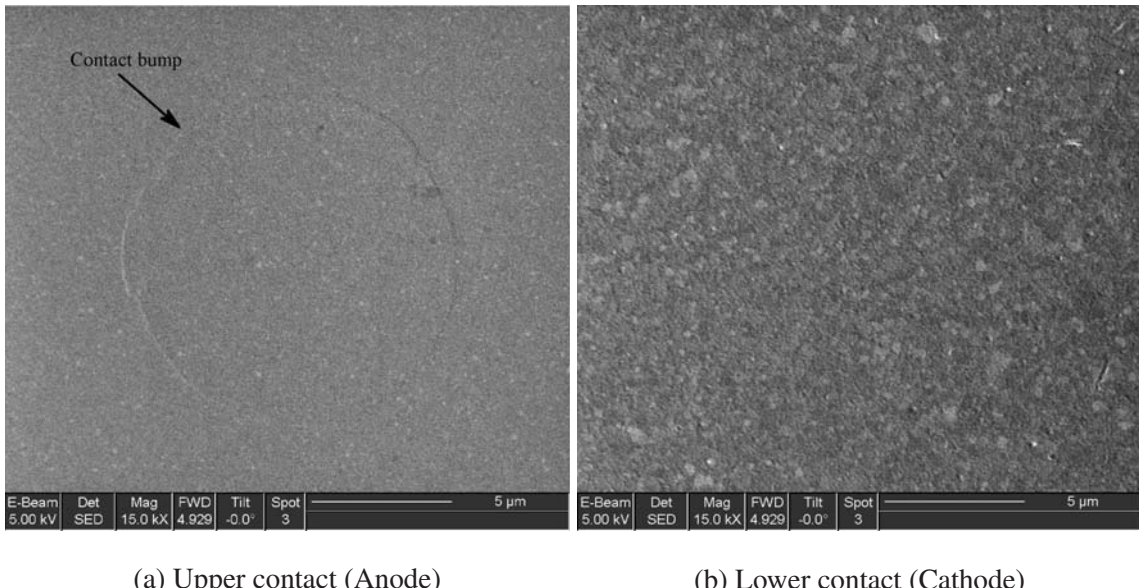
(a) Upper contact (Anode)   (b) Lower contact (Cathode)

Figure A.46: SEM image of the upper contact bump and lower contact pad.

A.4.1.7 *Micro-contact with* 5×10^5 *cycles.*

The 5×10^5 cycles test of a micro-contact was performed on Beam 12. The contact resistance plot is shown in Figure A.47. This contact failed after 100,000 cycles. SEM images for the contact bump is shown in Figure A.48a and for the contact pad in Figure A.48b.
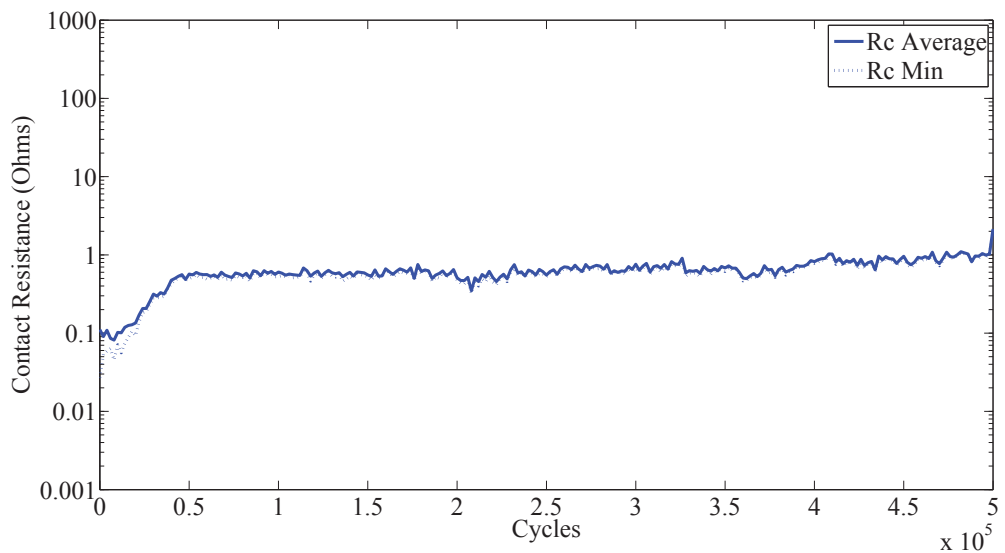
Figure A.47: Contact resistance of Au-Au $6\mu m$ radius contact for a 5×10^5 cycles. 'Rc Average' is the average for the last 5 resistance measurements at $\sim 200\mu N$ of contact force. 'Rc Min' is the minimum contact resistance measured.

(a) Upper contact (Anode)

(b) Lower contact (Cathode)
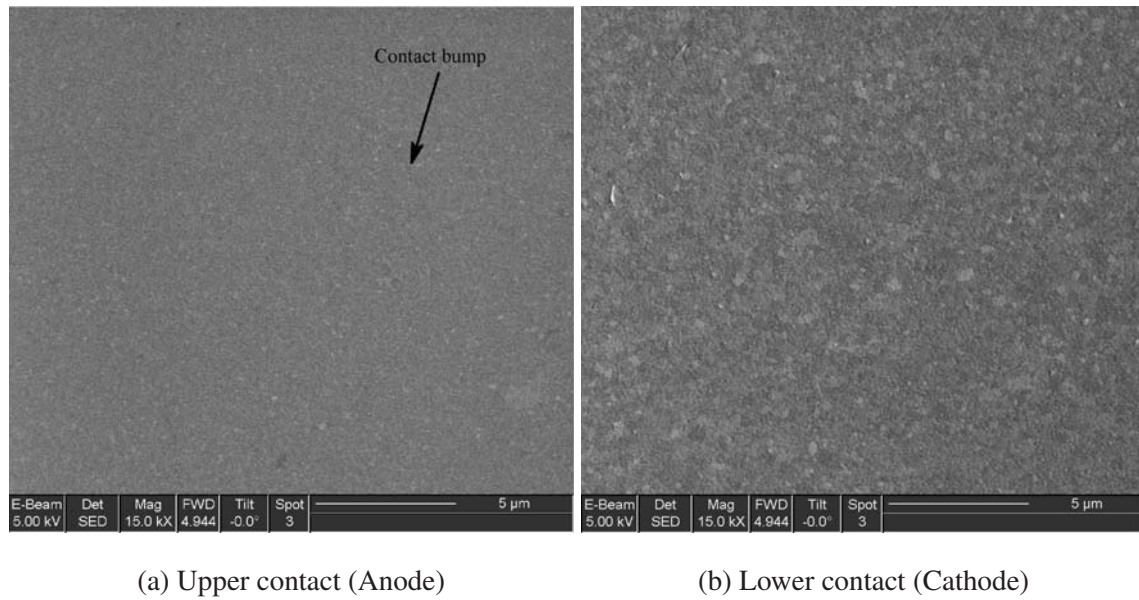
Figure A.48: SEM image of the upper contact bump and lower contact pad.

A.4.1.8 Micro-contact with 10^6 cycles.

The 10^6 cycles test of a micro-contact was performed on Beam 4 The contact resistance plot is shown in Figure A.49. SEM images for the contact bump is shown in Figure A.50a and for the contact pad in Figure A.50b.
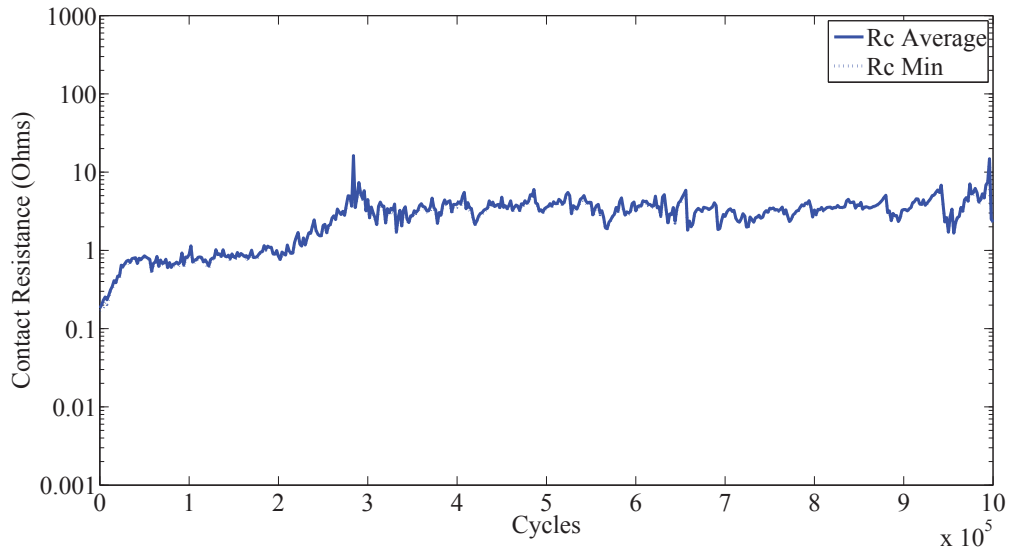
Figure A.49: Contact resistance of Au-Au $6\mu m$ radius contact for a 10^6 cycles. 'Rc Average' is the average for the last 5 resistance measurements at $\sim 200\mu N$ of contact force. 'Rc Min' is the minimum contact resistance measured.

(a) Upper contact (Anode)   (b) Lower contact (Cathode)
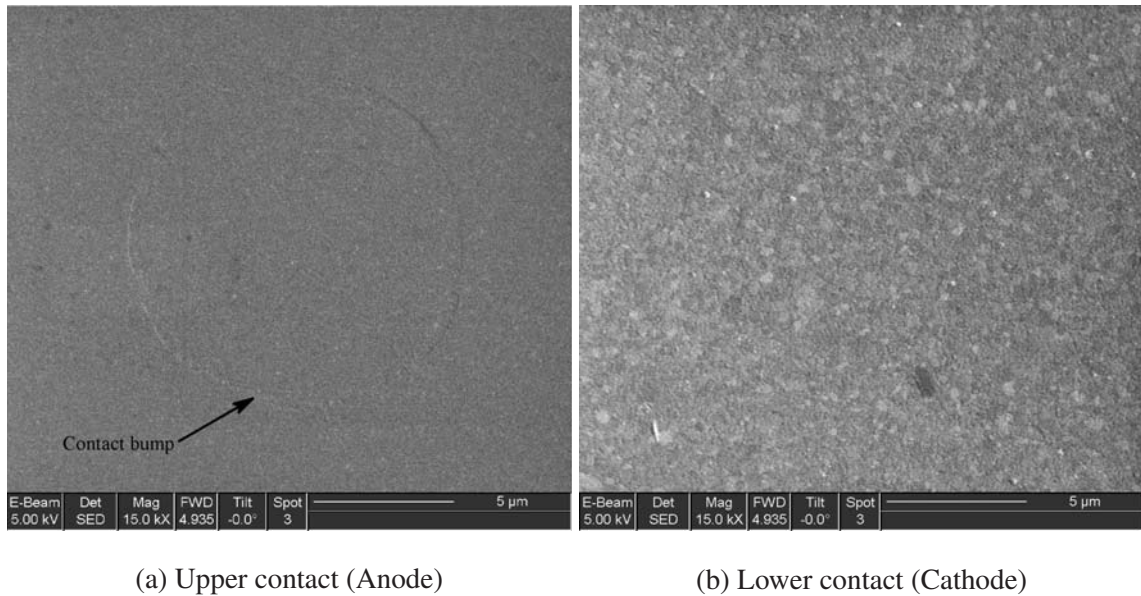
Figure A.50: SEM image of the upper contact bump and lower contact pad.

A.4.1.9 *Micro-contact with* 5×10^6 *cycles.*

The 5×10^6 cycles test of a micro-contact was performed on Beam 3. The contact resistance plot is shown in Figure A.33. SEM images for the contact bump is shown in Figure A.52a and for the contact pad in Figure A.52b.
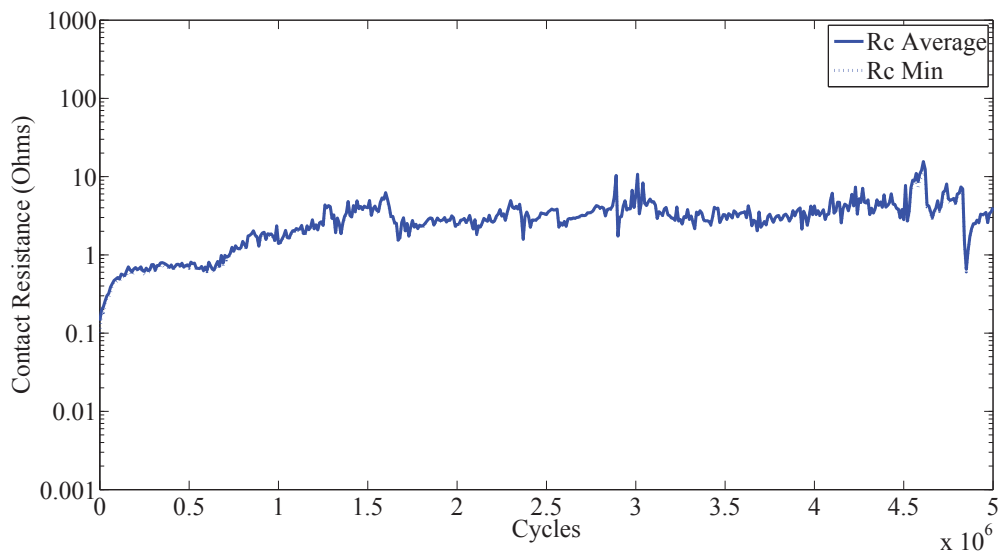
Figure A.51: Contact resistance of Au-Au $6\mu m$ radius contact for a 5×10^6 cycles. 'Rc Average' is the average for the last 5 resistance measurements at $\sim 200\mu N$ of contact force. 'Rc Min' is the minimum contact resistance measured.

(a) Upper contact (Anode)

(b) Lower contact (Cathode)
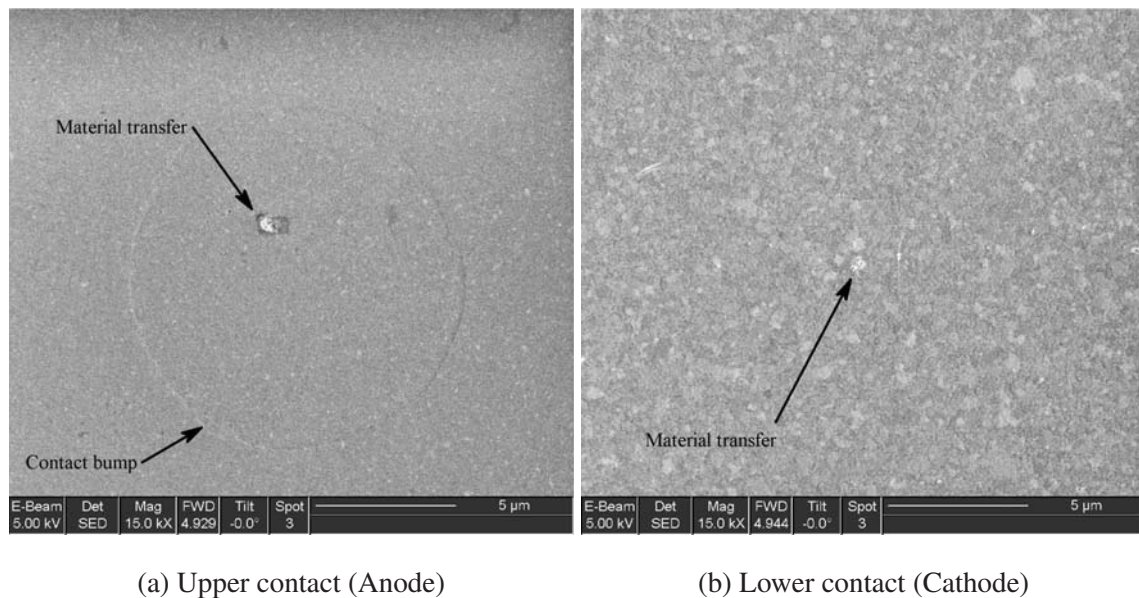
Figure A.52: SEM image of the upper contact bump and lower contact pad.

A.4.1.10 *Micro-contact with* 10^7 *cycles.*

The 10^7 cycles test of a micro-contact was performed on Beam 2. The contact resistance plot is shown in Figure A.53. SEM images for the contact bump is shown in Figure A.54a and for the contact pad in Figure A.54b.
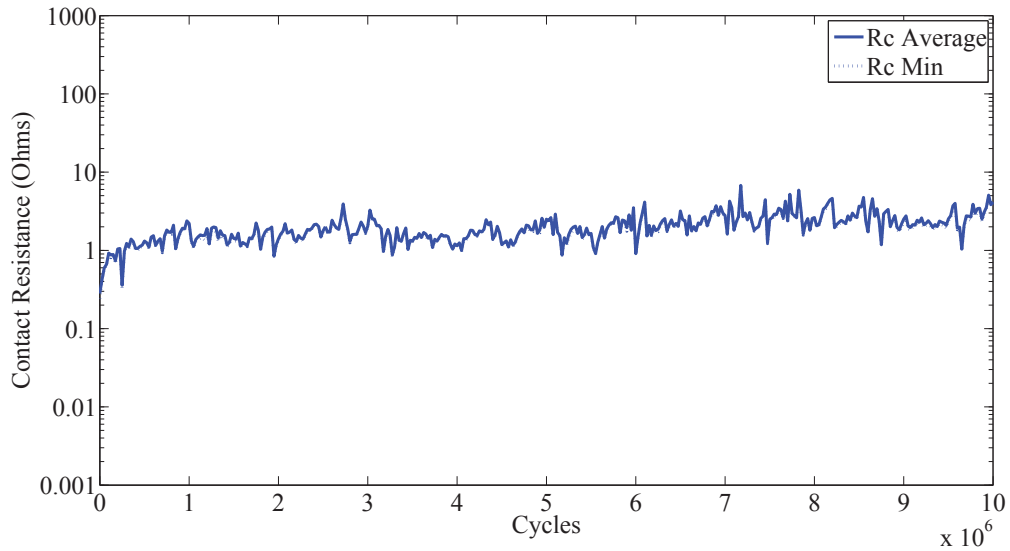
Figure A.53: Contact resistance of Au-Au $6\mu m$ radius contact for a 10^7 cycles. 'Rc Average' is the average for the last 5 resistance measurements at $\sim 200\mu N$ of contact force. 'Rc Min' is the minimum contact resistance measured.

(a) Upper contact (Anode)   (b) Lower contact (Cathode)
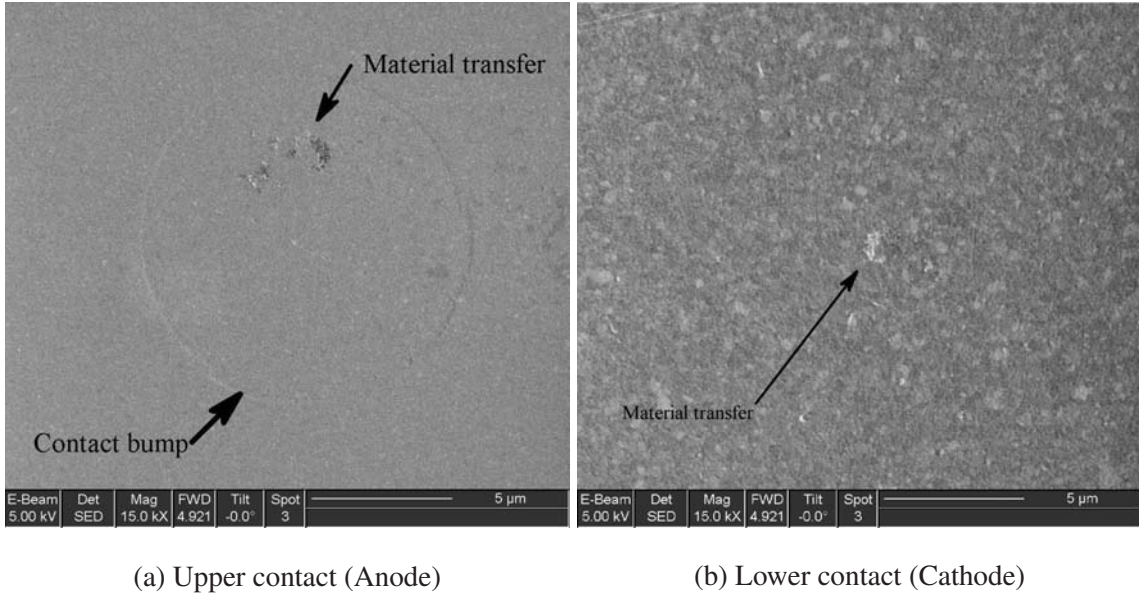
Figure A.54: SEM image of the upper contact bump and lower contact pad.

A.5   Testing of Au-Au micro-contact sample (2,3)

This sample was used to re-run the 10 million cycle cycles 3 times as well as map out a lifetime of a contact by testing the micro-contact until it failed.

A.5.1   Cold Switch Test.

A.5.1.1 10^7 cycles.

The 10^7 cycles test of a micro-contact was performed on Beam 2. The contact resistance plot is shown in Figure A.55. SEM images for the contact bump is shown in Figure A.56a and for the contact pad in Figure A.56b.

This contact shows only a little area of wear after 10^7 actuation. This matches the very low contact resistance seen throughout the lifetime of the micro-contact.

154
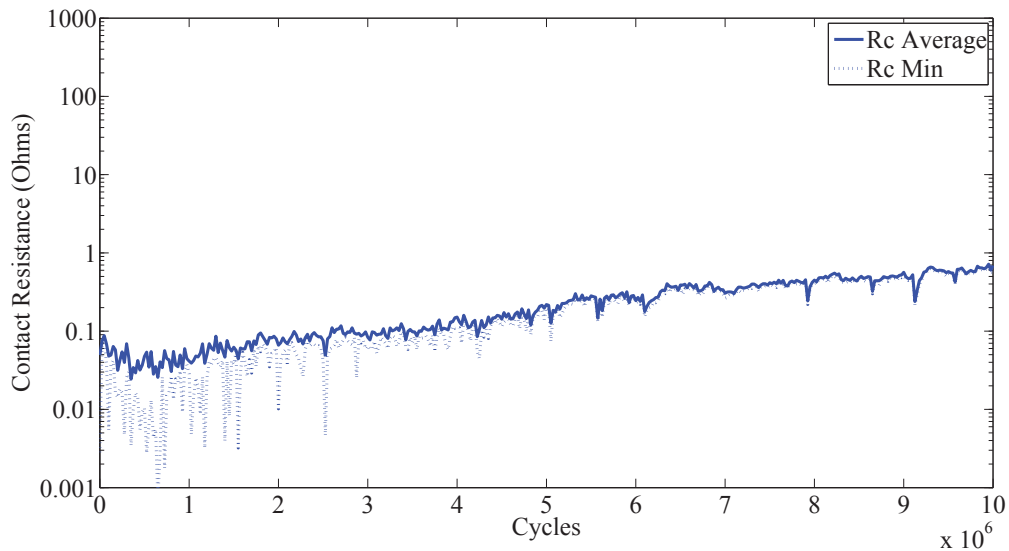
Figure A.55: Contact resistance of Au-Au $6\mu m$ radius contact for a 10^7 cycles. Rc Average is the average for the last 4 data point at $\sim 200\mu N$ of contact force. Rc Min is the minimum contact resistance measured during the measurement cycle

(a) Upper contact (Anode)

(b) Lower contact (Cathode)
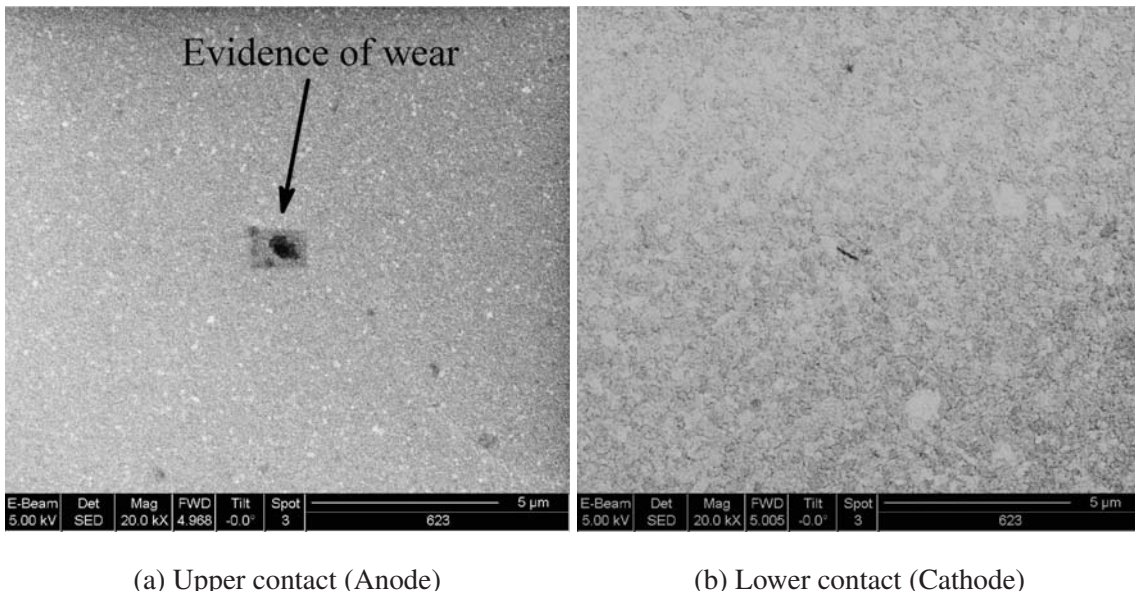
Figure A.56: SEM image of upper contact bump and lower contact pad after 10^7 actuation. A small area of material transfer is shown in the contact area.

155

A.5.1.2 10^7 ***cycles.***

The 10^7 cycles test of a micro-contact was performed on Beam 3. The contact resistance plot is shown in Figure A.57. SEM images for the contact bump is shown in Figure A.58a and for the contact pad in Figure A.58b.
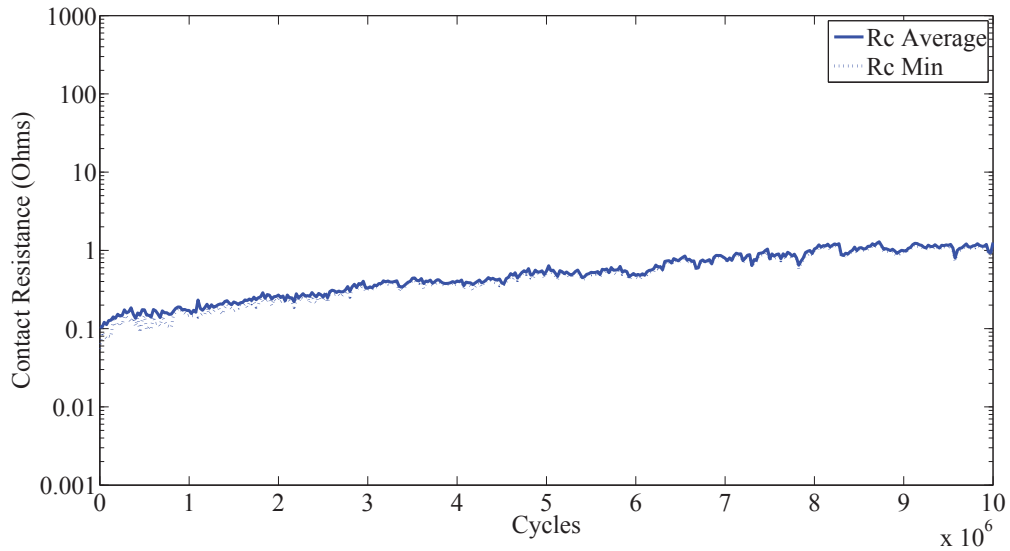

Figure A.57: Contact resistance of Au-Au $6\mu m$ radius contact for a 10^7 cycles. Rc Average is the average for the last 4 data point at $\sim 200\mu N$ of contact force. Rc Min is the minimum contact resistance measured during the measurement cycle

This contact shows no obvious wear after 10^7 actuation. This matches the very low contact resistance seen throughout the lifetime of the micro-contact.

(a) Upper contact (Anode)

(b) Lower contact (Cathode)
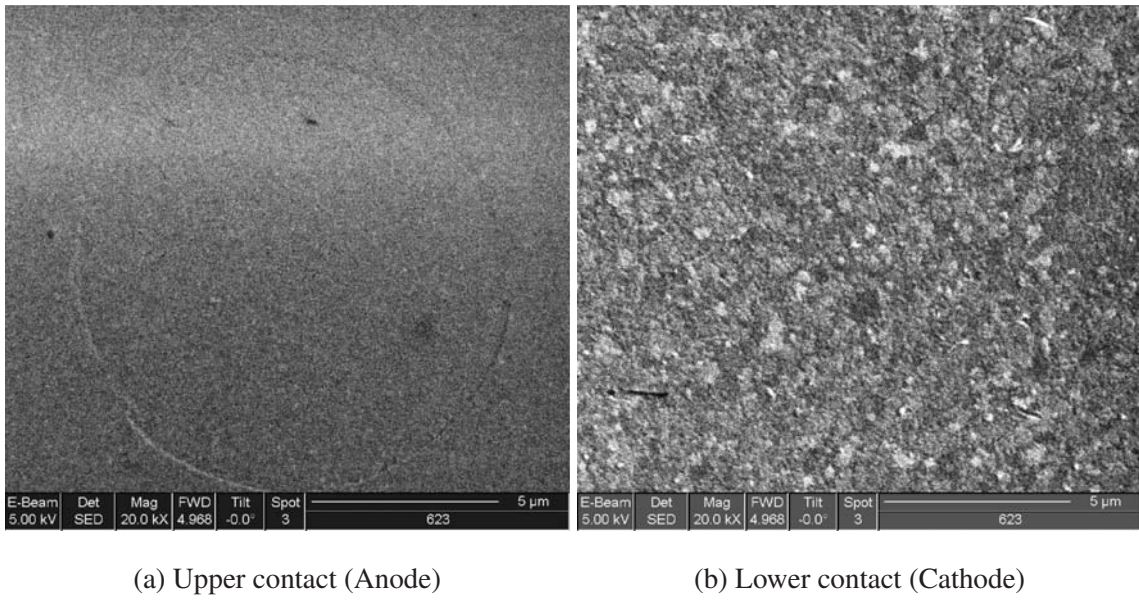
Figure A.58: SEM image of upper contact bump and lower contact pad after $10M$ actuation. A small area of material transfer is shown in the contact area.

A.5.1.3 10^7 *cycles.*

The 10^7 cycles test of a micro-contact was performed on Beam 4. The contact resistance plot is shown in Figure A.59. SEM images for the contact bump is shown in Figure A.60a and for the contact pad in Figure A.60b.

This contact shows no obvious wear after 10^7 actuation. This matches the very low contact resistance seen throughout the lifetime of the micro-contact.
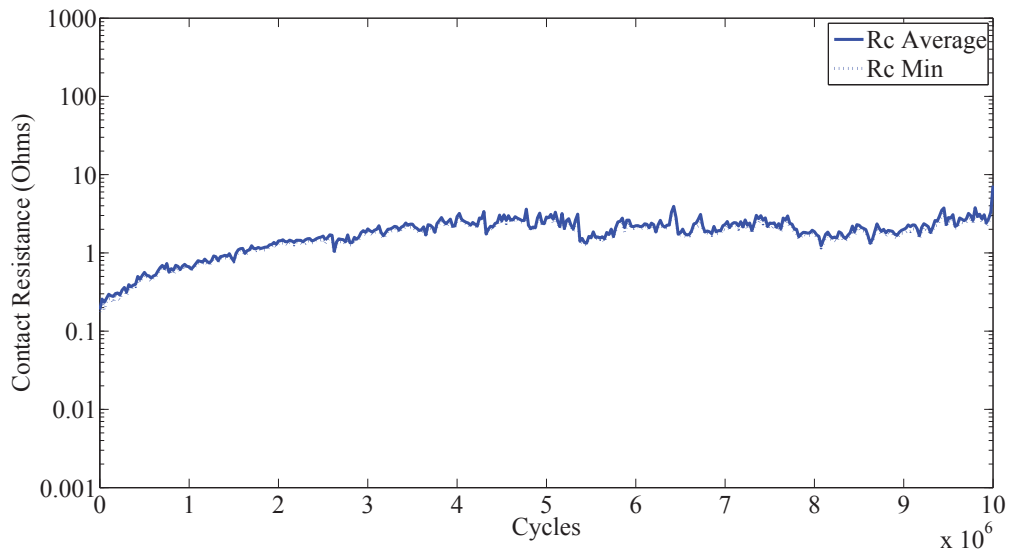
Figure A.59: Contact resistance of Au-Au $6\mu m$ radius contact for a 10^7 cycles. Rc Average is the average for the last 4 data point at $\sim 200\mu N$ of contact force. Rc Min is the minimum contact resistance measured during the measurement cycle

(a) Upper contact (Anode)

(b) Lower contact (Cathode)
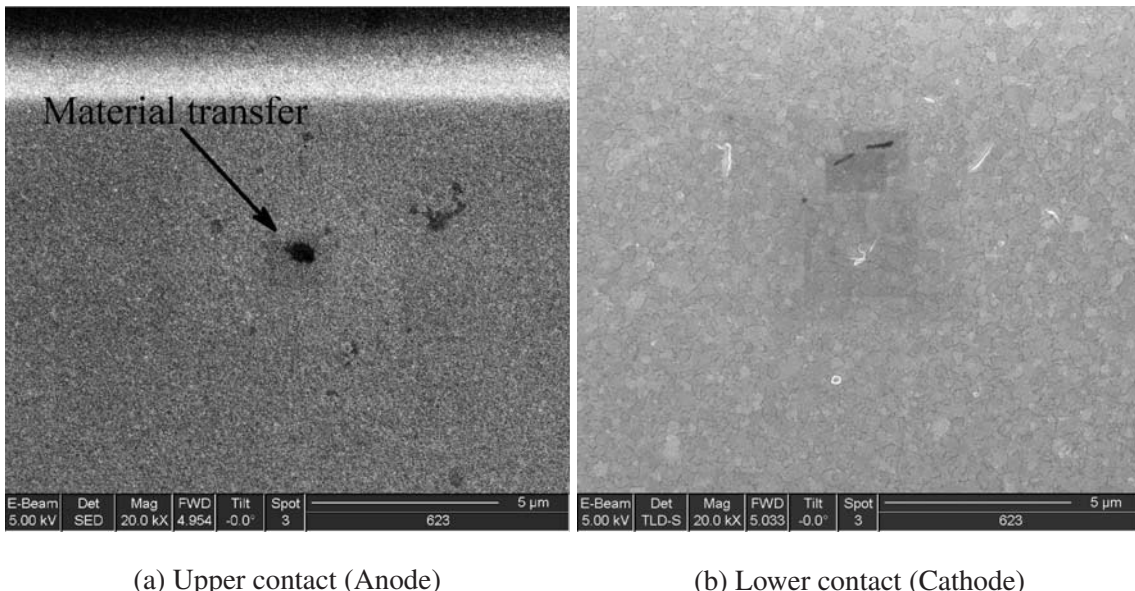
Figure A.60: SEM image of upper contact bump and lower contact pad after 10^7 actuation. A small area of material transfer is shown in the contact area.

158

A.5.2   Lifetime Contact Resistance Evolution.

For the cold-switch test (CST) of the $6\mu m$ contact radius Au-Au device, the amount of cycling was varied to observe the effects lifecycle performance. The device was actuated to 350 million cycles with measurements at every $100,000$ cycles for the first 50 Million cycles. Measurements every $250,000$ from 50 Million to 145 Million cycles. Finally the device was measured every $500,000$ cycles for the remaining life of the micro-contact. The contact resistance plot is shown in Figure A.61.
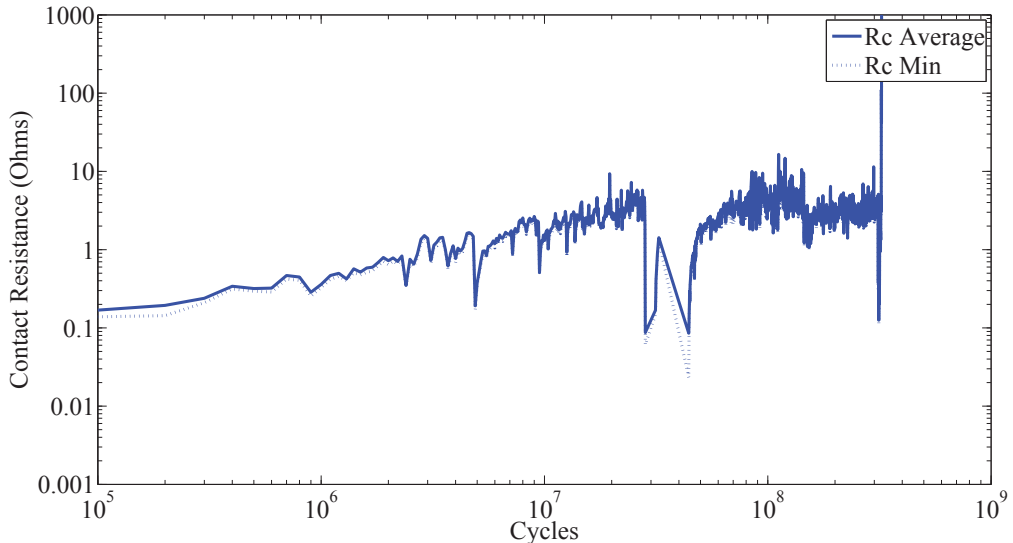
Figure A.61: Contact resistance of Au-Au $6\mu m$ radius contact until failure. Rc Average is the average for the last 4 data point at $\sim 200\mu N$ of contact force. Rc Min is the minimum contact resistance measured during the measurement cycle.

With this contact cycled until failure there are many interesting trends. The first is the steady increase of contact resistance from $100k - 28$ million cycles. At 28 million there is the first of two software glitches. During these times, at 28 million and 32 million cycles, the micro-contact structure was cycled, but the measurement cycles did not happen as plan. After this long continuous cycling, the next contact resistance measurement was

159

much lower than the previous. This could be due to the long continuous cycling ability to clean the contact area and caused a drop in contact resistance. After recovery from these two long cycles, the contact resistance remained steady till 322.6 million cycles, where the contact resistance spiked to 109Ω, then at 323.6 million cycles the contact failed to close. SEM images for the contact bump is shown in Figure A.62a and for the contact pad in Figure A.62b.


(a) Upper contact (Anode)　　　　　　(b) Lower contact (Cathode)
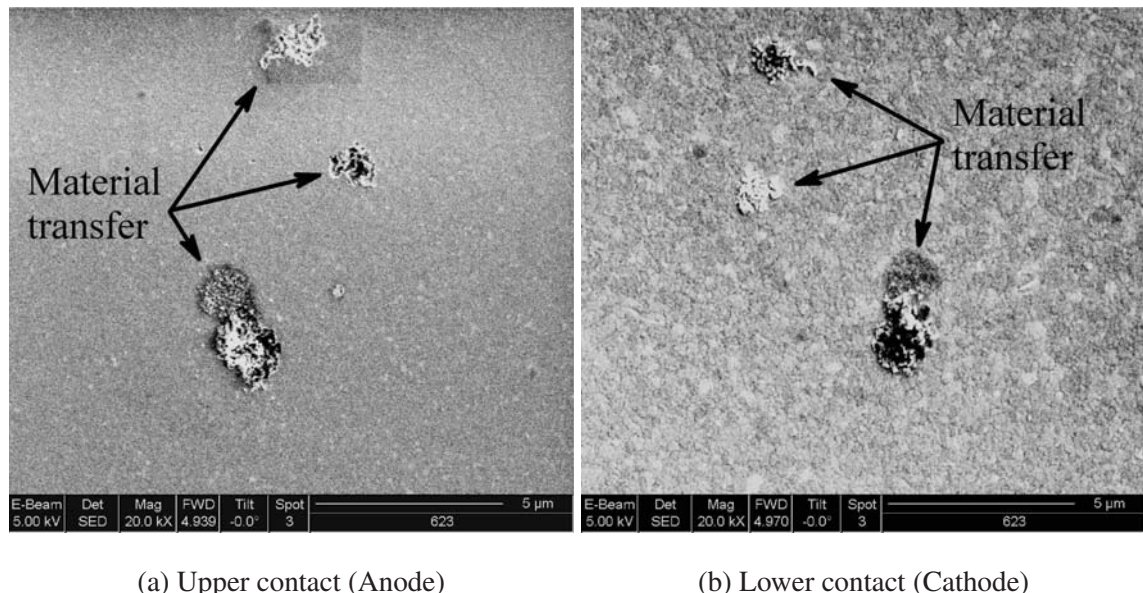
Figure A.62: SEM image of upper contact bump and lower contact pad after reliability testing. A small area of material transfer is shown in the contact area.

This contact shows three distinct wear spots on the upper and lower contact area. This material in the contact area is what caused the resistance to spike for the last set of measurements.

A.6　Appendix Summary

This chapter presented all the Au-Au data collected in this research

Appendix B: Gray-scale paper

The following is a copy of the paper on gray-scale lithography that was submitted and presented at the Photonics West 2014 Conference.

Fabrication of 3D surface structures using gray-scale lithography

Christopher Stilson, Rajan Pal and Ronald Coutu, Jr.*

Department of Electrical and Computer Engineering, Air Force Institute of Technology,
Wright Patterson AFB, Ohio 45433

ABSTRACT

The ability to design and develop 3D microstructures is important for microelectromechanical systems (MEMS) fabrication. Previous techniques used to create 3D devices included tedious steps in direct writing and aligning patterns onto a substrate followed by multiple photolithography steps using expensive, customized equipment. Additionally, these techniques restricted batch processing and placed limits on achievable shapes. Gray-scale lithography enables the fabrication of a variety of shapes using a single photolithography step followed by reactive ion etching (RIE). Micromachining 3D silicon structures for MEMS can be accomplished using gray-scale lithography along with dry anisotropic etching. In this study, we investigated: using MATLAB for mask designs; feasibility of using 1 µm Heidelberg mask maker to direct write patterns onto photoresist; using RIE processing to etch patterns into a silicon substrate; and the ability to tailor etch selectivity for precise fabrication. To determine etch rates and to obtain desired etch selectivity, parameters such as gas mixture, gas flow, and electrode power were studied. This process successfully demonstrates the ability to use gray-scale lithography and RIE for use in the study of micro-contacts. These results were used to produce a known engineered non-planer surface for testing micro-contacts. Surface structures are between 5 µm and 20 µm wide with varying depths and slopes based on mask design and etch rate selectivity. The engineered surfaces will provide more insight into contact geometries and failure modes of fixed-fixed micro-contacts.

Keywords: Grayscale, Direct Write, RIE, Micro-contacts

1. INTRODUCTION

The ability to develop 3D micro-structures is of great importance for increasing optical and electro-mechanical device performance. Previous technologies used multiple direct writing and photolithography steps, or customized equipment [1, 2, 3]. However, these technologies are restricted to a limited range of shapes and do not utilize batch processing cannot be utilized. Gray-scale technology has emerged enabling the development of arbitrary 3D micro-structures in various materials [3, 4, 5]. Use of gray-scale technology allows 3D shaping of silicon to be performed in a single photolithography step with subsequent dry etching [6].

Gray-scale lithography utilizes an optical mask patterned with varying intensities of gray pixels and spacing in Matlab. This optical mask combined with laser lithography allows a uniform intensity on the photoresist surface across the pattered region. Changing the size of the pattern and color of the gray, changes the intensity of the laser power; with each distinct power level given a gray level. The height profile in the photoresist after development (composed of photoresist gray levels) will depend upon the incident intensity, time of exposure, and photoresist contrast.

Gray-scale optical masks were designed and developed for a Heidelberg Mask Maker to produce various structures in positive photoresist for characterization of the profile. The gray levels were patterned on the optical mask by varying the size of structures. Due to machine limitations, only 100 of the 255 gray color variations are used to produce 100 unique height levels exist within the chosen method of patterning, yielding a stepped profile in the photoresist [7].

Also included on the optical masks were features to measure non-uniformity in the photoresist: fully exposed level heights and a conventional opaque region (no exposure). These features will give information on the uniformity of the photoresist spinning, where the gray level features include non-uniformity coming from all steps: photoresist spinning, exposure, and development [1].

*Ronald.coutu@afit.edu; phone (937) 255-3636 x7230

2. IMAGE CREATION

The first attempt at gray-scale lithography utilizing Matlab to create a gray-scale image, the first of the images can be seen in Figure 1. However, Matlab saved the image as a color .bmp format that resulted in blue-gray hues at different levels. These blue-gray hues caused an issue in the first test files that led to errors when writing into the photoresist, as shown in Figure 2. It was discovered that exporting the image into another program and saving in the correct format, a 24-bit bitmap image, fixed the error. What is also seen in this image is the border which should be fully exposed is not.
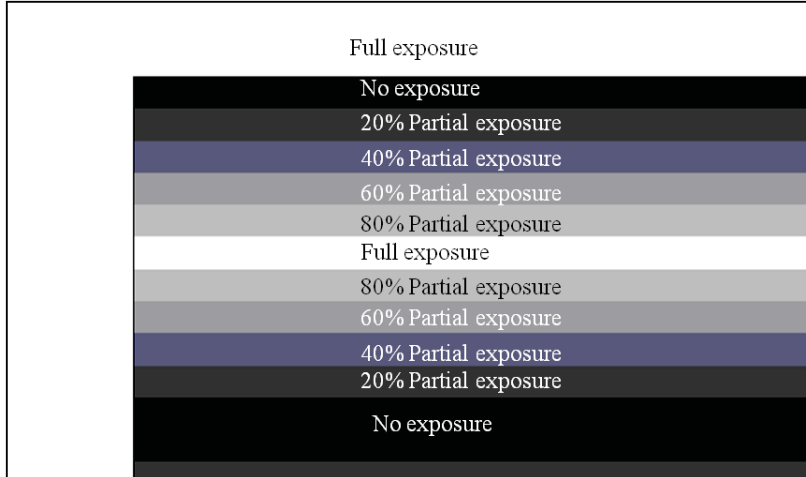
Figure 1. Image showing first 2D pyramid pattern attempted, this format of .bmp file, directly from Matlab, created blue-gray hues rather than only a gray-scale image.
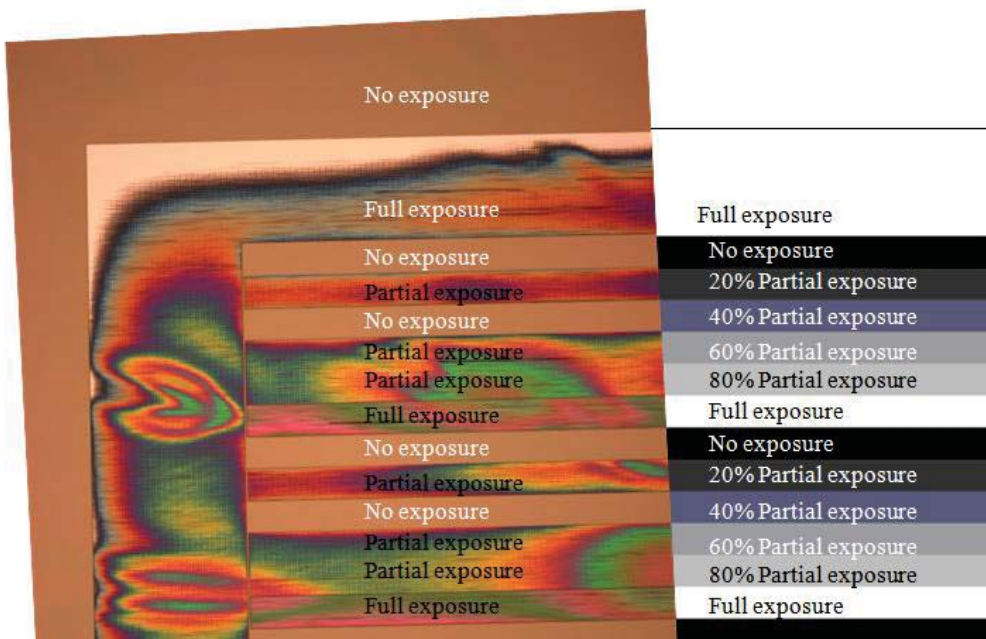
Figure 2. Image showing the caparison of the blue-gray hue with the resulting image in 1818 photoresist, this should be a step down from full height of photoresist down to no photoresist.

3. DIRECT WRITING INTO PHOTORESIST

Test were conducted to find the required power and exposure levels. This study was needed because the incorrect power level could lead to over or under exposure of the photoresist. After some testing it was found that a 14mW power at 10% allowed for exposure of 1.9 μm. Although this exposure power should be enough to fully expose the 1818 photoresist, due to colder than ideal temperatures, it was found that on some samples the power levels were too low to fully expose all of the photoresist.

3.1. Ramp pattern

Ramp design consisted of a ramp up from the substrate to max height, then immediately dropping back down to the substrate to start the ramp up again. This mimicked the layout of stepped ramp, thus the name "ramp". Figure 3(a) shows an example of this type of pattern in Matlab and the result of the direct write and (b) is the expected cross-section of the design. Figure 4 shows the surface profile measurement of this step function.

(a)

(b)
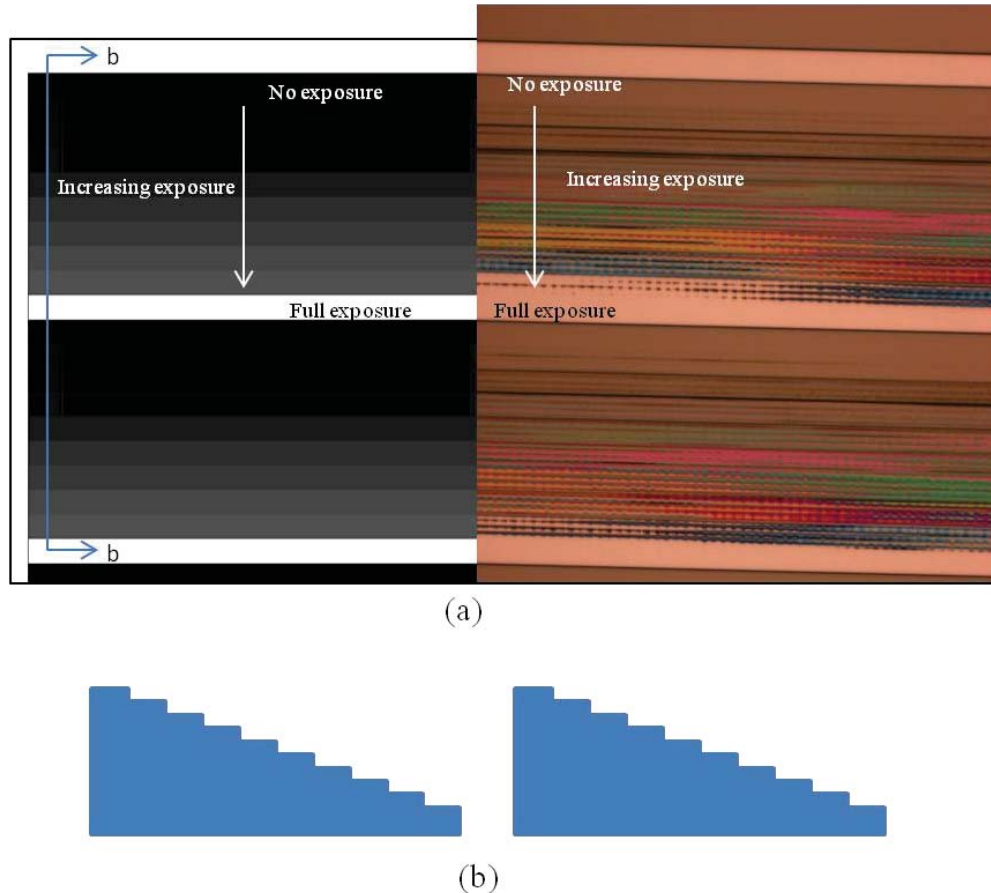
Figure 3. Ramp example (a) left is the Matlab image, right is the result of the direct write into 1818 photoresist, (b) is the expected cross-section of the designed along the line b-b.
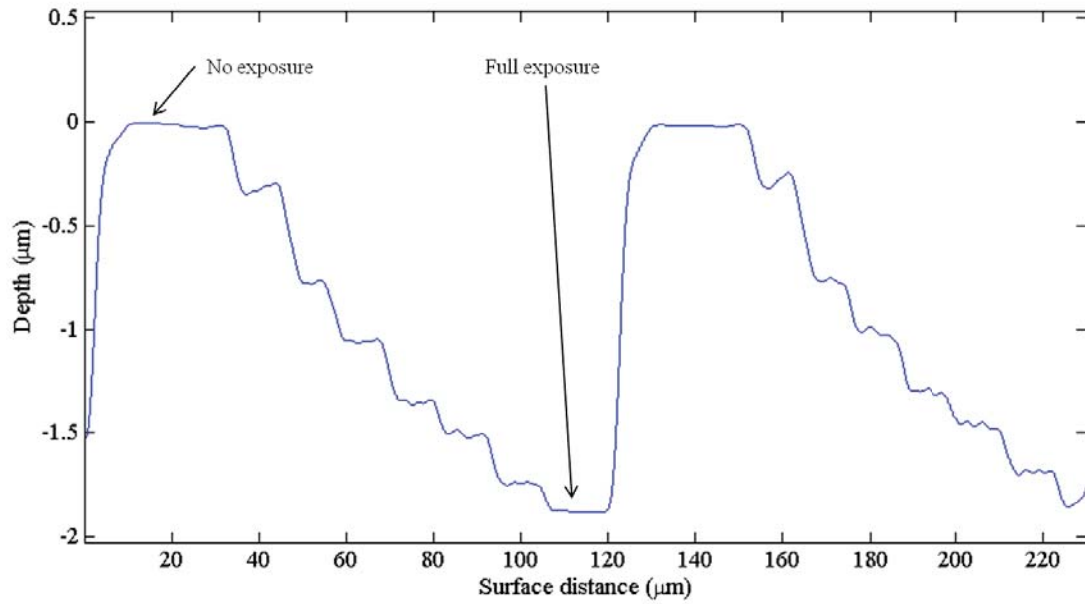
Figure 4. Surface profile plot of the ramp pattern created in Figure 3 along cross-section b-b.

3.2. 2D pyramid pattern

The 2D pyramid is a pattern that ramps up and down from the substrate, which creates a profile structure that looks like 2D pyramid. The profile was developed in Matlab to create a gray-scale image of varying line widths and steps. An example of this can be seen in Figure 5.
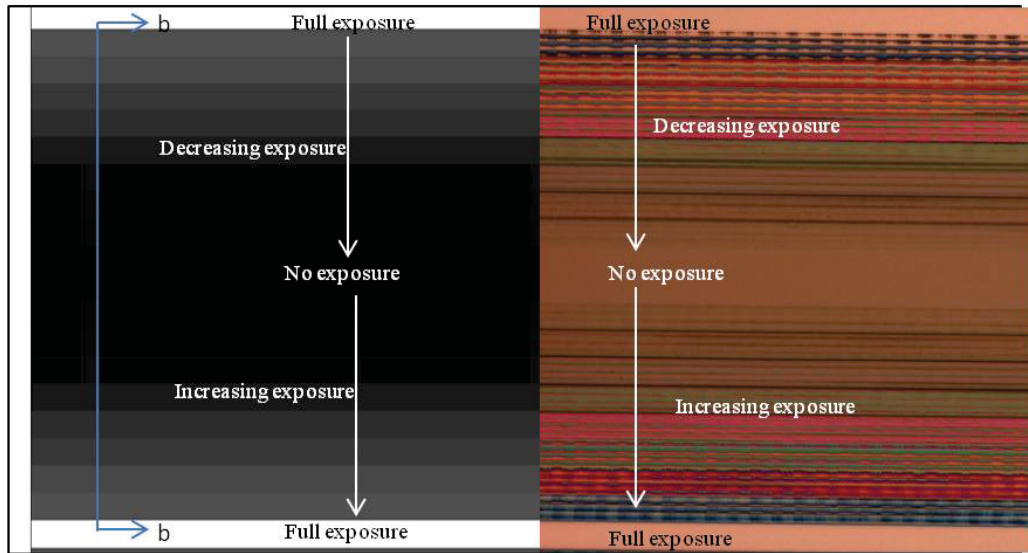
(a)

(b)

Figure 5. 2D pyramid example (a) left is the Matlab image, right is the result of the direct write into 1818 photoresist, (b) is the expected cross-section of the designed along the line b-b.
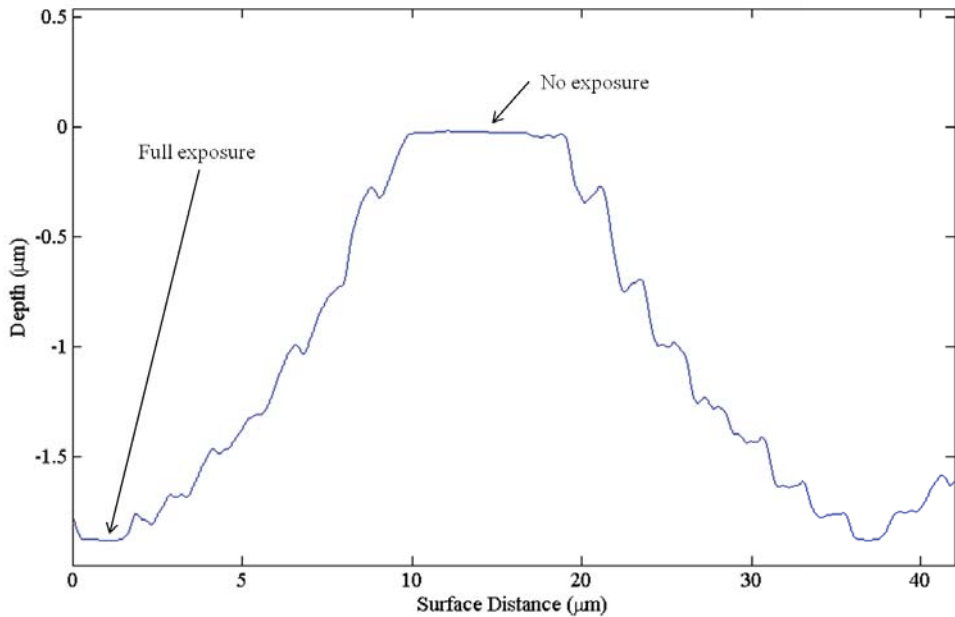
Figure 6. Plot of the 2D pyramid surface profile from the image in Figure 5 along cross-section b-b.

3.3. 3D Pyramid and Dip patterns

Additional variations that were created include a 3D pyramid and a dip pattern. Pyramids were created by ramp ramping from the substrate in the X and Y direction up to the full photoresist height, then ramp back down to the substrate. This pattern could be used to create a lower contact bump or bumps for the lower contact depending on the size and spacing of the pyramids. The dip is the opposite of the 3D pyramid, the structure is a ramp down in the X and Y direction from full photoresist to the substrate or a hole that could capture the upper hemispherical contact.
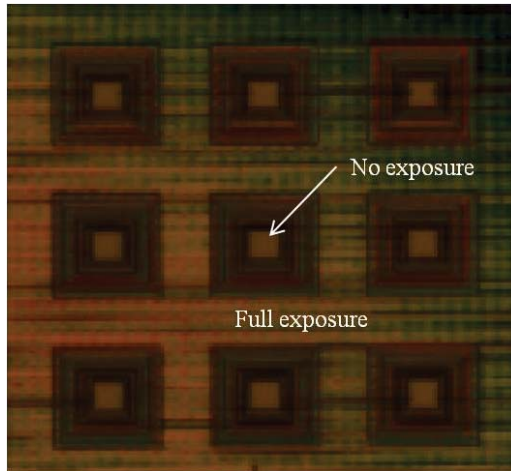
Figure 7. Example of the 3D pyramid structure created in photoresist. The 3D pyramid is formed by the stepping of fully exposed photoresist up to the top of the pyramid that is unexposed.
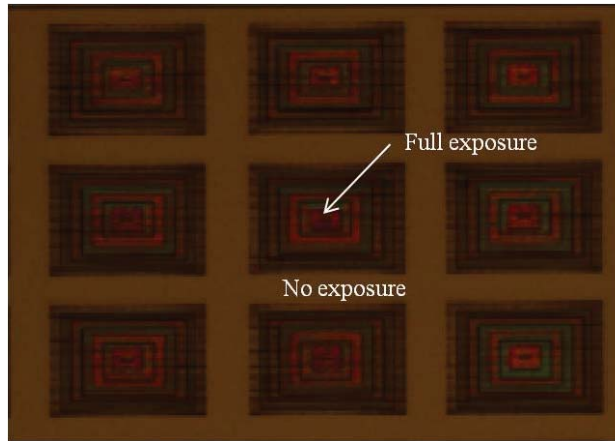
Figure 8. Example of the dip structure created in photoresist. The dip is the opposite of the 3D pyramid, where the center of the dip is fully exposed photoresist and is stepped up to the unexposed photoresist.

3.4. Re-flow of photoresist

As shown in the surface profiles, the stepping of power levels led to steps in the photoresists, but we required a smooth function. One attempt to obtain a smooth surface profile was with re-flowing of the photoresist. This method is used in many different applications, including creating micro-contacts bumps that this project supports. It was found that with 1818 photoresist, full melting of blocks of 1818 photoresist can be done at 150ºC at 15 mins [8]. After a few trials, it was determined that an acceptable amount of re-flow happened after 3 mins. Figure 9 plots the before and after re-flow results on the different pattern types.
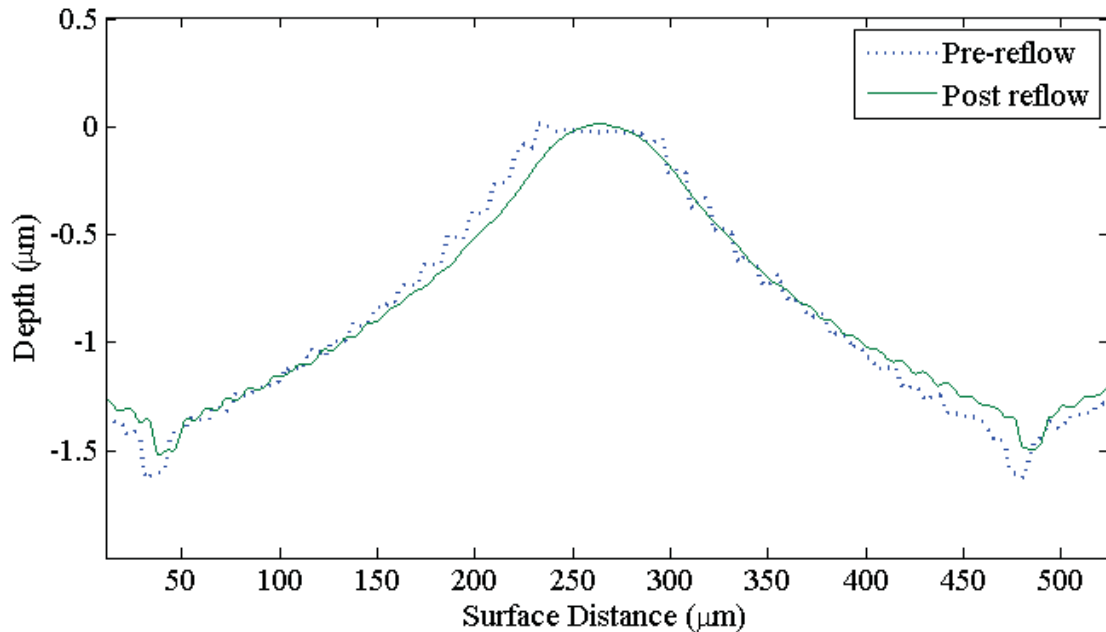
Figure 9. Plot of the 2D pyramid teeth surface profile before and after re-flow, demonstrating the smoothing of the steps on the slope.

3.5. Lower contact 2D pyramid

Tthe ultimate goal was to create a lower contact surface for use in micro-contact testing. The first attempt to design a lower contact structure was to input the design for the lower contact and superimpose the image into the existing design. This would ensure the size and spacing would be correct. Due to a limitation of the design software the images cannot be superimposed into the mask design, so another way to write these lower contacts were required. Two methods were attempted to create these lower pads with the 2D pyramid pattern, the first was an image to represent the entire die, this consisted of 16 beam, and therefore 16 lower contacts in a 5000 µm x 5000 µm area was needed. This was created with one large picture that was scaled to the correct overall size. Figure 10 shows a picture of one of these lower contact pads that worked out to be about 70 µm x 150 µm. The second method was by using the manual alignment of the mask maker to direct where these blocks should be located. This method was more labor intensive, but with the addition of some alignment marks on the wafer this allowed for precise alignment of the lower contact.
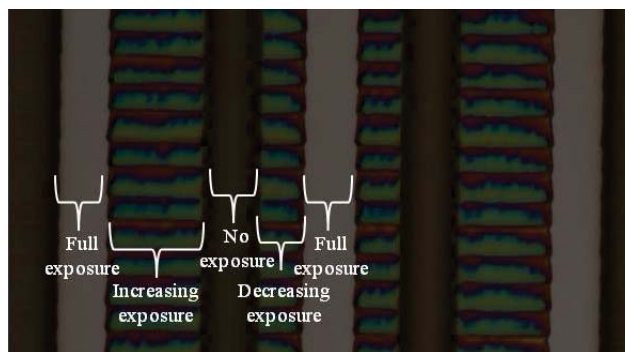
Figure 10. 2D pyramid design imposed into the overall die image, due to the laser direction from left to right, created the lines against the grain of the 2D pyramid.

4. ETCH STUDY

An etch study was conducted to determine etching parameters in the Trion RIE system that would allow for the most uniform and least selectivity of etching.

Table 1. Etch rates found by varying parameters in four tests, parameters held constant for each test is grayed, pressure was held at 200 Torr for all tests. Test 1 varied the flow of O_2. Test 2 varied the flow of both O_2 and SF_6. Test 3 varied the power level and test 4 varied the flow of SF_6.

Test	O_2 flow (SCCM)	SF_6 flow (SCCM)	Power level (W)	Delta Photoresist (μm)	Delta Silicon (μm)	Selectivity
1	52	52	100	0.3672	0.5961	1.62
	13	52	100	0.1068	2.0094	19.76
	6	52	100	0.1917	4.7848	24.96
	3	52	100	0.0895	10.995	112.79
2	52	52	100	0.4747	0.8744	1.84
	26	26	100	0.3956	0.8897	2.25
	13	13	100	0.3597	1.7137	4.76
3	52	52	200	0.9282	8.0864	8.71
	52	52	150	0.7768	5.5510	7.15
	52	52	100	0.4747	0.8744	1.84
	52	52	50	0.1057	0.0810	0.77
4	52	52	100	0.5850	1.1840	2.02
	52	39	100	0.5495	0.7198	1.30
	52	26	100	0.4789	0.2884	0.60
	52	13	100	0.5817	0.1275	0.21

As expected, decreasing the oxygen rate increased the effects of the SF_6 reactively etching the silicon. From the results of the 1st test, the lowest selectivity was determined to be when the O_2 and SF_6 percentages were equal. When changing the overall flow of both O_2 and SF_6 caused small changes in the selectivity. It was determined that the best option for selectivity desired is at 52 SCCM of SF_6 and O_2. Power variations also has an effect on the etch selectivity, with higher powers causing the selectivity to increase. From the results of this set of tests a power of 100 Watts was chosen. Finally varying the SF_6 follows the expectation of the flow of the SF6 controlling the etch rate of the silicon. This provides the key parameter when controlling the etching of the photoresist structures into the silicon wafers.

With the results of the etch study, the final selection of an O_2 and SF_6 Flow 52 SCCM, Pressure 200 Torr, Power 100 W, and an etch time of 1200 sec was the recipe needed to etch the gray-scale structure into the silicon substrate. The etch parameters were used on a 2D pyramid pattern to check the results of the etching of the pattern into a silicon substrate, the results of this etch is seen in Figure 11. The change in depth of the pattern due to the selectivity of the etch parameters can be seen in Figure 12

Figure 11. The results of etching of a 2D pyramid pattern into the silicon substrate, the image of the direct write pattern is on the right and the resulting etch into the silicon can be seen on the left.
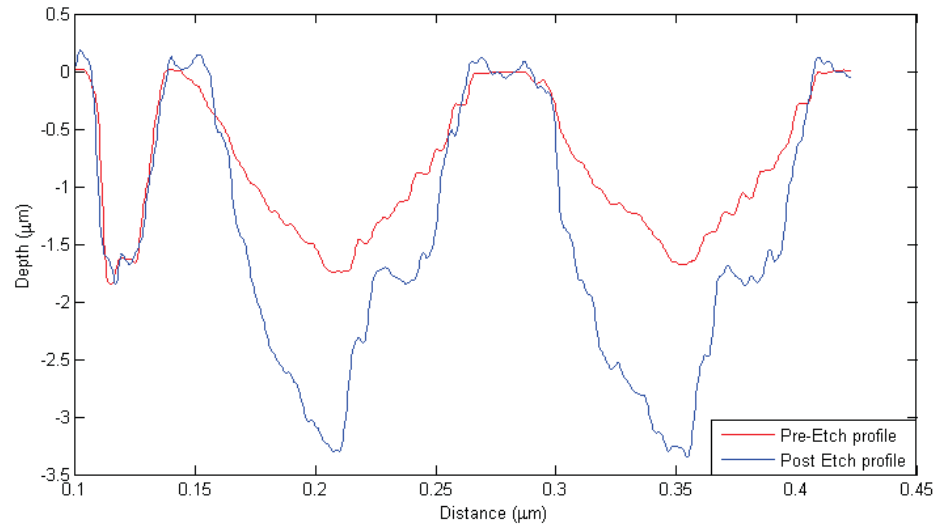
Figure 12. Showing the etch profile of the pattern shown in Figure 11. This demonstrates the close to 2:1 etch selectivity desired with the depth changing from ~1.8μm in the photoresist to ~3.4μm once etched into the silicon.

5. CONCLUSION

The ability to design and develop 3D microstructures is important for MEMS fabrication. Along with traditional fabrication techniques this paper presents how gray-scale lithography can be used in MEMs fabrication. It was shown that using the Heidelberg mask maker for patterning and RIE for etching, gray-scale lithography is achievable. Using this process, it will be possible to create many different 3D structures. This paper shows how these processes can be used to create profiles to a lower substrate that then can be processed with traditional surface micro-machining processes to create devices on non-planar surfaces.

ACKNOWLEDGEMENTS

REFERENCES

[1] C. Waits, B. Morgan, M. Kastantin and R. Ghodssi, "Microfabrication of 3D silicon MEMS structures using gray-scale lithography and deep reactive ion etching," Sensors and Actuators A: Physical, vol. 119, pp. 245-253, 2005.

[2] C. Beuret, G.-A. Racine, J. Gobet, R. Luthier and N. de Rooij, "Microfabrication of 3D multidirectional inclined structures by UV lithography and electroplating," in Micro Electro Mechanical Systems, 1994, MEMS'94, Proceedings, IEEE Workshop on, 1994.

[3] Y. Oppliger, P. Sixt, J. Stauffer, J. Mayor, P. Regnault and G. Voirin, "One-step 3D shaping using a gray-tone mask for optical and microelectronic applications," Microelectronic Engineering, vol. 23, pp. 499-454, 1994.

[4] T. J. Suleski and D. C. O'Shea, "Gray-scale masks for diffractive-optics fabrication: I. Commercial slide imagers," Appl. Opt., vol. 34, pp. 7507--7517, 1995.

[5] B. Wagner, H. Quenzer, W. Henke, W. Hoppe and W. Pilz, "Microfabrication of complex surface topographies using grey-tone lithography," Sensors and Actuators A: Physical, vol. 46, pp. 89-94, 1995.

[6] T.-K. Chou and K. Najafi, "Fabrication of out-of-plane curved surfaces in Si by utilizing RIE lag," in Micro Electro Mechanical Systems, 2002. The Fifteenth IEEE International Conference on, 2002.

[7] HEIDELBERG INSTRUMENTS μPG 101 User Manual, Heidelberg Instruments, 2008, p. 16.

[8] H. Wu, T. W. Odom and G. M. Whitesides, "Reduction photolithography using microlens arrays: applications in gray scale photolithography," Analytical chemistry, vol. 74, pp. 3267-3273, 2002.

Appendix C: Polymumps and Sandia layout

The following a discussion of my Polymumps and sandia layouts.

All designs have a metal upper contact and a Poly0 lower contact. All beams have the same hinge structure and the same length of $400\mu m$ with 4 Au contact pads to wire bond. The beam and contact bump construction has 6 variety. Those varieties are shown below in the following figures.
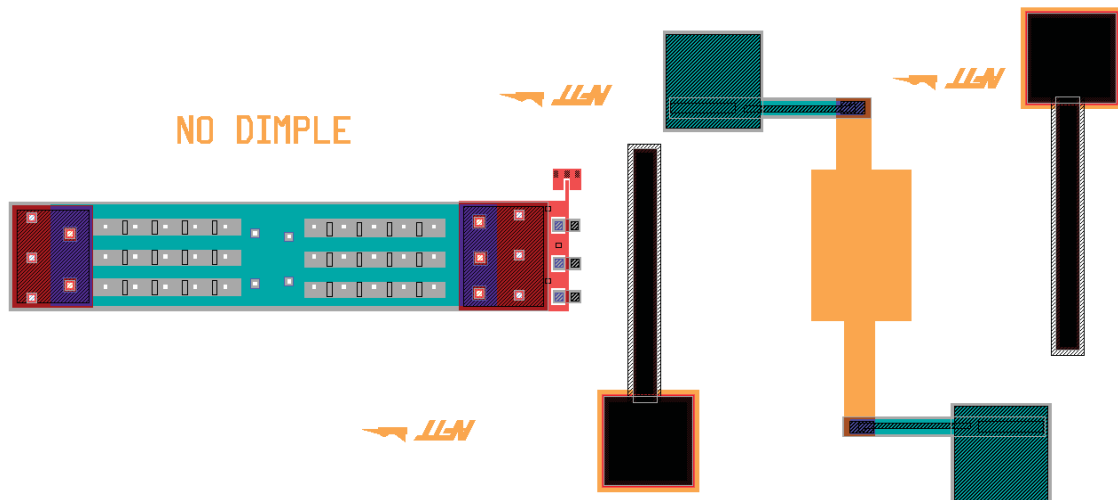
Figure C.1: Beam made of Poly 1 with no dimple cut to make a contact bump
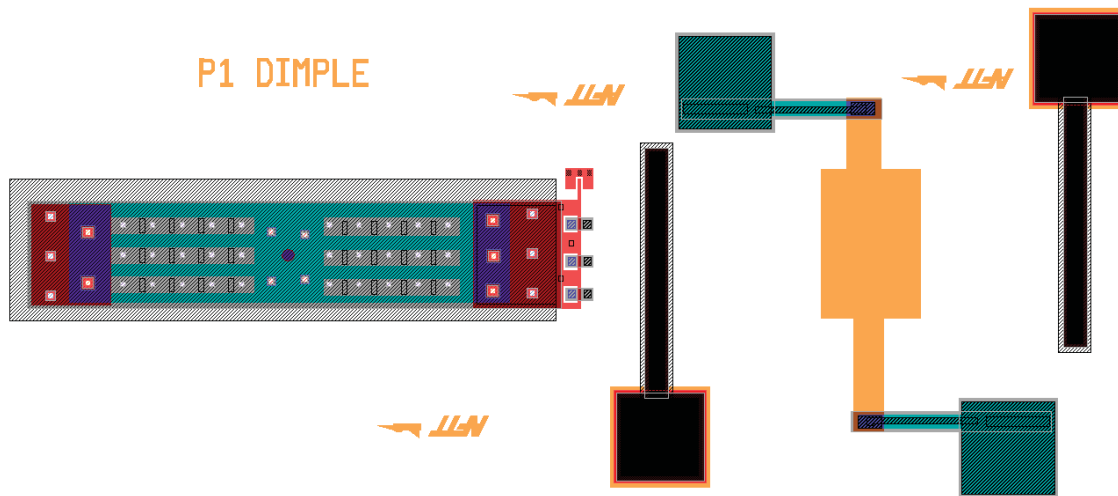
Figure C.2: Beam made of Poly 1 with large area of dimple cut to make a contact bump

P2 W/DIMPLE
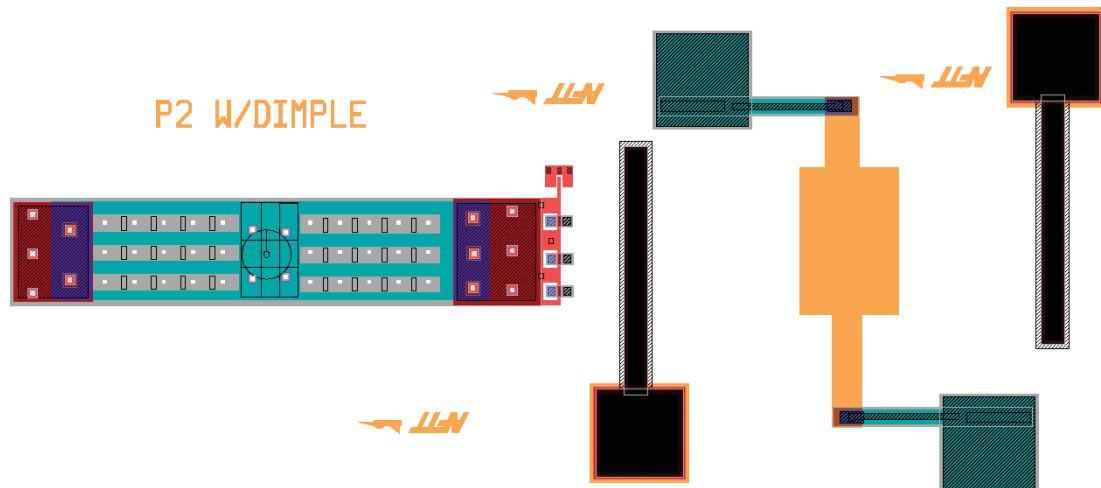
Figure C.3: Beam made of Poly 2 with large area of dimple cut to make a contact bump

P1/P2 W/ DIMPLE
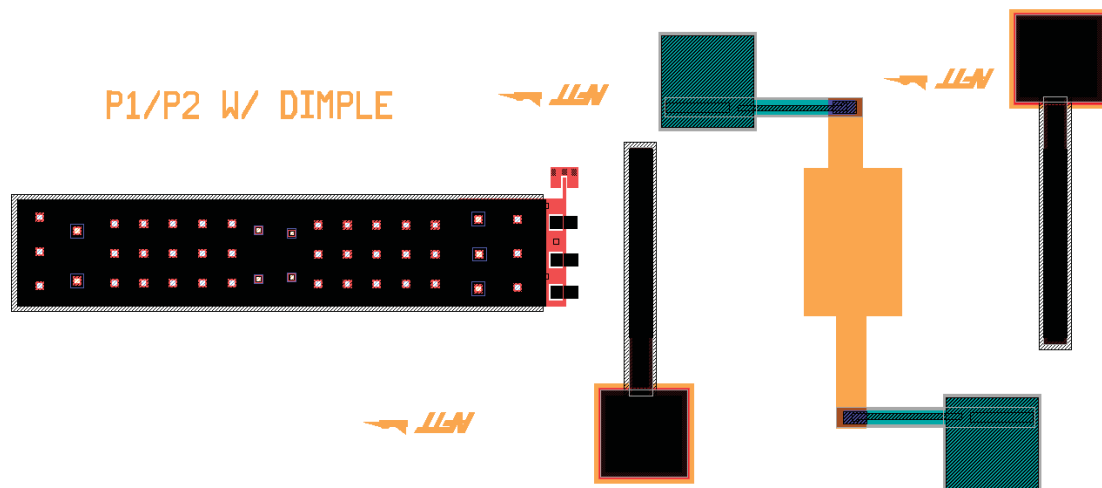
Figure C.4: Beam made of Poly 1 and 2 with large area of dimple cut to make a contact bump
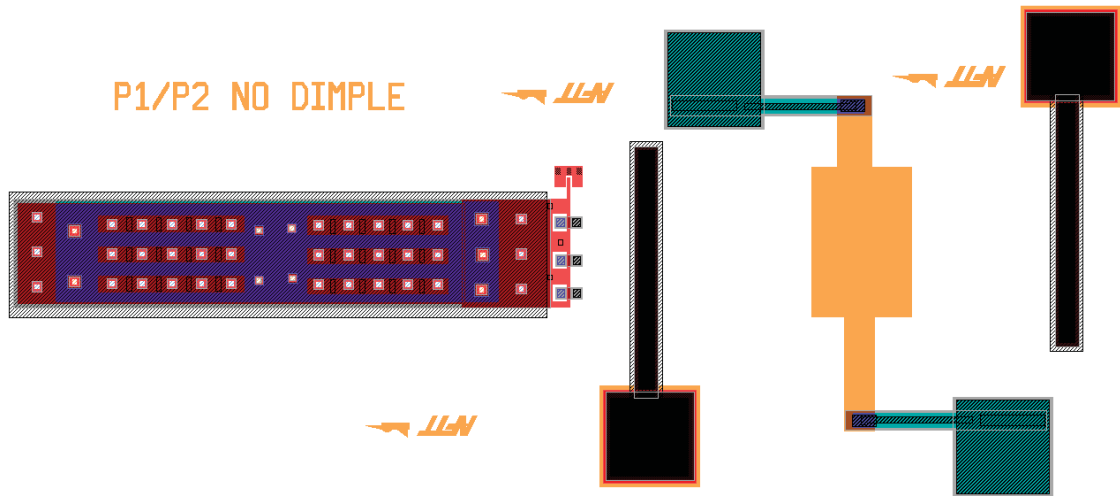
Figure C.5: Beam made of Poly 1 and 2 with no dimple cut to make a contact bump
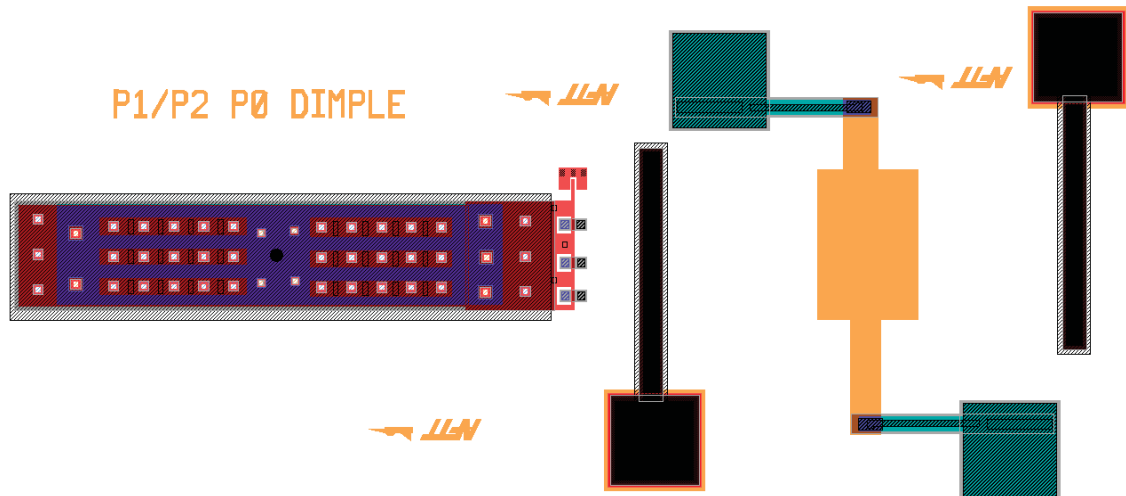
Figure C.6: Beam made of Poly 1 and 2 with dimple made with poly0 and using the conformal features of PolyMUMPs to transfer the design to the Poly 1-2 beam.

Similar to the the PolyMUMPs design, a design was submitted to Sandia as well.

That design can be seen below.
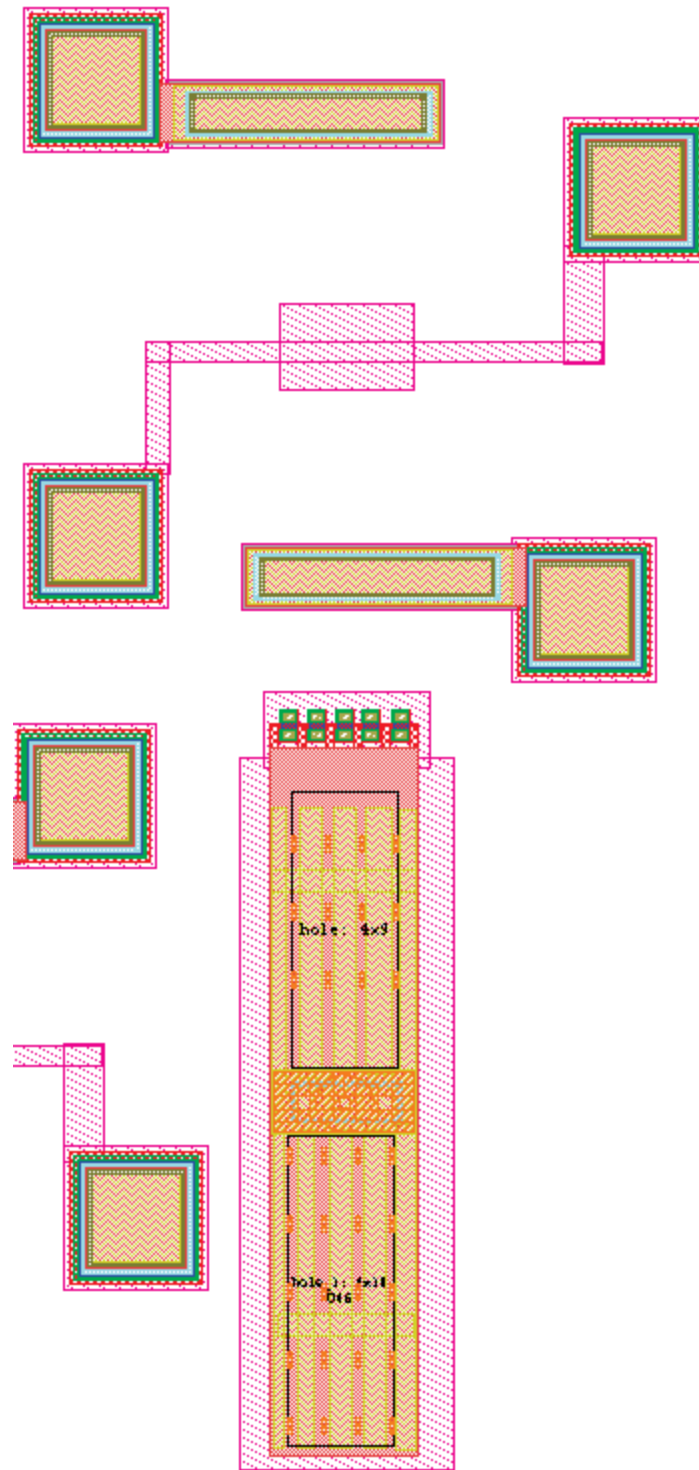
Figure C.7: Beam made using the Sandia Summit design process. This design has not ben built and its success as a useable design is still unknown.

Appendix D: Masks layout

The following a discussion the mask layouts used in this research. The mask set consisted of 4 masks to construct the fixed-fixed beam. Mask 1 was the bottom metal and alignment marks. Mask 2 was for exposure of the anchors for the fixed-fixed beam. Mask 3 consisted of the 4 different types of contacts, a single $4\mu m$ radius contact bump, a single $6\mu m$ radius contact bump, a single $8\mu m$ radius contact bump and 3 $6\mu m$ radius contact bumps. Mask 4 was for the construction of the beams, beam lenghts included $350\mu m$. $400\mu m$, $450\mu m$, and $500\mu m$ length beams. An overview of entire mask can be seen in Figure D.1.

This mask set improved on previous designs in a few areas, first is the abundance of large alignment marks in the center and radiating out from the center. These allowed for fast and accurate alignment of all masks. This set also limited the number of contact bump types to allow for easy identification of contact bump radius type. Figure D.2 shows the center and radiating alignment marks, as well as the 4 different types of contact radius.

Another feature of this mask set is the movement of the wire bond pads to the edge of the reticle. This design was important in a few ways. First in previous designs the structures required wire bonding close to the structure, which caused some wire bonds to cross over other structures in the carrier. This limited the number of devices that could be tested to 4 or 5 devices per carrier. In this improved design with the pads located around the edge, all devices could be wire bonded without interfering with the testing of other devices. This increased the yield of each carrier tested by 400% and allowed for testing of all 16 devices per redicle and the limiting factor on devices is the number of pins on the carrier. These reticles also were designed to fit inside the carrier and spaced to allow for dicing of devices. Figure D.3 shows a single reticle.
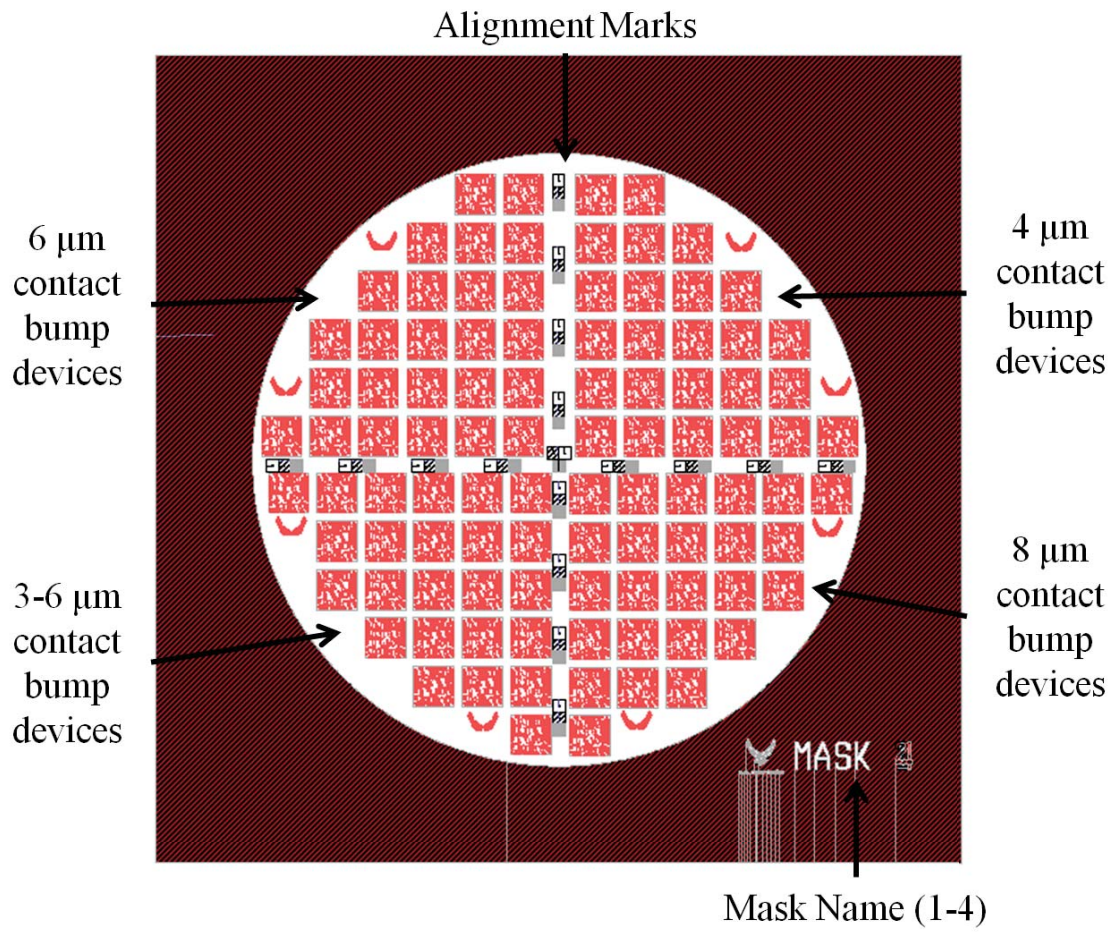
Figure D.1: Overview of the 4 masked used in this research

Also seen in Figure D.3 and Figure D.4 is the abundance of labels. This allows the tester to identify the contact radius type (upper corners of the reticle), the location in the quadrant (lower corners of the reticle) and labels of the beam length above each beam, this is useful when taking microscope or SEM images. A close-up of a single beam and pointing out the features of each mask is can be seen in Figure D.4.

With this improved mask set it was easy to build, test, and identify samples during this research.

6 um contact bump devices

4 um contact bump devices

Alignment Marks

3-6 um contact bump devices

8 um contact bump devices
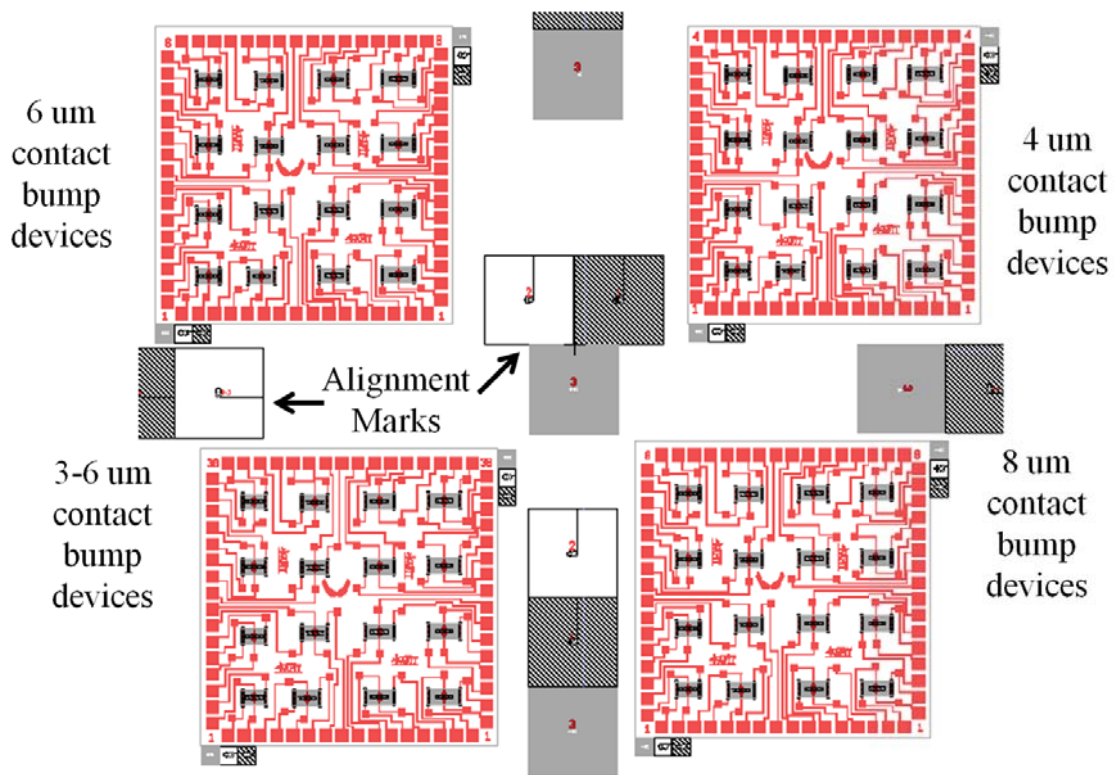
Figure D.2: Image of layout highlighting the center of the mask, with major highlights labeled
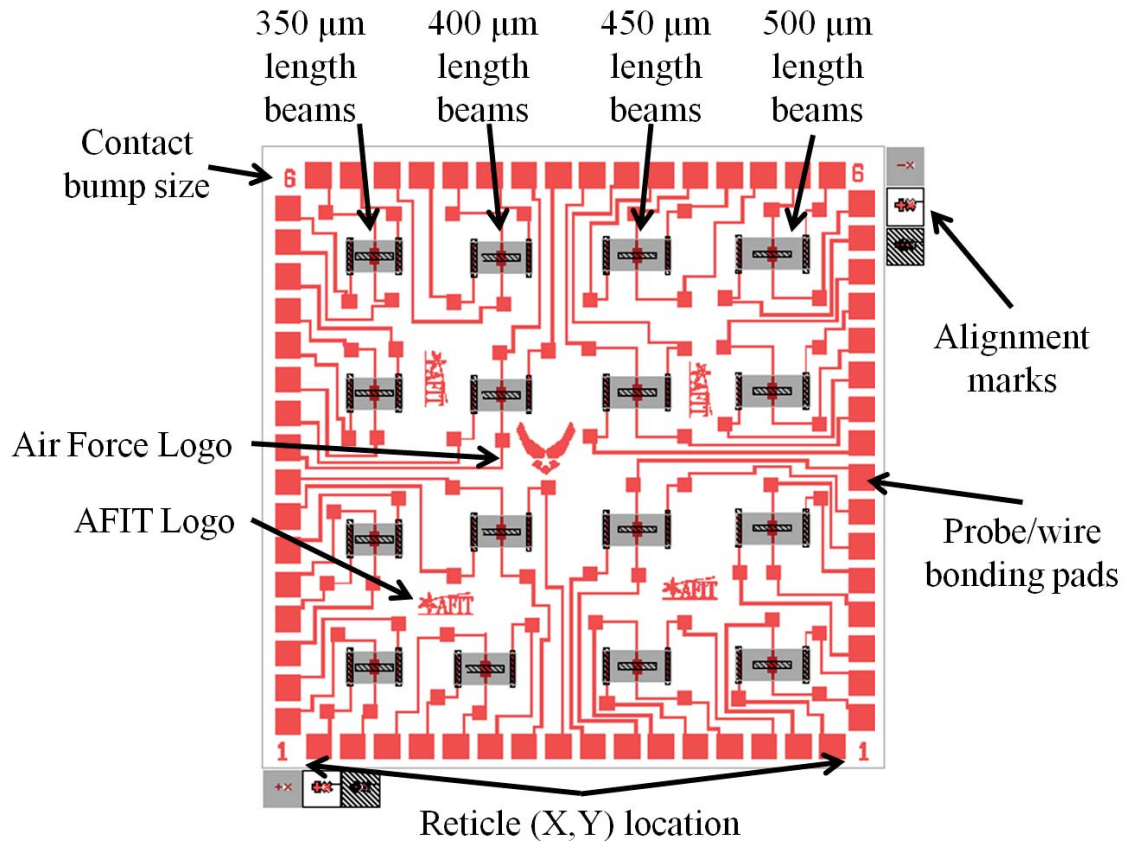
Figure D.3: Image of layout highlighting a single reticle, with major highlights labeled
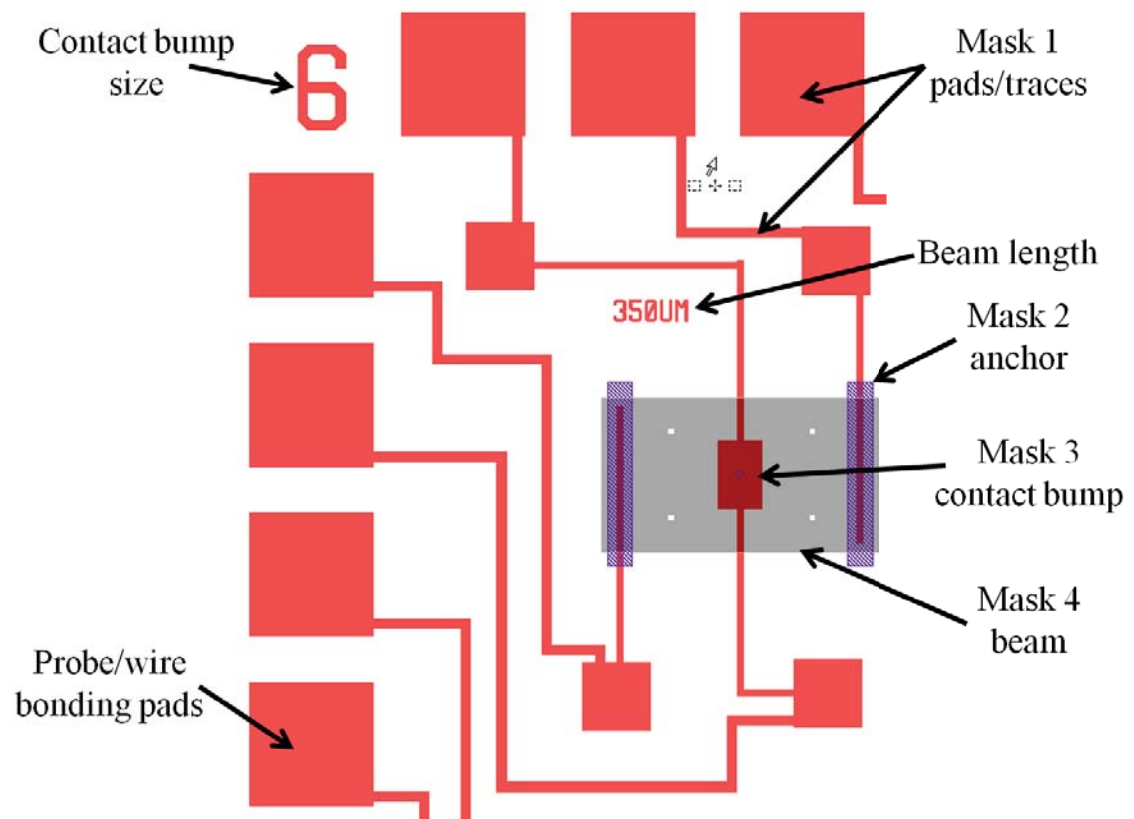
Figure D.4: Image of layout highlighting a single beam, with major highlights labeled

Appendix E: Process Followers

The following is a copy of process followers used in this research to created the Fixed-Fixed beams.

Init.	Process Step	Notes	Date Time
	INSPECT WAFER: ☐ Note any defects	**Start Date** **Start Time**	
	SOLVENT CLEAN WAFER: ☐ 30 sec acetone rinse at 500 rpm ☐ 30 sec methanol rinse at 500 rpm ☐ 30 sec isopropyl alcohol rinse at 500 rpm ☐ 30 sec DI water rinse at 500 rpm ☐ Dry with nitrogen at 500 rpm ☐ Dry wafer with nitrogen on clean texwipes		
	DEHYDRATION BAKE: ☐ 1 min 110°C hot plate bake		
	SF-11 RESIST COAT: ☐ Flood wafer with SF-11 ☐ 30 sec spin at 4,000 rpm - Hold swab between wafer and Al foil during spin to capture excess photoresist which spins like 'cotton candy' ☐ 2 min 200°C hot plate bake		
	1805 COAT: ☐ Flood wafer with 1805 ☐ 4 sec spread at 500 rpm ☐ 30 sec spin at 4,000 rpm, ramp=200 ☐ 75 sec 110°C hot plate bake ☐ Use acetone to remove 1805 on backside		
	EXPOSE 1805 WITH Bottom Metal MASK #1: ☐ No alignment for first level mask needed, however mask should be straight ☐ 4.0 sec exposure using EVG 620; 4 sec exposure using MJB3		
	1805 DEVELOP: ☐ 40 sec develop with 351:DI (1:5), use a spin/stop/spin/stop method at 500 rpm ☐ 30 sec DI water rinse at 500 rpm ☐ Dry with nitrogen at 500 rpm ☐ Dry wafer with nitrogen on clean texwipes		
	INSPECT RESIST: ☐ Inspect photoresist under microscope, look for fringe patterns indicating residual SF-11		
	SF-11 EXPOSURE (~1.5 um / cycle): ☐ Place wafer in center of circle ☐ 300 sec DUV exposure with OAI DUV		
	SF-11 DEVELOP: ☐ 60 sec bucket develop with SAL 101 ☐ 30 sec DI rinse at 500 RPM or hold under DI faucet for 30 sec ☐ Dry with nitrogen at 500 RPM ☐ Dry wafer with nitrogen on clean texwipes		
	INSPECT RESIST: ☐ Inspect photoresist under microscope		
	TENCOR MEASUREMENT: ☐ Measure metal step height T _____ C _____ B _____		
	ASHER DESCUM ☐ 4 min, 75W, LFE Barrel Asher - Immediately before Evaporation		
	BOTTOM METAL DEPOSITION ☐ *Evaporate* 200 Å Ti / 2800 Å Au		

Init.	Process Step	Notes	Date Time

Init.	Process Step	Notes	Date Time
	LIFT-OFF METAL: ☐ Heat 1165 remover to 90°C (set hot plate to 170°C) ☐ Use packing tape to lift off *evaporated* Au/Ti ☐ 5 min ultrasonic bath in acetone ☐ 30 sec acetone rinse at 500 rpm ☐ 30 sec isopropyl alcohol rinse at 500 rpm ☐ 30 sec DI water rinse at 500 rpm ☐ Dry with nitrogen at 500 rpm ☐ 5 min soak in 1165 at 90° C ☐ 30 sec DI rinse at 500 rpm ☐ Dry wafer with nitrogen on clean texwipes		
	INSPECT METAL: ☐ Inspect metal under microscope		
	ASHER DESCUM ☐ 4 min, 150W, LFE Barrel Asher		
	TENCOR MEASUREMENT: ☐ Measure metal step height T _____ C _____ B _____		
	Electrical Isolation Test: ☐ Verify electrical isolation between contact pads		

Wafer	Purpose	Masks	Process	Print Date
Wafer ID	**μ-contacts**	*Anchor/Bump*	**Anchor & Bump**	**2/3/2014**

Init.	Process Step	Notes	Date Time
	DEHYDRATION BAKE: ☐ 5 min 110°C hot plate bake	**Start Date** **Start Time**	
	FIRST SF-11 (PMGI) COAT: ☐ Flood wafer with SF-11 ☐ 30 sec spin at 4,000 rpm, ramp= 999, 5 sec spread=500 ☐ 2 min 200º hot plate bake		
	SECOND SF-11 (PMGI) COAT: ☐ Flood wafer with SF-11 ☐ 30 sec spin at 4,000 rpm ☐ 2 min 200º hot plate bake		
	Third SF-11 (PMGI) COAT: ☐ Flood wafer with SF-11 ☐ 30 sec spin at 4,000 rpm ☐ 2 min 200º hot plate bake		
	1805 COAT: ☐ Flood wafer with 1805 ☐ 4 sec spread at 500 rpm ☐ 30 sec spin at 4,000 rpm, ramp=200 ☐ 75 sec 110°C hot plate bake ☐ Use acetone to remove 1805 on backside		
	EXPOSE 1805 WITH Contact Bump MASK #3: ☐ Align to alignment mark "2" on bottom metal alignment marks ☐ 4 sec exposure using EVG 620; 4 sec exposure using MJB3		
	1805 DEVELOP: ☐ 40 sec develop with 351:DI (1:5), use a spin/stop/spin/stop method at 500 rpm ☐ 30 sec DI water rinse at 500 rpm ☐ Dry with nitrogen at 500 rpm ☐ Dry wafer with nitrogen on clean texwipes		
	INSPECT RESIST: ☐ Inspect photoresist under microscope		
	TENCOR MEASUREMENT: ☐ Measure metal step height T _____ C _____ B _____		
	PARTIAL DUV EXPOSURE (~0.7um BUMP DEPTH): ☐ 60 sec DUV exposure @ 35 mW/cm² , 254 nm		
	SF-11 DEVELOP: ☐ 60 sec bucket develop with SAL 101 ☐ 30 sec DI rinse at 500 RPM ☐ Dry with nitrogen at 500 RPM ☐ Dry wafer with nitrogen on clean texwipes		
	INSPECT RESIST: ☐ Inspect photoresist under microscope		
	TENCOR MEASUREMENT: ☐ Measure metal step height T _____ C _____ B _____		

Init.	Process Step	Notes	Date Time
	REMOVE 1805: ☐ ~12 sec acetone rinse at 500 rpm *As Needed* ☐ 30 sec isopropyl alcohol rinse at 500 rpm ☐ 30 sec DI rinse at 500 rpm ☐ Dry with nitrogen at 500 rpm ☐ Dry wafer with nitrogen on clean texwipes	When using Ace, the 1805 in the center of wafer will open up, immediately apply IPA to center and concurrently use ace to remove remaining 1805	
	INSPECT RESIST: ☐ Inspect photoresist under microscope		
	TENCOR MEASUREMENT: ☐ Measure metal step height T _____ C _____ B _____		
	1805 COAT: ☐ Flood wafer with 1805 ☐ 4 sec spread at 500 rpm ☐ 30 sec spin at 4,000 rpm, ramp =200 ☐ 75 sec 110ºC hot plate bake ☐ Use acetone to remove 1805 on backside		
	EXPOSE 1805 WITH Anchor MASK #2: ☐ Align to alignment mark "1" on the bottom metal alignment marks ☐ 4.0 sec exposure using EVG 620; 4 sec exposure using MJB3		
	1805 DEVELOP: ☐ 40 sec develop with 351:DI (1:5), use a spin/stop/spin/stop method at 500 rpm ☐ 30 sec DI water rinse at 500 rpm ☐ Dry with nitrogen at 500 rpm ☐ Dry wafer with nitrogen on clean texwipes		
	INSPECT RESIST: ☐ Inspect photoresist under microscope		
	FIRST DUV EXPOSURE (~1.5 um / cycle): ☐ Place wafer in center of circle ☐ 200 sec DUV exposure with OAI DUV		
	SF-11 DEVELOP: ☐ 60 sec bucket develop with SAL 101 ☐ 30 sec DI rinse at 500 RPM ☐ Dry with nitrogen at 500 RPM ☐ Dry wafer with nitrogen on clean texwipes		
	INSPECT RESIST: ☐ Inspect photoresist under microscope, look for fringe patters indicating residual SF-11		
	SECOND DUV EXPOSURE (~1.5 um / cycle): ☐ Place wafer in center of circle ☐ 200 sec DUV exposure with OAI DUV		
	SF-11 DEVELOP: ☐ 60 sec bucket develop with SAL 101 ☐ 30 sec DI rinse at 500 RPM ☐ Dry with nitrogen at 500 RPM ☐ Dry wafer with nitrogen on clean texwipes		
	INSPECT RESIST: ☐ Inspect photoresist under microscope, look for fringe patters indicating residual SF-11		

Init.	Process Step	Notes	Date Time
	TENCOR MEASUREMENT: ☐ Measure metal step height T _____ C _____ B _____		
	REMOVE 1805: ☐ ~12 sec acetone rinse at 500 rpm *As Needed* ☐ 30 sec isopropyl alcohol rinse at 500 rpm ☐ 30 sec DI rinse at 500 rpm ☐ Dry with nitrogen at 500 rpm ☐ Dry wafer with nitrogen on clean texwipes	When using Ace, the 1805 in the center of wafer will open up, immediately apply methanol to center and concurrently use ace to remove remaining 1805	
	INSPECT RESIST: ☐ Inspect photoresist under microscope		
	TENCOR MEASUREMENT: ☐ Measure metal step height T _____ C _____ B _____		
	ASHER DESCUM ☐ 8 min, 75W, LFE Barrel Asher		
	TENCOR MEASUREMENT: ☐ Measure metal step height T _____ C _____ B _____		
	ANCHOR AND BUMP REFLOW & INSPECT WAFER: ☐ 10 sec 270ºC hot plate bake		
	TENCOR MEASUREMENT: ☐ Measure metal step height T _____ C _____ B _____		

Wafer	Purpose	Masks	Process	Print Date
Wafer ID	**µ-contacts**	*Bridge Metal*	**Bridge Metal & Release**	**2/3/2014**

Init.	Process Step	Notes	Date Time
	ASHER DESCUM: ☐　4 min, 75W, LFE Barrel Asher	**Start Date** **Start Time**	
	SPUTTER CONTACT METAL LAYER: ☐　Sputter 2000 Å Au using Discovery-18		
	AZ3350 COAT: ☐　Flood wafer with AZ3350 ☐　4 sec spread at 300 rpm ☐　30 sec spin at 3,000 rpm, ramp=500 ☐　5 min 110°C hot plate bake		
	EXPOSE AZ3350 WITH Bridge Metal MASK 4: ☐　Align to alighment mark #3 on bottom metal alignment marks ☐　7 sec exposure using EVG 620; 22 sec exposure for AFRL		
	AZ3350 DEVELOP: ☐　60 sec develop with 300MIF, use a spin/stop/spin/stop method at 500 rpm ☐　30 sec DI water rinse at 500 rpm ☐　Dry with nitrogen at 500 rpm ☐　Dry wafer with nitrogen on clean texwipes		
	INSPECT RESIST: ☐　Inspect photoresist under microscope		
	TENCOR MEASUREMENT: ☐　Measure metal step height T _____　　　　C _____　　　　B _____		
	SOLVENT BAKE: ☐　Bake in 90ºC oven for 20 min		
	ASHER DESCUM ☐　4 min, 75W, LFE Barrel Asher		
	Electroplate BRIDGE METAL LAYER: ☐　Turn on bath and allow to heat up to 138°C ☐　Electroplate 2.4um Au using AFRL Electroplate, settings as follows: ☐　　I=0.02, V=2.5, Freq=100, On=4ms, Off=6ms, AmpHour=0.11 Ah		
	TENCOR MEASUREMENT: ☐　Measure metal step height T _____　　　　C _____　　　　B _____		
	REMOVE AZ3350: ☐　30 sec acetone rinse at 500 rpm ☐　30 sec isopropyl alcohol rinse at 500 rpm ☐　30 sec DI water rinse at 500 rpm ☐　Dry with nitrogen at 500 rpm ☐　Dry wafer with nitrogen on clean texwipes		
	ASHER DESCUM ☐　2 min, 75W, LFE Barrel Asher		
	CONTACT METAL ETCH: ☐　40 sec Au Etchant, agitated ☐　30 sec DI water rinse (stops the etching) ☐　Dry with nitrogen on clean texwipes		
	INSPECT CONTACT METAL: ☐　Make sure contact metal layer is completely removed		

Init.	Process Step	Notes	Date Time
	STRIP SF-11 SACRIFICIAL LAYER (RELEASE PROCESS): ☐ Do NOT place devices in ultrasonic bath ☐ Place devices in 1165 at room temperature ☐ Heat 1165 remover to 90ºC (set hot plate to 120ºC) ☐ 35 min soak in 1165 at 90ºC ☐ Wet transfer from 1165 beaker to 1st IPA in petri dish, 30 sec soak ☐ Wet transfer to 2nd IPA in petri dish, 30 sec soak ☐ Wet transfer to 3rd IPA in petri dish, 30 sec soak ☐ Wet transfer to 1st methanol in petri dish, 30 sec soak ☐ Wet transfer to 2nd methanol in petri dish, 30 sec soak ☐ Wet transfer to 3rd methanol in petri dish, 30 sec soak ☐ Fill CO2 dryer chamber with enough methanol to cover the wafer ☐ Remove wafer from 4th methanol dish and place in CO2 dryer chamber ☐ Immediately cover CO2 dryer and start process		
	ASHER DESCUM ☐ 5 min, 75W, LFE Barrel Asher		

Appendix F: Labview

The following is a copy of the labview guide created in previous research and updated to reflect changes made to the program [8].

Lab View

INITIAL CONTACT TEST INFORMATION

The following figure shows the initial contact test program block diagram.
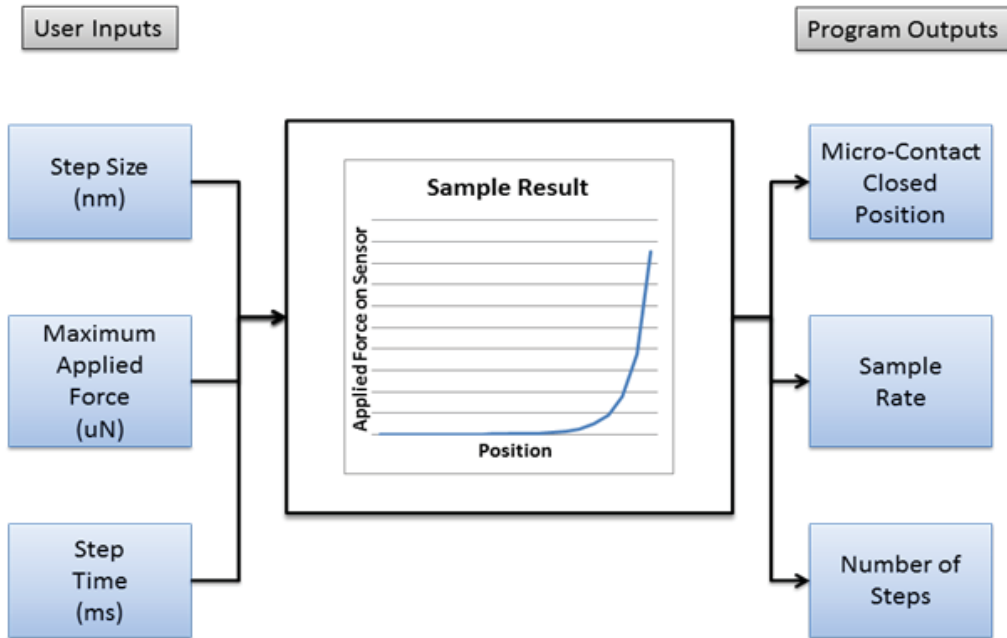
Figure 1 Initial Contact Test Program Block Diagram

Specification of the step size allows for variances in micro-contact fabrication and design. As the gap between the micro-contacts may be designed at varying distances, the ability to set a step size explicitly prevents an application of force to the micro-structure which could cause plastic deformation. Setting the maximum applied force provides protection from exceeding the limits of the force sensor as well as the micro-structure. In order to have a more controlled approach by the force sensor to the micro-contact, the user may set a time interval at each step. At each step, a reading for the applied force, contact voltage, and contact current takes place. The values of the readings are then stored in an excel file upon completion of the test.

The output of the initial contact test program is the applied force and position of the sensor required for a closed connection of the micro-contact. The sample rate is provided in order to verify the chosen time at each step and number of steps taken. The determination of a closed connection is performed by examining the recorded data for a real result in micro-contact resistance. The applied force and position required for a real result in micro-contact resistance are then offsets so that the true applied contact force is calculated. The position and applied force values are inputs for the next chosen type of testing: hot-switch or cold-switch.

HOT-SWITCH TEST INFORMATION

The following figure shows the hot-switch program block diagram.
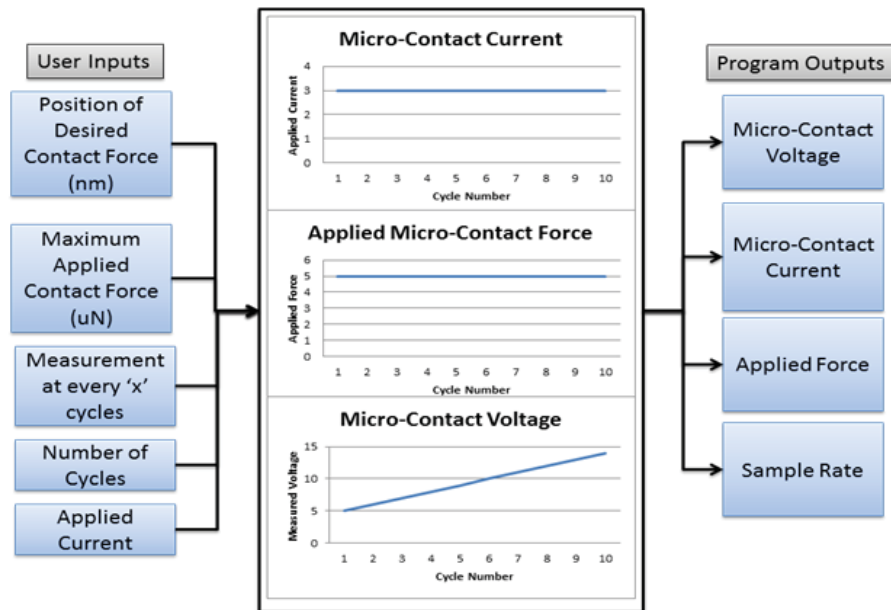
Figure 2 Hot-Switch Program Block Diagram

Most important for the hot-switch testing is knowing the position the force sensor needs to be in order to apply the appropriate and desired contact force. Setting the maximum applied contact force establishes a force limit to protect the force sensor and the micro-contact structure.

This limit is checked every measurement to ensure compliance. If the force applied is greater than the limit, which can be caused by position drift, then the program reduces the position accordingly to apply the desired contact force. Position drift occurs through the repeated commands sent to the piezo control unit. Due to systematic errors in converting from digital to analog control signals, i.e. lab view to piezo controller to piezo motor, the position requested by the user is given to the controller but slight variances in the piezo motor actuation capability cause a drift in position. To raise the sample rate, the user may input the number of cycles between measurements. The time in which it takes one iteration of an actuation and measurement decreases without having to take a measurement. If desired, this feature allows the user to see only those data points after so many actuations. Specification of the number of cycles to perform and current to apply to the micro-contact allows for a characterization of the micro-contact for the given performance requirements.

The output of the hot-switch program is an excel file which contains the applied current and force, measured voltage, and calculated micro-contact resistance. The sample rate is also provided for the interest of rate of actuation. The information provided from this test can then be used to characterize the performance of the micro-contact. The applied current and measured voltage across the micro-contact is used to calculate the micro-contact resistance. Plotting the micro-contact resistance against number of cycles will show the relative lifetime of the given micro-contact structure.

Hot-switch test will be stopped if one of these four conditions occur. First is if the desired number of cycles is completed. Second is if the distance of movement of the piezo actuator reaches its limit (19 μm). Third is if the max force sensor limit is reached without contact being made. This would occur if there was some film that cause the micro-contact not to make an

electrical contact. Lastly the test will stop if when the measurement cycle was started electrical contact was already made. This would occur if the upper and lower contact were already connected due to stiction.

COLD-SWITCH TEST

The following figure shows the block diagram for the cold-switch program.
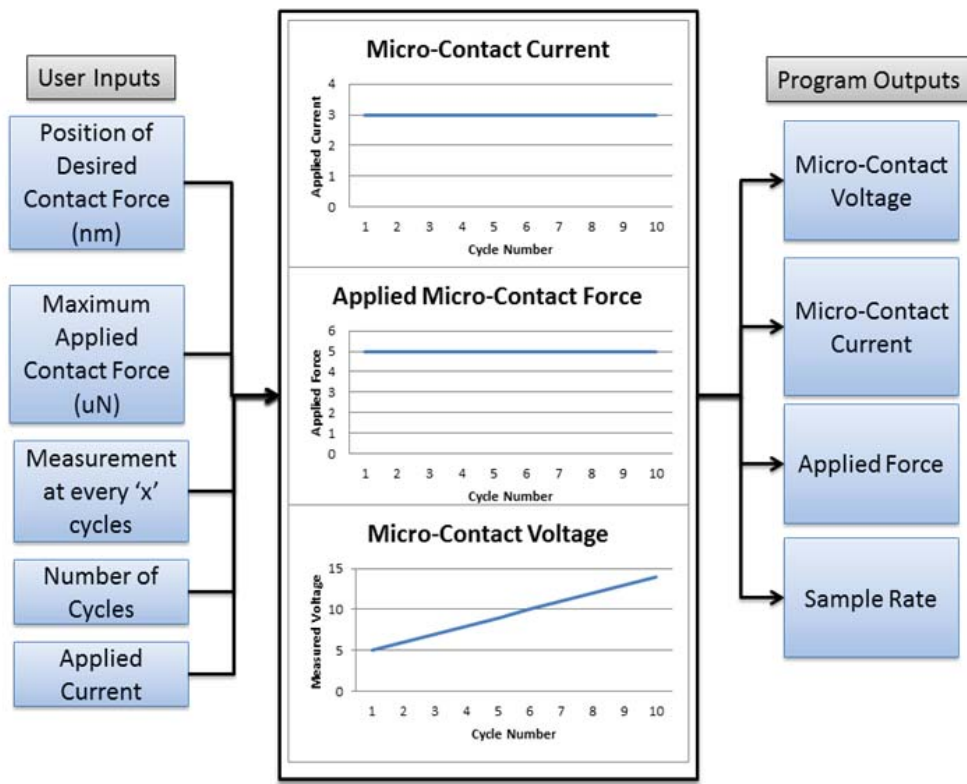
Figure 3 Cold-Switch Program Block Diagram

As with the hot-switch test program, the most important input is knowing the position the force sensor needs to be in order to apply the appropriate and desired contact force. Setting the maximum applied contact force establishes a force limit to protect the force sensor and the micro-contact structure. This limit is checked every measurement to ensure compliance. If the

force applied is greater than the limit, which can be caused by position drift, then the program reduces the position accordingly to apply the desired contact force. Position drift occurs through the repeated commands sent to the piezo control unit. Due to systematic errors in converting from digital to analog control signals, i.e. lab view to piezo controller to piezo motor, the position requested by the user is given to the controller but slight variances in the piezo motor actuation capability cause a drift in position. To raise the sample rate, the user may input the number of cycles between measurements. The time in which it takes one iteration of an actuation and measurement decreases without having to take a measurement. If desired, this feature allows the user to see only those data points after so many actuations. Specification of the number of cycles to perform and current to apply to the micro-contact allows for a characterization of the micro-contact for the given performance requirements.

The output of the cold-switch program is an excel file which contains the applied current and force, measured voltage, and calculated micro-contact resistance. The sample rate is also provided for the interest of rate of actuation. The information provided from this test can then be used to characterize the performance of the micro-contact. The applied current and measured voltage across the micro-contact is used to calculate the micro-contact resistance. Plotting the micro-contact resistance against number of cycles will show the relative lifetime of the given micro-contact structure.

Cold-switch test will be stopped if one of these four conditions occur. First is if the desired number of cycles is completed. Second is if the distance of movement of the piezo actuator reaches its limit (19 μm). Third is if the max force sensor limit is reached without contact being made. This would occur if there was some film that cause the micro-contact not to make an electrical contact. Lastly the test will stop if when the measurement cycle was started electrical

contact was already made. This would occur if the upper and lower contact were already connected due to stiction.

LAB VIEW PROGRAMMING INFORMATION

Lab View is a dataflow visual programming environment and general programming language. The interface allows users to 'code' based on the visualization of how data flows through the system they wish to implement. The following are screenshots of the graphical programming interface which comprise the automated data acquisition system. Following the screenshots is a general description of what each 'frame' of programming accomplishes.
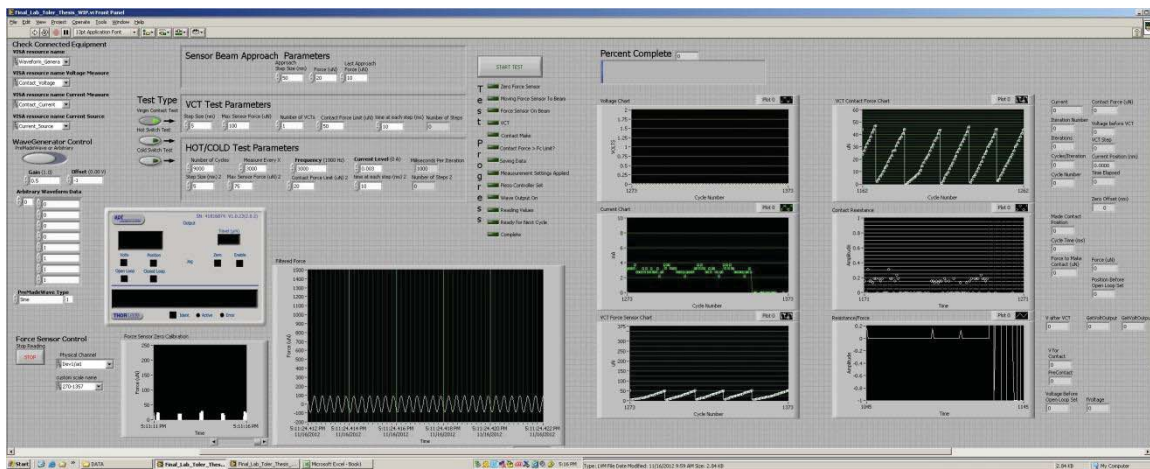
Figure 4 Lab View Data Acquisition System User Interface

Figure 4 shows the user interface for the automated data acquisition system. On this screen, the user may determine the test type to be performed, set the parameters, start and stop the test, and monitor the test's progress.
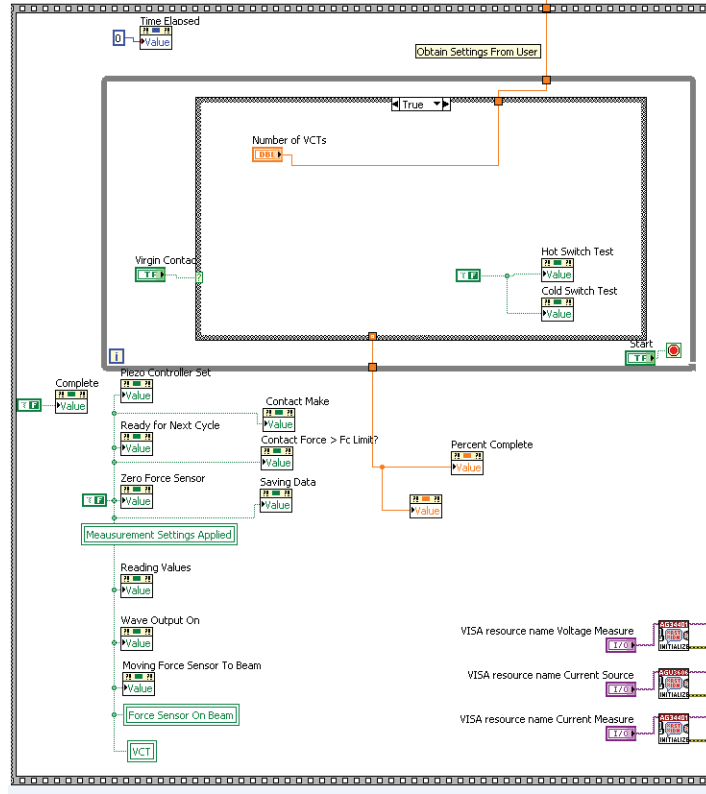
Figure 5 Frame 1 of the Graphical Programming for the Automated Data Acquisition System

Frame 1 is responsible for accepting the user's input for the desired test type and resetting the progress indicators on the main user interface screen. While loops within the frame allow the user to adjust parameters and settings before beginning the test.
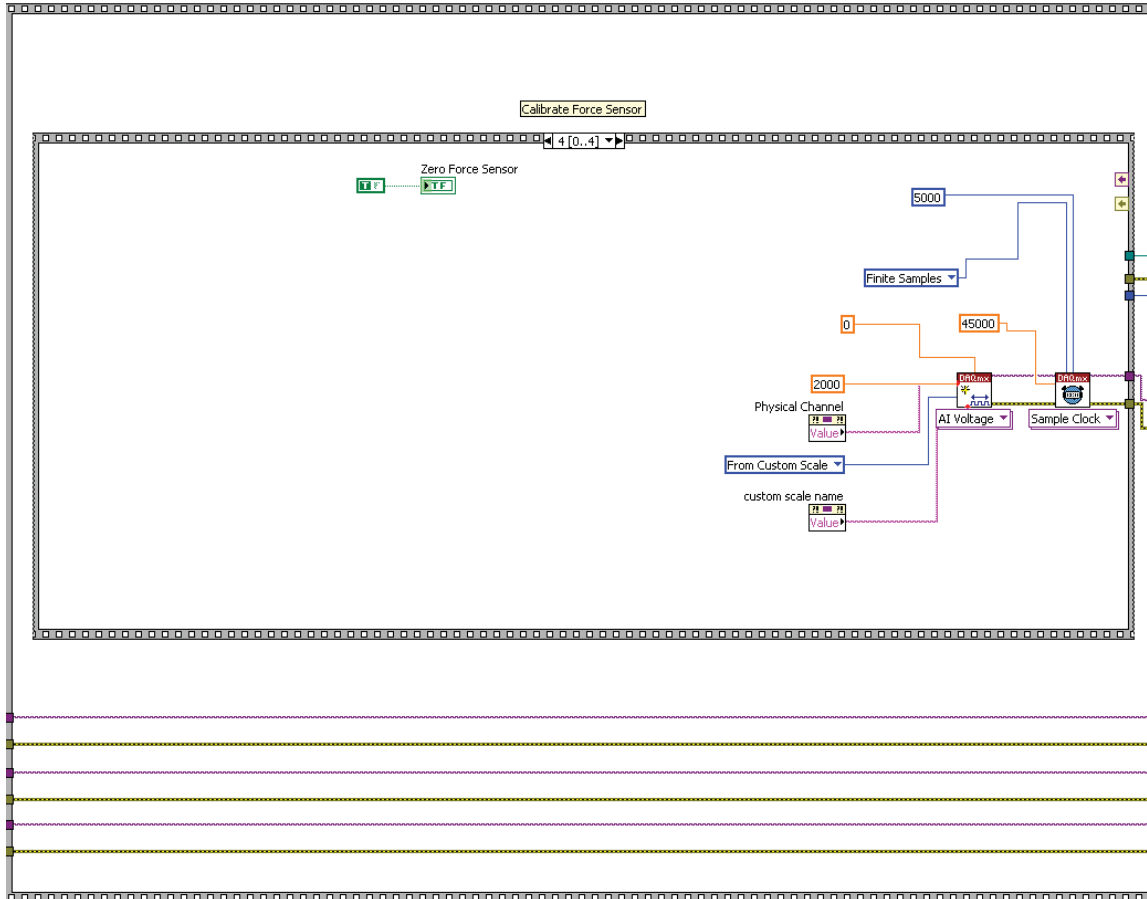
Figure 6 Frame 2 of the Graphical Programming for the Automated Data Acquisition System

Frame 2 is responsible for the calibration of the force sensor. In this frame, the piezo controller and the force sensor's sampling clock are initialized. The force sensor is then zeroed and the graph displaying the force sensor's output on the user interface screen is adjusted. The sampling condition of the force sensor is changed from continuous to finite sampling for the purpose of performing incremental measurements in the next frame.
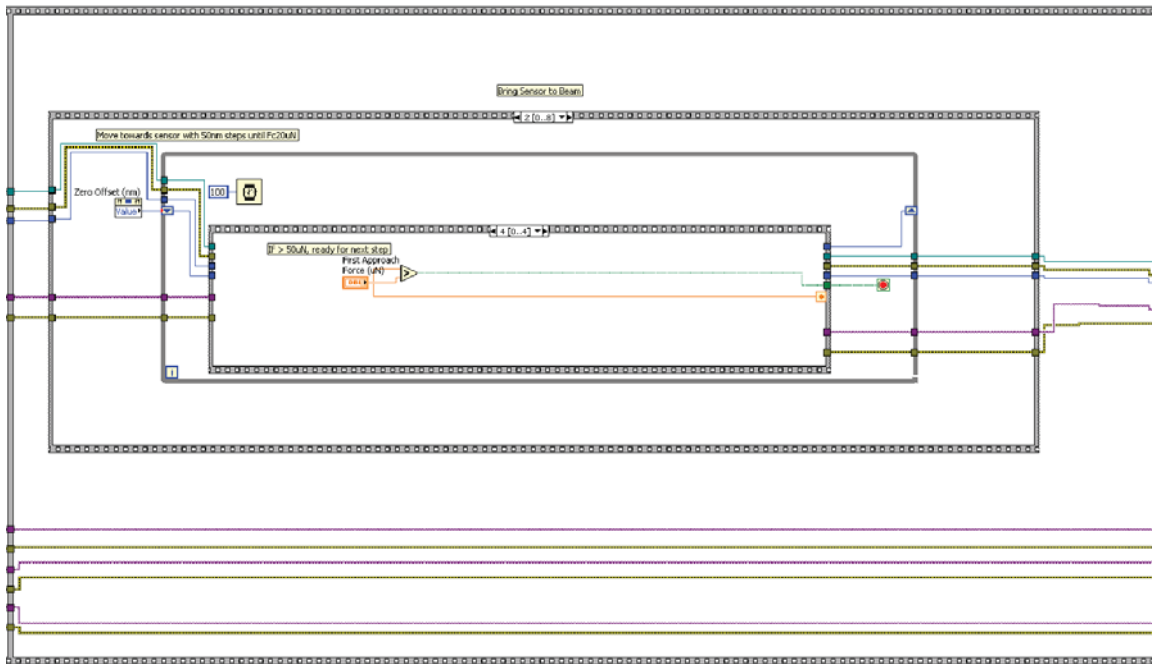
Figure 7 Frame 3 of the Graphical Programming for the Automated Data Acquisition System

In Frame 3, the force sensor is brought into contact with the micro-contact structure. To accomplish this, the user is prompted to use the micromanipulators on the test fixture in order to manually bring the force sensor into close, but not contact, proximity with the micro-contact structure. After the manual approach, the piezo actuator moves the sensor in steps set by the user before the start of the test until the force limit, also set by the user, is reached. The piezo actuator then moves the sensor away in 5 nm increments until a force less than 5 µN is read from the force sensor. The piezo actuator then moves the sensor towards the micro-contact structure until a force level greater than 5 µN is reached. The movement away and towards the micro-contact structure is repeated until a force of just less than 5 µN is measured on the last movement away from the micro-contact structure. The purpose of the back and forth movement is to verify contact with the micro-contact structure.
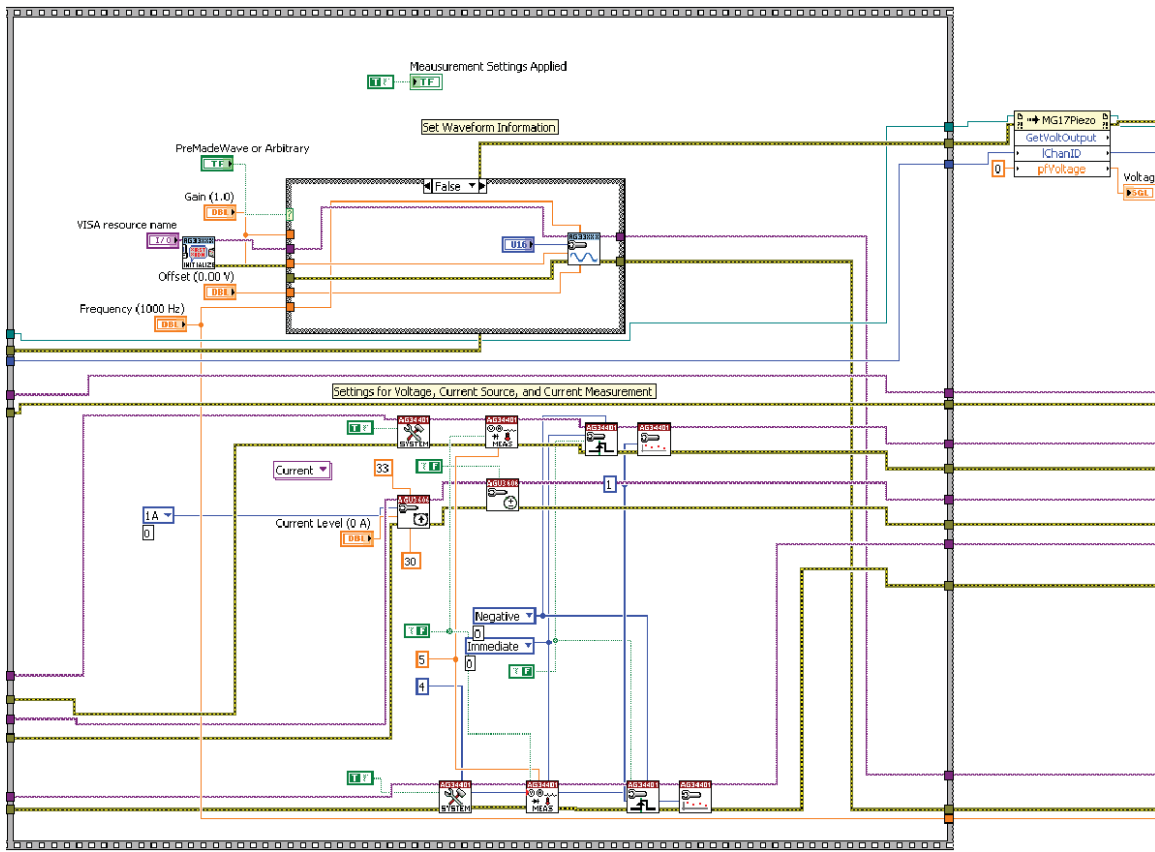
Figure 8 Frame 4 of the Graphical Programming for the Automated Data Acquisition System

At frame 4, the force sensor is now in contact with the micro-contact structure and the waveform information for the piezo controller is set. Also set in this frame are the voltage and current multimeters as well as the current source (if applicable).
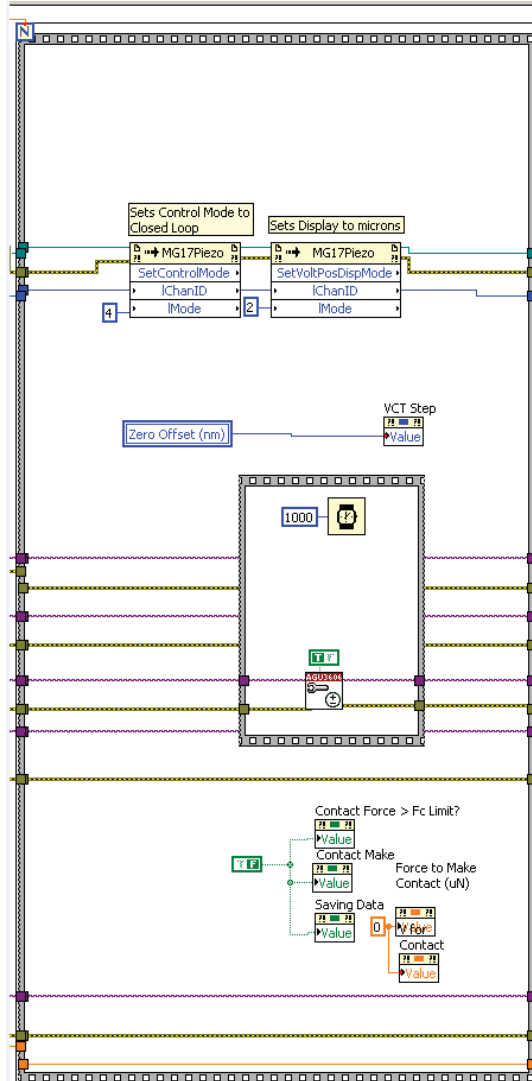
Figure 9 Frame 5 of the Graphical Programming for the Automated Data Acquisition System

Frame 5 is where the piezo controller is set to closed loop mode for accurate position control and the current source is turned on for the beginning of the ICT.
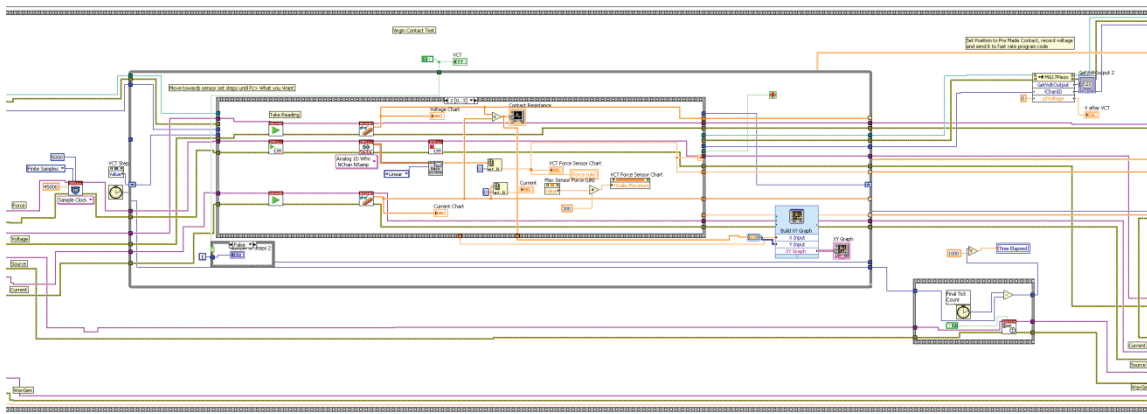
Figure 10 Frame 6 of the Graphical Programming for the Automated Data Acquisition System

Frame 6 is programmed to actually perform the ICT. In this frame, the force sensor is set to sample finite samples, then the piezo moves the sensor to actuate the micro-contact structure by increments set by the user. The system then waits at the incremental step for a period of time set by the user. Voltage, current, and force are read and displayed. The limits for contact force and maximum sensor force, which are set by the user, are checked. If the current measurement is greater than 0.02 mA then contact is considered to have been made. Once contact make has occurred, actual contact force is recorded. At this point, the ICT is complete and the position of the sensor is set back to its initial position.
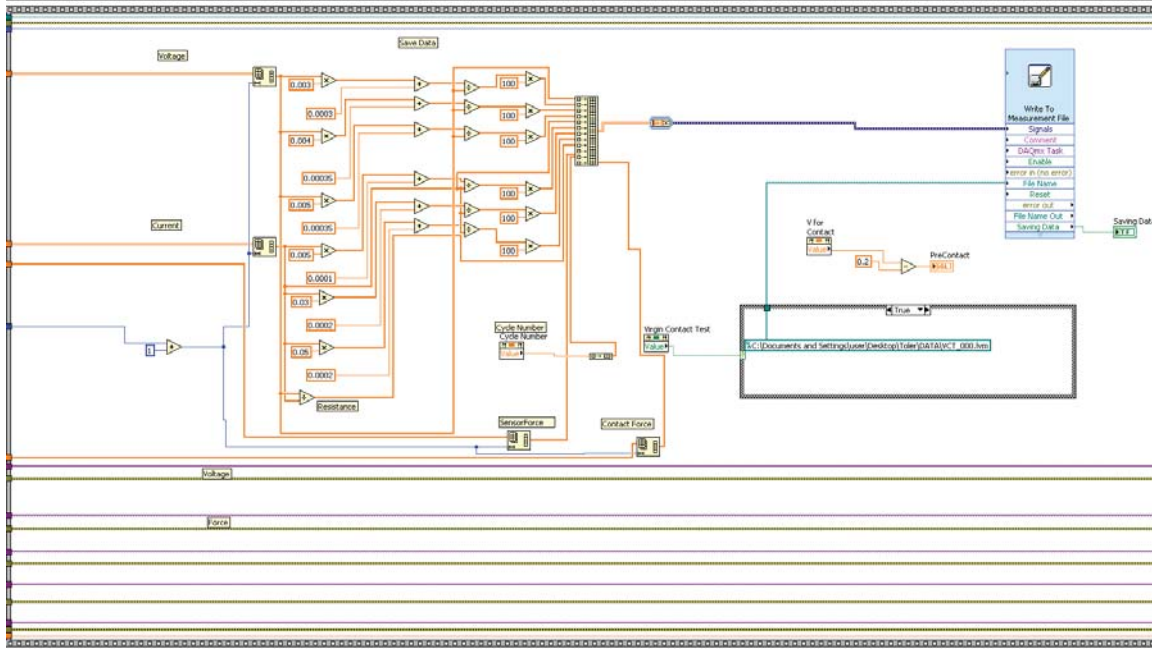
Figure 11 Frame 7 of the Graphical Programming for the Automated Data Acquisition System

In frame 7, the data from the ICT is recorded into an excel file. The data includes columns of voltage, current, resistance, sensor force, contact force, cycle number, and is placed in an excel file with a name designated for the test type being performed.
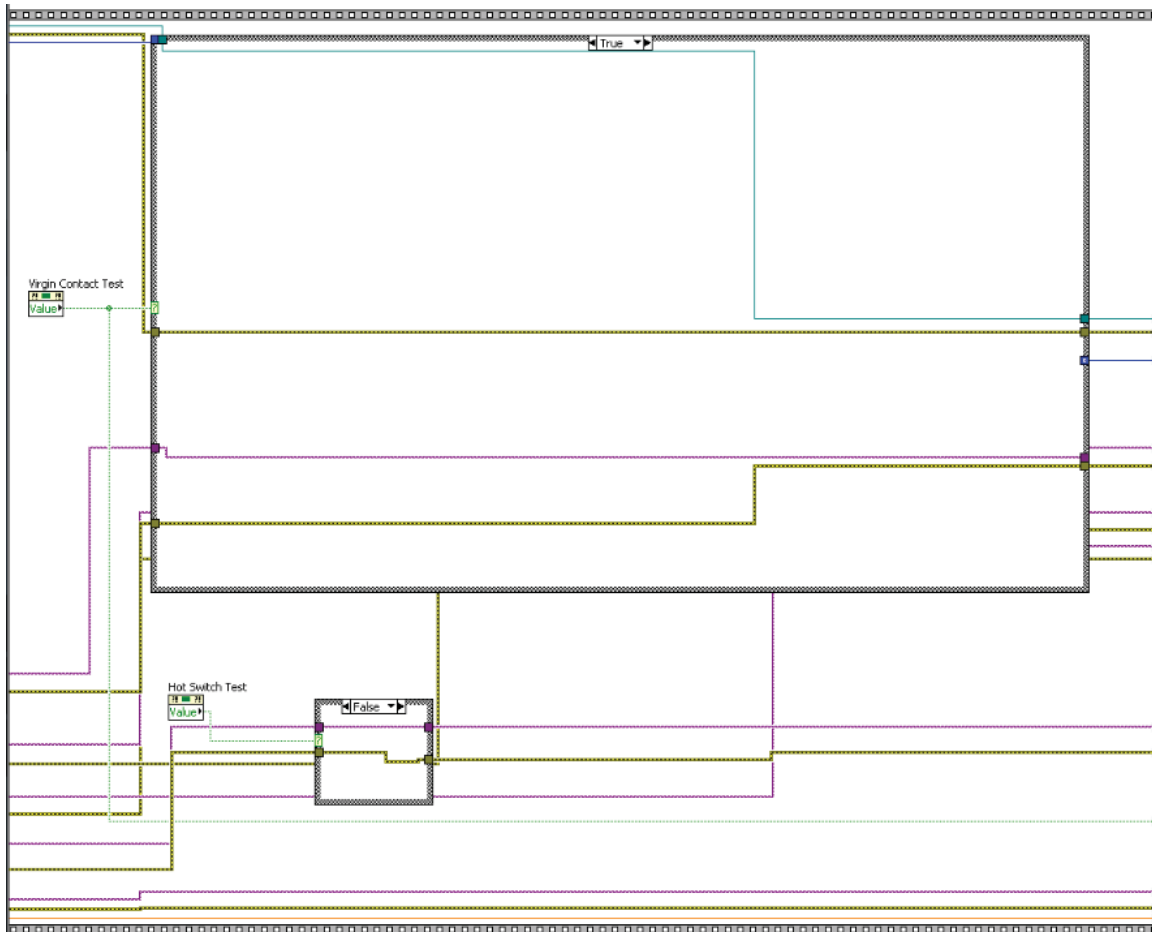
Figure 12 Frame 8 of the Graphical Programming for the Automated Data Acquisition System

Frame 8 is the programming responsible for the performance of a Hot or Cold test if applicable. The frame is skipped if the user has elected only to perform a ICT. In this frame, the current source is set and turned on for a Hot test or off for a Cold test. The piezo controller is then set to open loop mode in order to accommodate fast rate testing.
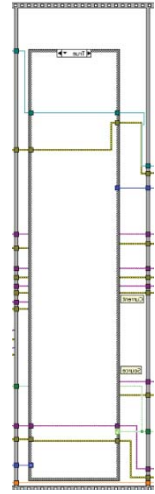
Figure 13 Frame 9 of the Graphical Programming for the Automated Data Acquisition System

Frame 9 contains the programming for applying the waveform chosen by the user to the

piezo controller. A conditional loop checks to see if the user desires a fast rate test and skips the

frame if false. Under the true condition, the frame applies the waveform.
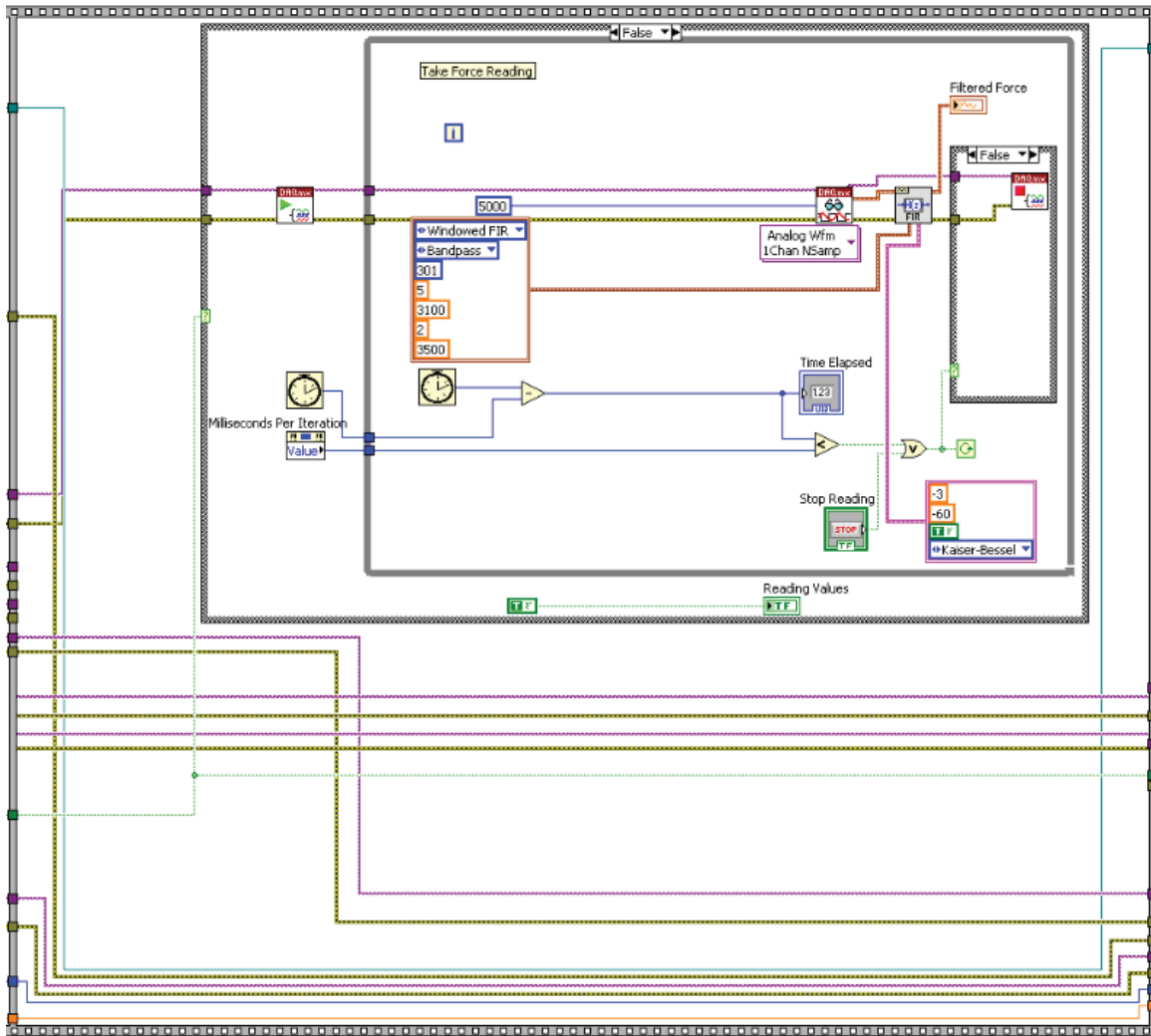
Figure 14 Frame 10 of the Graphical Programming for the Automated Data Acquisition System

The force sensor is set to continuous mode in order to display the force sensor readings on the user interface during a fast rate Cold or Hot test. Frame 10 filters the output of the force sensor appropriately to verify to the user that the desired waveform has been applied.
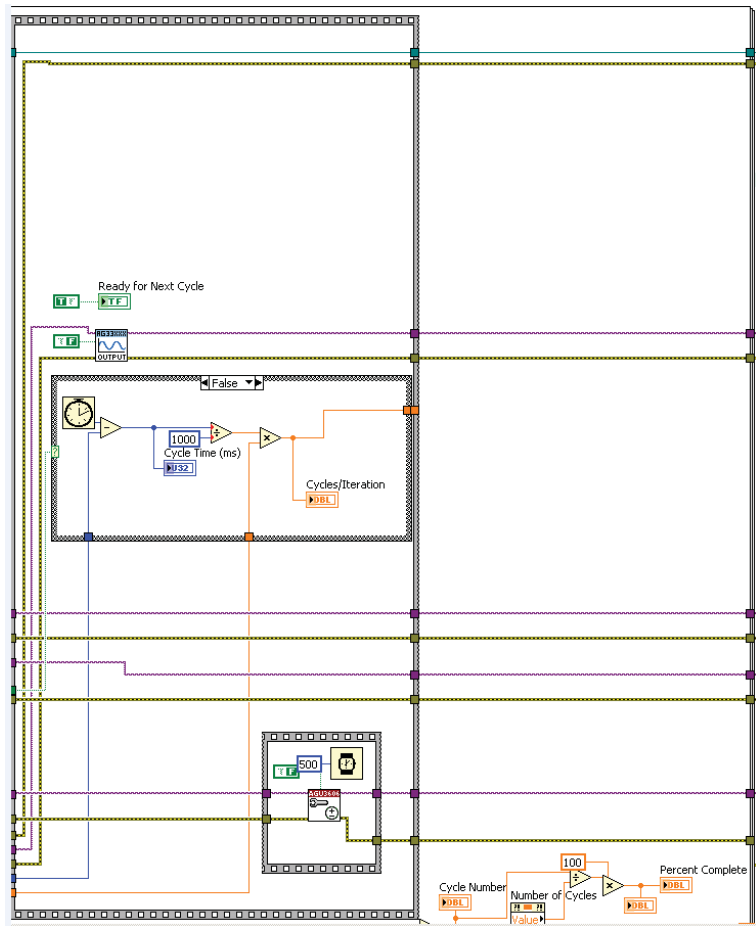
Figure 15 Frame 11 of the Graphical Programming for the Automated Data Acquisition System

In frame 11, the current source is turned off if needed and the cycle number is determined in order to check if the desired number of cycles have been performed. If the desired number of cycles have been performed then the for loop condition is complete and the program moves to frame 12. If the cycle count is below that of the set number, then the for loop iterates back to frame 5.
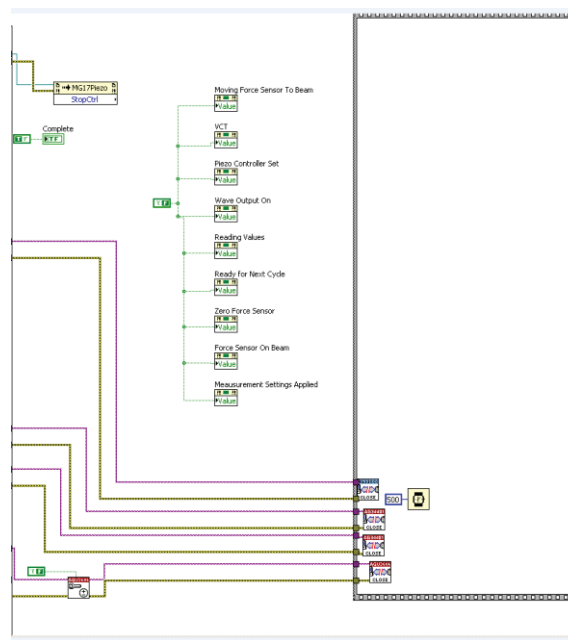
Figure 16 Frame 12 of the Graphical Programming for the Automated Data Acquisition System

Frame 12 contains the programming responsible for adjusting the progress indicators and closing communications with the equipment used to perform the testing.

Appendix G: Visual Bibliography

The following page is and example of a visual bibliography. A visual bibliography uses a picture containing connections between people and papers. Some examples of connections that can be made include topics, authors, schools, and funding sources. This can be used as a way to visual map these connections. Bing uses a type of visual bibliography to display there different formats including; connections between authors, co-author connections, and citations. The figure below is an example of Major Langley's co-author connections on Bing. The following page displays a visual bibliography covering key-words that was done on a few key papers to this research.
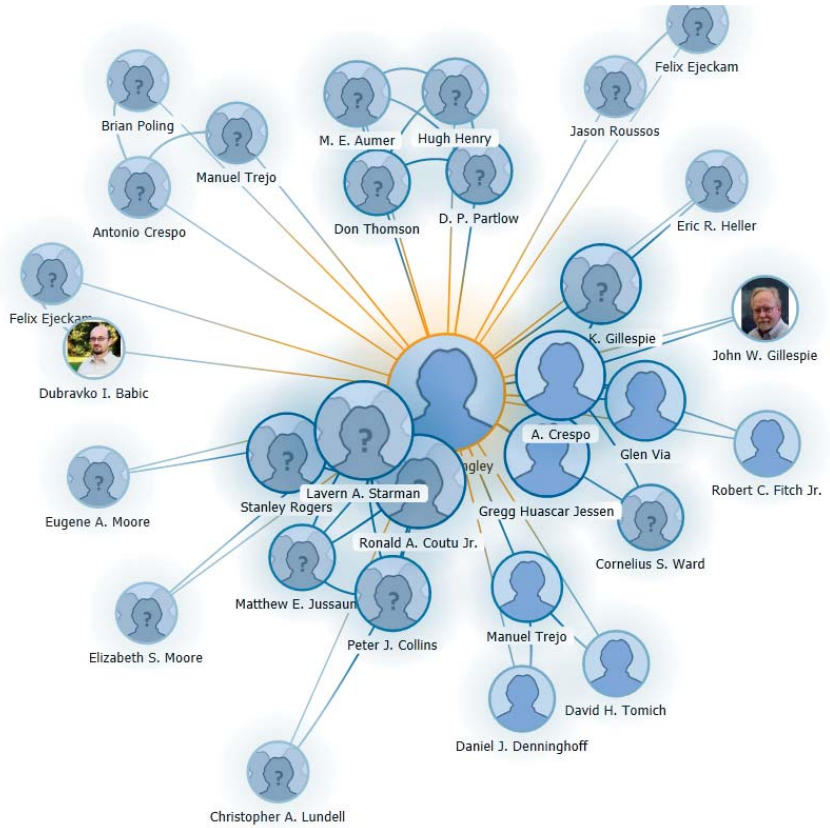
Figure G.1: An example of Major Langley's co-author connections are displayed on Bing
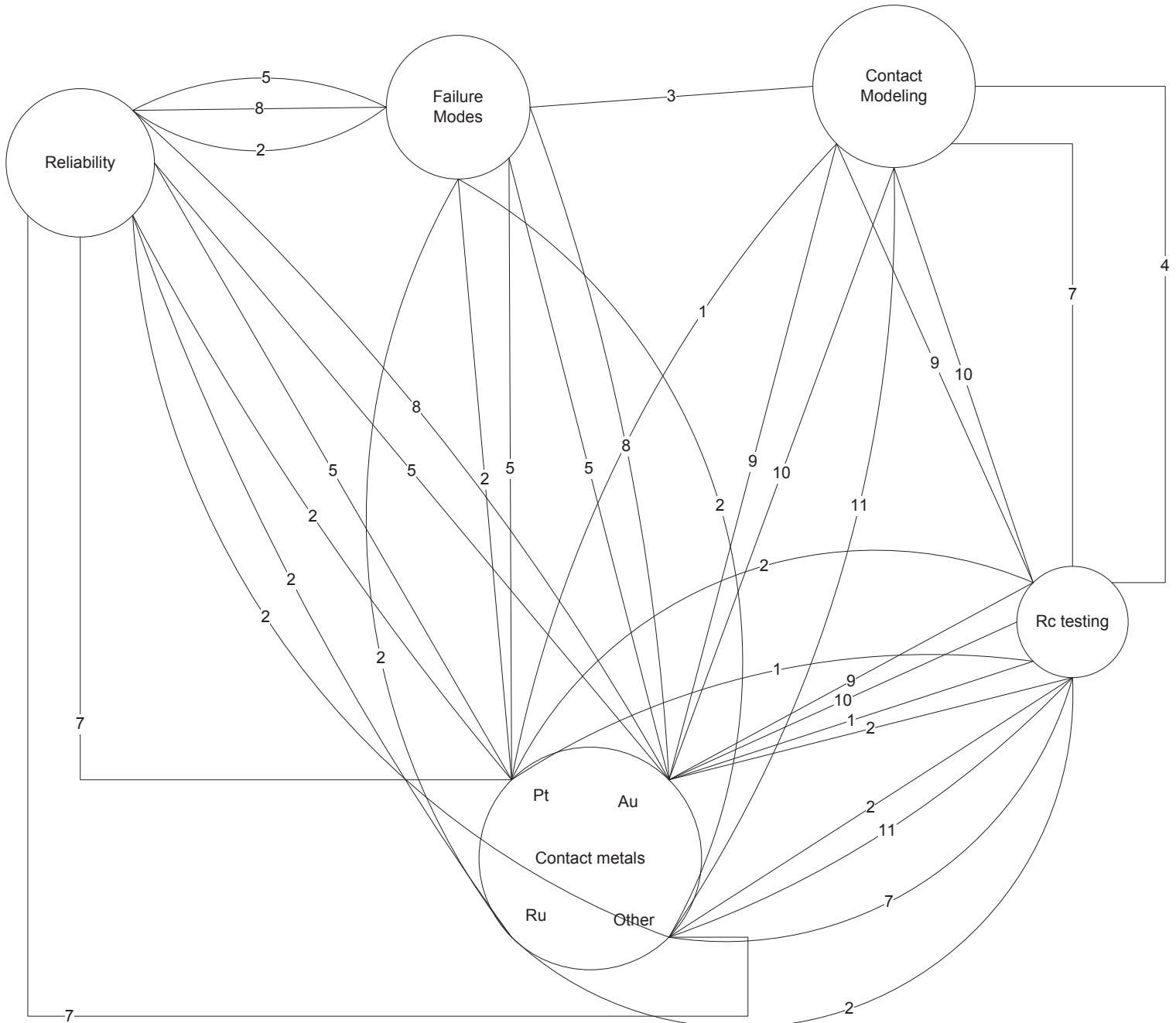
1	Selecting metal alloy electric contact materials for MEMS switches
2	Contact resistance study of noble metals and alloy films using a scanning probe microscope test station
3	A Micro–Macroapproach to Predict Stiction due to Surface Contact in Microelectromechanical Systems
4	A Finite Element Study of Elasto-Plastic Hemispherical Contact Against a Rigid Flat
5	Lifetime limitations of ohmic, contacting RF MEMS switches with Au, Pt and Ir contact materials
6	RF MEMs switches with RuO2-Au contacts switches to 10 billion cycles
7	Microswitches with Sputtered Au, AuPd, Au-on-AuPt, and AuPtCu Alloy Electrical Contacts
8	Contact degradation in hot/cold operation of direct contact micro-switches
9	Contact resistance of thin metal film contacts
10	Modeling, simulation and measurement of the dynamic performance of an ohmic contact, electrostatically actuated RF MEMS switch
11	Comparison of au and au–ni alloys as contact materials for mems switches

Bibliography

[1] G. Rebeiz, *RF MEMS: Theory, Design, and Technology*. Wiley, 2004.

[2] K. Van Caekenberghe, "Rf mems on the radar," *Microwave Magazine, IEEE*, vol. 10, no. 6, pp. 99–116, 2009.

[3] Z. Yang, D. J. Lichtenwalner, A. S. Morris, J. Krim, and A. I. Kingon, "Comparison of au and au–ni alloys as contact materials for mems switches," *Microelectromechanical Systems, Journal of*, vol. 18, no. 2, pp. 287–295, 2009.

[4] R. H. Dennard, J. Cai, and A. Kumar, "A perspective on todays scaling challenges and possible future directions," *Solid-State Electronics*, vol. 51, no. 4, pp. 518–525, 2007.

[5] K. Ehwald, R. Scholz, F. Korndorfer, C. Wipf, Y. Sun, B. Tillack, S. Zihir, Y. Gurbuz, *et al.*, "Characterization of an embedded rf-mems switch," in *Silicon Monolithic Integrated Circuits in RF Systems (SiRF), 2010 Topical Meeting on*, pp. 144–147, IEEE, 2010.

[6] P. M. Zavracky, S. Majumder, and N. E. McGruer, "Micromechanical switches fabricated using nickel surface micromachining," *Microelectromechanical Systems, Journal of*, vol. 6, no. 1, pp. 3–9, 1997.

[7] Z. Yang, D. Lichtenwalner, A. Morris, S. Menzel, C. Nauenheim, A. Gruverman, J. Krim, and A. Kingon, "A new test facility for efficient evaluation of mems contact materials," *Journal of Micromechanics and Microengineering*, vol. 17, no. 9, p. 1788, 2007.

[8] B. Toler, "Novel test fixture for characterizing microcontacts: Performacne and reliability," Master's thesis, Air Force Institute of Technology, 2013.

[9] R. Holm, *Electric Contacts: Theory and Applications, Fourth Edition ed.* fourth ed., 1967.

[10] M. Braunovic, N. K. Myshkin, and V. V. Konchits, *Electrical Contacts: Fundamentals, Applications and Technology*. Taylor & Francis, 2010. 2006015470.

[11] R. A. Coutu, J. W. McBride, and L. A. Starman, "Improved micro-contact resistance model that considers material deformation, electron transport and thin film characteristics," in *Electrical Contacts, 2009 Proceedings of the 55th IEEE Holm Conference on*, pp. 298–302, 2009. ID: 1.

[12] S. Majumder, N. E. McGruer, G. G. Adams, A. Zavracky, P. M. Zavracky, R. H. Morrison, and J. Krim, "Study of contacts in an electrostatically actuated

microswitch," in *Electrical Contacts, 1998. Proceedings of the Forty-Fourth IEEE Holm Conference on*, pp. 127–132, 1998. ID: 1.

[13] W.-R. Chang, "An elastic-plastic contact model for a rough surface with an ion-plated soft metallic coating," *Wear*, vol. 212, pp. 229–237, 12/10 1997.

[14] R. A. Coutu, J. R. Reid, R. Cortez, R. E. Strawser, and P. E. Kladitis, "Microswitches with sputtered au, aupd,au-on-aupt, and auptcu alloy electric contacts," *Components and Packaging Technologies, IEEE Transactions on*, vol. 29, no. 2, pp. 341–349, 2006. ID: 1.

[15] F. Firestone and E. Abbot, "Specifying surface quantity - a method based on the accurate measurement and comparison," *ASME Mech. Eng*, vol. 55, p. 569, 1933.

[16] H. Kwon, J.-H. Park, H.-C. Lee, D.-J. Choi, Y.-H. Park, H.-J. Nam, and Y.-C. Joo, "Investigation of similar and dissimilar metal contacts for reliable radio frequency micorelectromechanical switches," *Japanese Journal of Applied Physics-Part 1Regular Papers and Short Notes*, vol. 47, no. 8, p. 6558, 2008.

[17] S. Karmalkar, P. V. Mohan, and B. P. Kumar, "A unified compact model of electrical and thermal 3-d spreading resistance between eccentric rectangular and circular contacts," *Electron Device Letters, IEEE*, vol. 26, no. 12, pp. 909–912, 2005.

[18] R. Timsit, "Constriction resistance of thin film contacts," *Components and Packaging Technologies, IEEE Transactions on*, vol. 33, no. 3, pp. 636–642, 2010.

[19] P. Zhang, Y. Lau, and R. S. Timsit, "Spreading resistance of a contact spot on a thin film," in *Holm Conference on Electrical Contacts (HOLM), 2013 IEEE 59th*, pp. 1–7, IEEE, 2013.

[20] R. S. Timsit, "Electrical contact resistance: properties of stationary interfaces," *Components and Packaging Technologies, IEEE Transactions on*, vol. 22, no. 1, pp. 85–98, 1999.

[21] Y. H. Jang, J. Barber, and S. J. Hu, "Electrical conductance between conductors with dissimilar temperature-dependent material properties," *Journal of Physics D: Applied Physics*, vol. 31, no. 22, p. 3197, 1998.

[22] M. Read, J. Lang, A. Slocum, and R. Martens, "Contact resistance in flat thin films," Institute of Electrical and Electronics Engineers, 2009.

[23] P. Hall, "Resistance calculations for thin film patterns," *Thin Solid Films*, vol. 1, no. 4, pp. 277–295, 1968.

[24] S. Sawada, S. Tsukiji, S. Shimada, T. Tamai, and Y. Hattori, "Current density analysis of thin film effect in contact area on led wafer," in *Electrical Contacts (Holm), 2012 IEEE 58th Holm Conference on*, pp. 1–6, IEEE, 2012.

[25] F. Pennec, D. Peyrou, D. Leray, P. Pons, R. Plana, and F. Courtade, "Impact of the surface roughness description on the electrical contact resistance of ohmic switches under low actuation forces," *Components, Packaging and Manufacturing Technology, IEEE Transactions on*, vol. 2, no. 1, pp. 85–94, 2012.

[26] J. I. McCool, "Comparison of models for the contact of rough surfaces," *Wear*, vol. 107, no. 1, pp. 37–60, 1986.

[27] A. Majumdar and C. Tien, "Fractal characterization and simulation of rough surfaces," *Wear*, vol. 136, no. 2, pp. 313–327, 1990.

[28] L. Kogut and R. L. Jackson, "A comparison of contact modeling utilizing statistical and fractal approaches," *Journal of tribology*, vol. 128, no. 1, pp. 213–217, 2006.

[29] L. Kogut and I. Etsion, "A finite element based elastic-plastic model for the contact of rough surfaces," *Tribology Transactions*, vol. 46, no. 3, pp. 383–390, 2003.

[30] J. Greenwood, "A unified theory of surface roughness," *Proceedings of the Royal Society of London. A. Mathematical and Physical Sciences*, vol. 393, no. 1804, pp. 133–157, 1984.

[31] J. Greenwood and J. Williamson, "Contact of nominally flat surfaces," *Proceedings of the Royal Society of London. Series A. Mathematical and Physical Sciences*, vol. 295, no. 1442, pp. 300–319, 1966.

[32] W. E. Wilson, S. V. Angadi, and R. L. Jackson, "Electrical contact resistance considering multi-scale roughness," in *Electrical Contacts, 2008. Proceedings of the 54th IEEE Holm Conference on*, pp. 190–197, IEEE, 2008.

[33] R. L. Jackson, "A model for the adhesion of multiscale rough surfaces in mems," in *System Theory (SSST), 2011 IEEE 43rd Southeastern Symposium on*, pp. 257–262, IEEE, 2011.

[34] J. W. McBride, R. A. Coutu, and L. A. Starman, "Improved micro-contact resistance model that considers material deformation, electron transport and thin film characteristics," 2009.

[35] R. A. Coutu Jr, P. E. Kladitis, K. D. Leedy, and R. L. Crane, "Selecting metal alloy electric contact materials for mems switches," *Journal of Micromechanics and Microengineering*, vol. 14, no. 8, p. 1157, 2004.

[36] L. Chen, H. Lee, Z. Guo, N. E. McGruer, K. Gilbert, S. Mall, K. D. Leedy, and G. G. Adams, "Contact resistance study of noble metals and alloy films using a scanning probe microscope test station," *Journal of Applied Physics*, vol. 102, no. 7, pp. 074910–074910, 2007.

[37] A. Broue, J. Dhennin, P. Charvet, P. Pons, N. B. Jemaa, P. Heeb, F. Coccetti, and R. Plana, "Multi-physical characterization of micro-contact materials for mems switches," in *Electrical Contacts (HOLM), 2010 Proceedings of the 56th IEEE Holm Conference on*, pp. 1–10, IEEE, 2010.

[38] J. M. Gere and B. J. Goodno, *Mechanics of materials*. Cengage Learning, 1984.

[39] K. B. Lee, *Principles of microelectromechanical systems*. John Wiley & Sons, 2011.

[40] D. Koester, A. Cowen, R. Mahadevan, M. Stonefield, and B. Hardy, "Polymumps design handbook," *MEMSCAP Inc*, 2003.

[41] C. Waits, B. Morgan, M. Kastantin, and R. Ghodssi, "Microfabrication of 3d silicon mems structures using gray-scale lithography and deep reactive ion etching," *Sensors and Actuators A: Physical*, vol. 119, no. 1, pp. 245–253, 2005.

[42] C. Beuret, G.-A. Racine, J. Gobet, R. Luthier, and N. de Rooij, "Microfabrication of 3d multidirectional inclined structures by uv lithography and electroplating," in *Micro Electro Mechanical Systems, 1994, MEMS'94, Proceedings, IEEE Workshop on*, pp. 81–85, IEEE, 1994.

[43] Y. Oppliger, P. Sixt, J. Stauffer, J. Mayor, P. Regnault, and G. Voirin, "One-step 3d shaping using a gray-tone mask for optical and microelectronic applications," *Microelectronic Engineering*, vol. 23, no. 1, pp. 449–454, 1994.

[44] T. J. Suleski, D. C. O?Shea, *et al.*, "Gray-scale masks for diffractive-optics fabrication: I. commercial slide imagers," *Applied Optics*, vol. 34, no. 32, pp. 7507–7517, 1995.

[45] B. Wagner, H. Quenzer, W. Henke, W. Hoppe, and W. Pilz, "Microfabrication of complex surface topographies using grey-tone lithography," *Sensors and Actuators A: Physical*, vol. 46, no. 1, pp. 89–94, 1995.

[46] T.-K. Chou and K. Najafi, "Fabrication of out-of-plane curved surfaces in si by utilizing rie lag," in *Micro Electro Mechanical Systems, 2002. The Fifteenth IEEE International Conference on*, pp. 145–148, IEEE, 2002.

[47] Heidelberg Instruments, *HEIDELBERG INSTRUMENTS µPG 101 User Manual*, 2008.

[48] A. Broue, J. Dhennin, F. Courtade, C. Dieppedale, P. Pons, X. Lafontan, and R. Plana, "Characterization of au/au, au/ru and ru/ru ohmic contacts in mems switches improved by a novel methodology," in *Proceedings of SPIE*, vol. 7592, p. 75920A, 2010.

[49] B. Arrazat, P.-Y. Duvivier, V. Mandrillon, and K. Inal, "Discrete analysis of gold surface asperities deformation under spherical nano-indentation towards electrical

contact resistance calculation," in *Electrical Contacts (Holm), 2011 IEEE 57th Holm Conference on*, pp. 1–8, 2011.

[50] N. McGruer, G. Adams, L. Chen, Z. Guo, and Y. Du, "Mechanical, thermal, and material influences on ohmic-contact-type mems switch operation," in *Micro Electro Mechanical Systems, 2006. MEMS 2006 Istanbul. 19th IEEE International Conference on*, pp. 230–233, IEEE, 2006.

[51] A. Fortini, M. I. Mendelev, S. Buldyrev, and D. Srolovitz, "Asperity contacts at the nanoscale: Comparison of ru and au," *Journal of Applied Physics*, vol. 104, no. 7, pp. 074320–074320, 2008.

[52] L.-J. Meng and M. dos Santos, "A study of residual stress on rf reactively sputtered ruo¡ sub¿ 2¡/sub¿ thin films," *Thin Solid Films*, vol. 375, no. 1, pp. 29–32, 2000.

[53] H.-Y. Lee, Y.-W. Hsieh, C.-H. Hsu, and K. Liang, "Characteristics of sputter-deposited ru thin films on si substrates," *Materials chemistry and physics*, vol. 82, no. 3, pp. 984–990, 2003.

[54] O. Yaglioglu, A. J. Hart, R. Martens, and A. H. Slocum, "Method of characterizing electrical contact properties of carbon nanotube coated surfaces," *Review of Scientific Instruments*, vol. 77, p. 095105, September 2006 2006.

[55] E. M. Yunus, S. M. Spearing, and J. W. McBride, "The relationship between contact resistance and contact force on au-coated carbon nanotube surfaces under low force conditions," *Components and Packaging Technologies, IEEE Transactions on*, vol. 32, no. 3, pp. 650–657, 2009. ID: 1.

[56] J. Choi, J.-I. Lee, Y. Eun, M.-O. Kim, and J. Kim, "Microswitch with self-assembled carbon nanotube arrays for high current density and reliable contact," in *Micro Electro Mechanical Systems (MEMS), 2011 IEEE 24th International Conference on*, pp. 87–90, 2011. ID: 1.

[57] B. F. Toler, R. A. Coutu Jr, and J. W. McBride, "A review of micro-contact physics for microelectromechanical systems (mems) metal contact switches," *Journal of Micromechanics and Microengineering*, vol. 23, no. 10, p. 103001, 2013.

[58] R. Maboudian and R. T. Howe, "Critical review: adhesion in surface micromechanical structures," *Journal of Vacuum Science & Technology B: Microelectronics and Nanometer Structures*, vol. 15, no. 1, pp. 1–20, 1997.

[59] P. Prokopovich and S. Perni, "Comparison of jkr-and dmt-based multi-asperity adhesion model: Theory and experiment," *Colloids and Surfaces A: Physicochemical and Engineering Aspects*, vol. 383, no. 1, pp. 95–101, 2011.

[60] L. Wu, L. Noels, V. Rochus, M. Pustan, and J.-C. Golinval, "A micro–macroapproach to predict stiction due to surface contact in microelectromechanical systems," *Microelectromechanical Systems, Journal of*, vol. 20, no. 4, pp. 976–990, 2011.

[61] M. Braunovic, N. K. Myshkin, and V. V. Konchits, *Electrical contacts: fundamentals, applications and technology*, vol. 132. CRC press, 2010.

[62] M. Braunovic, N. Myshkin, and V. Konchits, *Electrical Contacts-Fundamentals, Applications and Technology* . New York: CRC Press, 2007.

[63] W.-R. Chang, "An elastic-plastic contact model for a rough surface with an ion-plated soft metallic coating," *Wear*, vol. 212, no. 2, pp. 229–237, 1997.

[64] B. Toler, C. Stilson, and R. Coutu, "Contact resistance evolution of au-au micro-contacts with encapsulated ag colloids," in *Holm Conference on Electrical Contacts (HOLM), 2013 IEEE 59th*, pp. 1–8, IEEE, 2013.

[65] C. Stilson, B. Toler, and R. Coutu, "Micro-contact performance characterization of carbon nanotube (cnt)-au composite micro-contacts," in *Holm Conference on Electrical Contacts (HOLM), 2013 IEEE 59th*, pp. 1–9, IEEE, 2013.

[66] Y.-T. Kim, "Achievement of zero temperature coefficient of resistance with ruox thin film resistors," *Applied Physics Letters*, vol. 70, no. 2, pp. 209–211, 1997.

[67] W. T. Lim, K. R. Cho, and C. H. Lee, "Structural and electrical properties of rf-sputtered ruo¡ sub¿ 2¡/sub¿ films having different conditions of preparation," *Thin Solid Films*, vol. 348, no. 1, pp. 56–62, 1999.

[68] Z. Yang, D. Lichtenwalner, A. Morris, J. Krim, and A. Kingon, "Contact degradation in hot/cold operation of direct contact micro-switches," *Journal of Micromechanics and Microengineering*, vol. 20, no. 10, p. 105028, 2010.

[69] G. Yang, X. Liao, and Z. Zhang, "Young's modulus and residual stress of mems gold beams based on the gaas mmic process," *Journal of Micromechanics and Microengineering*, vol. 23, no. 4, p. 045002, 2013.

[70] A. Volinsky, N. Moody, and W. Gerberich, "Nanoindentation of au and pt/cu thin films at elevated temperatures," *J. Mater. Res.*, vol. 19, no. 9, p. 2650, 2004.

REPORT DOCUMENTATION PAGE

Form Approved
OMB No. 0704–0188

1. REPORT DATE *(DD–MM–YYYY)*	2. REPORT TYPE	3. DATES COVERED *(From — To)*
27–03–2014	Master's Thesis	Oct 2013–Mar 2014

4. TITLE AND SUBTITLE

Contact Resistance Evolution and Degradation of Highly Cycled Micro-Contacts

5a. CONTRACT NUMBER

5b. GRANT NUMBER

5c. PROGRAM ELEMENT NUMBER

6. AUTHOR(S)

Stilson, Christopher L., Captain, USAF

5d. PROJECT NUMBER

5e. TASK NUMBER

5f. WORK UNIT NUMBER

7. PERFORMING ORGANIZATION NAME(S) AND ADDRESS(ES)

Air Force Institute of Technology
Graduate School of Engineering and Management (AFIT/EN)
2950 Hobson Way
WPAFB, OH 45433-7765

8. PERFORMING ORGANIZATION REPORT NUMBER

AFIT-ENG-14-M-73

9. SPONSORING / MONITORING AGENCY NAME(S) AND ADDRESS(ES)

Intentionally Left Blank

10. SPONSOR/MONITOR'S ACRONYM(S)

11. SPONSOR/MONITOR'S REPORT NUMBER(S)

12. DISTRIBUTION / AVAILABILITY STATEMENT

DISTRIBUTION STATEMENT A:
APPROVED FOR PUBLIC RELEASE; DISTRIBUTION UNLIMITED

13. SUPPLEMENTARY NOTES

This work is declared a work of the U.S. Government and is not subject to copyright protection in the United States.

14. ABSTRACT

Reliable microelectromechanical systems (MEMS) switches are critical for developing high performance radio frequency circuits like phase shifters. Engineers have attempted to improve reliability and lifecycle performance using novel contact metals, unique mechanical designs and packaging. Various test fixtures including: MEMS devices, atomic force microscopes (AFM) and nanoindentors have been used to collect resistance and contact force data. AFM and nanoindentor test fixtures allow direct contact force measurements but are severely limited by low resonance sensors, and therefore low data collection rates.

This thesis reports the contact resistance evolution results and fabrication of thin film micro-contacts dynamically tested up to 3kHz. The contacts consisted of a lower contact of evaporated Au and a thin film upper contact, consisting of sputtered Au, Ru or RuO_2, with an Au electroplated structural layer. The fixed-fixed beam was designed with sufficient restoring force to overcome adhesion. The hemisphere-upper and planar-lower contacts are mated with a calibrated, external load resulting in approximately $200\mu N$ of contact force and are cycled in excess of 10^7 times or until failure. In addition, Au-Au contact pairs with a hemispherical upper an engineered lower contact were tested. These lower engineered contacts were constructed using gray-scale lithography. Contact resistance was measured, in-situ, using Holm's a cross-bar configuration and the entire apparatus was isolated from external vibration and housed in an enclosure to minimize contamination due to the ambient environment. Additionally, contact cycling and data collection are automated using a computer, integrated lab equipment and LabVIEW. Results include contact resistance measurements of Au, Ru and RuO_2 samples and lifetime testing up to 323.6 million cycles.

15. SUBJECT TERMS

Micro-contact, Gray-scale, Ruthenium, Ruthenium Oxide, contact resistance

16. SECURITY CLASSIFICATION OF:			17. LIMITATION OF ABSTRACT	18. NUMBER OF PAGES	19a. NAME OF RESPONSIBLE PERSON
a. REPORT	b. ABSTRACT	c. THIS PAGE			Dr. Ronald Coutu, Jr. (ENG)
U	U	U	U	252	19b. TELEPHONE NUMBER *(include area code)* (937) 255-3636 x7230 Ronald.Coutu@afit.edu

Standard Form 298 (Rev. 8–98)
Prescribed by ANSI Std. Z39.18